UNIVERSITAT DE BARCELONA

Computational Modelling of TiO_2 and Mg-silicate nanoclusters and nanoparticles - Crystallinity and Astrophysical Implications

Antoni Macià Escatllar

Memòria presentada per

Antoni Macià Escatllar

Per a optar al grau de Doctor per la Universitat de Barcelona

Programa de doctorat en Química Teòrica i Computacional

Computational Modelling of TiO_2 and Mg-silicate nanoclusters and nanoparticles - crystallinity and astrophysical implications

Dirigida per:

Dr. Stefan T. Bromley i Dr. Francesc Illas Riera

Universitat de Barcelona i Institució Catalana de Recerca i Estudis avançats

UNIVERSITAT DE BARCELONA

Barcelona, 2020

UNIVERSITAT DE BARCELONA
FACULTAT DE QUÍMICA
DEPARTAMENT DE CIÈNCIA DE MATERIALS I QUÍMICA FÍSICA
INSTITUT DE QUÍMICA TEÒRICA I COMPUTACIONAL

COMPUTATIONAL MODELLING OF TiO_2 AND Mg-SILICATE NANOCLUSTERS AND NANOPARTICLES - CRYSTALLINIY AND ASTROPHYSICAL IMPLICATIONS.

Antoni Macià Escatllar

2020

Acknowledgments

The research performed in this thesis has only been possible thanks to a lot of people. First and foremost, I would like to thank the tuition done by my supervisors, Francesc Illas and specially Stefan T. Bromley, without your trust, guidance and encouragement to pursue my own ideas I would have never reached the feat this thesis and the research within represent. I also would like to acknowledge all the collaborators I had, as without all the expertise of this people this thesis would have not been possible: Angel Morales, Andy Cuko, Tomas Lazauskas, Lorenzo Zamirri, Joan Mariñoso, Piero Ugliengo and Scott Woodley. Finally, I would like to thank Cornelia Jaeger, John Plane and Thomas Henning for allowing me to perform research stays in their groups, as it allowed a great amount of scientific discussion which enriched the present thesis.

Però aquests quatre anys de tesi també han significat un canvi a nivell personal molt gran, i per tant m'agradaria agrair a tota la gent que sense estar directament involucrada en aquest treball, ha conviscut amb mi i m'ha fet créixer durant aquests quatre anys. Als meus companys de màster, l'Efrem, l'Alba, la Mireia i l'Àlex, amb qui he debatut moltíssim de tot, m'han donat suport en moltes mes ocasions de les que puc recordar, i m'han ensenyat el que és viure a Barcelona, al despatx 408 tant present com passat, l'Alberto, l'Isaac, la Cristina, en Raul, la Lorena i en Marc, i tot i que no és del despatx, en Sergi, que sempre m'han fet amena la feina i han generat un ambient de treball i post-treball meravellós. Necessàriament he de mencionar el SIRE de sants, especialment l'Emilia, en Jordi, en Juanjo i la Rosa, que m'han demostrat fins on pot arribar l'ésser humà i lo petits que som, així com ensenyat a superar-me. Als meus companys de pis, l'Assutzena i en, Raul? per fer de Muntaner un lloc acollidor. Com no, també vull dedicar un moment als meus companys de carrera, l'Helena, la Georgina, en Jordi, l'Adrià, la Judit i la Vane, que han hagut de veure'm desaparèixer aquests quatre anys. Esperem que el futur canviï una mica aquesta dinàmica. I, com no, agrair aquells que porten tants anys donant-me suport quan ho he necessitat i que sé que puc contar amb ells en qualsevol moment, en Carlos, en Jan i en Raul (un altre cop? Recoi si et conec de fa dos anys i estàs a tot arreu), moltes gràcies per la vostre paciència. I per acabar, agrair a la Clara aquest últim any, m'has donat molt de suport en aquest temps i has fet del confinament una temporada tant agradable com qualsevol altre.

Finalment, m'agradaria agrair i dedicar aquesta tesi a la meva família, que sempre m'han ajudat i m'han inculcat els valors que tinc: a les meves tietes, Fina i M. Carme, als meus cosins, i especialment als meus avis, Joaquim, Carme i Antoni, el meu germà, Santi i als meus pares, Montse i Eugeni. Gràcies a tots.

Table of Contents

List of abbreviations

$\boldsymbol{A}$	Einstein coefficient of spontaneous emission (s^{-1})
AGB	Asymptotic Giant Branch
AME	Anomalous Microwave Emission
Ant	Anatase
AR	Aspect Ratio
$\boldsymbol{B}$	Rotational constant (MHz)
$\boldsymbol{\beta}$	Dipole moment per square root of number of atoms ($\frac{Debye}{\sqrt{nºatoms}}$)
BO	Born-Oppenheimer
CNM	Cold Neutral Medium
DFT	Density Functional Theory
EA	Electron affinity (eV)
En	Enstatite
Fo	Forsterite
GO	Global Optimization
GM	Global Minimum
HF	Hartree-Fock
HIN	Hot Ionized Medium
$\boldsymbol{\Delta H_f}$	Enthalpy of formation (eV)
ISM	Interstellar Medium
IP (text)	Interatomic Potential
IP (Chapter 11)	Ionization Potential (eV)
IR	Infrared
MC	Molecular Cloud
MC-BH	Monte Carlo Basin Hopping
MD	Molecular Dynamics
MgO	Magnesium Oxide
$\boldsymbol{MgSiO_3}$	Magnesium silicate of pyroxenic composition
$\boldsymbol{Mg_2SiO_4}$	Magnesium silicate of olivinic composition
MM	Molecular Medium
$\boldsymbol{\mu}$	Dipole Moment (Debye)
MW	Microwave (GHz)

NP	Nanoparticle
$\boldsymbol{P}$	Power
PES	Potential Energy Surface
PAH	Polycyclic Aromatic Hidrocarbon
$\boldsymbol{q}$	Atomic charge (elementary charge)
$\boldsymbol{Q}$	Partition Function
QM	Quantum Mechanics
RMSD	Root Mean Square Deviation
Rt	Rutile
SED	Spectral Energy Distribution
$\mathbf{SiO_2}$	Silicon dioxide
$\mathbf{TiO_2}$	Titanium dioxide
XAFS	X-ray absorption fine structure
WF	Wavefuncion
WIM	Warm Ionized Medium
WNM	Warm Neutral Medium

Chapter 1: Overview of the thesis.

The following thesis has been carried out in the Computational Material Science Laboratory (CMSL) of the Institut de Química Teòrica i Computacional at the University of Barcelona. As such, the systems under scrutiny in this thesis follow two relevant lines of research of the CMSL: titanium dioxide (TiO_2, titania) and astronomical silicates (astrosilicates hereafter).

Thanks to the increasing capabilities of computers and the ever-continuing development and refinement of new theoretical methodologies, computational chemistry has become a prominent tool for nanoscale virtual laboratory experiments, for confirmation of experimental/observational results and prediction of new species and their properties. The wide applicability of this now well-established field is due to several factors, such as the possibility to study systems in conditions not easily available in experiments, the capability to predict properties without any experimental support or the possibility to uncover the importance that certain structural features have for the chemical and electronic properties of systems. The research presented in this thesis contributes to the understanding of both titania and silicate nanosystems by providing new information on energetic stability and properties of nanometer sized particles using computational modelling. Particular emphasis is placed on the importance of two nanosized regimes: i) tens of atoms, and ii) several hundred up to thousands of atoms. We differentiate these two size regimes by naming nanoclusters the structures containing between tens up to a hundred of atoms, and using the term nanoparticles (NPs) for the structures containing hundreds to thousands of atoms. Another topic explored in this thesis, with relevance to both nano oxide systems, is that of amorphous surface-crystalline core NPs.

Even when describing the properties of nanoscale systems and understanding the amorphous to crystalline transition are the bridging point between both systems, the published articles deal with the relevance such topics have in the applied research for each specific system. Titania (TiO_2) is the most studied photocatalyst, and thus research is mostly focused on understanding the electronic properties of different morphologies of TiO_2 NPs. In detail, for TiO_2 the present thesis benchmarks the ability of several interatomic potentials (IPs) to reduce the computational cost of Density Functional Theory (DFT) calculations, as well as a detailed analysis of the energetic stability of three different morphologies of NPs together with an analysis of their band-gap. On the other hand, research on astrosilicates is mainly focused on calculating the properties of nanoclusters and NPs, with the objective of obtaining a better understanding of the relevance of such species in interstellar space. In detail, for astrosilicates, we propose global minima (GM) candidates for numerous nanoclusters based on global optimization (GO) searches and compare their spectroscopic and chemical properties with literature values, where the later values are mostly derived from extrapolation using macroscale laboratory samples. We also evaluate whether silicate nanoclusters can be the origin of the anomalous microwave emission (AME), a foreground emission in the microwave (MW) region of the spectra from an unknown source. Finally, the IR spectra of large NPs are compared on the basis of their crystallinity.

The structure of the thesis follows the specific relevance of the research performed. In Chapter 2 we provide an overview of the computational methodologies used in this work. As such, we discuss the Born-Oppenheimer approximation and the Potential Energy Surface (PES), Quantum Mechanics (QM) and DFT, IPs, GO with basin-hoping (BH) methods and Molecular Dynamics (MD). A list of references follows to end the Chapter. The first part of the research performed in this thesis, centered on TiO_2, starts in Chapter 3, which provides an introduction on known properties of TiO_2, basic photocatalysis, morphology of NPs, and the state-of-the-art in computational modelling of TiO_2 surfaces and NPs. Chapter 4 gives the scientific objectives of the research performed on TiO_2. Chapter 5 compares the ability of different IPs to pre-optimize the structures of faceted NPs as a preliminary step prior to DFT optimizations. Chapter 6 describes the energetic and band-gap trends for differently shaped TiO_2 NPs and compares their calculated band-gaps with experimental results. Chapter 7 provides a summary of the results, an outlook of possible future research available after this thesis and the references for this part of the thesis. The second part of thesis, devoted to astronomical silicates, starts in Chapter 8. An historical overview on astronomical dust and astrosilicates is given, followed by a brief description of the stellar and dust cycles and a discussion of the nature of astronomical dust, providing evidence of the importance of magnesium silicates with a description of the known silicates on Earth. Finally, the current knowledge on astronomical silicates is reviewed, with emphasis on the importance of nano-astrosilicates. In Chapter 9 the objectives of the research on nano-astrosilicates are outlined. In Chapter 10 we develop an IP for magnesium silicates and propose GM candidates for nanoclusters of Mg_2SiO_4 and $MgSiO_3$ stoichiometries with 1 to 10 formula units. We describe the structure, atomic charges, energetics with respect to size, and IR spectra of our candidate structures. In Chapter 11 we analyze the dipole moments and MW emission of the presented astrosilicate nanoclusters, providing theoretical evidence to relate the AME to astrosilicate nanoclusters. In Chapter 12 we evaluate the energies and IR spectra of different models of NPs including faceted crystalline structures and amorphous structures generated by annealing of crystalline structures and by gas-phase aggregation. Chapter 13 provides a summary of the scientific results obtained for nano-astrosilicates, an outlook for future research opened after this thesis, and the bibliography of the astrosilicate part of the thesis.

Chapter 2. Methodology

The Born-Oppenheimer approximation and Potential Energy Surfaces

The properties of a chemical system are dependent on the positions of the constituent electrons and nuclei, as they determine the chemical and electronic structure from which all properties arise. Hence, a central problem in computational chemistry is to obtain representative structures of a chemical system in order to compute realistic properties that match experiments and observations.

In quantum mechanics (QM), to describe the static properties of a molecular system one must solve the time independent Schrödinger equation, which is given by:

$$\hat{H}\Psi = E\Psi \quad (1)$$

where $\hat{H}$ corresponds to the Hamiltonian operator, Ψ is the wavefunction of the system and E its energy. The Hamiltonian operator contains both the kinetic energy operators $\hat{T}$ of electrons (e) and nuclei (N) and the potential energies ($\hat{V}$, as described by the Coulomb operator) between $e-e$, $e-N$ and $N-N$. In atomic units, the operators have the form:

$$\hat{H} = \hat{T}_N + \hat{T}_e + \hat{V}_{NN} + \hat{V}_{Ne} + \hat{V}_{ee} \quad (2)$$

$$= -\frac{1}{2}\sum_{i=1}^{P}\frac{\nabla_i^2}{m_i} - \frac{1}{2}\sum_{\mu=1}^{S}\nabla_\mu^2 + \sum_{i=1}^{S}\sum_{j>i}^{S}\frac{Z_i Z_j}{R_{ij}} - \sum_{\mu}^{S}\sum_{i}^{P}\frac{Z_i}{r_{\mu i}} + \sum_{\mu=1}^{S}\sum_{\upsilon>\mu}^{S}\frac{1}{r_{\mu\upsilon}} \quad (3)$$

where P is the number of nuclei, S the number of electrons, ∇^2 the Laplacian operator, m_i the mass of the i nuclei, Z_i and Z_j the atomic number of the nuclei, R_{ij} the distance between nuclei i and j, and r the $e-e$ or the $e-N$ distance. Taking notice that the nuclei are at least three orders of magnitude more massive than electrons, the Born-Oppenheimer (BO) approximation states that electrons respond instantaneously to the motions of nuclei, and thus the motions of electrons and nuclei can be decoupled. This allows one to describe the wavefunction as the product of electronic ($\psi(r)$) and nucleic ($\phi(R)$) wavefunctions:

$$\Psi(R,r) = \psi(r)\phi(R) \quad (4)$$

The Schrödinger equation can now be separated into two sets of equations, one for the electronic wavefunction and one for the nucleic wavefunction:

$$\left(\hat{T}_e + \hat{V}_{ee} + \hat{V}_{eN} + \hat{V}_{NN}\right)\psi(r) = \varepsilon(R)\psi(r) \quad (5)$$

$$\left(\hat{T}_N + \varepsilon(R)\right)\phi(R) = E\phi(R) \quad (6)$$

Equation 5 corresponds to the electronic wavefunction, while equation 6 corresponds to the nucleic wavefunction. In equation 5, the electronic energy ($\varepsilon(R)$) depends parametrically on the positions of the nuclei. On the other hand, equation 6 shows that the electronic energy defines the potential in which the nuclei are moving. Thus, in quantum mechanics and under the BO approximation, the nuclei move over a potential energy

surface (PES) defined by the electronic energy. The PES of a chemical system is a hyperspace composed of all the possible geometrical conformations of the nuclei with their associated energy. Critical points associated to minima of the PES correspond to important chemical states. Minima are points of the PES where no forces are acting on the nuclei -i.e, $\partial V/\partial r = -F = 0$-, and correspond to stable molecules. Moreover, first-order saddle points join two adjacent minima, and thus correspond to transition states between different conformations or reactants and products. The search of stable chemical structures thus corresponds to finding minima on the PES.

Density Functional Theory

In the BO approximation, the electronic energy represents the most complex term to calculate. Currently, there are two main families of methods to obtain the electronic energy from first principles (*ab initio*): wavefunction (WF) methods and density functional theory (DFT) methods. Methods within WF theory have their root in the Hartree-Fock (HF) approximation; because of that, such methods are usually referred as post-HF methods. In the HF approximation, the N-electron problem is approximated to N effective independent-particle problems. Because electrons are fermions, the HF approximation maintains the antisymmetry of the wavefunction by describing it in terms of a Slater determinant (see equation 18). Because of this, repulsion of same-spin electron pairs is described in HF (Fermi correlation); however, Coulombic interactions between electrons are not directly treated in HF, which approximates the repulsion by means of a mean field potential (mean-field approximation). This makes opposite-spin electron pairs completely uncorrelated. This approximation results in underestimated repulsive potentials between electrons and thus the obtained energy from HF methods is an upper bound to the true energy of the system. The difference between the exact, completely correlated energy and the HF one is known as electron correlation energy. Post-HF methods improve the HF description by introducing some correlation of the electronic motion, such as Coupled Cluster, Møller-Plesset (MP) perturbational theory or Complete Active Space methodologies. However, introducing electron correlation requires a huge computational effort. One of the simplest post-HF methods, such as MP-2, already has a computational cost that increases between N^4 to N^5, where N is the number of electrons of the system, while more precise methods such as coupled cluster with single and double excitations (CCSD) scale as N^6. On the other hand, DFT methods can provide energies, structures and properties with accuracies between HF and post-HF methods with a computational cost smaller than that of most post-HF methods, or in some cases, with similar scalability to HF methods. In general, post-HF accuracy can be achieved with HF scalability (N^4)[1–4].

The basis of DFT can be found in the paper by Hohenberg and Kohn, where they prove the following theorems[5]:

1. The external potential is a unique functional of the electron density. Since the external potential fixes the Hamiltonian, the properties of the full many-particle ground state are a unique functional of the external potential.

In essence, the previous statement says that an "external potential", which in our case corresponds to the electron-Nuclei potential ($V_{ext} = V_{eN}$), is uniquely defined by the electron density $\rho(r)$. The external potential then defines the Hamiltonian, which in turn provides the ground state wavefunction, with all the properties of the system. This first theorem can be easily demonstrated by *reductio ad absurdum* for non-degenerate ground-states. We start by defining the electron density ($\rho(r)$) as a function of the ground state wavefunction:

$$\rho(r) = \langle \Psi_0 | \hat{\rho} | \Psi_0 \rangle = \mathrm{N} \int \dots \int |\Psi(\overrightarrow{x_1}, \overrightarrow{x_2}, \dots, \overrightarrow{x_N})|^2 \, ds_1 d\overrightarrow{x_2} \dots d\overrightarrow{x_N} \quad (7)$$

Where $\overrightarrow{x_i}$ represents the ith spin coordinate for the ith electron and s_i is the spin of the ith electron. Now, we suppose that two different external potentials V_{ext} and V'_{ext} arising from the Coulomb potential of the nuclei (as we decoupled the motions of the nuclei and electrons with the BO approximation) with different wavefunctions Ψ_0 and Ψ'_0 give the same electron density, $\rho(r)$. The variational principle establishes that for a given system the energy of a trial wavefunction is always higher than the energy computed from the real wavefunction:

$$E = \langle \Psi | \widehat{H} | \Psi \rangle < \langle \Psi' | \widehat{H} | \Psi' \rangle \quad (8)$$

Where Ψ is the wavefunction associated with E and where we use Ψ' as a trial wavefunction. The Hamiltonians have the form:

$$\widehat{H} = \hat{T}_e + \widehat{U}_{ee} + \hat{V}_{ext} \quad (9)$$

and

$$\widehat{H'} = \hat{T}_e + \widehat{U}_{ee} + \widehat{V'}_{ext} \quad (10)$$

Both Hamiltonians are related by the difference in the external potential. From equations 9 and 10, we can rewrite $\widehat{H} = \widehat{H'} + \widehat{V_{ext}} - \widehat{V'_{ext}}$. The inequality 8 can be expressed, also using equation 7, as:

$$E < \langle \Psi' | \widehat{H'} + \hat{V}_{ext} - \hat{V}'_{ext} | \Psi' \rangle = E' + \langle \Psi' | \hat{V}_{ext} - \hat{V}'_{ext} | \Psi' \rangle$$

$$= E' + \int dr \, \rho(r) [V_{ext}(r) - V'_{ext}(r)] \quad (11)$$

The same result appears if we substitute the energy for E', it's wavefunction to Ψ' and the trial wavefunction to be Ψ:

$$E' < \langle \Psi | \widehat{H} + \hat{V}'_{ext} - \hat{V}_{ext} | \Psi \rangle = E + \int dr \, \rho(r) [V'_{ext}(r) - V_{ext}(r)]$$

$$= E - \int dr \, \rho(r) [V_{ext}(r) - V'_{ext}(r)] \quad (12)$$

Adding equations 11 and 12 we obtain the contradiction:

$$E + E' < E + E' \quad (13)$$

Which proves that the electron density $\rho(r)$ has a one to one relationship with the external potential, i.e., for each configuration of nuclei there exist only one electron density,

and vice versa. Similarly the wavefunction (Ψ) and energy are uniquely defined by the electron density (i.e, Ψ is a functional of the electron density).

The second theorem reads:

2. The density that minimizes the total energy is the exact ground state density.

This statement is equivalent to the variational principle. The second theorem can be complied as long as the electron density satisfies the boundary conditions that its integration provides the number of electrons of the system and is positive:

$$\int \rho(r)\, dr = N \quad (14)$$

$$\rho(r) \geq 0. \quad (15)$$

As Ψ is a functional of the electron density, it also implies that the potential and kinetic energy are functionals of the electron density as well. If we define the functional $F[\rho]$ as the functional which describes the electron-electron potential and kinetic energy $F[\rho] = T_e[\rho] + V_{ee}[\rho]$, we can describe the electronic energy of the system as:

$$E_v[\rho] \equiv \int V_{ext}(r)\rho(r)dr \; + \; F[\rho] \quad (16)$$

Which is equivalent to:

$$E_v = \langle\psi|\hat{F}|\psi\rangle + \langle\psi|\widehat{V_{eN}}|\psi\rangle \quad (17)$$

A trial density $\rho'(r)$ in the same external potential as the ground state density would return a wavefunction ψ' which by variational principle would give a higher energy unless $\psi' = \psi_0$. If the two wavefunctions are equal, the densities must also be equal and therefore the trial density corresponds to the real density ($\rho'(\mathrm{r}) = \rho(\mathrm{r})_0$).

The Hohenberg-Kohn theorem proves that DFT can give the exact solution for the ground state energy, provided that we know the electronic functional $F[\rho]$. However, the form of this functional is unknown. The energy can be obtained directly from the density by describing the energy functional as a sum of functionals describing the kinetic energy of the electrons $T[\rho]$, the electron-electron interaction $E_{ee}[\rho]$ and the electron-nuclei interaction $E_{Ne}[\rho]$. The electron-electron interaction term is also divided into the classical Coulomb interaction $J[\rho]$ and the exchange part $K[\rho]$. The functionals that describe the nuclei-electron interaction and the Coulomb interaction from the electron density are directly connected with classical expressions, but the electron kinetic energy and exchange functionals are unknown, and therefore, initial research on DFT tried to obtain functionals able to relate electron densities with the kinetic and exchange energies. This approach however hasn't been able to give correct results for molecules, mainly due to a poor representation of the kinetic energy and led to the re-introduction of orbitals in the Kohn-Sham theory[6].

Kohn and Sham realized that the kinetic energy of a non-interacting N electron system can be exactly calculated using WF methods. For this non-interacting system, the electronic wavefuncion can be described as the product of one electron wavefuncions that

move in the mean potential generated by the rest of the electrons. Moreover, the wavefuncion has to be anti-symmetric and the electrons must be indistinguishable, and therefore all electrons should be able to occupy all the different orbitals. For this reason, this product is written as a determinant known as Slater Determinant (SD):

$$\Psi_0 \approx \Psi_{SD} = \frac{1}{\sqrt{N!}} det\{\varphi_1(\vec{x}_1)\, \varphi_2(\vec{x}_2) \dots \varphi_N(\vec{x}_N)\} \quad (18)$$

Where N represents the number of electrons, and $\varphi_i(\vec{x}_i)$ corresponds to the i[th] spin-orbital composed of a spatial part, $\phi_i(\vec{r})$, and spin part, either $\alpha(\vec{s})$ or $\beta(\vec{s})$. The kinetic energy is exactly obtained from the spin-orbital:

$$T = -\frac{1}{2}\sum_i^N \langle \varphi_i | \nabla^2 | \varphi_i \rangle \quad (19)$$

Now, as one can obtain the kinetic energy exactly for this non-interacting system, Kohn and Sham proposed to work with a fictitious system of non-interacting electrons under an external potential such that the electron density obtained from the Slater determinant of this fictitious system ($\rho_S(\vec{r})$) is the density of the real system:

$$\rho_S(\vec{r}) = \sum_i^N \sum_s |\varphi_i(\vec{r}, s)|^2 = \rho_0(\vec{r}) \quad (20)$$

To find $\rho_S(\vec{r})$ that corresponds to the real $\rho_0(\vec{r})$, we iteratively solve a set of equations similar to the Hartree-Fock equations, known as the Kohn-Sham equations. The energy can be described both as a functional of the density as well as an operator of the orbitals. We define the electronic energy functional $E[\rho(\vec{r})]$ as the sum of kinetic $T[\rho]$, classical Coulomb interaction $J[\rho]$, non-classical correction $E_{XC}[\rho]$, which includes exchange and correlation, but also kinetic energy in a small amount, and finally the nuclei-electron interaction $E_{Ne}[\rho]$:

$$E[\rho(\vec{r})] = T_S[\rho] + J[\rho] + E_{XC}[\rho] + E_{Ne}[\rho]$$

$$= T[\rho] + \frac{1}{2}\iint \frac{\rho(\vec{r}_1)\rho(\vec{r}_2)}{r_{12}} d\vec{r}_1 d\vec{r}_2 + E_{XC}[\rho] + \int V_{Ne}\rho(\vec{r}) d\vec{r}$$

$$= -\frac{1}{2}\sum_i^N \langle \varphi_i | \nabla^2 | \varphi_i \rangle + \frac{1}{2}\sum_i^N \sum_j^N \iint |\varphi_i(\vec{r}_1)|^2 \frac{1}{r_{12}} \left|\varphi_j(\vec{r}_2)\right|^2 d\vec{r}_1 d\vec{r}_2$$

$$+E_{XC}[\rho(\vec{r})] - \sum_i^N \int \sum_A^M \frac{Z_A}{r_{1A}} |\varphi_i(\vec{r}_1)|^2 \, d\vec{r}_1 \quad (21)$$

The $E_{XC}[\rho]$ term is unknown, and so is the potential related to it. The associated potential is defined as the derivative of $E_{XC}[\rho]$ with respect to the density:

$$V_{XC} = \frac{\delta E_{XC}[\rho]}{\delta \rho} \quad (22)$$

We can calculate the energy of the Kohn-Sham orbitals with the equation:

$$\left(-\frac{1}{2}\nabla^2 + V_{XC} + \int \frac{\rho(r_2)}{r_{12}}dr - \sum_A^M \frac{Z_A}{r_{1A}}\right)\varphi_i = \varepsilon_i\varphi_i \quad (23)$$

Even though the form of E_{XC} is not known, much work has been devoted to find approximate forms which can describe with precision the effects of exchange and correlation. The uniform electron gas allows one to obtain a first approximation of E_{XC} which is the basis for the most important functionals available, and the ones used in this work. Under this approximation, also called the Local Density Approximation (LDA)[7] the exchange-correlation energy is assumed to arise from the interaction of electrons with a homogeneous field:

$$E_{XC}^{LDA} = \int \rho(r)\epsilon_{XC}\big(\rho(r)\big)dr \quad (24)$$

From this equation the single electron energy interaction with the homogeneous field ($\epsilon_{XC}\big(\rho(r)\big)$) can be obtained by separating the exchange (ϵ_X) and correlation parts (ϵ_C):

$$\epsilon_{XC}\big(\rho(r)\big) = \epsilon_X\big(\rho(r)\big) + \epsilon_C\big(\rho(r)\big) \quad (25)$$

The ϵ_X term was derived separately by Bloch and Dirac[8,9] to be:

$$\epsilon_X = -\frac{3}{4}\sqrt[3]{\frac{3\rho(r)}{\pi}} \quad (26)$$

On the other hand, the ϵ_C does not have an explicit expression. Nevertheless, analytical expressions have been computed by several authors[7,10].

The LDA functionals perform very well taking into account the underlying assumption of homogeneous electronic distribution. Nevertheless, molecules and clusters are clearly non-homogeneous systems, and further approximations are needed. An improvement over the LDA functionals is to include not only the density at a given point but also the gradient, as in a Taylor series. This gives rise to the General Gradient Approximation (GGA) functionals, which in general describe the exchange correlation energy as:

$$E_{XC}^{GGA} = \int \rho(r)\epsilon_{XC}\big(\rho(r), \nabla\rho(r)\big)dr. \quad (27)$$

The exchange correlation function ϵ_{XC} is not univocally defined for GGA functionals. The PBE functional[11], developed by Perdew, Burke and Ernzerhof, is a GGA functional developed completely without any fitting procedures. It is one of the most used and well established GGA functionals, and it has been used in the calculations in Chapter 5, 6 and 12.

A final approach is to calculate the ϵ_X within the HF scheme instead, since the term arises naturally in HF theory, and add some fraction of it to the exchange-correlation energy. Such functionals receive the name of hybrid functionals. Different proportions and rationales can be used in order to add the E_X^{HF} into the hybrid exchange correlation term (E_{XC}^{Hyb}), most of them fitted to a dataset of molecular properties obtained with a combination of the most accurate WF methods, the G2 set[12]. The PBE functional has its own hybrid version which follows the equation:

$$E_{XC}^{Hyb} = E_{XC}^{GGA} + a_0\left(E_X^{HF} - E_X^{GGA}\right) \quad (28)$$

Where the a_0 parameter is argued to be 0.25 using arguments from perturbation theory. Such functional is known as PBE0[13]. The PBE0 functional is extensively used in Chapter 10 of the present thesis.

Interatomic Potentials.

While QM methods allow for the most accurate assessment of the structure and energy of a chemical system, their computational cost is large. In general, structural features such as bond distances and angles are usually quite constant for the same types of atoms in many chemical systems –e.g., the Si-O bond length normally is ~1.66 Å-. This generality has allowed the development of parametrized functions, known as interatomic potentials (IPs), that can efficiently describe the interactions between collections of atoms. A simplified IP-PES can be constructed which reproduces the minima positions of the real PES and the relative energies between the different minima.

Overall, IPs define the internal energy (U) of the system as the sum of interactions involving two, three or more bodies as in:

$$U(r_N) = \sum_i^N \sum_{j\neq i}^N \phi(r_i, r_j) + \sum_i^N \sum_{j\neq i}^N \sum_{k\neq i\neq j}^N \phi(r_i, r_j, r_k) + \cdots \quad (29)$$

Where ϕ is a function which describes the energy interaction between two, three or more bodies. The exact number of N-body interactions depends on the actual model used to define the IP. Several different types of IPs (also called force-fields) have been developed to tackle different families of materials, from general reactive forcefields to ionic models. The later models are based on the Born description of ionic crystals[14], where the main interactions are Coulombic interactions, Van der Waals attraction, and Pauli repulsion.

The chemical systems studied in this thesis are mostly regarded as ionic, and the thus the IPs we use are based on the previously cited Born model. As such, the Coulomb interaction is the dominant force in ionic materials and is defined by the Coulomb Law:

$$U_{ij}^{Coulomb} = \sum_i^N \sum_j^N \frac{q_i q_j}{4\pi\epsilon_0 r_{ij}} \quad (30)$$

Where q_i is the charge of the i-atom, ϵ_0 is the vacuum permittivity and r_{ij} is the distance between atom i and j. In the Born model, atoms -or rather ions, as the Born model requires them to possess a formal charge- are treated as point-charges. As a consequence, the effect of polarization -i.e., distortion of the electronic structure around an atom by the presence of a nearby ion- is completely neglected. The Born model can thus be improved by including polarization, mostly of anionic species. The core-shell model[15] divides anions into two particles: the core, positively charged, and the shell, representing the electron cloud, which are bonded by an harmonic potential:

$$U_{C-S} = \frac{1}{2}kr^2 \quad (31)$$

In the core-shell model, Coulomb interaction is evaluated between all pairs of shells and cores on separate ions, but not for cores and shell of the same ion. On the other hand, short-range interactions -Pauli repulsion and Van der Waals attraction- are only applied among non-shell atoms and shells.

The approximation of ions to point-charges neglects the repulsion arising from the superposition of the electron clouds of ions (Pauli repulsion) and the short-range attraction due to Van der Waals forces. These two interactions can be taken into account using several analytical equations, from which the most typical are the Lennard-Jones, Buckingham and Morse potentials. Selecting any potential is a matter of preference. For ionic models, the most used functional is the Buckingham potential, which is defined as:

$$U_{ij}^{Buckingham} = \Lambda_{ij} \mathrm{e}^{(-r_{ij}/\rho_0)} - \frac{C_a}{r_{ij}^6} \qquad (32)$$

Where Λ_{ij}, C_a and ρ_0 are constant parameters obtained from fitting to *ab initio* or experimental data and r_{ij} is the interatomic distance between pairs of atoms. Figure 1 shows a representation of the Buckingham potential function of the Mg-O interaction in Mg-FFSiOH[16]. The first term of equation 32 accounts for the Pauli repulsion, while the second corresponds to Van der Waals attraction. Overall, at short distances the repulsive term dominates, while at long distances we see dominance of the attractive term. The balance of these two terms generate an equilibrium position at a certain interatomic distance (see Figure 1).

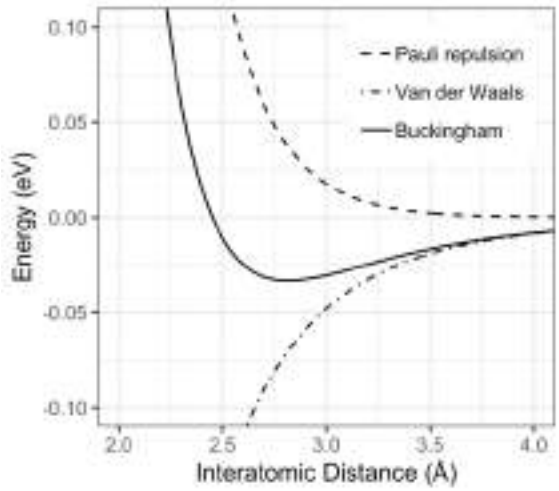

Figure 1. Decomposition of the Buckingham potential (solid line) into the constituent functions that describe the Pauli repulsion (dashed line) and Van der Waals attraction (dot-dashed line), using the parameters from Mg-FFSiOH: Λ =3200, $\rho_0 = 0.2477$ and $C_a = 35$.

Global Optimization

In nature, most chemical systems are composed by ensembles of clusters, and thus measured properties correspond to the average properties of the individual clusters in the ensemble. The number of different stable conformations -i.e. structures that correspond to minima points in the PES- increases exponentially with size, with each structure showing

differences in properties. Finding representative structures is therefore mandatory in order to obtain reliable properties of computational methods.

Following thermodynamics principles, for a given system in equilibrium the most populated structures should be those of lowest energy. For example, observed spectra in metallic and oxide cluster beam experiments[17–19] can often be understood using computational chemistry models by studying the properties of energetically low lying isomers. Thefore, the problem to solve is that of finding the lowest possible energy structure of a given system, i.e., to perform a global optimization (GO) search on a given PES. Since the number of possible minima is already large for systems containing tens of atoms, methodologies to find GM candidates are typically probabilistic. In such approaches, since the PES is not completely explored, it is never guaranteed that the lowest energy isomer is found.

Monte Carlo Basin Hopping

Different methodologies try to overcome the difficulties faced in efficiently and thoroughly exploring the PES. For relatively small systems containing from tens up to hundreds of atoms, the Monte Carlo Basin-Hopping methodology (MC-BH) is often used[20,21]. In this scheme, it is not the real PES that is being explored, but rather a transformed PES made of the minima structures. Figure 2 shows a graphical representation of the original PES and the PES explored using MC-BH. The procedure of the MC-BH algorithm is as follows:

1. an initial structure is optimized within a certain level of theory,
2. the structure is randomly distorted,
3. the distorted structure is re-optimized,
4. the probability of acceptance of the re-optimised structure in 3, $P(x)$, is calculated,
5. if accepted, the re-optimised structure is used as the base of the new cycle starting from 2. If the structure is not accepted, the cycle is repeated from 2 using the previously optimized structure.

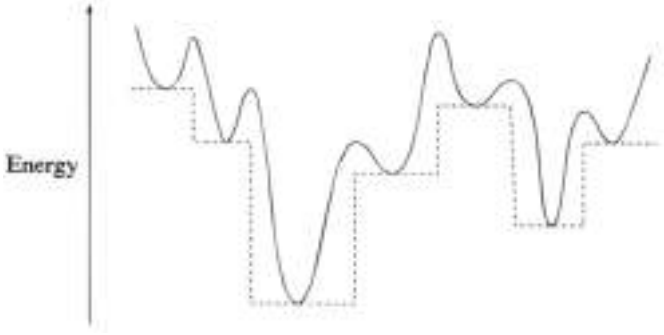

Figure 2. Fictional PES (solid line) and Monte Carlo-Basin Hopping PES (dashed line). Notice how for each point the associated energy corresponds to the energy of the closest minimum

The probability of acceptance ($P(x)$) for a structure follows the Metropolis criterion and is mathematically described in equation 33: if the energy of the current step (x) is lower

than the previous accepted structure ($x-1$), the structure is accepted ($P(x)=1$), else, a random number in the interval [0,1) is compared to the Maxwell Boltzmann distribution as in equation 33, where ΔE is the difference in energy between the current step and the previously accepted step, k_b is the Boltzmann constant and T is an arbitrary temperature with no physical meaning.

$$P(x)\begin{cases} =1, & E(x)<E(x-1) \\ =e^{-\Delta E/k_bT}, & E(x)>E(x-1) \end{cases} \quad (33)$$

In the 2nd step, the random displacement, the atomic positions are randomly displaced (both direction and distance) within an interval from zero to a user defined parameter, which is typically taken to be 80% of a typical bond-distance in the system under study. In this way, at each step the randomly distorted structure is largely confined to be in a nearby region of the PES close to the previous structure. The temperature criterion in the 4th step allows to tune the probability to escape from deep regions of the PES with large barriers, and thus some codes allow this value to change according to a user-defined value of the ratio of accepted structures (acceptance ratio), rather than having a fixed temperature value.

In practice, the MC-BH algorithm -or in general any GO technique- requires several runs of tens of thousands of steps with different initial conditions of structure and simulation temperature/acceptance ratio in order to efficiently explore the PES. As such, the computational cost is huge. Assuming that a local optimization takes 10 seconds, a GO run with 10.000 steps would require at least one day to complete. Any increase in the number of GO steps or in the precision of the energy evaluation by increasing the accuracy of the optimization method (e.g. from IP-based methods to DFT) will increase the total GO time inmensely, resulting in computational times of years. The most efficient way to perform GO relies on the use of IPs to fast evaluate hundreds of structures in a matter of seconds. While the use of IPs solves the time issue, new problems arise from optimizing a PES generated from IPs. The two important issues that had to be dealt with in the course of this thesis are the correspondence between the IP-PES and the DFT-PES, and the optimization of core-shell IPs, as a random displacement of the core and shell would cause severe computational issues. With regard to IP-PES and DFT-PES correspondence, it is clear that the simple description of an IP will never be able to reproduce all peculiarities of the electronic structure of nanoscale systems. The only possible solution is to evaluate a large number of candidate structures and test whether the relative energies between structures are similar in both DFT and IP.

A new variant of MC-BH was developed in a joint paper with Dr. Andy Cuko[22], named Cascade MC-BH. In this work, we added a two-step local optimization prior to energy evaluation in the GO methodology: the first local optimization is handled by a simple potential without shell polarization, bringing the random structure into a more reasonably bound cluster, the second optimization with the complete IP then further refines the structure and provides the energy by which the Metropolis criterion is evaluated. The Cascade MCBH was implemented in the Atomic Simulation Environment (ASE)[23], and contains most of the capabilities of MCBH algorithms. In order to enrichen the GO

searches, we also included an option in the MCBH code to allow for swapping positions of dissimilar cations, with a pre-defined probability.

In this thesis, to obtain accurate results on the GM candidates, the IPs used were finely tuned to reproduce as accurately as possible the relative energies of sets of isomers for the chemical systems at hand. Moreover, large sets of low lying GM candidate isomers were optimized by DFT calculations in order to refine the selection of the energetically lowest lying energy structures.

Molecular Dynamics

For large particles containing hundreds or thousands of atoms the MC-BH is inefficient, as every optimization even at the IP level will take several minutes. In addition, the conformational space is huge, thus requiring to evaluate a larger number of structures. Hence, any BH algorithm would require at least hundreds of thousands if not millions of steps, rendering its application impractical. A complete exploration of the PES of such large systems is therefore computationally unaffordable. It is possible however to explore the local region of the PES and find structures with lower energy than the initial guess by performing Molecular Dynamics (MD) simulations.

Since the nuclei are heavy particles which behave classically, the Newton second law allows one to determine the forces acting on each atom based on their corresponding positions in the system:

$$F = -\frac{dV}{d\boldsymbol{r}} = m\frac{d^2\boldsymbol{r}}{dt^2} \quad (34)$$

Where F is the force, V is the potential, $\boldsymbol{r}$ is the vector containing the positions of all atoms, m their masses, and t time. The positions of a set of atoms r_i at after a small time-step (Δt) are given by a Taylor expansion:

$$r_{i+1} = r_i + \frac{\partial r}{\partial t}(\Delta t) + \frac{1}{2}\frac{\partial^2 r}{\partial t^2}(\Delta t)^2 + \frac{1}{6}\frac{\partial^3 r}{\partial t^3}(\Delta t)^3 + \cdots$$

$$r_{i+1} = r_i + v_i(\Delta t) + \frac{1}{2}a_i(\Delta t)^2 + \frac{1}{6}b_i(\Delta t)^3 + \cdots. \quad (35)$$

Where the first derivative of the position with respect to time is the velocity (v_i), the second derivative the acceleration (a_i) and the third the hyperacceleration (b_i). Several methods allow one to efficiently determine the position of an atom at the step $i + 1$, such as the Velocity Verlet, or the leap-frog algorithm. All the methodologies have accuracies up to Δt^3. In practice, numerical convergence and energy conservation are assured if the time-step of the MD simulation is one order of magnitude smaller than the faster process involved (e.g., the vibrational frequency of bonds involving the lightest atoms).

In principle, the forces acting on the atoms can be evaluated with any chosen methodology. In practice, usage of *ab initio* methods to evaluate the forces increases the computational cost up to the point that just tens of picoseconds can be simulated on systems having ~30 atoms in a period of weeks. Hence, the most common method to evaluate forces are IPs.

Optimization of a structure using MD simulations have at least two different stages. In the first stage, equilibration, a system is gradually heated to high temperatures in order to incorporate enough energy into the system so that it can overcome the energetic barriers between different conformations. Once the system is thermalized, the production run allows the particle to explore the PES landscape. A further MD run slightly lowering the simulation temperature will restrict the particle movement over the PES. If the cooling down is done with a very small variation in temperature per unit of simulation time, the minima over the sampled PES will be found. This method is called Simulated Annealing.

References

[1] G. de Oliveira, J.M.L. Martin, F. de Proft, and P. Geerlings, Phys. Rev. A **60**, 1034 (1999).
[2] M. Alcamí, A.I. González, O. Mó, and M. Yáñez, Chem. Phys. Lett. **307**, 244 (1999).
[3] V. Barone and C. Adamo, Int. J. Quantum Chem. **61**, 443 (1997).
[4] A.C. Scheiner, J. Baker, and J.W. Andzelm, J. Comput. Chem. **18**, 775 (1997).
[5] P. Hohenberg and W. Kohn, Phys. Rev. **136**, B864 (1964).
[6] W. Kohn and L.J. Sham, Phys. Rev. **140**, A1133 (1965).
[7] S.H. Vosko, L. Wilk, and M. Nusair, Can. J. Phys. **58**, 1200 (1980).
[8] F. Bloch, Z. Phys. **57**, 545 (1929).
[9] P.A.M. Dirac, Math. Proc. Cambridge Philos. Soc. **26**, 376 (1930).
[10] J.P. Perdew and Y. Wang, Phys. Rev. B **45**, 13244 (1992).
[11] J.P. Perdew, K. Burke, and M. Ernzerhof, Phys. Rev. Lett. **77**, 3865 (1996).
[12] P.C. Redfern, J.-P. Blaudeau, and L.A. Curtiss, J. Phys. Chem. A **101**, 8701 (1997).
[13] C. Adamo and V. Barone, J. Chem. Phys. **110**, 6158 (1999).
[14] M.P. Tosi, in (1964), pp. 1–120.
[15] B.G. Dick, a. W. Overhauser, Phys. Rev. **112**, 90 (1958).
[16] A.M. Escatllar, T. Lazaukas, S.M. Woodley, and S.T. Bromley, ACS Earth Sp. Chem. acsearthspacechem.9b00139 (2019).
[17] A. Fielicke, R. Mitrić, G. Meijer, V. Bonačić-Koutecký, and G. von Helden, J. Am. Chem. Soc. **125**, 15716 (2003).
[18] M. Haertelt, A. Fielicke, G. Meijer, K. Kwapien, M. Sierka, and J. Sauer, Phys. Chem. Chem. Phys. **14**, 2849 (2012).
[19] P. Claes, E. Janssens, V.T. Ngan, P. Gruene, J.T. Lyon, D.J. Harding, A. Fielicke, M.T. Nguyen, and P. Lievens, Phys. Rev. Lett. **107**, 173401 (2011).
[20] D. Wales and J.P.K. Doye, J. Phys. Chem. A **101**, 5111 (1997).
[21] Z. Li and H.A. Scheraga, Proc. Natl. Acad. Sci. **84**, 6611 (1987).
[22] A. Cuko, A. Macià, M. Calatayud, and S.T. Bromley, Comput. Theor. Chem. **1102**, 38 (2017).
[23] A. Hjorth Larsen, J. Jørgen Mortensen, J. Blomqvist, I.E. Castelli, R. Christensen, M. Dułak, J. Friis, M.N. Groves, B. Hammer, C. Hargus, E.D. Hermes, P.C. Jennings, P. Bjerre Jensen, J. Kermode, J.R. Kitchin, E. Leonhard Kolsbjerg, J. Kubal, K. Kaasbjerg, S. Lysgaard, J. Bergmann Maronsson, T. Maxson, T. Olsen, L. Pastewka, A. Peterson, C. Rostgaard, J. Schiøtz, O. Schütt, M. Strange, K.S. Thygesen, T. Vegge, L. Vilhelmsen, M. Walter, Z. Zeng, and K.W. Jacobsen, J. Phys. Condens. Matter **29**, 273002 (2017).

Part I. Titania Nanoparticles

Chapter 3: Introduction.

TiO_2 overview.

Titanium dioxide (titania, TiO_2) naturally occurs in several different crystal structures. The most well-known polymorphs are Rutile (Rt), Anatase (Ant) and Brookite. Several high-pressure polymorphs have also been investigated[1–3] due to their possible relevance in understanding the Earth's Mantle, with some of the high-pressure polymorphs actually found in meteorite impact craters[2,4]. In terms of technological applications, Rt and Ant phases are the most important polymorphs. Figure 3 show a representation of the crystal structure of Rt and Ant. Rt and Ant are formed from the chemical building blocks: TiO_6 octahedral units. These octahedral structures combine together such that O atoms are three coordinated while Ti atoms are six coordinated. The TiO_6 units are is slightly distorted in both Rt and Ant: Rt has four equatorial $Ti-O$ distances of 1.946 Å and two apical distances of 1.984 Å, while Ant has four equatorial distances of 1.937 Å and two apical distances of 1.964 Å. The crystal structure is tetragonal in both cases, but Ant contains four TiO_2 units while Rt contains only two. The unit cell volumes are 62.43 Å^3 for Rt and 136.82 Å^3 for Ant, giving densities of 4.25 g/cm^3 for Rt and 3.88 g/cm^3 for Ant. Both materials have large refractive indices (~2.5 for Ant and ~2.8 for Rt).

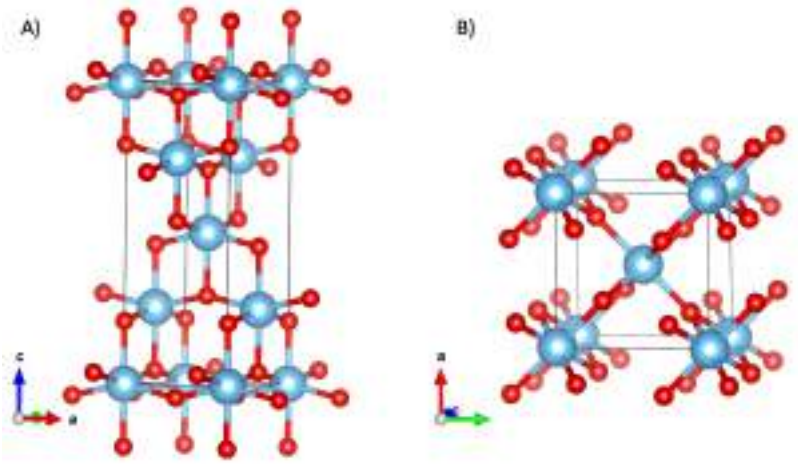

Figure 3. Crystal structure of Ant (A) and Rt (B). O atoms are represented by red spheres while Ti atoms are represented by blue spheres

Rt and Ant are widely used, with several industrial applications. The current importance of titania is highlighted by the large market around it which has a value of ~15.000 million USD[5]. To put such number in context, sulfuric acid has a market value of ~10.000 million USD[6] while ammonia's market value is around 48.000 million USD[7]. The main use of Rt and Ant is in paintings and coatings due to their great brightness and refractive index, but market projections highlight that titania is the leading compound in photocatalysis. Water remediation is the most promising short to mid-term application of photocatalysis[8], with decades of research showing how UV-irradiated TiO_2 NPs are an efficient way to remove dyes and pathogens[9–11]. Other important applications of titania involve its usage in biomedicine and batteries. For biomedical applications, TiO_2 is used as

coating of titanium implants[12,13] to facilitate the integration of such implants by promoting the growth of bone cells (osteoblasts) on it. For application in batteries, nanocrystallite Ant phases can be used as anodes in rechargeable batteries, increasing the capacity and reducing recharge times[14–16].

Basic photocatalysis and titania.

Photocatalysis emerged as a field after the seminal work of Fujishima and Honda[17] in which they presented a photo-electrochemical cell based on a TiO_2 cathode and a platinum anode for water-splitting. A photocatalyst is a material (mostly a semiconductor) capable of absorbing light and providing the absorbed energy to a chemical compound, promoting the generation of radical species which can trigger chemical reactions with other compounds. In detail, upon irradiation with light, an electron (e^-) is promoted to the conduction band of the semiconductor generating an electron hole (h^+) in the valence band. If the recombination time of e^- and h^+ is sufficiently slow, chemical species adsorbed on the surface of the semiconductor can react with both e^- and h^+, causing the generation of radical species. The following equations exemplify how titania reacts in water:

$$TiO_2 + h\nu \rightarrow h^+ + e^- \quad (36)$$

$$h^+ + H_2O_{adsorbed} \rightarrow H^+ + {}^{\bullet}OH \quad (37)$$

$$h^+ + OH^-_{adsorbed} \rightarrow {}^{\bullet}OH \quad (38)$$

Photocatalysis has received a lot of attention due to the possibility of achieving three promising applications: (I) water splitting as a potential method to generate H_2 gas, (II) CO_2 reduction to CH_4, CH_3OH or other organic compounds with high industrial value and (III) water remediation. The first photocatalytic application would help move society from a carbon-based economy to a hydrogen-based economy, the second would lower the impact of fossil fuels introducing novel methods to recycle CO_2 and the third would provide a more efficient and sustainable method for water purification.

While several chalcogenides such as ZnO[18], CeO_2[19] or CdS[20] have shown photocatalytic activity, TiO_2 is seen as the most promising photocatalyst due to several of its advantages[21]. Titania is non-toxic, highly-photostable, cheap and can be synthesized at the nanoscale with high crystallinities using sol-gel processes, allowing a good degree of tailoring, as will be shown later. On the other hand, it suffers from some disadvantages such as short electron-hole recombination time[22,23] and a wide band gap. The band gap determines the range of light frequencies capable of triggering the initial electronic excitation. The irradiance (E_ν power received per square meter per wavelength) of the sun at sea level is plotted in Figure 4. The maximum irradiance happens at around 500 nm, in the visible range, and drops very fast as the frequency moves towards the UV region of the spectrum due to absorption and scattering in the atmosphere. The band-gap of the bulk Rt phase is 3.02 eV while that of the Ant phase is 3.2 eV. Such energies correspond to frequencies of 410 and 387 nm. As a consequence, only 10% of all incoming solar radiation can be taken advantage of in photochemical applications using bulk Ant and Rt (see Figure 4).

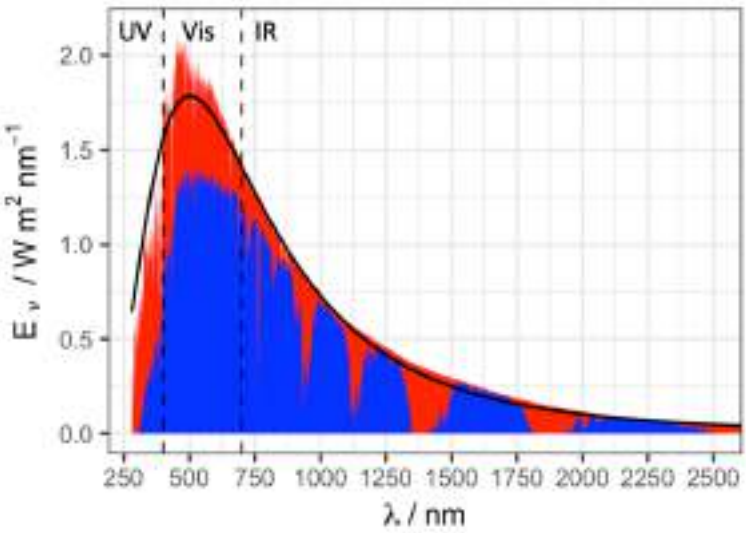

Figure 4. Sun Irradiance at a frequency range between 250 nm to 2500 nm, thus covering the UV, visible and IR spectrum. In black a blackbody model with a temperature of 5780K, in red the sunlight radiation at the upper atmosphere and in blue the sea level irradiance. The large dips are due to absorption and scattering in the atmosphere. The vertical dashed lines mark the limits on the UV, visible and IR spectra.

While a smaller bandgap increases the number of photons capable of generating the h^+/e^- pairs, other effects must be considered in order to determine the efficiency of a photocatalyst. It was established quite early that, in fact, Ant has larger photoactivity than Rt[24,25] although having a larger band gap. Explanation of this behavior has been linked to larger O^{2-} and O^- absorption on the surface of Ant in comparison to Rt[24,26]. Currently, the most efficient commercially available TiO_2 photocatalyst consists in a mixture of Ant and Rt NPs commercialized by Evonik Degusa under the name of Aeroxide P-25[27]. It is thought that the mixture of both phases may have a synergetic effect on their photocatalytic activity[28]. The use of NPs greatly improves the efficiency per kg of compound, as the surface to bulk ratio is largely increased when the particles reach the nano-sized regime.

Morphology of nanoparticles

As previously mentioned, the atomic structure of a NP has several consequences on the bandgap of a given NP, but that is only one example on the impact structure has on both physical and chemical properties of a given material. Another well-known example is the larger reactivity of high energy surfaces with respect to the corresponding low energy facets[29]. In the case of TiO_2, the theoretical study of Vittadini et al.[30] pointed out the differences of water adsorption between the {001} and {101} surfaces of the Ant phase: for the most stable {101} surfaces, water adsorbs molecularly at all coverages, while for the {001} surfaces, metastable with respect to the {101}, the adsorption is dissociative for a coverage range from low to one water molecule per surface Ti atom, which could have an impact on photovoltaic efficiency. Clearly, the properties of a given NP will depend on both the crystal structure and morphology. Theoretical knowledge on the formation processes and stability of different surfaces and their properties is a powerful tool to increase our capabilities to maximally engineer the synthesis of NPs tailored for specific applications.

It is well established that the geometry of a particle during growth is governed by the surface free energy. The Gibbs-Wulff theorem[31] states that the equilibrium shape of a crystal in a given medium is that which minimizes the surface free energy. Equation 39 allows one to calculate the difference in free energy (ΔG_i) of a NP with i stoichiometric units and composed of j surfaces with respect to the periodic solid. The free energy difference is equal to the sum of the surface free energy (γ) of each surface (j) times the area of the surface O_j:

$$\Delta G_i = \sum_j \gamma_j O_j \qquad (39)$$

The second part of the theorem states that the length of a vector normal to the j-plane (h_j) is proportional to γ_j:

$$h_j = \lambda \gamma_j \qquad (40)$$

Application of the Gibbs-Wulff theorem gives rise to the Wulff construction. For Ant, the surface energy of the most stable (101) surface is 0.44 Jm^{-2}, and therefore is the most expressed facet. Figure 5 A depicts the most stable Wulff construction for the Ant phase, which also shows the (001) surface. Single crystal NPs with the Wulff construction shape are easily obtained.

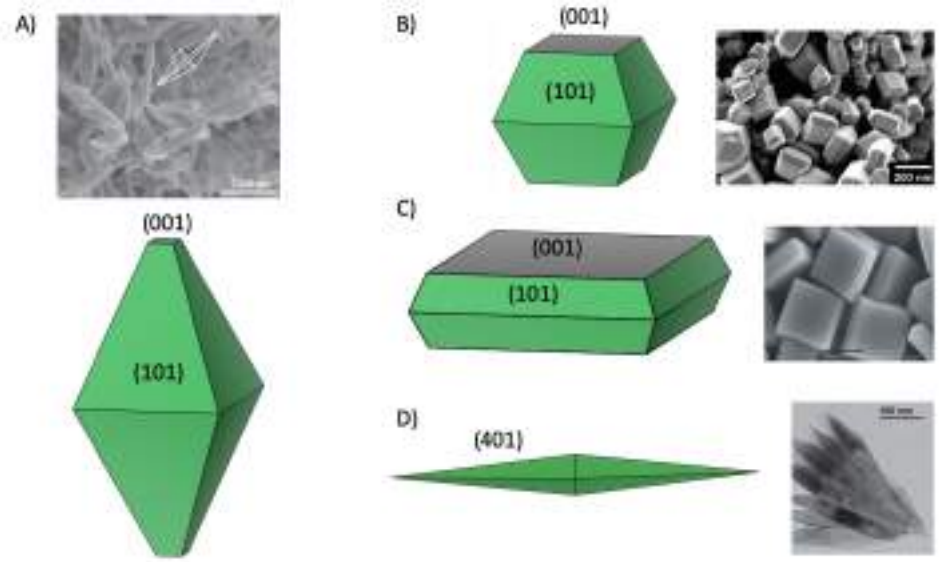

Figure 5. Crystal shapes and STEM images of bipyramidal[35] (A), octahedral[37] (B), slab[38] (C) and needle[36] (D) NPs with the corresponding facets labelled. For (A), the surfaces are proportional to their surface energy, while (B) and (C) have non-equilibrium proportion of facets, and (D) shows a high-index facet.

Extensive experiments on TiO_2 NPs revealed that, if the diameter is kept below several tens of nm, the most abundant crystal structure during synthesis is the Ant phase rather than Rt. This is the opposite to what would be expected from classical thermodynamic arguments where bulk Rt has a larger thermodynamic stability than the bulk Ant phases[32]. The reason is that for such small NPs the contribution of the surface free energy can be of the same order of magnitude as the free energy of the core. The Ant (101) surface has a free energy of 0.39 J/m^2, while the Rt (110) surface has a free energy of 0.47 J/m^2 as computed by DFT using the PW91 functional[33]. The total energy of an Ant NP is

therefore smaller than for Rt for a size range where the surface contribution is sufficiently large. The crossover between Rt and Ant phases at the nanoscale has been studied by several groups both experimentally and theoretically. Experimentally, the phase transition has been observed to occur at a size of 14nm. The theoretical study of Barnard et al.[33] also computed the crossover between Rt and Ant phases to happen at 9 nm.

The synthesis of high energy facets also comes from the interplay between theory and experiment. Following theoretical predictions by Barnard et al.[34], Yang et al.[35] calculated the surface energy of different TiO_2 Ant facets with several adsorbate atoms on the surface, finding that F^- stabilized the {001} surface to energies even below the {101} surface. Synthesis using TiF_4 as precursor allowed Yang et al. to obtain Ant single crystals with a large fraction of {001} surfaces, thus confirming theoretical predictions. Several synthesis mechanisms have appeared since the work of Yang et al. which allowed the synthesis of several other low index facets: {010}, {110} and high index facets {103}, {105} or {107}. The significant degree of control over NP growth due to the stabilization of different surfaces has also led to the synthesis of tailored structures such as nanoneedles[36], nanoslabs[37], bypiramids[38] or cuboctahedrons[39]. Some of the structures are depicted in Figure 5 B, C and D.

Another relevant structural phase is the amorphous phase. The amorphous phase is obviously metastable in the bulk limit, and thus annealing of amorphous nanostructures causes the appearance of crystallinity[40]. However, despite the thermodynamic preference of the Rt phase at sizes larger than several nm, annealing of amorphous particles at low temperature results in the crystallization of the Ant phase[40–43]. Justification for such observation is actually divided into two points of view: a more crystallographic point of view justifies Ant to form faster due to the less constrained nature of its atomic structure than Rt, while a more thermodynamic point of view suggests that the lower surface energy of Ant with respect to Rt favors the nucleation of the Ant phase[44].

The arguments of the discussion so far had their foundations on the properties of macroscopic objects such as bulk free energy and surface free energy of extended solids. From a computational point of view, they involve the use of periodic structures of either the bulk or surfaces, which are less computational demanding than computing a whole NP. However, at sizes below the Ant-Rt crossover, such top-down approaches become more difficult to justify. The reason for such difficulties lays in the fact that for NPs with hundreds to thousands of atoms, at the border with the nanocluster regime, it is not easy to differentiate between bulk and surface, nor the effect of surface atoms on the internal structure. This size regime is important as the structure of the smallest clusters can influence the structural evolution of nanostructured TiO_2 under thermal annealing[45]. From this point of view, the previous observation of the amorphous to Ant transition could be related to a closer similarity between structures as size grows, rather than the random appearance of crystallite nucleation centers on the grain. A combined experimental and computational study on TiO_2 nanoclusters with particle sizes of 2 nm found that the most promising way to reproduce the experimental pair distribution function of synthesized

amorphous clusters was with a NP model which contained an ant core and a distorted amorphous shell[46].

More evidence of crystalline core/amorphous shell NPs of TiO_2 has also appeared with the synthesis of black TiO_2[47]. Black TiO_2 is a metastable synthetic phase with promising photocatalytic applications, since its bandgap is well below that of Ant and Rt with a value around 2.2 eV[47]. While the precise structure of these NPs is highly dependent on the synthesis method, it is well agreed that their photocatalytic application arises from its core-shell structure[48,49].

State of the art in computational modelling of TiO_2 nanoparticles

Computational studies have been a valuable tool to understand the physical and chemical properties of TiO_2. Wulff constructed NPs have been investigated by assuming that their properties can be described as a combination of the properties of its facets. Hence, the body of literature examining the properties of the {101} and {001} Ant facets is extensive, with most of the work centered on understanding the reactivity of the surfaces and their structure. For instance, the energetic stability of different surfaces seems to be related to the presence of 4 coordinated Ti centers, with larger fraction of 4 coordinated Ti centers decreasing the stability of the surface. Thus the (110) and (103) facets have larger energies than surfaces with higher amount of 5 coordinated Ti centers[50]. Another explored effect is the presence of oxygen vacancies, their characterization and the energetics for their diffusion[51,52]. In terms of adsorption, DFT calculations have been used to understand experimental results such as IR spectra of CO_2 adsorbed on Ant surfaces[53] and STM images of the O_2 interaction with surfaces containing O vacancies[54]. Also relevant in the field are the studies of the effect of several adsorbates on the band-gap of different surfaces[55] and the adsorption energies of formic acid[56]. More recently, the use of full NP models following the Wulff construction have been employed. The size evolution of the electronic properties of ground state and excited state have found the convergence of NP properties towards the bulk limit at a size around 20 nm[57,58]. For spherical particles, the effect of curvature in reactivity and electronic structure has also been modelled by using hydroxylated spherical NPs[59], although such comparison does not exist for anhydrous spherical models. The effect of defective sites on nanocrystals and the comparison with extended surface has also been studied, showing a great variation in properties as a function of defective site position in the NP[60].

A detailed thermodynamic study of the different phases and structures of NPs from the cluster size to nanometer size containing several thousands of atoms could provide new clues to understand the transitions between amorphous material and crystal phases, as well as finding unexpected reactivity at the nanoscale regime. Several papers have performed theoretical searches of TiO_2 global minima structures for clusters containing up to 38 stoichiometric units[61,62]. While the smallest clusters tend to have some symmetry, their structure cannot be compared to either the Rt or Ant phases. In this regard, the work of Lamiel et al[63] showed how Ant cut structures can be found to be from 8 to 10 eV higher in total energy than the respective global optimized clusters for particles of 28, 35 and 38

stoichiometric units. Energetically, the cross-over between amorphous globally optimized particles and Ant Wulff constructed NPs was determined to happen in a size range around 2 nm. The position of spherical crystalline and amorphous NPs in such phase diagrams is not yet stablished. Understanding the stability of spherical NPs can also hold clues on the degree of hydration that such NPs can possess, which is necessary to properly evaluate the properties of such NPs.

The work presented in this thesis aims to further explore the energetic stability, structure and electronic properties of nanoscale TiO_2, with emphasis on spherical NPs. In order to facilitate computational calculations using high accuracy methods, we evaluate the ability of IPs to efficiently pre-optimize nanostructures. In addition, we use IPs to generate spherical NP models and compare their internal energy with respect to directly generated bulk cuts. Finally, we analyze the evolution of band gap with size and particle morphology, as well as describe the structural motifs which differentiate the spherical amorphous NPs.

Chapter 4: Objectives

As seen in the previous chapter, knowledge on nanometre sized TiO_2 NPs is still far from complete. For one, the preferential crystallization of amorphous NPs in the Ant phase is currently controversial. For structures smaller than 2 nm in diameter, the lowest energy clusters reported by means of GO are amorphous, and do not yet seem to have any resemblance to the Ant structure. As the structures of Ant core / Amorphous shell NPs seem to be most compatible with the experimental X-ray spectra of small NPs, it is important to evaluate the relative energy of core-shell NPs with respect to other morphologies. As core-shell NPs are of spherical geometry, it is necessary to generate fully crystalline models of spherical particles, as such crystalline spherical particles represent an extreme case of core-shell particles in which the amorphous shell is non-existent. In addition, having proper models of spherical NPs structures with their relative energy also serves as a starting point for further studies aimed to evaluate the effect of hydration of these structures. Finally, a comparison of non-hydroxylated TiO_2 NPs with several geometries can allow a better understanding of the effect of structure on the electronic structure of the system.

Specifically, the objectives of this part of the thesis are:

1. Determine the most appropriate IP to pre-optimize models of Wulff constructed and spherical NPs to speed up DFT calculations of TiO_2 nanosystems containing hundreds or thousands of atoms.
2. Determine whether MD simulations using IPs can properly stabilize spherical cut models with lower internal energies than direct bulk cuts and reproduce the energetical stability as obtained from DFT methods.
3. Determine the energetic stability of different anhydrous TiO_2 NP models.
4. Characterize the structure of core-shell amorphous NP models.
5. Understand the factors that play a key role in the energetic stability of NPs.
6. Understand the factors that play a key role in determining the bandgap of spherical NP models.

Chapter 5: Efficient preparation of TiO_2 nanoparticle models using interatomic potentials.

Introduction

As seen in Chapter 3, the shape of $\mathrm{TiO_2}$ NPs can be tailored to obtain specific properties[29,56]. Among the different tuneable physical characteristics which affect the properties of the material one can vary crystal structure, shape, composition or size. With respect to geometry, the shape of a large NP is mostly governed by the free energy of the different possible surfaces[31]. Thus, synthesis conditions which stabilize different surfaces allow the generation of facetted NPs with different morphologies. Spherical NPs can also be synthesized both in the amorphous -as observed in X-ray- and crystalline state depending on size[40,41].

Despite the great degree of control over the synthesis, the NP products generally exhibit a variety of surfaces and sizes, which complicates ascribing an obtained property to a single chemical or structural motif. In some circumstances, even the characterization of the produced NP is not obvious. Examples of such cases are black $\mathrm{TiO_2}$ and amorphous NPs, where it is thought that the amorphous surface may hide a crystalline core in its interior[46,64].

Computational methods have been used to identify the precise importance of different structural features on material properties. Different modelling approaches are used depending on the type of study at hand. For static properties such as band-gap, IR spectra or energetics of bulk, surfaces, and small finite clusters, DFT methods are the most popular choice, as even moderate computer capabilities allow such calculations. For dealing with large nanoclusters or NPs and/or time dependent processes such as amorphization or growth, other methodologies must be used such as Tight Binding DFT methods[65] (TB-DFT) or interatomic potentials (IPs) coupled with MD simulations[64,66–71]. While IPs have extremely low computational cost, they can only offer structural derived data, but not electronic structure properties. TB-DFT methods on the other hand parametrize the electronic interaction between pairs of elements. The computational cost is therefore reduced with respect to pure DFT methods while retaining some components of the electronic structure.

Synthesized NPs have a typical size between 10 to 100 nm[72], with lower limits of 3 to 4 nm[46]. Accurately computing the electronic properties of such experimentally obtained species face several difficulties. Such NPs are composed of several thousands of atoms and even a small size increase means a huge increase in number of atoms, as volume increases as the cube of radius ($V \propto r^3$). For instance, a particle of 3.1 nm is composed of around 500 units of $\mathrm{TiO_2}$ (i.e., 1500 atoms), while a particle of 3.3 nm is composed of 600 units of $\mathrm{TiO_2}$ (i.e., 300 more atoms). The computational cost of DFT methods increase approximately as N_e^4, where N_e is the number of electrons. Consequently, each Self Consistent Field cycle has a very large computational cost. Even the optimization of a Wulff constructed NP, whose structure is closest to the bulk structure, requires several SCF steps and thus has a large computational cost. On the other hand, experimental results typically

involve ensembles of structures, especially for non-annealed samples. Obtained properties are therefore averages of the present structures which may not correspond to thermodynamically stable NPs. It is therefore necessary to explore large portions of the PES and analyze the properties of large sets of structures. However, evaluating a large number of structures is not possible with DFT methods.

With respect to DFT, the use of TB-DFT and IP methods as a faster way to obtain properties is well established. However, investigations assessing the time saved in using such methodologies as pre-optimizers for subsequent more accurate DFT calculations is not common. Although pre-optimization is unlikely to change the order of magnitude of the computational cost of a calculation, for NPs that can only be computed in High Performance Computing centers the time savings could imply a large increment of the achievable research for a fixed computational time budget. In the following article we benchmark several IPs with respect to their capability as pre-optimizers and compare them to TB-DFT methods. As it is reasonable to expect that reducing the time needed for a DFT calculation is related to having a starting structure closer to the DFT minima, it follows that the PES of the IP should be related to the PES as obtained from DFT. We therefore evaluate the energetic impact of IP-based simulated annealing on directly cut spherical NPs by calculating the induced energy change using DFT.

In the following paper, led by the author of this thesis, we investigate the capability of four different IPs to lower to computational cost of DFT calculations. This work was done in collaboration of Dr. Angel Morales. The author of the thesis generated all amorphous models by means of MD simulations and analyzed the speed-up obtained due to the pre-optimization using IPs. The DFT calculations were performed by Dr. Angel Morales and the discussion of the paper was done by all authors.

Results

The Journal of Chemical Physics ARTICLE scitation.org/journal/jcp

Efficient preparation of TiO_2 nanoparticle models using interatomic potentials

Cite as: J. Chem. Phys. 150, 214305 (2019); doi: 10.1063/1.5095071
Submitted: 7 March 2019 • Accepted: 1 May 2019 •
Published Online: 6 June 2019

Antoni Macià Escatllar,[1] Ángel Morales-García,[1] Francesc Illas,[1] and Stefan T. Bromley[1,2,a]

AFFILIATIONS

[1]Departament de Ciència de Materials i Química Física & Institut de Química Teòrica i Computacional (IQTCUB), Universitat de Barcelona, c/ Martí i Franquès 1-11, 08028 Barcelona, Spain

[2]Institució Catalana de Recerca i Estudis Avançats (ICREA), Passeig Lluis Companys 23, 08010 Barcelona, Spain

[a]Author to whom correspondence should be addressed: s.bromley@ub.edu

ABSTRACT

Computational modeling has proven to be extremely useful for understanding how the morphology, size, and structure of TiO_2 nanoparticles (NPs) affect their electronic properties and their usage in targeted applications (e.g., photocatalysis). Density functional theory (DFT) based calculations of NPs (on the order of hundreds to thousands of atoms) are, however, computationally highly demanding. Herein, we show that interatomic potentials (IPs) can provide a highly computationally efficient means to prepare NP structures which are sufficiently accurate to significantly reduce the computational cost of subsequent DFT calculations. We first compare the direct DFT optimization of faceted NPs directly cut from the anatase bulk crystal with the same calculation where the NP is preoptimized using four different IPs. We then establish the subsequent computational time saving for the respective complete DFT optimizations. We show that IP-based preoptimizing can greatly speed up DFT convergence, with speed-ups of 3×–10× for single point DFT energy evaluations. Moreover, as IP preoptimized NP structures can be closer to those of DFT energy minima, further speed-ups of 2× for DFT structure optimizations can be achieved. Finally, taking NPs derived from anatase spherical cuts, we show that IP-based molecular dynamics annealing gives rise to significant structural reconstruction with an associated high energetic stabilization, as confirmed by DFT calculations. Although similar results can be achieved using DFT tight binding methods, IP-based methods are 3–4 orders of magnitude faster and thus provide a particularly highly computationally efficient route to the preparation and design of large and diverse NP sets.

I. INTRODUCTION

Titanium dioxide (TiO_2) is a multipurpose semiconducting material with a wide range of applications, including solar cells,[1,2] drug delivery,[3,4] and photocatalysis.[5,6] Often these applications employ TiO_2 nanoparticles (NPs) where the nanotailored electronic structure and reactivity play a key role. From a theoretical perspective, several recent computational studies have used density functional theory (DFT) based calculations to model TiO_2 NPs in order to better understand their structural stability, reactivity, and optical and electronic properties.[7–11] Calculating the structures and properties of large and realistic TiO_2 NPs composed of thousands of atoms by means of DFT based calculations faces a number of difficulties. First, even the low end of the typical experimental TiO_2 NP size regime (i.e., ~10–100 nm diameter)[12] is barely achievable within DFT based methods, even when using supercomputer resources and highly parallelized computational codes. Practical state-of-the-art DFT based calculations are limited to TiO_2 NPs with diameters of less than 10 nm, containing, at most, a few thousand atoms. A second constraint involves the appropriate modeling of NPs with realistic structures, chemical compositions, and morphologies. To this end, NP models are usually initially based upon top-down cuts from a parent TiO_2 crystal to make either (i) faceted NPs, using the Wulff construction,[13] or (ii) spherical NPs, using a radially symmetric geometric constraint. The former seeks to provide NPs with the lowest energy surfaces, whereas the as-cut spherical NPs have larger proportion of low coordinated surface sites. Thus, prepared bare spherical NP models are thus generally energetically metastable with respect to the faceted NPs.[14] In practice, most uncoordinated sites in spherical as-cut NP models are either removed or hydroxylated prior to structural optimization. In addition, the structures of the NPs may be thermally annealed via use of molecular dynamics (MD)

The Journal of Chemical Physics ARTICLE scitation.org/journal/jcp

calculations in order to help overcome barriers to energy-lowering structural reconstructions. All these procedures will tend to converge the stabilities of both spherical and faceted NPs, as confirmed by both experiments[15,16] and computational modeling,[17] suggesting that control of the NP environment can facilitate the synthesis of NPs with either faceted or spherical shapes. Finally, in experiment, we typically have an ensemble of NPs and thus computational modeling of such systems should reflect this. As such, ideally, we should generate a large number of NPs with a range of structures, morphologies, and sizes in order to sample the experimental variability. Efficient sampling of large numbers of NP isomers is also inherent to global optimization searches, MD annealing calculations, and for preparing datasets for machine learning. Clearly, the cumulative computational expense of accurately calculating the properties of large sets of diverse NPs, involving both large NPs and MD-annealed NPs, can become very high. Finding strategies to increase the practical computational efficiency of such calculations is thus very desirable.

In order to calculate the accurate electronic structure of prepared NP models, their structures are typically first optimized to a local energy minimum using DFT based calculations. The numerous energy and gradient evaluations involved in these optimizations constitute the most computationally expensive obstacle to evaluate experimentally relevant NP properties. The computational time required for an optimization tends to be correlated with the extent of the difference between the starting structure and that of the nearest local minimum. Herein, we explore the benefits of preparing as-cut NP structures using classical interatomic potentials (IPs) in order to obtain improved starting structures in order to substantially reduce the subsequent DFT optimization cost. Although IP-based calculations can only provide structural and energetic information with a lower accuracy than DFT, they are typically five orders of magnitude faster than comparable DFT calculations. As such, IPs have been used in the literature to study nonelectronic properties of TiO_2 systems that are computationally unaffordable at the DFT level.[17–19] Early benchmark studies reported on the capability of TiO_2 IPs to reproduce experimental and ab initio properties of several bulk[20] and surface[21] systems. Since then, several IPs have been reported (e.g., see Refs. 9, 26, and 27). As far as we are aware, there has been no comparative study regarding the performance of IPs for preparing accurate TiO_2 NP structures. Herein, we provide a systematic study of four IPs for preoptimizing the structures of as-cut NP models and thus reducing the time required for subsequent DFT based calculations. We also thermally anneal a selection of TiO_2 NPs using IP-based MD runs with the aim of inducing energy-lowering structural reconstructions. The IP-annealed reconstructed NPs are subsequently optimized at the DFT level in order to confirm the usefulness of such procedures for producing more realistic structurally stabilized NPs. We also compare our IP-based results with those from using tight binding (TB) calculations. In terms of providing accurate NP structures for increasing the efficiency of DFT postoptimizations, we find that TB methods have no significant practical advantage over much faster IP-based approaches.

II. COMPUTATIONAL DETAILS AND METHODOLOGY

For our comparative IP study, we select the well-established and widely used Matsui-Akaogi (MA) IP[22] and three more recent IPs reported by Pedone *et al.*,[23] Swamy and Gale,[24] and Lamiel-Garcia *et al.*,[9] hereafter denoted as PMMCS, TVQIP, and NanoTiO, respectively. Although not considered in this work, we note that the ReaxFF[25] approach is also gaining popularity in classical IP simulations involving TiO_2.[26–28] This more complex and flexible IP-based approach is often reparametrized to account for specific features of the chemical environment of interest and aims to provide more realistic simulations of chemical systems (e.g., reactions) than possible with simple IPs. Herein, our objective is to establish an efficient and accurate procedure to provide improved initial NP structures for enabling efficient DFT evaluations of their properties and is less concerned with the ability of IPs for directly modeling NP systems. We note that the NanoTiO IP is a reparameterization of the MA IP. Specifically, NanoTiO was designed for obtaining improved energies and structures of small $(TiO_2)_n$ nanoclusters, where the MA IP is expected to not to perform particularly well due to its preference toward highly compact structures,[24,29] which have been confirmed to be generally less energetically stable than more open clusters in DFT-based studies.[30,31]

Structure optimizations and MD simulations are performed by using IPs as implemented in the GULP4.4 code.[32] The four IPs selected for the present study (MA, PMMCS, TVQIP, and NanoTiO) are all classified as ionic potentials and, therefore, long-range interactions follow the Coulomb potential $U_{long\ range}(r) = \frac{q_i q_j}{r}$, where q_i is the charge of the element type i and r is the interatomic distance between i and j. While MA, PMMCS, and NanoTiO have fixed charges for the elements, TVQIP has been parameterized using the Morse Stretch charge equilibrium scheme (MS-Q)[33] to account for the variation of ionic charge in different chemical environments. This charge variation scheme is intrinsically more computationally expensive than the use of fixed charges. Hence, the scaling of TVQIP with system size is worse than that of MA, PMMCS, and NanoTiO. Three different functions are used to model short and medium range interactions. Both MA and NanoTiO use the Buckingham potential, defined as

$$U(r) = Ae^{-r/\rho} - \frac{C}{r^6}, \tag{1}$$

where A, ρ, and C are fitting parameters. The PMMCS and TVQIP use the Morse potentials defined as

$$U(r) = D_e\left[\left(1 - e^{\{a(r-r_0)\}}\right)^2 - 1\right], \tag{2}$$

where D_e and r_0 are the bond energy and the equilibrium distance, respectively. Finally, the PMMCS also adds an extra short length repulsive term as follows:

$$U(r) = \frac{C}{r^{12}}, \tag{3}$$

with C being also a fitting parameter. With the previously described IPs, it is possible to optimize large TiO_2 NPs composed of thousands of atoms on a standard desktop computer in minutes or a few hours. However, because of the empirical character of the IPs, the outcome of such geometry optimizations needs to be validated against first principles-based methods. Here, we use DFT based calculations employing the Perdew-Burke-Ernzerhof (PBE) exchange correlation functional.[34] The present DFT based calculations explicitly include all electrons, and the electron density is described through a numerical atom-centered orbital basis set, as implemented in the

The Journal of Chemical Physics ARTICLE scitation.org/journal/jcp

FHI-aims code.[41] A light grid and tier-1 basis set was used, which has an accuracy comparable to a Triple-Zeta Valence Polarized (TZVP) Gaussian-type orbital basis set.[3] The convergence threshold for individual atomic forces during the relaxation of the structure of the NPs was set to 10^{-1} eV Å^{-1}. The DFT based calculations were carried out at the Marenostrum IV supercomputer of the Barcelona Supercomputer Center using 1024 cores.

To establish the performance of the MA, NanoTiO, TVQIP, and PMMCS IPs for preparing reliable NP structures, we analyze the results of (a) direct DFT based optimizations of a Wulff cut anatase NP containing 84 TiO_2 units and (b) DFT optimizations after preoptimizing the same Wulff cut with each of the four considered IPs. First, we analyze whether the final structures of (a) and (b) correspond to the same energy minimum in order to discard any IP that provides a different description to that obtained by DFT. Afterwards, we compare the computational cost required to reach structural convergence. Next, we explore the capability of the IPs to accurately preoptimize other TiO_2 NPs sizes, both smaller and larger. In particular, we select Wulff constructed anatase $(TiO_2)_n$ NPs with n = 10, 35, 84, and 165.

Finally, we explore the ability of IPs to thermally anneal spherical NPs cut from the bulk anatase crystal in order to induce energy-lowering structural reconstructions. These NPs were generated by cutting spheres of the anatase crystal structure following a procedure reported in other studies.[7,31] In the cited studies, the TiO_2 stoichiometry is preserved by addition of hydroxyl groups and hydrogen atoms to defective Ti and O centers, respectively, which results in the generation of hydrated TiO_2 NPs. Herein, we ensured that the TiO_2 stoichiometry was always preserved without the addition of any element and therefore modified the cited procedure by randomly eliminating enough three coordinated Ti centers until the particle became stoichiometric. The IP-based preparation and DFT-calculated properties of such anhydrous annealed spherical NPs as compared to experiment are discussed in Ref. 14. Here, we consider two spherical NP sizes containing 162 and 237 TiO_2 units. To carry out the annealing simulations, we used MD simulations using the NanoTiO IP. The MD simulations were carried out in the canonical ensemble. Initial random velocities of the atoms were generated corresponding to a NP temperature of 800 K. During 5 picoseconds (ps), the temperature was gradually increased up to 1000 K and the NP was equilibrated. Subsequently, a 30 ps run at 1000 K was performed with energy and structure sampling every 0.01 ps. The five NP structures with the lowest energies obtained during each MD run were then selected. The energetic stability change in each of these five NPs with respect to the initial bulk cut NP structure was assessed using the MA and NanoTiO IPs, DFT, and SCC-DFTB in order to compare the ability of each method to describe the structure and energetics of noncrystalline NPs. SCC-DFTB calculations were performed with the DFTB+ code[42] and the matsci-0-3 parameter set.[43]

III. RESULTS AND DISCUSSION

We first consider the structural optimization of a Wulff-constructed faceted bulk cut $(TiO_2)_{84}$ NP. DFT optimizations of this NP structure that were first preoptimized with MA, NanoTiO, and TVQIP all converged to the same energy minimum as that from a direct DFT optimization of the initial Wulff constructed bulk cut NP [see Fig. 1(a)]. This was checked by confirming that the differences between both the root mean square deviation (RMSD) of atomic positions and the final total energies of the final DFT optimized structures were negligible. We found that the DFT optimization of the structure obtained by PMMCS led to a different energy minimum [see Fig. 1(b)] than that from a direct DFT optimization. Specifically, with respect to the directly DFT optimized NP structure in Fig. 1(a), the PMMCS derived structure is higher in total DFT-calculated energy by 0.36 eV and has a RMSD value of 1.37 Å. The main difference between the two NP structures in Fig. 1 is caused by a lower coordination of Ti atoms in the PMMCS derived structure. The direct DFT optimized structure maintains the anatase crystal nature of the as-cut NP with an average Ti coordination of 5.1. However, the PMMCS derived structure distorts the atomic environments of the Ti atoms in the central part of the NP in order maximize the number of 4-fold coordinated Ti atoms, causing an artificial amorphization and a reduction in the average coordination of Ti atoms to 4.38. Consequently, we exclude PMMCS from our further analysis. Although speculative, it seems reasonable that the origin of the poor performance of PMMCS may be due to the lack of TiO_2 structures used in its fitting. PMMCS was mainly devised to reproduce both structural and mechanical properties of silicate glasses of variable composition, and the only pure TiO_2 structure used in the fitting dataset was the rutile crystal structure. On the other hand, MA, NanoTiO, and TVQIP were all parameterized with several TiO_2 structures, providing a better representation of the overall characteristics of TiO_2 materials.

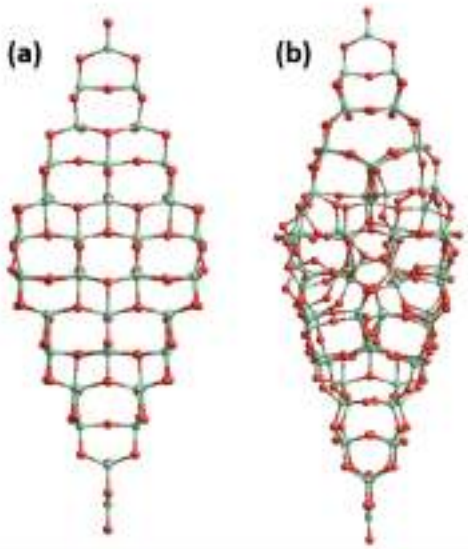

FIG. 1. (a) DFT and (b) PMMCS optimized structures of the $(TiO_2)_{84}$ NP obtained from the same initial anatase bulk cut following the Wulff construction. Notice the amorphization in the equatorial part of the NP in (b). Atom color code: red—oxygen and green—titanium.

The Journal of Chemical Physics ARTICLE scitation.org/journal/jcp

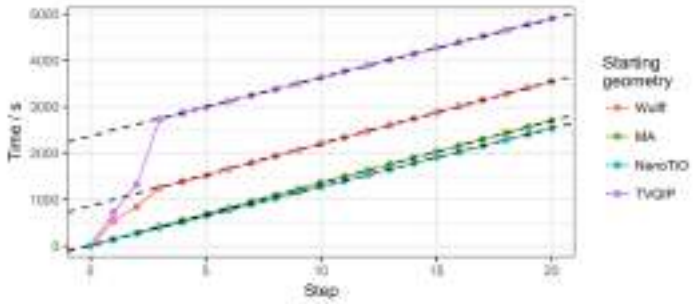

FIG. 2. Total time of the DFT optimization of each preoptimized $(TiO_2)_{84}$ NP in seconds with respect to the number of optimization steps. The colors relate to the different starting geometries of the NP as preoptimized using different IPs. The dashed lines highlight where the different DFT optimizations take the same number of SCF cycles per step.

For any DFT optimization procedure, the computational time is mainly constrained by two different factors: (i) the number of self-consistent field (SCF) cycles required within each optimization step and (ii) the number of steps required to reach the desired convergence criteria. Both are related to the difference between the initial structure of the NP and that of the closest energy minimum on the potential energy surface (PES). In Fig. 2, we show the time evolution with respect to the number of DFT optimization steps, both with and without IP preoptimization, for the faceted bulk cut $(TiO_2)_{84}$ NP. For the calculations starting from the directly cut NP structure and from the TVQIP optimized NP structure, the first three geometry optimization steps require a relatively large computational cost, whereas the subsequent time needed for each subsequent step is consistently lower (~20 s). By contrast, when starting from MA and NanoTiO preoptimized NP structures, the DFT geometry optimization steps have a constant low computational cost (~20 s) per step throughout the full optimization. The underlying reason for this difference is due to the relative number of SCF cycles required for the initial steps. The first three optimization steps of the TVQIP preoptimized NP require 101, 117, and 290 SCF cycles, respectively, adding up to a total time of 2738 s. For the as-cut Wulff constructed NP, the three initial optimization steps need 60, 54, and 78 SCF cycles, with a total added time of 1258 s.

Timing information for each optimization step does not provide an estimate of how many such steps will be required for a full optimization. However, when the time per step is almost constant, this strongly suggests that the optimization is proceeding in a regular predictable fashion to close the nearest local energy minimum. This situation also implies that the optimization is acting on a structural configuration on the PES which is somehow close to that of the final energy minimum. In order to provide a measure of the configurational distance between the NP structure at any one optimization step and the final step, we use the RMSD of atomic positions of a partially optimized NP with respect to the fully DFT optimized NP structure. We note that NPs with similar RMSD values do not necessarily have similar structures. For example, very distorted local regions in one NP structure can increase the RMSD by a similar amount to the addition of many distributed small distortions in another. With increasing optimization, NP structures become very close to the DFT local energy minimum and the associated RMSD becomes closer to zero. Here, the likelihood of energetically costly large structural distortions greatly reduces, and NP structures with low RMSDs become very similar. We define a very tight RMSD criterion to gauge when NPs are structurally converged, whereby two structures can only differ on average by 1% of a typical Ti–O bond length, that is, when their RMSD is below 0.02 Å. Figure 3 shows the evolution in RMSD of the $(TiO_2)_{84}$ bulk-cut NP with respect to DFT optimization time for the as-cut structure and with preoptimized structures using all considered IPs. NP structures preoptimized with both the MA and NanoTiO IPs have a very similar DFT optimization time of around ~1630 s, while without

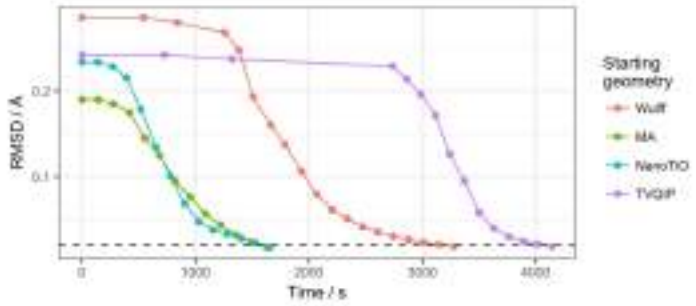

FIG. 3. RMSD evolution of atomic positions in Å for each IP preoptimized $(TiO_2)_{84}$ NP with respect to the DFT optimized final structure vs optimization time. Every point corresponds to an optimization step except for the initial t = 0 point. The dashed line indicates our structural convergence criterion of RMSD < 0.02 Å.

The Journal of Chemical Physics ARTICLE ecitation.org/journal/jcp

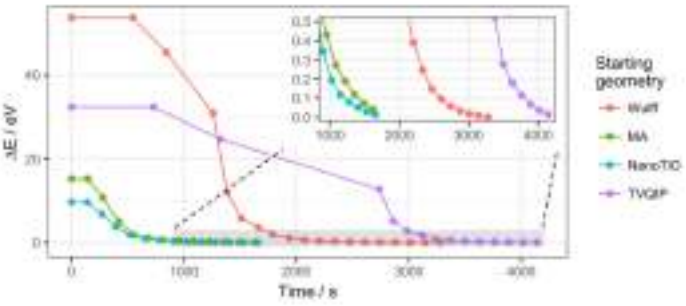

FIG. 4. Evolution of the relative energy (in eV) stability throughout optimization of the IP preoptimized $(TiO_2)_{84}$ NPs with respect to optimization time until structure convergence (RMSD < 0.02 Å). Every point corresponds to an optimization step. The inset shows a zoom of the optimization highlighting the final steps of each optimization over a 0.5 eV relative energy interval with respect to the converged NP structures.

preoptimizing the structure (i.e., using the bulk cut NP as starting point) a DFT optimization requires 3780 s to converge to the same final structure. This means that the preoptimization allows one to reduce the computational cost for DFT optimization by ~50% (i.e., a 2× speed-up). By contrast, preoptimizing using TVQIP leads to a DFT optimization time of 4140 s, and consequently, it increases the computational time by ~10%. We note that the NanoTiO and TVQIP optimized TiO_2 NPs have a quite similar initial RMSD but lead to a very different DFT optimization times. As noted above, NP structures far from the energy minimum may have different deformations that can produce similar RMSDs. Another reasonable criterion to help understand differences in optimization time, especially during the initial steps, is the difference in the energy of the NP structure with respect to the final fully optimized structure. In Fig. 4, we plot the energy difference of each initial $(TiO_2)_{84}$ NP structure with respect to the completely DFT optimized NP energy. At the first step of the optimization, the as-cut bulk NP is ~50 eV higher in energy than when fully optimized. This is a large difference with respect to the corresponding values for all the considered IP preoptimized NP structures. However, the TVQIP preoptimized NP is ~30 eV higher in energy than the final DFT optimized NP. This difference is significantly higher than the MA and NanoTiO preoptimized structures which have total DFT energies ~15 eV and ~10 eV above that of the fully DFT optimized NP structure, respectively. Surprisingly, although the TVQIP preoptimized NP has a lower initial DFT energy than the as-cut NP structure (with a correspondingly lower RMSD), it leads to a relatively longer time for its total DFT optimization time (see Table I). The main problem appears to be due to the high number of SCF cycles required for the initial optimization steps of the TVQIP preoptimized NP structure. In order to understand the differences between the different IP preoptimizations, we compare the average Ti–O bond lengths in each IP preoptimized NP. As one may expect, the average Ti–O bond length seems to be correlated with the energy difference. At the final energy minimum, the NP has an average bond length of 1.91 Å, while the Wulff constructed NP has an average bond length of 1.97 Å, the longest for all evaluated systems. The DFT optimization therefore compresses the as-cut NP structure. The TVQIP structure shows a value of 1.96 Å, very close to the original Wulff constructed NP, while MA and NanoTiO average bond lengths are much smaller, 1.91 and 1.90 Å, respectively. Both MA and

TABLE I. Comparison of time (in seconds) and number of SCF cycles for the first optimization step and total optimization time (19 optimization steps) for the as-cut and IP preoptimized $(TiO_2)_{84}$ NP structures.

Initial structure	Time for first step	Number of SCF cycles at the first step	Total optimization time
As-cut Wulff	542.5	60	3279.8
MA preopt.	142.3	21	1626.4
NanoTiO preopt.	138.4	22	1654.9
TVQIP preopt.	725.6	101	4141.0

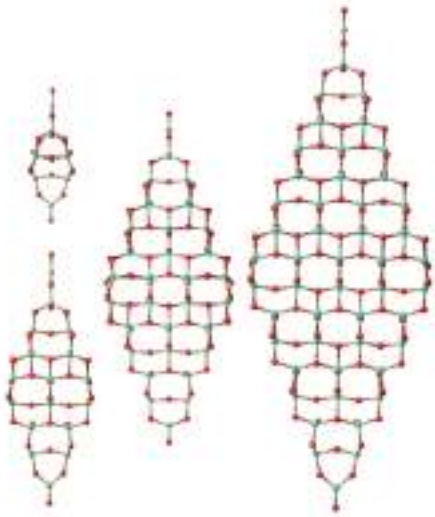

FIG. 5. Structure of anatase Wulff-constructed bulk cut $(TiO_2)_n$ NPs with n = 10, 35, 84, and 165. Atom color code: red—oxygen and green—titanium.

The Journal of Chemical Physics ARTICLE scitation.org/journal/jcp

NanoTiO preoptimizations compress the as-cut NP structure in line with DFT optimization, thus helping to explain their relatively improved performance.

In order to test whether the results found for the $(TiO_2)_{84}$ NP can be extrapolated to other sizes, we compare the single point (SP) energies and corresponding SCF times for a selected set of faceted bulk cut $(TiO_2)_n$ NPs, with n = 10, 35, 84, and 165. The considered NP structures are shown in Fig. 5, and their coordinates are available in the supplementary material. Figure 6 (top) shows the fraction of time for an SP DFT calculation of each of the IP preoptimized NP structures with respect to the time for an SP DFT calculation of the corresponding fully DFT optimized NP structures. The relative total energies from these SP calculations on the IP preoptimized NPs are also given in Fig. 6 (bottom) with respect to that of the corresponding fully DFT optimized NP structures. In this latter plot, we also include the SP energies calculated using as-cut structures for the $(TiO_2)_{35}$ NP preoptimized using a Self-Consistent Tight-Binding (SCTB) method parameterized for TiO_2 by Barnard *et al.*[44] and for the $(TiO_2)_{84}$ NP preoptimized using the self-consistent charge density-functional-based tight-binding (SCC-DFTB) method.[45] Preoptimization of TiO_2 NPs using the SCTB method was suggested in Ref. 8, while SCC-DFTB has been used both as preoptimizer and to directly obtain properties of titania systems.[7,21,23,46] We note that although calculations using TB methods are significantly faster than DFT-based calculations, they are still two to three orders of magnitude more computationally expensive than those employing IPs, as can be seen in a comparison between SCC-DFTB, MA, NanoTiO, and TVQIP in Table II.

TABLE II. Optimization time of the $(TiO_2)_{35}$ NP with MA, NanoTiO, and TVQIPs in comparison with the SCC-DFTB method on a single core personal computer. The computer used was a HP Z420 workstation with Intel Xeon 8-core CPU.

Method	Total CPU time (s)
NanoTiO	0.58
MA	1.09
TVQIP	28.29
SCC-DFTB	329.17

In terms of DFT SP calculation timings, MA and NanoTiO exhibit a quite similar performance. Except for the smallest $(TiO_2)_{10}$ NP, the DFT SP calculations of the MA and NanoTiO preoptimized NPs require ≤30% of the time needed for the DFT SP calculations of the corresponding direct bulk cut NPs (i.e., at least a 3.3× speed up). On the other hand, the DFT SP calculation timings for the TVQIP preoptimized NPs shows a very erratic behavior. For the $(TiO_2)_{35}$ and $(TiO_2)_{84}$ NPs, TVQIP preoptimization does not lead to any improvement over the DFT SP timings for the corresponding as-cut NPs, while for $(TiO_2)_{10}$ and $(TiO_2)_{165}$, it gives rise to a time

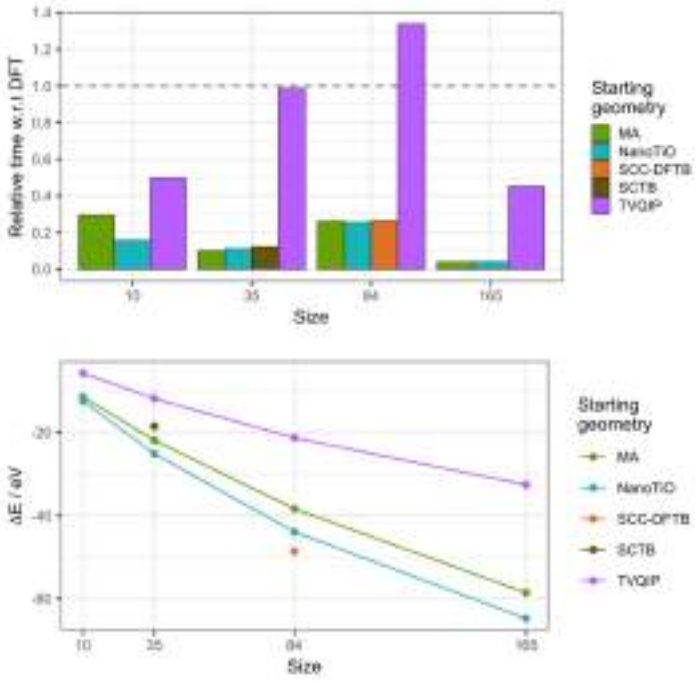

FIG. 6. Top: Fraction of time for a DFT SP calculation for a range of preoptimized NP structures relative to that for the corresponding direct bulk cut NP structure for the set of $(TiO_2)_n$ NPs with n = 10, 35, 84, and 165. Bottom: Total DFT energy difference between preoptimized NP structures and the correspondingly sized bulk cut structure.

The Journal of Chemical Physics ARTICLE scitation.org/journal/jcp

reduction of ~50%. In terms of DFT SP total energies, the picture is quite similar, and both MA and NanoTiO preoptimizations provide a significant energetic stabilization of all NPs relative to the corresponding direct bulk cut. The extent of the energetic stabilization increases with NP size. The TVQIP also energetically stabilizes all NPs, but to a lesser extent. For instance, for the $(TiO_2)_{162}$ NP, the structures from IP preoptimization using MA and NanoTiO have a DFT energy which is 60 eV lower than that of the direct bulk cut, while TVQIP preoptimization provides an energy stabilization of 32 eV. The relatively large energy stabilization in this case for MA and NanoTiO preoptimization leads to a DFT SP energy evaluation calculation taking <10% of the time required for the Wulff constructed bulk cut $(TiO_2)_{162}$ NP structure (i.e., more than 10× speed-up). In Fig. 6, we also include data for the $(TiO_2)_{39}$ NP preoptimization using the SCTB method and for the NP preoptimization $(TiO_2)_{84}$ using the SCC-DFTB method. The SCTB preoptimization yields a NP structure with a DFT SP energy slightly higher than that obtained through preoptimization using MA and NanoTiO IPs, with a very similar SP time. On the other hand, SCC-DFTB yields a slightly lower total energy than IPs, but, in terms of time, the corresponding DFT SP calculation requires a similar amount of time as the NanoTiO and MA IPs. In summary, for efficient preoptimization, we find that these relatively computationally expensive (in comparison with IPs) TB methods have a similar performance to IPs.

Finally, we explore the energetic stabilization obtained by thermal annealing considering two sets of NPs derived from spherical anatase $(TiO_2)_n$ cuts with n = 162 and 237. Both sets of NPs were first generated with the method described above and optimized using DFT. Figure 7 shows the original bulk cut spherical NP and one of the NPs after the MD annealing. Although the structures visually look very similar, the RMSD values show that the annealing has induced some structural reconstruction. The RMSD value between the lowest energy annealed NP structure and the original spherical bulk cuts, both after DFT optimization, is 1.12 Å for the $(TiO_2)_{162}$ NP and 0.89 Å for the $(TiO_2)_{237}$ NP. Considering all five extracted annealed NPs from each MD run for each NP size, the five $(TiO_2)_{162}$ NPs have an average RMSD of 0.54 Å, while the average RMSD of the five $(TiO_2)_{237}$ NPs is 0.34 Å. The average total energy decrease in the annealed NPs with respect to the direct spherical cuts, as evaluated using DFT, is found to be fairly large for both systems: −13.10 eV for $(TiO_2)_{162}$ NPs and −8.98 eV for $(TiO_2)_{237}$ NPs. We notice that the DFT optimized energy for the five different annealed NPs structures in each set is fairly similar, hinting that the annealing procedure brought the five NPs in each case to close-lying energy minima on each respective PES. From this analysis of structure and energetics, we conclude that the annealing was carried out at a temperature that allowed for surface reconstruction while keeping the internal structure relatively intact.[47]

In Table III, we compare the relative energies of the NanoTiO-annealed NPs after optimization using NanoTiO, MA, SCC-DFTB, and DFT methods where we also show the energy differences with respect to the DFT optimizations and the mean error (ME) between

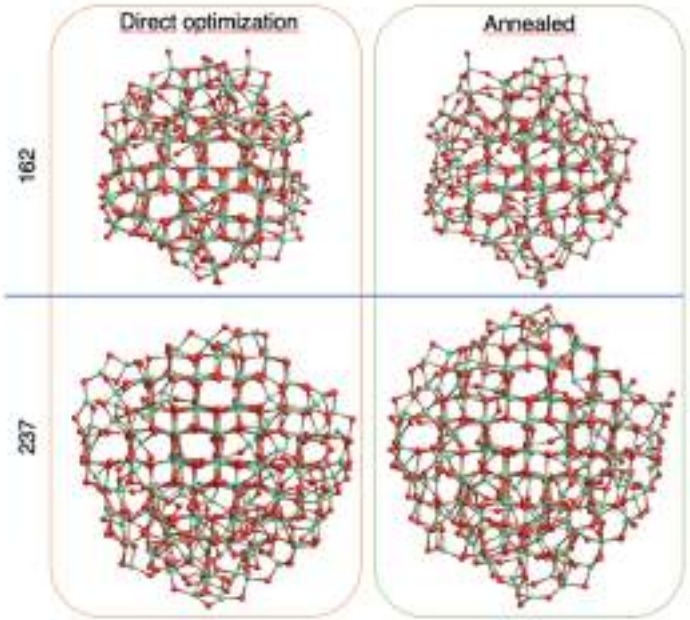

FIG. 7. Structure of DFT optimized spherical particles both directly from bulk cuts (left) and after annealing using NanoTiO-based MD simulations (right), for $(TiO_2)_{162}$ (top) and $(TiO_2)_{237}$ (bottom) NPs. The RMSD of the shown annealed $(TiO_2)_{162}$ NPs is 1.12 Å relative to the directly optimized structure (0.539 Å on average for all five considered annealed NPs). For the shown annealed $(TiO_2)_{237}$ NPs, the RMSD is 0.891 Å relative to the directly optimized structure (0.338 Å on average for all five considered annealed NPs). Atom color code: red—oxygen and green—titanium.

The Journal of Chemical Physics ARTICLE scitation.org/journal/jcp

TABLE III. Each column shows the energy differences between the spherical bulk-cut NP and five annealed NP $(TiO_2)_{162}$ structures (A-1 to A-5, see also upper part of Fig. 7) as optimized using DFT, MA, NanoTiO, and SCC-DFTB. In brackets, we provide the difference in the relative energies with respect to those from the DFT optimizations. Also reported is the mean error (ME) of the energy differences with respect to DFT.

Structure	DFT	MA	NanoTiO	SCC-DFTB
Bulk cut	0	0	0	0
A-1	−13.72	−0.93 [12.80]	−15.89 [−2.16]	−9.84 [3.88]
A-2	−12.19	4.19 [16.38]	−16.25 [−4.06]	−11.71 [0.38]
A-3	−13.70	3.03 [16.73]	−15.95 [−2.25]	−11.33 [2.37]
A-4	−12.69	−1.65 [11.04]	−16.05 [−3.36]	−10.77 [1.92]
A-5	−13.10	3.69 [16.79]	−17.46 [−4.36]	−11.10 [2.13]
ME for A-1–A-5		14.75	−3.24	2.13

the NanoTiO, MA, and SCC-DFTB methods and DFT. While the DFT optimizations confirm that the annealed NPs are more stable than the bulk-cut particle by 13.08 eV on average, optimization using the MA IP shows that some of the NPs are found to increase in energy while some decrease relative to the bulk-cut NP. In terms of energetics, the MA IP thus is not reliable for generating accurate structurally reconstructed annealed NPs. On the other hand, NanoTiO consistently predicts that the formation of reconstructed core-shell NPs is energetically stabilizing with an average overestimation of the stabilization by 3.24 eV with respect to the DFT values. SCC-DFTB optimizations also generally follow the DFT trend in predicting annealed NPs to be lower in energy than the spherical crystalline cut with an underestimation of the energy stabilization that DFT provides by 2.13 eV on average. These results confirm that both NanoTiO and SCC-DFTB provide a similar and reasonable description of the energetics of structurally reconstructed NPs.

We note that these results contrast somewhat with the results reported for as-cut and hydroxylated spherical particles reported by Selli *et al.*[13] where annealing was performed using SCC-DFTB on NPs with 101, 223, 399, and 1265 TiO_2 units. Here, moderate temperature annealing produced only a marginal increase in NP energetic stability less than 0.7 eV in all studied NPs. Annealing at higher temperatures, however, promoted the appearance of amorphous regions near the surface of the NPs which caused a decrease in their energetic stability. Two possible explanations for the observed different behavior are (i) either the SCC-DFTB PES does not accurately describe the relative stabilities of different NPs with variable crystallinity or (ii) hydroxylation energetically stabilizes a higher degree of NP crystallinity even at the surface, which is reasonable as it allows for a higher coordination of the surface atoms. We note that NanoTiO has recently been extended to also model –OH groups[17] and will be tested in future studies with respect to its performance in preparing hydroxylated TiO_2 NPs.

In order to use either NanoTiO or SCC-DFTB to prepare thermally annealed NPs, MD calculations are necessary. As a simple benchmark to compare the computational cost of running MD calculations, we ran 10 steps of a microcanonical MD simulation for the $(TiO_2)_{162}$ NP both with using NanoTiO and SCC-DFTB. In both cases, the simulation was run at a time step of 0.1 fs with random velocities according to a temperature of 100 K. In addition, the SCC-DFTB calculation used preoptimized charges for the initial step. We found that the IP-based NanoTiO MD calculation took 0.29 s, while the SCC-DFTB method required 1551.81 s. The approximately four orders of magnitude speed-up of the IP-based MD simulation relative to the SCC-DFTB calculation is even more pronounced than the three orders of magnitude performance improvement noted for the structural optimization of the $(TiO_2)_{35}$ NP (see Table III). This extra improvement is likely largely due to the larger size of the NP considered in the MD simulations and the fact that IP-based methods tend to scale with size as $n^{1.5}$, whereas DFTB methods tend to scale as n^3.

In light of our results, we can conclude that NanoTiO is the best performing IP of those considered for preparing TiO_2 NPs for efficient DFT calculations. While MA and NanoTiO provide similar preoptimization results both in terms of their structural accuracy and in the resultant time saving in subsequent DFT optimizations, the energetics associated with annealing of the surface structure of NPs are better represented with NanoTiO. The performance of NanoTiO is also found to be similar to TB methods in terms of preparing accurate optimized and annealed NPs for efficient subsequent DFT calculations. However, the significantly higher computational efficiency of NanoTiO over TB methods (3–4 orders of magnitude speed-up) means that NanoTiO could provide significant advantages for MD-based annealing and/or preoptimizing large sets of NPs (e.g., for sampling, machine learning datasets, or global optimization) for subsequent DFT evaluation, especially where large NPs (i.e., containing hundreds to thousands of atoms) are involved.

IV. CONCLUSIONS

The DFT-based modeling of realistic TiO_2 NP-based systems increasingly involves evaluation of (i) large sets of varied NPs, (ii) NPs with 100s–1000s atoms, and (iii) thermally annealed NPs. Much of the large computational effort in such studies can be significantly reduced by preparing accurate NP structural models using computationally efficient methods for subsequent more efficient DFT evaluation. In the present work, we assessed the ability of several IPs to prepare reliable structures for TiO_2 NPs via optimization and MD simulations. Of the tested IPs, overall, NanoTiO was found to perform the best. Preoptimizing bulk-cut NPs with the NanoTiO IP can improve

The Journal of Chemical Physics ARTICLE scitation.org/journal/jcp

the computational efficiency of subsequent DFT calculations, with 3×–10× speed-ups for DFT SP energy evaluations and speed-ups of 2× for DFT structure optimizations. NanoTiO-based MD simulations used to anneal NPs are also found to lead to energy-lowering structural reconstructions in line with those predicted by DFT calculations. The overall accuracy of NanoTiO for preparing suitable NPs for subsequent DFT evaluation is found to be similar to that of TB-based methods. However, NanoTiO is 3–4 orders of magnitude more computationally efficient than TB methods and is thus particularly well suited for studies involving thermal annealing of large TiO_2 NPs and/or preparation of large sets of diverse TiO_2 NPs.

SUPPLEMENTARY MATERIAL

See supplementary material for parameters for all IPs considered and Cartesian coordinates of all reported NP structures.

ACKNOWLEDGMENTS

The authors acknowledge financial support from the Spanish MINECO/FEDER Grant Nos. CTQ2015-64618-R and MICIUN RTI2018-095460-B-I00 and Spanish Structures of Excellence María de Maeztu program through Grant No. MDM-2017-0767 and, in part, by Generalitat de Catalunya (Grant Nos. 2017SGR13 and XRQTC). A.M.-G. acknowledges the Spanish MINECO for the Juan de la Cierva postdoctoral grant (No. IJCI-2017-31979), and F.I. acknowledges additional support from the 2015 ICREA Academia Award for Excellence in University Research. Computational time at the *Marenostrum IV* supercomputer was provided by the Barcelona Supercomputing Centre (BSC) through a grant from the Partnership for Advanced Computing in Europe (PRACE) under the EXCIPHOCAT project (No. 2016163940).

REFERENCES

[1]J.-W. Lee, T.-Y. Lee, P. J. Yoo, M. Grätzel, S. Mhaisalkar, and N.-G. Park, J. Mater. Chem. A **2**, 9251 (2014).
[2]S. Y. Huang, G. Schlichthörl, A. J. Nozik, M. Grätzel, and A. J. Frank, J. Phys. Chem. B **101**, 2576 (1997).
[3]Y.-Y. Song, P. Schmuki-Stein, S. Bauer, and P. Schmuki, J. Am. Chem. Soc. **131**, 4230 (2009).
[4]Z. Fei Yin, L. Wu, H. Gui Yang, and Y. Hua Su, Phys. Chem. Chem. Phys. **15**, 4844 (2013).
[5]A. Fujishima and K. Honda, Nature **238**, 37 (1972).
[6]B. A. Marinho, R. Djellabi, R. O. Cristóvão, J. M. Loureiro, R. A. R. Boaventura, M. M. Dias, J. C. B. Lopes, and V. J. P. Vilar, Chem. Eng. J. **318**, 76 (2017).
[7]G. Fazio, L. Ferrighi, and C. Di Valentin, J. Phys. Chem. C **119**, 20735 (2015).
[8]O. Lamiel-Garcia, K. C. Ko, J. Y. Lee, S. T. Bromley, and F. Illas, J. Chem. Theory Comput. **13**, 1785 (2017).
[9]O. Lamiel-Garcia, A. Cuko, M. Calatayud, F. Illas, and S. T. Bromley, Nanoscale **9**, 1049 (2017).
[10]O. Cho, K. C. Ko, O. Lamiel-Garcia, S. T. Bromley, J. Y. Lee, and F. Illas, J. Chem. Theory Comput. **12**, 3751 (2016).
[11]D. Selli, G. Fazio, and C. Di Valentin, J. Chem. Phys. **147**, 164701 (2017).
[12]M. Cargnello, T. R. Gordon, and C. B. Murray, Chem. Rev. **114**, 9319 (2014).
[13]G. Wulff, Z. Kristallogr. **34**, 449 (1901).
[14]Á. Morales-García, A. Macià Escatllar, F. Illas, and S. T. Bromley, Nanoscale **11**, 9032 (2019).
[15]H. Li, Y. Zeng, T. Huang, L. Piao, Z. Yan, and M. Liu, Chem. —Eur. J. **18**, 7525 (2012).
[16]H. G. Yang, G. Liu, S. Z. Qiao, C. H. Sun, Y. G. Jin, S. C. Smith, J. Zou, H. M. Cheng, and G. Qing (Max) Lu, J. Am. Chem. Soc. **131**, 4078 (2009).
[17]V. N. Koparde and P. T. Cummings, ACS Nano **2**, 1620 (2008).
[18]D. R. Collins, W. Smith, N. M. Harrison, and T. R. Forester, J. Mater. Chem. **7**, 1543 (1997).
[19]Y. Zhou and K. A. Fichthorn, J. Phys. Chem. C **116**, 8314 (2012).
[20]P. M. Oliver, G. W. Watson, E. T. Kelsey, and S. C. Parker, J. Mater. Chem. **7**, 563 (1997).
[21]B. Durkina, M. L. Sushko, J. Liu, and D. M. Duffy, Phys. Chem. Chem. Phys. **16**, 9441 (2014).
[22]P. K. Naicker, P. T. Cummings, H. Zhang, and J. F. Banfield, J. Phys. Chem. B **109**, 15243 (2005).
[23]H. Zhang, B. Chen, J. F. Banfield, and G. A. Waychunas, Phys. Rev. B **78**, 214106 (2008).
[24]D. R. Collins and W. Smith, *Evaluation of TiO2 Force Fields* (Council for the Central Laboratory of the Research Councils, UK, 1996).
[25]A. V. Bandura and J. D. Kubicki, J. Phys. Chem. B **107**, 11072 (2003).
[26]A. Pedone, G. Malavasi, M. C. Menziani, A. N. Cormack, and U. Segre, J. Phys. Chem. B **110**, 11780 (2006).
[27]V. Swamy and J. D. Gale, Phys. Rev. B **62**, 5406 (2000).
[28]M. Matsui and M. Akaogi, Mol. Simul. **6**, 239 (1991).
[29]A. C. T. Van Duin, S. Dasgupta, F. Lorant, and W. A. Goddard, J. Phys. Chem. A **105**, 9396 (2001).
[30]M. Raju, S.-Y. Kim, A. C. T. van Duin, and K. A. Fichthorn, J. Phys. Chem. C **117**, 10558 (2013).
[31]S. Hergh, A. Bogaerts, A. C. T. van Duin, and E. C. Neyts, Comput. Mater. Sci. **95**, 579 (2014).
[32]L. Huang, K. E. Gubbins, L. Li, and X. Lu, Langmuir **30**, 14832 (2014).
[33]S. Selcuk, X. Zhao, and A. Selloni, Nat. Mater. **17**, 923 (2018).
[34]S. Ganguly Neogi and P. Chaudhury, J. Comput. Chem. **35**, 51 (2014).
[35]S. Hamad, C. R. A. Catlow, S. M. Woodley, S. Lago, and J. A. Mejías, J. Phys. Chem. B **109**, 15741 (2005).
[36]L. Tang, L. Sai, J. Zhao, and R. Qiu, J. Comput. Chem. **33**, 163 (2012).
[37]M. Chen and D. A. Dixon, J. Chem. Theory Comput. **9**, 3189 (2013).
[38]J. D. Gale and A. L. Rohl, Mol. Simul. **29**, 291 (2003).
[39]E. Dvinskikh, T. Çağın, and W. A. Goddard, Phys. Rev. Lett. **82**, 1708 (1999).
[40]J. P. Perdew, K. Burke, and M. Ernzerhof, Phys. Rev. Lett. **77**, 3865 (1996).
[41]V. Blum, R. Gehrke, F. Hanke, P. Havu, V. Havu, X. Ren, K. Reuter, and M. Scheffler, Comput. Phys. Commun. **180**, 2175 (2009).
[42]B. Aradi, B. Hourahine, and T. Frauenheim, J. Phys. Chem. A **111**, 5678 (2007).
[43]R. Luschtinetz, J. Frenzel, T. Milek, and G. Seifert, J. Phys. Chem. C **113**, 5730 (2009).
[44]A. S. Barnard, S. Erdin, Y. Lin, P. Zapol, and J. W. Halley, Phys. Rev. B **73**, 205405 (2006).
[45]M. Elstner, D. Porezag, G. Jungnickel, J. Elsner, M. Haugk, T. Frauenheim, S. Suhai, and G. Seifert, Phys. Rev. B **58**, 7260 (1998).
[46]K. Shirai, G. Fazio, T. Sugimoto, D. Selli, L. Ferraro, K. Watanabe, M. Haruta, B. Ohtani, H. Kurata, C. Di Valentin, and Y. Matsumoto, J. Am. Chem. Soc. **140**, 1415 (2018).
[47]A. Cuko, A. Macià Escatllar, M. Calatayud, and S. T. Bromley, Nanoscale **10**, 21518 (2018).

Conclusions

1. From the analysis of the 84 units Wulff constructed TiO_2 NP, the equilibrium geometry obtained using the PMMCS IP deviates significantly from the corresponding DFT optimised structure. Such a result is surprising as the Wulff constructed NPs are the most bulk-like possible and are those expected to be most easily reproduced by IPs. However, the PMMCS was not fitted to reproduce the Ant crystal structure, but rather silicate glasses with Ti inclusions and the Rt TiO_2 crystal structure. We conclude that PMMCS is not appropriate to pre-optimize Ant TiO_2 NPs and highlight the necessity of adequate fitting or careful selection of an IP for correct usage.
2. The total DFT optimization time can be both increased and decreased by using IPs as pre-optimizers, with respect to a DFT-only optimization. By checking the time taken per each optimization step, we show that the main difference between large optimization times and short optimization times depends on the time to converge the wavefunction in the initial steps of the optimization. This, in turn, is related to structural differences between the initial NP and the final DFT-optimized equilibrium geometry at DFT level, thus implying that a suitable IP for efficient pre-optimization shares the position of the optimized energy minimum on the PES with that from DFT.
3. The MA and NanoTiO pre-optimized 84 units NPs allowed for a convergence of the structure at the DFT level three times faster than from direct DFT optimization. The total optimization time when pre-optimizing using TVQIP was longer than for the direct DFT optimization.
4. In order to evaluate if NP size may change the time saving capabilities of preoptimizing with IPs, we performed a test comparing different NP sizes. As single point (SP) calculations are a good proxy for understanding if a stucture will be optimized faster, we evaluated the SP time of several NPs with 10, 35, 84 and 165 TiO_2 units with each IP with respect to DFT results. Both MA and NanoTiO achieve faster SP convergence and energies closer to the DFT optimized structure independently of NP size.
5. We also compared the performance of using DFTB and SCC-DFTB as pre-optimizers with respect to IPs. We found that such methodologies, albeit providing more information than IPs, have similar performances in terms of their structural and pre-optimization capabilities. However, their optimization time is two orders of magnitude longer than for IPs. In conclusion, we believe that if the objective is purely to pre-optimize a NP for efficient subsequent DFT optimization, it is better to use IPs. However, if exploratory data on the approximate electronic structure of a NP is rapidly required the usage of DFTB methods is a reasonable option.
6. MD annealing using the NanoTiO IP resulted in core-shell NP structures which were lower in energy than the direct spherical cuts from the Ant crystal. Comparison of

the relative energies between the original as-cut spheres and the annealed NPs with DFT, IPs and SCC-DFTB shows that their relative energetic stabilities are better reproduced with NanoTiO than with the MA IP. DFT results show that annealed nanospheres are between 12 to 13 eV more stable than the original spherical cut NPs. NanoTiO was found to ascribe similar annealing induced stabilization energies of ~15 eV for five different annealed NP structures. Conversely, the MA IP predicted the as-cut spherical NP to be more stable than the annealed NPs in three out of the five considered cases. In the other two cases, the MA-predicted energy difference was smaller than 2 eV. Finally, SCC-DFTB was found to have a similar performance to NanoTiO, providing stabilization energies between 10 to 12 eV for all five cases.

Chapter 6: Understanding the interplay between size, morphology and energy gap in photoactive TiO_2 nanoparticles

Introduction

As previously mentioned, the performance of TiO_2 NPs with respect to specific applications relies on their optical, electronic, structural, morphological and surface properties. Experimental synthesis techniques have achieved a great control in the structure and morphology of TiO_2 NPs. A novel achievement in the tailoring of TiO_2 NPs has been the synthesis of the so-called black TiO_2 NPs. With the objective of extending the valence or conduction band and increase the amount of light capable of triggering electronic excitations, Chen et al[47] used a high-pressure hydrogen atmosphere to amorphize the surface of crystalline NPs. The resulting black TiO_2 NPs have much lower band-gaps than crystalline NPs. The work of Liu et al[73] evaluated the reason why amorphization induced by H adsorption increased the electron-hole recombination time, in contrast to established knowledge which assumed that amorphization lowers the catalytic activity. However, the internal and surface structure of black TiO_2 is still a subject of debate, with claims of stoichiometric surface and vacancies in the internal structure[49] or, conversely, a surface layer of Ti_2O_3 composition with a stoichiometric TiO_2 interior[48]. As the structures obtained in the MD simulations of the preceding chapter can be defined as containing an internal crystalline core and an amorphous shell, their electronic structure can give insights into the structure of black TiO_2.

The annealing dynamics of amorphous TiO_2 NPs has also been related to crystalline core-amorphous shell NPs. To obtain single crystal NPs from sol-gel synthesis, amorphous TiO_2 NPs are heated at temperatures between 400 to 500 ºC[74]. While the dominance of Ant has been justified by the thermodynamic preference of Ant with respect to Rt at the nanoscale, it is not clear why the Brookite phase does not form, even when Brookite is the most stable phase for a size range between 11 to 33 nm[75]. Comparison of the Pair Distribution Function (PDF) of sol-gel synthesized amorphous particles with computational models revealed that core-shell particles are the most appropriate models to reproduce the experimental PDF of spherical amorphous particles of ~2nm[46].

The work of Fazio et al.[59] compared the effect of shape on the structure of TiO_2 NPs. In their work, they compare the type and fraction of sites of Ant Wulff constructed NPs versus spherical ones. However, in order to generate spherical crystalline NPs, their work cuts spheres from the bulk structure and saturated undercoordinated atoms by adding OH and H. Thus, these NP models have differences in chemical composition and, while they could represent the NPs in low water environments, the electronic properties may be influenced by the presence of hydroxyl groups on their surfaces. Moreover, the surface of these models is completely crystalline, in contrast to the core-shell structure reported in the work of Zhang[46]. Another hindrance is that the models provided by Fazio et al. cannot be used to explain important effects such as stabilization due to hydroxylation, nor compute the adsorption energy of water, as a definite NP size can only be saturated in a unique way.

Hence, a complete picture of the differences between spherical stoichiometric and faceted NPs is still required.

Following the work of Chapter 5 and building upon previous results from our group[63], in this paper we evaluate the evolution of internal energy with respect to size for differently shaped TiO_2 NPs. We expand previous work by adding larger sizes, allowing a better determination of the cross-over between amorphous nanoclusters obtained from global optimization and Wulff constructed NPs. In this work we also include spherical NPs as cut directly from the crystal structure and modified by simulated annealing, with the later structures characterized by a core-shell structure. In addition, we perform high temperature simulated MD annealing on three moderately sized NPs to compare the energetic stability of amorphous NPs against the crystalline core-amorphous shell NPs. With the energetic results we propose a tentative structure vs stability diagram. We also rationalize the energetic stability in terms of coordination number for Ti and O elements. Finally, we evaluate the band-gap of the different families of structures, finding significant differences in band gap values, and we rationalize the structural features causing the differences.

In this work, led by Dr. Angel Morales performed all the DFT calculations. The author of this thesis generated both the as-cut spherical models and the core-shell models and performed the MD simulations to obtain amorphous structures from the spherical particles. All the codes to extract structural data have also been written by the present author. Finally, the author has contributed in the discussion of the phase diagram and energy vs size of the differently shaped NPs.

Results

Nanoscale

PAPER

View Article Online
View Journal | View Issue

Cite this: Nanoscale, 2019, 11, 9032

Understanding the interplay between size, morphology and energy gap in photoactive TiO_2 nanoparticles†

Ángel Morales-García, * Antoni Macià Escatllar, * Francesc Illas * and Stefan T. Bromley *a,b

Anatase TiO_2 nanoparticles (NPs) have the potential to photocatalyse water splitting using UV light, to thus provide hydrogen fuel in a clean and sustainable manner. Such NPs have optical gaps covering a small range of relatively high energy solar photons, giving rise to low photo-efficiencies. Although anatase NPs with 10–20 nm diameters thermodynamically prefer crystalline faceted morphologies, application of physico-chemical procedures can produce more rounded NPs with amorphous shells. Such engineered metastable core–shell NPs (so-called black TiO_2 NPs) have reduced band gaps due to shell-induced band edge broadening, resulting in higher photoactivities. For <5 nm diameters, TiO_2 NPs typically exhibit spherical-like NP morphologies, which also display enhanced photoactivity. For smaller NPs it is difficult to experimentally determine their thermodynamic stability and internal atomic structure, to help rationalise their higher photoactivities. Employing accurate electronic structure calculations, we establish the relative stability of spherical and faceted stoichiometric TiO_2 NPs with 1–3.4 nm diameters. Mirroring experimental preparation, simulated thermal annealing is found to significantly stabilise relaxed spherical cut anatase NPs. We find that the smallest spherical NPs become amorphized by annealing, but, for diameters >2 nm, annealing yields NPs with anatase-cores and amorphous-shells. Like larger black TiO_2 core–shell NPs, we confirm that our core–shell NPs are metastable relative to faceted anatase NPs and have significantly smaller optical gaps than faceted NPs. Our calculated gaps are in excellent agreement with experimental data, strongly supporting the validity of our NP models. Energy gap narrowing in these core–shell NPs is found to be due to broadening of valence band states induced by the amorphous shell, analogous to the mechanism proposed for black TiO_2 NPs. Our stoichiometric NPs also show that this band narrowing effect does not require the disordered shells to be non-stoichiometric or for incorporation of other atom types. Instead, we find that this effect mainly arises from 4-coordinated Ti atoms in the amorphous shell. Our careful and systematic computational investigation, using NP models of unprecedented realism, thus provides direct confirmation that the enhanced photoactivity in small spherical TiO_2 NP observed in experiment is due to the formation of metastable core–shell NPs with 4-coordinated Ti centres.

Received 25th January 2019,
Accepted 2nd April 2019

DOI: 10.1039/c9nr00812h

rsc.li/nanoscale

Introduction

Titania (TiO_2) is a multifunctional semiconducting material that is used in many practical applications due to its excellent stability, remarkable physical and chemical properties and low cost.[1,2] The discovery that TiO_2 can split water under ultraviolet (UV) light,[3] in particular, has led to ongoing intensive research in areas such as solar fuels, photovoltaics, and environmental remediation.[4–9] Bulk titania polymorphs exhibit band gaps of ≥3 eV,[10] enabling them to capture only ~10% of the photons from the sunlight reaching the Earth surface, thus limiting their practical use. Incorporation of noble metals, formation of heterojunctions with other semiconductors, use of dopant agents, and the generation of intrin-

*Departament de Ciència de Materials i Química Física & Institut de Química Teòrica i Computacional (IQTCUB), Universitat de Barcelona, c/Martí i Franquès 1-11, 08028 Barcelona, Spain. E-mail: s.bromley@ub.edu
*Institució Catalana de Recerca i Estudis Avançats (ICREA), Passeig Lluís Companys 23, 08010 Barcelona, Spain

†Electronic supplementary information (ESI) available: Parameters for the fits reported in Fig. 1 are compiled in Table S1. In addition, G_{sol} values calculated using the PBE functional are included in Fig. S1 together with those estimated through using the HSEh hybrid functional. Finally, the atomic coordinates of all faceted and annealed spherical TiO_2 NPs are compiled in the xyz format. See DOI: 10.1039/c9nr00812h

sic defects such as oxygen vacancies have been studied as potential means to improve the photoactivity and solar use of TiO_2.[11–13] The photocatalytic activity of TiO_2 is also a fundamental nanoscale phenomenon, which emerges in suitably sized nanoparticles (NPs). Under ambient conditions, bulk TiO_2 thermodynamically favours the rutile crystal structure, however, the photoactive anatase polymorph is mainly observed at the nanoscale due to its lower surface energy.[14] The performance of anatase TiO_2 in many applications largely depends on its optical, electronic, structural, morphological, and surface properties, which can all be tuned through the use of NPs with different sizes, shapes, crystallinities, and surface facets.[4,17–19] Of particular note in this respect are so-called black TiO_2 NPs which are morphologically and structurally manipulated to absorb light in the visible energy range, thus covering a greater range of solar-radiation with concomitant efficiency improvements in photocatalytic applications.[20] Clearly, the design of tailored anatase TiO_2-based nanotechnologies relies on both the ability to synthesize appropriate NPs with well-controlled sizes and morphologies, and a detailed understanding of how the intrinsic physical and chemical properties depend on these two factors. To enhance the efficiency of NP-based photocatalysts, it is usually desirable to decrease the NP size as much as possible to increase the proportion of available surface area while maintaining the intrinsic activity of the material. Such considerations, however, should also take into account the fact that decreasing the size of an anatase NP will also increase quantum confinement which will act to increase the optical energy gap, and thus reduce photoefficiency.[21] Both experiment[22] and theory[23,24] have pointed to a lower size limit of 2–3 nm for the anatase phase, beyond which the NPs are too small to maintain any crystallinity. Our detailed theoretical study focusses on relative stabilities and properties of realistic NPs with different morphologies, structures, and crystallinities in this important nanosized regime in order to rationalise experimental results and to provide insights into how photoactivity can be enhanced in these systems.

Several synthetic strategies have demonstrated that the morphology of TiO_2 NPs depends significantly on the Ti precursor and the surfactants used.[25–28] Nonhydrolytic and surfactant-assisted solvothermal methods appear to be most effective for both controlling NP size and shape and producing NPs with high crystallinity.[29] Anatase TiO_2 NPs with tailored morphologies in the 10–100 nm size range have been successfully synthesised by using approaches based on a seeded growth technique.[30] Both bipyramidal and truncated octahedral anatase TiO_2 NPs have been reported.[30] The bipyramidal NPs exhibit (101) surfaces only whereas the truncated octahedra exhibit (001) and (101) surfaces. Fazio *et al.* have argued that partial dissolution of these faceted TiO_2 NPs could lead to the formation of hydroxylated NPs with diameters ($\varnothing$) between 3–5 nm that exhibit more curved surfaces.[31] Further theoretical work has examined the structural and electronic properties of partially hydroxylated anatase TiO_2 NPs with faceted and spherical morphologies with diameters of ~3 nm.[19,32,33] These studies suggest that the interplay between hydroxylation and morphology is significant for enhancing the hole trapping ability in spherical NPs, while being less important for faceted NPs.[32,34] All these theoretical works employ cuts from the anatase crystal structure to derive their spherical and faceted NP models. Removal of low coordinated Ti atoms and subsequent hydroxylation of remaining relatively low coordinated centres on the surfaces of these cuts are then used to produce stoichiometric hydroxylated NP models, which are then structurally relaxed. This well-defined protocol has the drawback that it produces NPs with uncontrolled varying degrees of hydroxylation dependent on the size and morphology of the original crystal cut. Thus, use of such models makes it difficult to assess the intrinsic relative stabilities of different NPs families with respect to size, morphology and internal structure. Calculations applying thermal annealing to hydroxylated spherical anatase NPs have also resulted in different predictions as to what extent this treatment has on the NP electronic structure.[19,35] Where some annealing-induced electronic change was calculated,[35] the intrinsic reason for the effect was not clearly ascribed.

Herein, we focus on a varied set of stoichiometric anhydrous NPs with a range of sizes, for which a more controlled comparative analysis of stability, structure and properties can always be made. Bare anhydrous spherical anatase TiO_2 NPs have also been produced in numerous experiments.[16,17] This indicates that, although hydration may sometimes play a role in promoting more spherical NPs, it is not necessary to maintain the stability of such NPs. As such, this raises fundamental questions about the intrinsic stability and electronic/optical properties of anhydrous TiO_2 NPs with respect to their morphology and size.

For anhydrous stoichiometric TiO_2 NPs with ~1 nm diameters, global optimisation searches have established that non-crystalline NPs with quasi-spherical morphologies are the most energetically stable.[23] For larger sizes, the atomic and electronic structure of anhydrous faceted anatase TiO_2 NPs with maximum diameters up to 6 nm have also been recently theoretically investigated.[36] Towards the upper end of this size regime, truncated octahedral and bipyramidal NP structures are found to be almost energetically degenerate with one another, with both exhibiting a low degree of structural distortion relative to the bulk anatase crystal.[24,40] By interpolating between these two size regimes, it has been estimated that faceted crystalline NPs become more stable than non-crystalline quasi-spherical NPs for a diameter range of 2–3 nm.[23] This estimate is in line with studies of experimentally prepared anhydrous spherical NPs, where crystallinity is found to be severely diminished in ~2 nm NPs due to the structurally disruptive influence of the surface atoms.[22] This result is also consistent with atomistic simulations of stress in TiO_2 NPs.[24] As kinetic factors can strongly influence the morphology of small NPs in experiment, the thermodynamically preferred morphologies of TiO_2 NPs in the $\lesssim$5 nm diameter range has not yet been established. Computational modelling offers an alternative, controlled approach to assess whether observed NP morphologies are determined mainly by intrinsic stability (*e.g.*

crystalline or non-crystalline structure), preparatory conditions (*e.g.* kinetic trapping), or by the NP's environment (*e.g.* hydration). Herein, we use state-of-the-art electronic structure methods and nanoscale models of unprecedented realism to provide a predictive guide to the stabilities and properties of 0.5–3.5 nm diameter stoichiometric TiO_2 NPs and how they depend on morphology, size and crystallinity. Specifically, we pay particular attention to the accurate modelling of anhydrous NPs with spherical morphologies and, as in experiment,[41,42] we apply thermal annealing to all our NPs. We compare the stabilities of such annealed NPs both with NPs obtained from simple relaxed spherical cuts and with faceted NPs, enabling us to provide a tentative stability *versus* size diagram for the TiO_2 NP size range considered. Moreover, we estimate the lowest optical transition by inspecting the energy gaps of all our NPs and show that our annealed stoichiometric spherical NPs have reduced gaps which match particularly well with those from experiments on small spherical NPs with enhanced photoactivity. Analysis of the underlying reason for the gap reduction in spherical NPs points confirms the existence of gap edge broadening due to their core–shell structure, fully in line with the analogous effect in larger black TiO_2 NPs.[20,43] Specifically, we are able to ascribe the gap narrowing to atoms with reduced coordination environments in the surface amorphized shells of our stoichiometric NPs.

Methodology

The stability of faceted and spherical stoichiometric $(TiO_2)_n$ NPs with structure derived from the anatase bulk phase (Fig. 1) was studied for sizes n = 29–595. The faceted NPs were obtained *via* the Wulff construction,[44] which relates the shape of a NP to the areas and relative stabilities of the exposed surfaces. The bipyramidal NPs exhibit the most stable (101) surface and display octahedral symmetry (Fig. 1a), whereas the truncated octahedral NPs display both (101) and (001) surfaces (Fig. 1b).[28] Spherical TiO_2 NPs (Fig. 1c) were generated by cutting spheres of the desired diameters from the anatase crystal structure following a procedure reported in other works,[45–47] while ensuring that the TiO_2 stoichiometry was always preserved. For all NPs, the initial structure was relaxed using total energy minimization as described below. In addition to relaxation, molecular dynamics (MD) simulations runs were carried out to mimic an annealing process with the aim to induce energy lowering structural reorganization of the

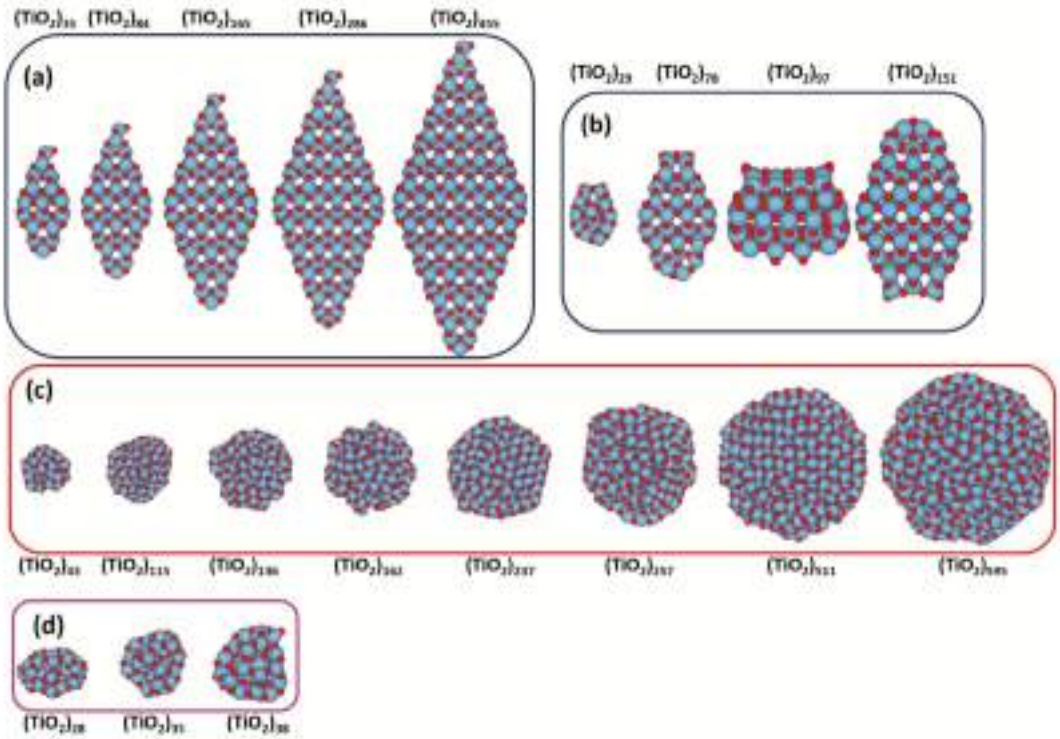

Fig. 1 Structures of $(TiO_2)_n$ NPs in the size range n = 29–595 with: (a) bipyramidal, (b) cuboctahedral, (c) spherical morphologies, and (d) selected globally optimised structures from ref. 23. Further details about the bipyramidal and cuboctahedral TiO_2 nanoparticles can be found in ref. 38. Red and blue spheres correspond to O and Ti atoms, respectively.

NPs. The MD simulations were performed within the canonical ensemble (NVT) and consisted of 5 ps of equilibration time followed by 30 ps of production at 1000 K. These calculations were performed using both an interatomic potential (IP) parameterised for bulk TiO_2 by Matsui and Akaogi (MA)[48] and an IP specifically parameterised for nanoscale TiO_2 (Nano-TiO).[23] Structures and energies were sampled every 0.01 ps and the lowest five energies obtained during each MD run were selected and further relaxed using DFT based calculations as described below.

The structures of the three smallest NPs considered were directly taken from a recent global optimisation study.[23] For the larger NPs, the initial structures were cut from the bulk anatase crystal. All NPs were directly optimised using DFT based calculations carried out without symmetry constraints employing the PBE functional.[50] For the spherical cuts it was found that IP-based pre-optimisation helped to heal dangling oxygen defects on the NP surfaces while retaining the anatase core intact, before DFT-based optimisation. Optical gaps were estimated from the electronic gaps calculated using DFT calculations using the PBEx hybrid functional.[49] For the largest NPs, where such calculations would be computationally very demanding, the gap values from the PBE calculations were corrected using a known correlation between electronic gaps calculated using the PBE and PBEx functionals.[39] The DFT based calculations explicitly include all electrons, where the electron density is described through numerical atom-centered orbital basis sets, as implemented in FHI-aims package.[51] A light grid and tier-1 basis set was used, which has an accuracy comparable to a TZVP Gaussian-type orbital basis set.[38] The convergence threshold for atomic forces during the relaxation of the structure of the NPs was set to 10^{-3} eV $Å^{-1}$.

Results and discussion

We consider four sets of stoichiometric TiO_2 NPs: (i) bipyramidal and cuboctahedral faceted NPs, (ii) spherical NPs directly cut from the anatase crystal structure, (iii) spherical NPs from (ii) which have been thermally annealed, and (iv) quasi-spherical globally optimised NPs, see Fig. 1 (atomic coordinates of all NPs are provided in the ESI†). To assign a common measure of diameter for each of these four sets of $(TiO_2)_n$ NPs, we use the diameter of sphere containing n TiO_2 units, with the volume of a single TiO_2 unit taken as that in bulk anatase. A similar approach was used in recent study comparing morphologically diverse ZnO NPs.[19] As noted above, it has been estimated that the anatase structure can persist in NPs down to a ~2–3 nm size,[32–34] which strongly suggests that this is the nanoscale region where NPs of different morphologies and crystallinities could be energetically competing. Our TiO_2 NP models have sizes throughout the range ~1.0–3.4 nm and thus cover this interesting size regime. In Fig. 2 we show the size-dependent energetic stabilities of faceted (blue), spherical (red), annealed spherical (green), and global optimized[23] (pink) TiO_2 NPs. The later set contains $(TiO_2)_n$ nanoclusters

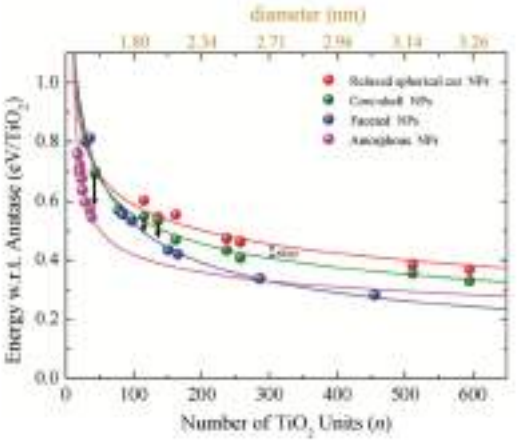

Fig. 2 Evolution of the energy per TiO_2 unit relative to the anatase bulk phase (set to zero) of: faceted (blue), spherical cut (red), core–shell spherical (green), and amorphous (pink) TiO_2 NPs as a function of the number of TiO_2 units (n). An approximate diameter is included on the upper x-axis. The fits for each set are depicted by solid lines (fitting parameters are reported in the ESI†). Faceted NPs correspond to the bipyramidal and cuboctahedral geometries depicted in Fig. 1a and b, respectively. Spherical NPs are shown in Fig. 1c. Further information regarding the globally optimized TiO_2 NPs (Fig. 1d) can be found in ref. 23. The black arrows indicate the energetic stabilisation of the $(TiO_2)_{153}$, $(TiO_2)_{113}$ and $(TiO_2)_{136}$ core–shell NPs when they are further annealed to become NPs with fully amorphised structures (see Table S2 in ESI†).

with n = 28, 35 and 38 (see Fig. 1). The relative stability of all TiO_2 NPs in Fig. 2 is given per TiO_2 unit with respect to that of bulk the anatase phase. From the so-called spherical cluster approximation (SCA),[52] it is assumed that the energetic stability of a $(TiO_2)_n$ NP, E_s, relative to that of bulk anatase, E_{bulk}, can be approximately fitted by a scaling law following

$$E_s = E_{bulk} + a_1 n^{-a}, \quad (1)$$

where a_1 is a fitting parameter related the NP morphology, and a is taken to be 1/3, reflecting the surface area to bulk ratio, and both E_s and E_{bulk} are per TiO_2 unit. Note that eqn (1) is derived based on consideration of the geometric shape of a NP only, whereas realistic NPs are more complex entities composed of interacting aggregates of atoms/ions. As such, other contributions to E_s (*e.g.* surface stresses) can become significant which can be approximately included through the inclusion of higher order terms (*e.g.* $a_2(n^{-1/3})^2$, $a_3(n^{-1/3})^3$, ...).[16,23,49] Further details and fitting parameters employed to construct the plot in Fig. 2 are provided in the ESI.†

From the fitted curves in Fig. 2, we first note that the crossover from non-crystalline NPs (pink) to crystalline facetted NPs (blue) occurs at n = 280. In a previous study,[23] this crossover was estimated to occur at a smaller value of n = 125. Firstly, we point out that the diameter of a NP with n = 125 (Ø = 2.01 nm, assuming a spherical shape) and that of one with n = 280

(Ø = 2.68 nm) is similar, and thus the original prediction that this crossover occurs for NP sizes between 2–3 nm in ref. 23 is confirmed. The relatively small upward shift of the specific size for the crossing point of the two fitted lines is mainly due to the inclusion of extra data points for larger faceted NPs in the present work, which slightly improves the fit for this family of NPs.

In Fig. 2 we also can compare the relative stability of faceted (blue) *versus* spherical NPs (red and green) as a function of NP size. For spherical bulk-cut NPs that have been relaxed to their nearest local minimum energy structure (red), we find that relaxed faceted TiO_2 NPs (blue) are more energetically stable for all NP sizes. For NPs with Ø ≥2 nm the energy difference in favour of the faceted NPs becomes almost constant with a value close to 1.1 eV per TiO_2 unit. Note that this implies that, in terms of total energy, the difference between spherical relaxed and faceted structures grows approximately linearly with the number of TiO_2 units explaining the dominance of faceted NP at larger sizes. The large difference in the stability between these NP types can be rationalized by noting the relatively higher proportion of low coordinated atoms in the spherical cut NPs which leads to a small degree of partial amorphization at the surface of the NP.

Experimentally, thermal annealing[42,53] is often used to reduce the number of defects and to induce changes in the crystallinity and morphology of titania NPs.[34,54] Depending on the annealing temperature different structural changes can be observed.[55] For instance, in absence of annealing, TiO_2 thin films tend to exhibit the rutile phase, while annealing at 723 K causes the anatase phase to become dominant.[42] Mirroring such experiments, we annealed our spherical cut relaxed NPs using MD simulations (see Methodology for details) followed by a optimization of the most energetically stable NP structures found during the MD runs. For faceted NPs, even for small sizes, we found that annealing does not significantly change the internal structure or morphology. Correspondingly, the energetic stabilisation induced by annealing for such NPs is very small (*e.g.* 0.02 eV per TiO_2 unit for the $(TiO_2)_{37}$ faceted NP). These results confirm the relative high stability of these NPs. For spherical NPs directly relaxed from bulk cuts, however, we found that annealing can increase their energetic stability. In this case, annealing using the MA IP always resulted in NPs in which some degree of surface relaxation/reconstruction occurs but which maintained their crystalline anatase cores. We refer to such annealed NPs as core–shell NPs. Comparing the red and green lines in Fig. 2 we can see that the energetic stabilization induced *via* annealing relaxed spherical cut NPs to form core–shell NPs is fairly constant for all NP sizes. For the smallest spherical cut NP, the core–shell NP obtained from annealing using the MA IP was found not to be significantly more stable than the original relaxed NP. As annealing is expected to mainly affect the surface atoms, which become a larger proportion of the total atoms as the NP size decreases, we would perhaps expect that the difference in stability between the non-annealed and annealed NPs should be larger at small NP sizes. When annealing using the Nano-TiO IP we indeed found a significantly larger energetic stability increase for the three smallest relaxed spherical cut NPs than was found when annealing using the MA IP. The arrows in Fig. 2 indicate the extent of increase in energetic stability through annealing using the Nano-TiO IP with respect to the three smallest core–shell NPs (*i.e.* for $(TiO_2)_n$ sizes with n = 43, 115, 136) obtained through annealing using the MA IP. Analysis of these more stable annealed spherical $(TiO_2)_n$ NP structures shows that the original crystalline bulk core disappears in all cases. These NPs are thus no longer core–shell but are very similar to the larger globally optimised NPs in Fig. 1 (*i.e.* $(TiO_2)_n$ for n = 28, 35, 38) with respect to both morphology (*i.e.* quasi-spherical) and structure (*i.e.* non-crystalline). This finding is in line with other work indicating that a crystalline bulk core cannot easily be maintained for spherical NPs with Ø ≤2.0 nm.[22,24] We note that in ref. 22 annealing using the MA IP is used to derive a $(TiO_2)_n$ spherical core–shell NP with 115 < n < 136. Considering our results, it is likely that this core–shell NP is metastable with respect to a more disordered NP. For the smallest annealed $(TiO_2)_n$ NP with n = 43 the disordered NP structure is predicted to be more energetically stable than a correspondingly sized faceted anatase NP (see Fig. 2). This result is in line with the fact that non-crystalline NPs from global optimisation are the most stable NPs in this size regime. Strictly speaking, globally optimised NPs are, by definition, the lowest in energy for any size and thus should include crystalline faceted NPs for larger sizes. Following the approach in ref. 23, however, we interpret these globally optimised NPs as forming the set of lowest energy non-crystalline NPs.

To better understand the effect of the annealing process, especially for larger NP sizes, we analysed the change of the atomic coordination environments of Ti and O atoms when going from the relaxed spherical cut NPs to the core–shell NPs for $(TiO_2)_n$ with n = 257, 595. In particular, we focused on the percentage of Ti atoms with 6-fold coordination [Ti_{6c}] and O atoms with 3-fold coordination (O_{3c}), both corresponding to the atomic environments found in the bulk anatase phase. With or without annealing, a clear trend of an increasing percentage Ti_{6c} and O_{3c} with increasing NP size is observed in both set of spherical NPs (Table 1). This tendency clearly shows that the Ti_{6c} and O_{3c} coordination environments in spherical NPs become closer to those corresponding to the anatase bulk phase in larger NPs. More specifically, in Table 1 one can see that the percentages of Ti_{6c} and O_{3c} centres in the large $(TiO_2)_{595}$ annealed spherical NP are quite comparable to those in the large faceted crystalline $(TiO_2)_{455}$ NP. Upon annealing the percentage of bulk-like Ti_{6c} and O_{3c} centres in the spherical NPs slightly decreases. However, at the same time, we note in Table 1 that the percentage of four coordinated Ti_{4c} centres increases. As annealing increases the energetic stability of the relaxed spherical NPs this suggests that the increase in the proportion of Ti_{4c} centres helps to increase the structural integrity of the NPs.

The above described results are schematically brought together in a tentative structure *versus* stability diagram in Fig. 3. Here zero energy corresponds to the lowest energy struc-

Table 1 Percentages of Ti_{4c}, Ti_{5c} and O_{2c} centres (with respect to the total number of Ti and O centres respectively) in optimized $(TiO_2)_{257}$ and $(TiO_2)_{355}$ spherical NPs with and without annealing. Corresponding data for the faceted $(TiO_2)_{355}$ NP is also included for comparison. The effect of annealing is reflected in the fractional change in the percentages. Note that a cut-off radius of 2.4 Å was used to compile the data

	Spherical NPs						Faceted NPs		
	$(TiO_2)_{257}$			$(TiO_2)_{355}$			$(TiO_2)_{355}$		
	Ti_{4c}	Ti_{5c}	O_{2c}	Ti_{4c}	Ti_{5c}	O_{2c}	Ti_{4c}	Ti_{5c}	O_{2c}
Non annealed	17.1	43.2	53.5	13.6	61.3	68.8	3.1	58.2	77.8
Annealed	29.6	37.7	50.8	17.5	59.1	66.6	3.1	58.2	77.8
Diff (%)	+12.5	−5.5	−2.7	+3.9	−2.1	−2.2	0	0	0

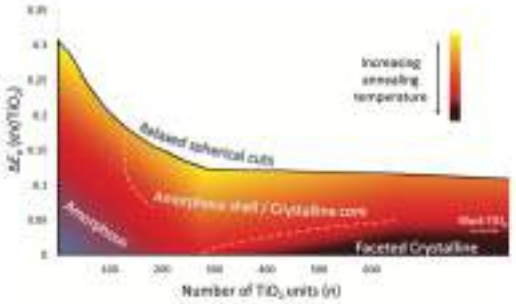

Fig. 3 Tentative structure versus stability diagram for TiO_2 NPs with respect to the relaxed spherical cut NPs (upper black line) based on the fitted tendencies and the NP structures corresponding to the data points in Fig. 2.

ture for each size and the uppermost black curve follows the metastability of the relaxed spherical cut NPs. The shading in the figure indicates the relative annealing temperature and labels and dashed lines approximately delimit regions where different NP types are more stable. The smallest spherical cut NPs become most stable when fully amorphised upon annealing in line with the small globally optimised NPs, and thus non-crystalline NPs dominate for small NP sizes. With increasing size relaxed spherical cut NPs can persist but are metastable with respect to NPs with amorphous shells and/or fully amorphous NPs. Above a diameter of about 2.7 nm moderate annealing of spherical relaxed cut NPs will still lead to core–shell type NPs but the most stable annealed NPs are crystalline faceted NPs.

Although, annealed spherical NPs are thus always predicted to be metastable species, depending on experimental conditions, a range of NPs with energies above that of the ideal global minima will typically be produced. For the larger NPs considered (Ø >2 nm), our results show that even after annealing, an anatase crystal core can be maintained in the spherical NPs. Here, although faceted NPs are most energetically stable, experimental NP preparation conditions will largely influence the final morphology and structure. As small anhydrous spherical NPs are often observed,[37,57] solely gas-phase thermodynamic stability does not appear to be the main driving force in experiment. Moreover, there is experimental evidence that annealing in vacuum environments appears to be an effective method to activate TiO_2 NPs and enhance their visible-light photocatalytic activity.[58] It thus may be expected that our anhydrous annealed spherical NP may be good models of the spherical NPs in such experiments. Comparison of the data in Table 1 with experimental data from X-ray absorption spectra as performed in ref. 22 would help to confirm the type and structure of NPs in any particular experimental set-up.

The shape, size and internal structure of TiO_2 NPs can have a significant influence on the optical absorption energy gap (O_{gap}),[38] which, in turn, dictates their usefulness in photocatalysis. In Fig. 4a we report O_{gap} values as predicted from the Kohn–Sham orbital energies from our DFT calculations for all considered NPs. Since the PBE functional[59] exhibits a systematic error with respect to calculated O_{gap} values, we report corrected values obtained from a linear relationship between PBE values and values obtained using the hybrid PBEx (12.5% Fock exchange) functional.[59] We note that the PBEx functional reproduces the experimental band gap of anatase and rutile, and properly described the corresponding reduced systems.[60,61] In order to assess the validity of our NP models with respect to experiment, we include a gray shaded region in Fig. 4 delimiting the range of measured O_{gap} values (2.85–3.0 eV) for dried and annealed anatase TiO_2 NPs possessing near spherical morphologies and diameters between 2–10 nm.[57] For NPs with Ø <2 nm (*i.e.* outside of the experimentally measured range) nearly all considered NPs have O_{gap} values higher than that of bulk anatase (*i.e.* >3.2 eV). Only the relaxed $(TiO_2)_n$ spherical cut NP with n = 115 has a slightly smaller gap than anatase, which is probably due to a persistent surface defect, which is subsequently removed upon annealing. The consistently high gaps in this size range for both annealed and global optimised NPs confirm the effectiveness of these approaches at producing stable NP structures with few under-coordinated defects. In the Ø >2 nm size regime, although the O_{gap} values of the faceted NPs remain quite high with respect to the experimental range, the O_{gap} values for both sets of spherical NPs (*i.e.* relaxed and annealed) become significantly lower and much closer to the measured values. The agreement with experiment is particularly good for the annealed core–shell spherical NPs which, for all five NP sizes considered, the calculated O_{gap} values are within, or very close to, the experimentally measured range.[62] We note that these reduced

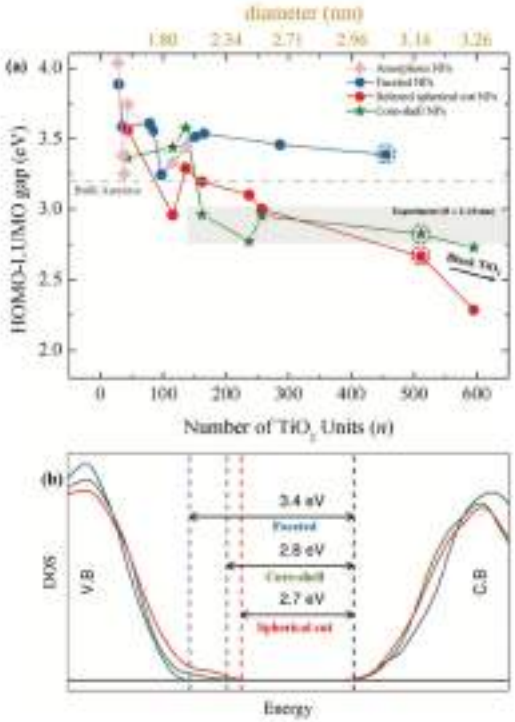

Fig. 4 (a) The optical gap (O_{gap}) as estimated via the difference between the highest occupied molecular orbital (HOMO) and the lowest unoccupied molecular orbital (LUMO) of faceted, spherical cut, core–shell and amorphous TiO_2 NPs calculated using the hybrid PBEx exchange correlation functional.[59] Note that the data for the relaxed spherical cuts and the core–shell NPs were determined following the correlation found between O_{gap}(PBE) and O_{gap}(PBEx) reported in ref. 59. The grey horizontal bar represents experimentally measured O_{gap} results for TiO_2 NPs with near spherical shapes and with diameters ranging from 2 to 10 nm.[67] Two different isomers for $(TiO_2)_{141}$, $(TiO_2)_{115}$, and $(TiO_2)_{128}$ NPs are labelled as amorphous and core–shell NPs, which correspond to pre-optimizations using NanoTiO and MA interatomic potentials, respectively. The dashed line indicates the band gap in bulk TiO_2 anatase phase (*i.e.* 3.2 eV). (b) The density of state (DOS) of faceted $(TiO_2)_{415}$ and relaxed direct cut and annealed spherical $(TiO_2)_{511}$ NPs – corresponding to the circled data points in (a). The structural disorder near the surfaces of the spherical NPs creates broadened tails in their valence band (VB) edges, leading to the reduction of the energy gap. Conversely the conduction band (CB) is similar for all three considered NPs.

energy gaps are not simply due to the morphology of the spherical NPs. For example, the slightly hydroxylated spherical cut NP models reported by Fazio *et al.*[51] maintain energy gaps above that of the anatase bulk crystal. As noted above, higher-than-bulk energy gaps in small anatase NPs could be rationalised due to quantum confinement.[34] Although our spherical NPs are affected by quantum confinement, it appears that the surface structural disorder outweighs this effect in our larger NPs to bring the gap below that of anatase. An analysis of the density of states (DOS) near the gap edges of one of larger spherical NPs in our study (see Fig. 4b) reveals a broadening of the valence band edge, which reduces their energy gap by 0.6–0.7 eV with respect to that of a similar sized faceted NP.

For all NP families considered, as expected, the optical gap tends to decrease with increasing NP size as the effect of quantum confinement diminishes. We also note that for the largest spherical NPs considered, although the annealed NP has an O_{gap} value more consistent with experiment, the O_{gap} value for the relaxed spherical cut NP is significantly lower. This difference is likely due to the fact that annealing increases the energetic stability of the spherical cut NPs by reducing the strain in the near surface structure, and thus reducing the high energy tail of the broadened valence band edge. These results strongly suggest that small experimentally prepared 2–3 nm diameter spherical TiO_2 NPs are likely to have an anatase core and an amorphized shell in line with a previous structural study using the MA IP.[22] Our accurate quantum mechanical DFT based calculations allow us to further demonstrate that, relative to faceted crystalline NPs, annealed spherical core–shell NPs are metastable species which display relatively smaller O_{gap} values through the formation of valence band edge tails and thus should exhibit improved photocatalytic activity.

A more detailed analysis of the valence band edge in the core shell NPs is shown in Fig. 5 where the corresponding partial DOS of the thermally annealed spherical $(TiO_2)_{257}$ core–shell NP shows that O_{2c} and Ti_{4c} contribute significantly to the broadening. These low coordinated atoms are located mainly in the NP shell as depicted in Fig. 5b. As noted above these Ti_{4c} centres are created upon annealing and appear to be involved, along with O_{2c} centres, in creating energy-lowering near-surface reconstructions. Note that the presence of a single O_{2c} centre depicted in white colour in Fig. 5b, also contributes to the broadening as shown by dashed line in Fig. 5a. This gap edge broadening, and consequent gap reduction, is analogous to that observed in larger core–shell black TiO_2 NPs, and is associated with the disordered structure in their near surface shell.[23] The metastable black TiO_2 NPs are produced by engineering surface disorder in thermodynamically favoured faceted anatase NP by various physicochemical procedures. Although these methods typically produce NPs with non-stoichiometric shells,[13,62,64] our results show that significant energy gap engineering can be induced, in principle, by inducing disorder in stoichiometric NPs. Although, terminal defective oxygen species can influence the gap edge, annealing is often found to remove such energetically unfavourable and reactive species in other NPs, leaving only Ti_{4c} and O_{2c} as the only gap narrowing species. We note that our analysis is also in line with detailed experimental studies of a nanostructured stoichiometric TiO_2(001) surface, where it is suggested that surface Ti_{4c} atoms cause significant band gap narrowing.[65] As such, these surface science studies and our NP-based results strongly suggest that promoting the formation of surface Ti_{4c} sites could be a general means to sig-

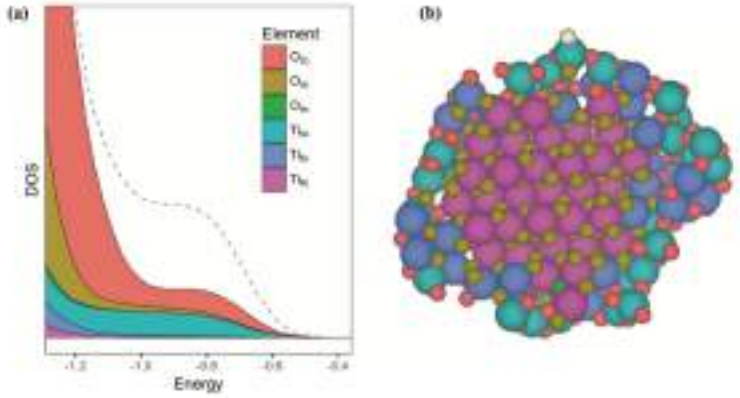

Fig. 5 (a) Partial DOS plot of an annealed core–shell $(TiO_2)_{357}$ NP with energies given eV. Each colour indicates the contribution of Ti or O atoms with different coordinations (the dashed line shows the contribution of a single terminating O_{1c} centre). (b) Cross sectional cut through the annealed core–shell $(TiO_2)_{357}$ NP where Ti and O atoms with different coordination are shown by the same colour coding in the partial DOS plot. The cut clearly shows a bulk-like crystalline core (dominated by Ti_{6c} and O_{3c} centres) and a disordered shell (dominated by Ti_{4c}, Ti_{5c} and O_{2c} centres). Note that the white sphere corresponds to the single O_{1c} centre.

nificantly elevate photocatalytic activity in stoichiometric TiO_2 nanosystems.

Generally, our results highlight that a detailed understanding of the structure, size and morphology of NPs is crucial in order to understand experimentally measured properties of these important nanosystems. By showing that stoichiometric TiO_2 NPs with sizes <5 nm have highly tuneable optical energy gaps (above and below that of bulk TiO_2) our results point to ways in which these factors could be tailored in experiment to optimise the photoactivity of TiO_2 NPs.

Conclusions

In this work, we have systematically studied the stability of realistic, stoichiometric $(TiO_2)_n$ NPs containing up to almost 1800 atoms, covering the corresponding NP diameter range from 1.0–3.4 nm. We focus mainly on faceted and spherical morphologies, both with initial structures cut from the bulk anatase crystal structure. After relaxing their geometry, we compare the relative stability and electronic structure properties using accurate all-electron DFT-based calculations. Moreover, we also take into account the effect of the thermal annealing on the structures and properties of these NPs. Our results show that annealing spherical NPs leads to a significant increase in their energetic stability. This effect can be rationalised by the concomitant increase in the proportion of Ti_{4c} and O_{2c} centres involved in energy lowering surface reconstruction upon annealing. For the faceted NPs, however, annealing induced only very minor structural change which causes negligible energetic stabilisation. Non-annealed spherical NPs are always metastable with respect to both annealed spherical NPs and faceted NPs. Although faceted NPs are the most stable species for the larger NP sizes considered, for the smaller $(TiO_2)_n$ NPs annealing produces low energy amorphized NP structures. Our analysis of the electronic structure of each NP family reveals that morphology, structure and size, all have a notable influence on the optical absorption energy gap. Specifically, our calculations confirm that that metastable annealed spherical NPs with anatase cores and amorphized shells and Ø >2 nm sizes exhibit O_{gap} values which match particularly well with those measured for annealed NPs with 2–10 nm diameters.[37] These O_{gap} values for spherical core–shell NPs are also significantly lower, and thus more favourable for photocatalysis, than those calculated for the thermodynamically favoured faceted NPs which are above that of bulk anatase. We confirm that these results can be rationalised through a disorder-induced broadening of the valence band edge as observed in experiment for larger black TiO_2 NPs. Our study using pure TiO_2 NPs also implies it is not necessary to employ procedures which introduce non-stoichiometry or dopant atoms for this band gap reducing effect. Instead the presence of Ti_{4c} and O_{2c} sites in the disordered shell of the core–shell NPs are found to be sufficient to produce valence band tails to reduce the energy gap. The impressive agreement between our calculations and experiment for core–shell NPs with 2–3 nm diameters implies that the conditions employed to prepare these NPs tends to lead to kinetically trapped core–shell structures. Our results clearly show that stoichiometric TiO_2 NPs with sizes <5 nm have highly tuneable optical energy gaps (above and below that of bulk TiO_2) and point to ways in which these factors could be tailored in experiment to optimise their photoactivity.

Conflicts of interest

There are no conflicts to declare.

Acknowledgements

This research was supported by the Spanish Ministerio de Economía y Competitividad/FEDER CTQ2015-64618-R and Ministerio de Ciencia, Innovación y Universidades (MCIU) Spanish Structures of Excellence María de Maeztu program through grant MDM-2017-0767 and, in part, by Generalitat de Catalunya (grants 2017SGR13 and XRQTC). A. M.-G. thanks to Ministerio de Ciencia, Investigación y Universidades (MCIUN) for the Juan de la Cierva postdoctoral grants (FJCI-2015-23760 and IJCI-2017-31979) and F. I. acknowledges additional support from the 2015 ICREA Academia Award for Excellence in University Research. Computational time at the MareNostrum supercomputer has been provided by the Barcelona Supercomputing Centre (BSC) through the grant of the Partnership for Advanced Computing in Europe AISBL (PRACE) under the EXCIPHOCAT project (2016163940).

References

1 L. Liu and X. Chen, *Chem. Rev.*, 2014, **114**, 9890–9918.
2 H. Xu, S. Ouyang, L. Liu, P. Reunchan, N. Umezawa and J. Ye, *J. Mater. Chem. A*, 2014, **2**, 12642–12661.
3 A. Fujishima and K. Honda, *Nature*, 1972, **238**, 37–38.
4 X. Chen and S. S. Mao, *Chem. Rev.*, 2007, **107**, 2891–2959.
5 M. G. Walter, E. L. Warren, J. R. McKone, S. W. Boettcher, Q. Mi, E. A. Santori and N. S. Lewis, *Chem. Rev.*, 2010, **110**, 6446–6473.
6 M. Murdoch, G. I. Waterhouse, M. A. Nadeem, J. B. Metson, M. A. Keane, R. F. Howe, J. Llorca and H. Idriss, *Nat. Chem.*, 2011, **3**, 489–492.
7 H. Reiche and A. J. Bard, *J. Am. Chem. Soc.*, 1979, **101**, 3127–3128.
8 D. A. Tryk, A. Fujishima and K. Honda, *Electrochim. Acta*, 2000, **45**, 2363–2367.
9 A. L. Linsebigler, G. Q. Lu and J. T. Yates, *Chem. Rev.*, 1995, **95**, 735–758.
10 D. O. Scanlon, C. W. Dunnill, J. Buckeridge, S. A. Shevlin, A. J. Logsdail, S. M. Woodley, C. R. A. Catlow, M. J. Powell, R. G. Palgrave, I. P. Parkin, G. W. Watson, T. W. Keal, P. Sherwood, A. Walsh and A. Sokol, *Nat. Mater.*, 2013, **12**, 798–801.
11 M. Anpo and M. J. Takeuchi, *J. Catal.*, 2003, **216**, 505–516.
12 S. G. Kumar and L. G. Devi, *J. Phys. Chem. A*, 2011, **115**, 13211–13241.
13 L. Liu, P. Y. Yu, X. Chen, S. S. Mao and D. Z. Shen, *Phys. Rev. Lett.*, 2013, **111**, 065505.
14 I. Nakamura, N. Negishi, S. Kutsuna, T. Ihara, S. Sugihara and K. Takeuchi, *J. Mol. Catal. A: Chem.*, 2000, **161**, 205–212.
15 X. Pan, M.-Q. Yang, X. Fu, N. Zhang and Y.-J. Xu, *Nanoscale*, 2013, **5**, 3601–3614.
16 A. S. Barnard and P. Zapol, *Phys. Rev. B: Condens. Matter Mater. Phys.*, 2004, **70**, 235403.
17 X. Chen, C. Li, M. Graetzel, R. Kostecki and S. S. Mao, *Chem. Soc. Rev.*, 2012, **41**, 7909–7937.
18 D. Selli, G. Fazio and C. Di Valentin, *Catalysts*, 2017, **7**, 357.
19 Y.-F. Li and Z.-P. Liu, *J. Am. Chem. Soc.*, 2011, **133**, 15743–15752.
20 X. Chen, L. Liu, P. Y. Yu and S. S. Mao, *Science*, 2011, **331**, 746–750.
21 K. C. Ko, S. T. Bromley, J. Y. Lee and F. Illas, *J. Phys. Chem. Lett.*, 2017, **8**, 5593–5598.
22 H. Zhang, B. Chen, J. F. Banfield and G. A. Waychunas, *Phys. Rev. B: Condens. Matter Mater. Phys.*, 2008, **78**, 214106–214101.
23 O. Lamiel-García, A. Cuko, M. Calatayud, F. Illas and S. T. Bromley, *Nanoscale*, 2017, **9**, 1049–1058.
24 R. Dorkins, M. L. Sushko, J. Liu and D. M. Duffy, *Phys. Chem. Chem. Phys.*, 2014, **16**, 9441–9447.
25 R. Merad, A. M. Peiró, J. R. Durrant and M. S. P. Shaffer, *Chem. Mater.*, 2006, **18**, 6059–6068.
26 D. V. Bavykin, J. M. Friedrich and F. C. Walsh, *Adv. Mater.*, 2006, **18**, 2807–2824.
27 M. Cargnello, T. R. Gordon and C. B. Murray, *Chem. Rev.*, 2014, **114**, 9319–9345.
28 C.-T. Dinh, T.-D. Nguyen, F. Kleitz and T.-O. Do, *ACS Nano*, 2009, **3**, 3737–3743.
29 C. Chen, R. Hu, K. Mai, Z. Ren, H. Wang, G. Qian and Z. Wang, *Cryst. Growth Des.*, 2011, **11**, 5221–5226.
30 T. R. Gordon, M. Cargnello, T. Paik, F. Mangolini, R. T. Weber, P. Fornasiero and C. B. Murray, *J. Am. Chem. Soc.*, 2012, **134**, 6751–6761.
31 G. Fazio, D. Selli, L. Ferraro, G. Seifert and C. Di Valentin, *ACS Appl. Mater. Interfaces*, 2018, **10**, 29943–29953.
32 G. Fazio, L. Ferrighi and C. Di Valentin, *J. Phys. Chem. C*, 2015, **119**, 20735–20746.
33 K. Shirai, G. Fazio, T. Sugimoto, D. Selli, L. Ferraro, K. Watanabe, M. Haruta, B. Ohtani, C. Di Valentin and Y. Matsumoto, *J. Am. Chem. Soc.*, 2018, **140**, 1415–1422.
34 G. Fazio, L. Ferrighi and C. Di Valentin, *Nano Energy*, 2016, **27**, 673–689.
35 X. Chen, L. Liu, M. A. Marcus, W.-C. Wang, N. A. Oyler, M. E. Grass, B. Mao, P.-A.- Glans, P. Y. Yu, J. Guo and S. S. Mao, *Sci. Rep.*, 2013, **3**, 1510.
36 S. Mugundan, B. Rajamannan, G. Viruthagiri, N. Shanmugam, R. Gobi and P. Praveen, *Appl. Nanosci.*, 2014, **5**, 449–456.
37 A. Ansari, S. Sachar and S. S. Garje, *New J. Chem.*, 2018, **42**, 13358–13366.
38 O. Lamiel-García, K. C. Ko, J. Y. Lee, S. T. Bromley and F. Illas, *J. Chem. Theory Comput.*, 2017, **13**, 1785–1793.
39 O. V. Prezhdo, W. R. Duncan and V. V. Prezhdo, *Prog. Surf. Sci.*, 2009, **84**, 30–68.
40 F. Nunzi, L. Storchi, M. Manca, R. Giannuzzi, G. Gigli and F. De Angelis, *ACS Appl. Mater. Interfaces*, 2014, **6**, 2471–2478.
41 S. Sugapriya, R. Sriram and S. Lakshmi, *Optik*, 2013, **124**, 4971–4975.
42 A. Dussan, A. Bohórquez and H. F. Quiroz, *Appl. Surf. Sci.*, 2017, **424**, 111–114.
43 X. Zhou, E. Wierzbicka, N. Liu and P. Schmuki, *Chem. Commun.*, 2019, **55**, 533–536.

44 G. Wulff, *Z. Kristallogr.*, 1901, **34**, 449–530.
45 E. Rabani, *J. Chem. Phys.*, 2001, **115**, 1493–1496.
46 H. Zhang, F. Huang, B. Gilbert and J. F. Banfield, *J. Phys. Chem. B*, 2003, **107**, 13051–13060.
47 H. Zhang, B. Gilbert, F. Huang and J. F. Banfield, *Nature*, 2003, **424**, 1025–1029.
48 M. Matsui and M. Akaogi, *Mol. Simul.*, 1991, **6**, 239–244.
49 F. Viñes, O. Lamiel-García, F. Illas and S. T. Bromley, *Nanoscale*, 2017, **9**, 10067–10074.
50 J. P. Perdew, K. Burke and M. Ernzerhof, *Phys. Rev. Lett.*, 1996, **77**, 3865–3868.
51 V. Blum, R. Gehrke, P. Hanke, P. Havu, V. Havu, X. Ren, K. Reuter and M. Scheffler, *Comput. Phys. Commun.*, 2009, **180**, 2175–2196.
52 R. Johnson, *Masters Series in Physics and Astronomy in Atomic and Molecular Clusters*, Taylor and Francis, 2002.
53 S. Liu, J. Yu and M. Jaroniec, *Chem. Mater.*, 2011, **23**, 4085–4093.
54 D. P. Padiyan and S. T. Nishanthi, *Trans. Mater. Res. Soc. Jpn.*, 2013, **38**, 127–130.
55 D. Selli, G. Fazio and C. Di Valentin, *J. Chem. Phys.*, 2017, **147**, 164701.
56 G. Okeke, R. B. Hammond and J. Antony, *Chem. Eng. Sci.*, 2016, **146**, 144–158.
57 V. M. Ramakrishnan, M. Natarajan, A. Santhanam, V. Asokan and D. Velauthapillai, *Mater. Res. Bull.*, 2018, **97**, 351–360.
58 M. Samiee and J. Luo, *Mater. Lett.*, 2013, **98**, 205–208.
59 Á. Morales-García, R. Valero and F. Illas, *Phys. Chem. Chem. Phys.*, 2018, **20**, 18907–18911.
60 K. C. Ko, O. Lamiel-García, J. Y. Lee and F. Illas, *Phys. Chem. Chem. Phys.*, 2016, **18**, 12357–12367.
61 Á. Morales-García, R. Valero and F. Illas, *J. Chem. Theory Comput.*, 2017, **13**, 3746–3753.
62 A. Naldoni, M. Allieta, S. Santangelo, M. Marelli, F. Fabbri, S. Cappelli, C. L. Bianchi, R. Psaro and V. Dal Santo, *J. Am. Chem. Soc.*, 2012, **134**, 7600–7603.
63 S. G. Ullattil, S. B. Narendranath, S. C. Pillai and P. Periyat, *Chem. Eng. J.*, 2018, **343**, 708–736.
64 S. Chen, Y. Wang, J. Li, Z. Hu, H. Zhao, W. Xie and Z. Wie, *Mater. Res. Bull.*, 2018, **98**, 280–287.
65 H. Ariga, T. Taniike, H. Morikawa, M. Tada, B. K. Min, K. Watanabe, Y. Matsumoto, S. Ikeda, K. Saiki and Y. Iwasawa, *J. Am. Chem. Soc.*, 2009, **131**, 14670–14672.

Conclusions

1. Evaluation of the energetic stability of a variety of different anhydrous titania NP shapes and structures shows that GO NPs, which we ascribe to the family of amorphous structures up to the analyzed sizes, are most stable until a diameter of 2.5 nm. Beyond this size, in vacuum, crystalline Ant NPs with a Wulff-constructed faceted bypiramidal shape are the most stable. Directly cut spherical Ant NPs are always metastable with respect to such bipyramidal NPs.
2. Annealing spherical cut Ant NPs using the MA IP resulted in core-shell NPs which were lower in energy than the direct cuts for all sizes, but still metastable with respect to Wulff-constructed faceted NPs. Annealing using the NanoTiO IP for the smallest NP sizes resulted in complete amorphization of the structures and a large energy stabilization compared to the MA annealing, providing amorphous NPs with energies similar to those of faceted NPs. We ascribe the energy stabilization of the core-shell structures to an annealing-induced increase of four coordinated sites in the surface of the NP.
3. Based on the energetic results of our MD simulations, we propose an energy versus shape stability diagram as a function of size with an upper energy bound taken to be that of as-cut spherically shaped Ant NPs.
4. We evaluated the band-gap of our NPs with respect to size and family of the structure using DFT calculations. As expected, we find that the band-gap diminishes as the NP size increases. However, we find a large difference between the band-gap of spherical NPs and faceted ones. In particular, we find that annealed and spherical NPs have band-gaps below that of bulk ant and in line with the band-gap values of experimentally tailored anhydrous TiO_2 NPs.
5. Analyzing the density of states of the different NP models we ascribe the difference in band-gap to the presence of a long tail in the valence band of spherical and core-shell NPs. Looking at the contribution of each atom in the density of states, we find that low coordination centers (two-fold coordinated O and four coordinated Ti sites) are the origin of the tail.

Chapter 7: Conclusions on TiO_2 nanoparticles and Outlook

The work done in the present thesis provides valuable advances in the modelling of TiO_2 NPs, with implications on understanding both their electronic structure -and hence the band-gap- of differently shaped NPs and their crystallization processes. The first published result stress the benefits of using IPs even when target properties can only be obtained through *ab initio* theory. We highlight two important advantages as: 1) IPs can reduce the time of DFT calculations by half or even more, as both the initial SCF cycle time and the number of steps to find the appropriate minima are diminished, and 2) NP models which cannot be generated by hand -such as annealed spherical cut particles- can be produced accurately with IPs in several steps to provide insight into the PES of the system and point to clues on the stability of NPs. We conclude that while the MA IP can provide slightly faster optimization times than the NanoTiO IP, the latter is able to accurately stabilize spherical NPs, as judged via posterior DFT optimizations providing similar stabilization energies. The second published result uses the NP structures generated in the preceding paper to extend the analysis of the energetic stability of different NP shapes: direct-cut spherical, faceted, core-shell and GO amorphous NPs. For small NP sizes, spherically cut Ant NPs are highly metastable with respect to GO amorphous NPs. In this regime core-shell NPs are slightly more stable than as-cut spherical ant NPs and faceted ant NPs. However, the family of faceted Ant NPs become the most stable species once they reach a size of 2.5 nm in diameter. Analyzing the stability of the core-shell NPs, we find that the structure has an increase of 4 coordinated Ti centers with respect to the original Ant spherical cuts. We ascribe the energetic stability to this increase of 4 coordinated Ti centers. We also analyze the band-gap of the different NP families and find that spherical and core-shell NPs have smaller band-gaps than faceted NPs. The diminished band-gap in the former species can be attributed to low coordination centers, such as 4 coordinated Ti atoms and 2 coordinated O atoms.

The NP models provided in this thesis open new opportunities for research in the field of TiO_2 NPs. Starting with the core-shell NPs, it seems reasonable to assume that amorphous NPs from GO will, at some point, be large enough to allow the presence of a crystalline region in their core. Whether they are the global minima for a certain size, it is not known, but they could provide information on the interface between crystalline NPs and reconstructed/amorphous surfaces. The interplay between IP and DFT methods can allow the modelling and energy evaluation of such models. Analysis of the effect of hydroxylation could show differences between faceted NPs and spherical ones, thanks to the possibility to generate spherical NPs with any degree of hydroxylation. Current hydrated NP models used in the literature are derived from direct crystal cuts where the low coordinated centers are saturated with H or OH groups, which cause that for a certain size there is only one possible degree of hydroxylation. Comparison between constructing hydroxylated models by either annealing anhydrous NPs for posterior hydroxylation or directly saturating dangling bonds will also allow a better understanding on the effect that hydroxylation has on the crystallinity of nanostructures.

References

[1] N.A. Dubrovinskaia, L.S. Dubrovinsky, R. Ahuja, V.B. Prokopenko, V. Dmitriev, H.-P. Weber, J.M. Osorio-Guillen, and B. Johansson, Phys. Rev. Lett. **87**, 275501 (2001).
[2] A. El Goresy, L. Dubrovinsky, P. Gillet, G. Graup, and M. Chen, Am. Mineral. **95**, 1362 (2010).
[3] L.S. Dubrovinsky, N.A. Dubrovinskaia, V. Swamy, J. Muscat, N.M. Harrison, R. Ahuja, B. Holm, and B. Johansson, Nature **410**, 653 (2001).
[4] M. Chen, X.P. Gu, X. De Xie, and F. Yin, Chinese Sci. Bull. **58**, 4655 (2013).
[5] Titanium Dioxide (TiO2) Market Size, Share & Trends Analysis Report By Application (Paints & Coatings, Plastics, Pulp & Paper, Cosmetics), by Region (North America, Europe, APAC, MEA, CSA), and Segment forecasts, 2019 - 2025 Grand View Research, https://www.grandviewresearch.com/industry-analysis/titanium-dioxide-industry.
[6] Sulfuric Acid Market Analysis By Raw Material (Elemental Sulfur, Base Metal Smelters, Pyrite Ore), By Application (Fertilizers, Chemical Manufacturing, Refinery, Textile), And Segment Forecasts, 2018 - 2025. https://www.grandviewresearch.com/industry-analysis/sulfuric-acid-market
[7] Ammonia Market Analysis By Product Form (Liquid, Gas, Powder), By Application (Fertilizers, Textile, Pharmaceuticals, Refrigerants), By Region, And Segment Forecasts, 2018 - 2025. https://www.grandviewresearch.com/industry-analysis/ammonia-market
[8] Photocatalyst Market Size, Analysis | Global Industry Report, 2018-2025, www.grandviewresearch.com/industryanalysis/photocatalyst-market.
[9] S.-Y. Lee and S.-J. Park, J. Ind. Eng. Chem. **19**, 1761 (2013).
[10] I.K. Konstantinou and T.A. Albanis, Appl. Catal. B Environ. **49**, 1 (2004).
[11] C. McCullagh, J.M.C. Robertson, D.W. Bahnemann, and P.K.J. Robertson, Res. Chem. Intermed. **33**, 359 (2007).
[12] Y. Sugita, K. Ishizaki, F. Iwasa, T. Ueno, H. Minamikawa, M. Yamada, T. Suzuki, and T. Ogawa, Biomaterials **32**, 8374 (2011).
[13] J.M. Ruso, V. Verdinelli, N. Hassan, O. Pieroni, and P. V. Messina, Langmuir **29**, 2350 (2013).
[14] P.G. Bruce, B. Scrosati, and J.-M. Tarascon, Angew. Chemie Int. Ed. **47**, 2930 (2008).
[15] C. Natarajan, K. Setoguchi, and G. Nogami, Electrochim. Acta **43**, 3371 (1998).
[16] M. Wagemaker, A.P.M. Kentgens, and F.M. Mulder, Nature **418**, 397 (2002).
[17] A. Fujishima and K. Honda, Nature **238**, 37 (1972).
[18] A. Wolcott, W.A. Smith, T.R. Kuykendall, Y. Zhao, and J.Z. Zhang, Adv. Funct. Mater. **19**, 1849 (2009).
[19] Q.-L. Meng, C. Lee, T. Ishihara, H. Kaneko, and Y. Tamaura, Int. J. Hydrogen Energy **36**, 13435 (2011).
[20] E. Baniasadi, I. Dincer, and G.F. Naterer, Appl. Catal. A Gen. **455**, 25 (2013).
[21] J.M. Herrmann, Catal. Today **53**, 115 (1999).
[22] J. Zhu and M. Zäch, Curr. Opin. Colloid Interface Sci. **14**, 260 (2009).
[23] E. Pulido Melián, O. González Díaz, A. Ortega Méndez, C.R. López, M. Nereida Suárez, J.M. Doña Rodríguez, J.A. Navío, D. Fernández Hevia, and J. Pérez Peña, Int. J. Hydrogen Energy **38**, 2144 (2013).
[24] J. Augustynski, Electrochim. Acta (1993).
[25] N. Serpone, D. Lawless, R. Terzian, C. Minero, and E. Pelizzetti, in *Photochem. Convers. Storage Sol. Energy* 451 (1991).
[26] A. Sclafani and J.M. Herrmann, J. Phys. Chem. **100**, 13655 (1996).
[27] T. Ohno, K. Sarukawa, K. Tokieda, and M. Matsumura, J. Catal. **203**, 82 (2001).
[28] D.O. Scanlon, C.W. Dunnill, J. Buckeridge, S.A. Shevlin, A.J. Logsdail, S.M. Woodley, C.R.A. Catlow, M.J. Powell, R.G. Palgrave, I.P. Parkin, G.W. Watson, T.W. Keal, P. Sherwood, A. Walsh, and A.A. Sokol, Nat. Mater. **12**, 798 (2013).
[29] N. Tian, Z.-Y. Zhou, S.-G. Sun, Y. Ding, and Z.L. Wang, Science (80-.). **316**, 732 (2007).
[30] A. Vittadini, A. Selloni, F.P. Rotzinger, and M. Grätzel, Phys. Rev. Lett. **81**, 2954 (1998).
[31] G. Wulff, Zeitschrift Für Krist. - Cryst. Mater. **34**, (1901).
[32] A.A. Gribb and J.F. Banfield, Am. Mineral. **82**, 717 (1997).
[33] A.S. Barnard and P. Zapol, Phys. Rev. B - Condens. Matter Mater. Phys. **70**, 235403 (2004).
[34] A.S. Barnard and P. Zapol, J. Chem. Phys. **121**, 4276 (2004).
[35] H.G. Yang, C.H. Sun, S.Z. Qiao, J. Zou, G. Liu, S.C. Smith, H.M. Cheng, and G.Q. Lu, Nature **453**, 638 (2008).
[36] H. Bin Wu, J.S. Chen, X.W. (David) Lou, and H.H. Hng, Nanoscale **3**, 4082 (2011).
[37] F. Amano, O.-O. Prieto-Mahaney, Y. Terada, T. Yasumoto, T. Shibayama, and B. Ohtani, Chem. Mater. **21**, 2601 (2009).

[38] Q. Deng, M. Wei, X. Ding, L. Jiang, K. Wei, and H. Zhou, J. Cryst. Growth **312**, 213 (2010).
[39] N. Murakami, Y. Kurihara, T. Tsubota, and T. Ohno, J. Phys. Chem. C **113**, 3062 (2009).
[40] M. Pal, J.G. Serrano, P. Santiago, and U. Pal, J. Phys. Chem. C **111**, 96 (2007).
[41] O. Khatim, M. Amamra, K. Chhor, A.M.T. Bell, D. Novikov, D. Vrel, and A. Kanaev, Chem. Phys. Lett. **558**, 53 (2013).
[42] K. Okada, N. Yamamoto, Y. Kameshima, A. Yasumori, and K.J.D. MacKenzie, J. Am. Ceram. Soc. **84**, 1591 (2004).
[43] H. Shin, H.S. Jung, K.S. Hong, and J.-K. Lee, J. Solid State Chem. **178**, 15 (2005).
[44] D.A.H. Hanaor and C.C. Sorrell, J. Mater. Sci. **46**, 855 (2011).
[45] I.N. Kholmanov, E. Barborini, S. Vinati, P. Piseri, A. Podestà, C. Ducati, C. Lenardi, and P. Milani, Nanotechnology **14**, 1168 (2003).
[46] H. Zhang, B. Chen, J.F. Banfield, and G.A. Waychunas, Phys. Rev. B **78**, 214106 (2008).
[47] X. Chen, L. Liu, P.Y. Yu, and S.S. Mao, Science **331**, 746 (2011).
[48] M. Tian, M. Mahjouri-Samani, G. Eres, R. Sachan, M. Yoon, M.F. Chisholm, K. Wang, A.A. Puretzky, C.M. Rouleau, D.B. Geohegan, and G. Duscher, ACS Nano **9**, 10482 (2015).
[49] A. Naldoni, M. Allieta, S. Santangelo, M. Marelli, F. Fabbri, S. Cappelli, C.L. Bianchi, R. Psaro, and V. Dal Santo, J. Am. Chem. Soc. **134**, 7600 (2012).
[50] M. Lazzeri, A. Vittadini, and A. Selloni, Phys. Rev. B - Condens. Matter Mater. Phys. **63**, 155409 (2001).
[51] H. Cheng and A. Selloni, Phys. Rev. B **79**, 092101 (2009).
[52] H. Cheng and A. Selloni, J. Chem. Phys. **131**, 054703 (2009).
[53] L. Mino, G. Spoto, and A.M. Ferrari, J. Phys. Chem. C **118**, 25016 (2014).
[54] M. Setvin, B. Daniel, U. Aschauer, W. Hou, Y.-F. Li, M. Schmid, A. Selloni, and U. Diebold, Phys. Chem. Chem. Phys. **16**, 21524 (2014).
[55] N. Martsinovich, D.R. Jones, and A. Troisi, J. Phys. Chem. C **114**, 22659 (2010).
[56] A. Vittadini, A. Selloni, F.P. Rotzinger, and M. Grätzel, J. Phys. Chem. B **104**, 1300 (2000).
[57] D. Cho, K.C. Ko, O. Lamiel-García, S.T. Bromley, J.Y. Lee, and F. Illas, J. Chem. Theory Comput. **12**, 3751 (2016).
[58] O. Lamiel-Garcia, K.C. Ko, J.Y. Lee, S.T. Bromley, and F. Illas, J. Chem. Theory Comput. **13**, 1785 (2017).
[59] G. Fazio, L. Ferrighi, and C. Di Valentin, J. Phys. Chem. C **119**, 20735 (2015).
[60] K. Morita and K. Yasuoka, AIP Adv. **8**, 035119 (2018).
[61] S. Bhattacharya, B.H. Sonin, C.J. Jumonville, L.M. Ghiringhelli, and N. Marom, Phys. Rev. B **91**, 241115 (2015).
[62] Z. Qu and G.-J. Kroes, J. Phys. Chem. C **111**, 16808 (2007).
[63] O. Lamiel-Garcia, A. Cuko, M. Calatayud, F. Illas, and S.T. Bromley, Nanoscale **9**, 1049 (2017).
[64] K. Yang, A. Kachmar, B. Wang, N.M.A. Krishnan, M. Balonis, G. Sant, and M. Bauchy, J. Chem. Phys. **149**, 094501 (2018).
[65] G. Seifert, J. Phys. Chem. A **111**, 5609 (2007).
[66] K. Trachenko, M.T. Dove, E. Artacho, I.T. Todorov, and W. Smith, Phys. Rev. B **73**, 174207 (2006).
[67] X. Zhang, H. Gao, and X. Li, Extrem. Mech. Lett. **22**, 131 (2018).
[68] V. Van Hoang, Nanotechnology **19**, 105706 (2008).
[69] J. Houska, Comput. Mater. Sci. **134**, 1 (2017).
[70] N. Baguer, V. Georgieva, L. Calderin, I.T. Todorov, S. Van Gils, and A. Bogaerts, J. Cryst. Growth **311**, 4034 (2009).
[71] D. Selli, G. Fazio, G. Seifert, and C. Di Valentin, J. Chem. Theory Comput. **13**, 3862 (2017).
[72] M. Cargnello, T.R. Gordon, and C.B. Murray, Chem. Rev. **114**, 9319 (2014).
[73] X. Chen, L. Liu, Z. Liu, M.A. Marcus, W.C. Wang, N.A. Oyler, M.E. Grass, B. Mao, P.A. Glans, P.Y. Yu, J. Guo, and S.S. Mao, Sci. Rep. **3**, 1510 (2013).
[74] H. Zhang, M. Finnegan, and J.F. Banfield, Nano Lett. **1**, 81 (2001).
[75] H. Zhang and J.F. Banfield, J. Phys. Chem. B **104**, 3481 (2000).

Part II. Astronomical silicates

Chapter 8: Introduction

Astronomical dust

The study of the universe has its foundation on the light gathered from the sky. Through the light received, the brightness and effective temperature of stars can be determined, and properties such as mass, age or relative motion estimated. It was soon realized though that stars often showed a lower emission than expected in the blue component of light and absorption features in very specific regions of the infrared spectra[1]. This effect, named by the astronomical community as extinction or interstellar reddening, has a dependency on the observed direction in the sky: regions pointing toward the galactic plane and distant objects have smaller emissivity (i.e., larger extinction) than other directions or closer objects. Thus, extinction is caused by something within our galaxy, and not as a consequence of the properties of the interstellar medium (ISM) itself. In addition, evolved stars (i.e., stars in the last stages of their life-cycle) show deviations from black body emission, implying that the mechanism causing the extinction is more prominent in the final stages of stellar evolution. It was later suggested that the extinction was caused by the presence of solid particles: grains of different chemical nature which, upon interaction with light, absorb, scatter and reemit radiation, changing the Spectral Energy Distribution (SED) of the source. Such solid particles have been called dust grains due to their size, which ranges from nanometers to micrometers[2].

Figure 6: Picture of the milky way. Dark patches correspond to obscured light due to dust grains. Photo by Denis Degioanni on Unsplash

Although the density of such particles is very small, the vast distances between stars compensate such low density. The effects of the interaction between dust and light become easily apparent even to the amateur astrophotographer in the dark regions of galaxies like our own Milky Way (Figure 6). It is important to note that interstellar dust has been estimated to reprocess between 30% to 50% of the light in the entire universe[3,4]. A precise knowledge

of the obscuration caused by dust is of uttermost importance if one wishes to accurately determine the brightness and therefore SED of the parent source in order to determine its current state, which in turn is necessary to understand the evolution of the universe.

Although improving our understanding of observational measurements is a good reason on its own to perform research on astronomical dust, this is just one of several reasons which make astronomical dust a very important scientific subject. While obscuration is caused by dust being in between a light source and the observer, light that does not travel towards us also interacts with dust and some fraction of it is reemitted in our direction at a different wavelength. The two possible scenarios are pictured in Figure 7; in one (left), the cloud is irradiated by light which is not traveling towards the observer, but scattered and emitted light does travel toward the observer. In the second (right), the cloud of dust is between the light source and the observer, obscuring the light source. The emission of dust therefore allows us to determine the spatial extent and geometry of dust clouds, providing insights into the physics relating the interactions between stars, dust clouds and the ISM. Absorption and emission of light can also reveal dust properties such as composition, temperature or size. Other heating mechanisms such as gas-grain collisions and reactivity on the surface also increase the temperature of the grains and cause some regions of space to become visible in the IR without the need of a light source. The physical conditions of the ISM can thus be explored by analyzing the dust in it.

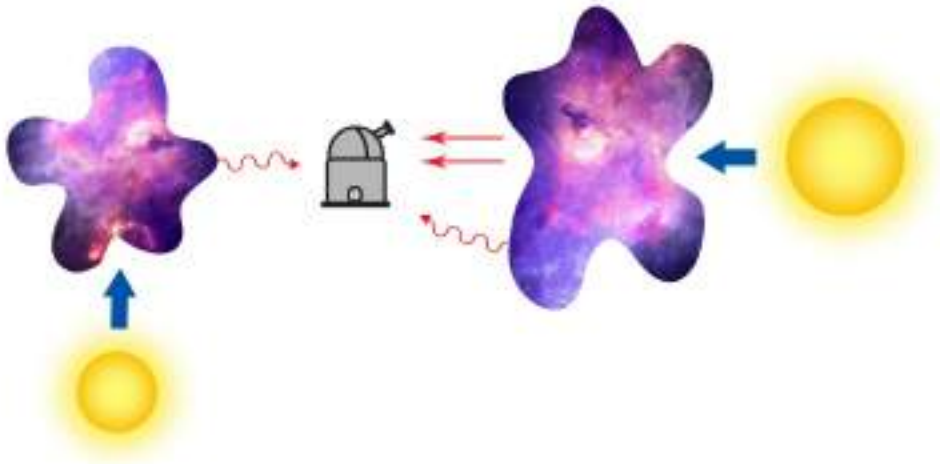

Figure 7. two scenarios showing the interaction of light between a light source and the observer. In the left, the light from a source interacts with the ISM cloud which radiates certain wavelengths in other directions. In the right, the light from the source goes through the ISM cloud, which lowers the intensity and loses part of the high frequency region due to scattering. Blue arrows represent the original light emitted by an object, while red straight arrows indicate the light which has passed through the dust, with a lower component of blue light. Red sinusoidal arrows indicate emission from dust due to absorption of light.

Dust also plays a major role in determining the chemical properties of the ISM, as it is involved in the formation of H_2 as well as the depletion -i.e, disappearance of atomic lines in the UV-vis part of the spectrum, an indication of the removal of free atoms- of heavy elements by condensation into grains[5,6]. Dust also plays a role in the formation and chemistry of molecular clouds, and their evolution into new stars. Since star forming regions correspond to high density zones where collisions between matter are more abundant, dust emission is linked to star forming regions[7–10]. This allows one to characterize the star formation rates for different galaxies, a parameter related to the time a galaxy formed and

even to the overall evolution of the Universe. It is also clear that the early stages of formation of rocky planets, and quite likely also giant planets[11], require seeds of dust particles in order to nucleate and grow[12].

There are also several astrochemical processes in which astronomical dust is relevant. Gas-phase chemical reactions in space are very slow due to the extremely low concentrations of reactants. The low densities have two important effects. Firstly, the reaction rates are consequently very small. Secondly, the reaction yields also suffer from such low densities: the energy generated in combination reactions ($\mathrm{A} + \mathrm{B} \rightarrow \mathrm{AB}$) must be dissipated, otherwise the product will mostly decompose into reactants. The low density implies that the reaction energy cannot be dissipated by inelastic collisions with third bodies, and thus the newly formed molecules dissociate into the parent species. However, if reactants are adsorbed or chemically bound onto dust species, the energy released in the surface reaction can be distributed among the dust grain. This mechanism allows, as previously mentioned, the formation of $\mathrm{H_2}$[13–16]. In the same way, after gas phase species such as $\mathrm{CH_4}$, $\mathrm{H_2O}$, $\mathrm{NH_3}$ or CO are deposited on the surface of grains in the form of ices, complex chemical reactions can take place on the surface of grains or inside the ices after irradiation of UV light, allowing the formation of complex organic molecules[17,18]. Hence, there is great interest in understanding the adsorption of organic species onto dust grains and elucidating if dust itself has a major role in such reactions.

Finally, understanding the formation of dust particles and their chemical and physical evolution throughout their life cycle is a major challenge to current models of nucleation and crystallization. Using classical nucleation theory (CNT), the net dust formation in outflows of dying stars is calculated to be lower than the net destruction of dust in the ISM[19,20]. These theoretical results are in clear contradiction with observational evidence of dust in interstellar space and highlight the need to find new formation pathways or a revision of the models used in calculating dust formation rates.

In summary, dust is present everywhere in the universe, and understanding its properties and its interaction with various environmental factors such as electromagnetic radiation and gas phase molecules is paramount in order to describe processes such as how planetary seeds are formed, the conditions found in different astronomical environments, or even to understand large scale processes such as star formation at different stages of the universe.

The stellar and dust life-cycle.

The life cycle of stars and dust are intimately related. An overall view of both cycles helps understand why dust is related to such a large number of astronomical environments, provides clues of where we should detect dust and which are their most likely compositions. It is also important to know the different classes of stellar objects as these are classified (among other things) as a consequence of their stage in the stellar life-cycle and their current path (which depends on its mass). Finally, knowledge of the stellar life-cycle also provides an understanding of the actual feasibility of observing and studying certain events related with the formation and destruction of dust.

Figure 8 provides a summarized scheme of the stellar life-cycle. Stars are formed from the collapse of clouds of gas. Under the approximation of a homogeneous spherical cloud of gas, the Virial theorem states that the kinetic energy (K) is equal to half the potential energy (U) if the matter is under thermodynamic equilibrium:

$$K = \frac{1}{2}U \quad (41)$$

If the kinetic energy is less than half the potential energy, the cloud of gas is said to be under gravitational collapse, causing its shrinking and the formation of proto-stars. Under more realistic conditions, i.e, inhomogeneities caused by differences in density of several regions or the interplay between magnetic-fields and cloud matter, the cloud will give rise to hundreds of proto-stars, where the temperature of each of this proto-stars will increase due to the increase in kinetic energy and pressure. Stellar objects in their early phase can be classified in several categories with respect to different properties, where mass is one of the most important. Two classes of stellar objects are important in this stage: T-Tauri stars and Herbig stars. T-Tauri stars are low mass objects that lay in the transition between stars shrouded in dust and main sequence stars (i.e, stellar objects where H fusion is the main source of energy). The lifetime of this stage of stellar evolution is of the order of 10^7 years, and, as a consequence of the dynamics of stellar formation, they have mass loss rates of 10^{-8} solar masses ($M_\odot$) per year. On the other hand, Herbig stars are the high-end masses of T-Tauri stars. Their lifetime is shorter, between 10^6 and 10^4 years.

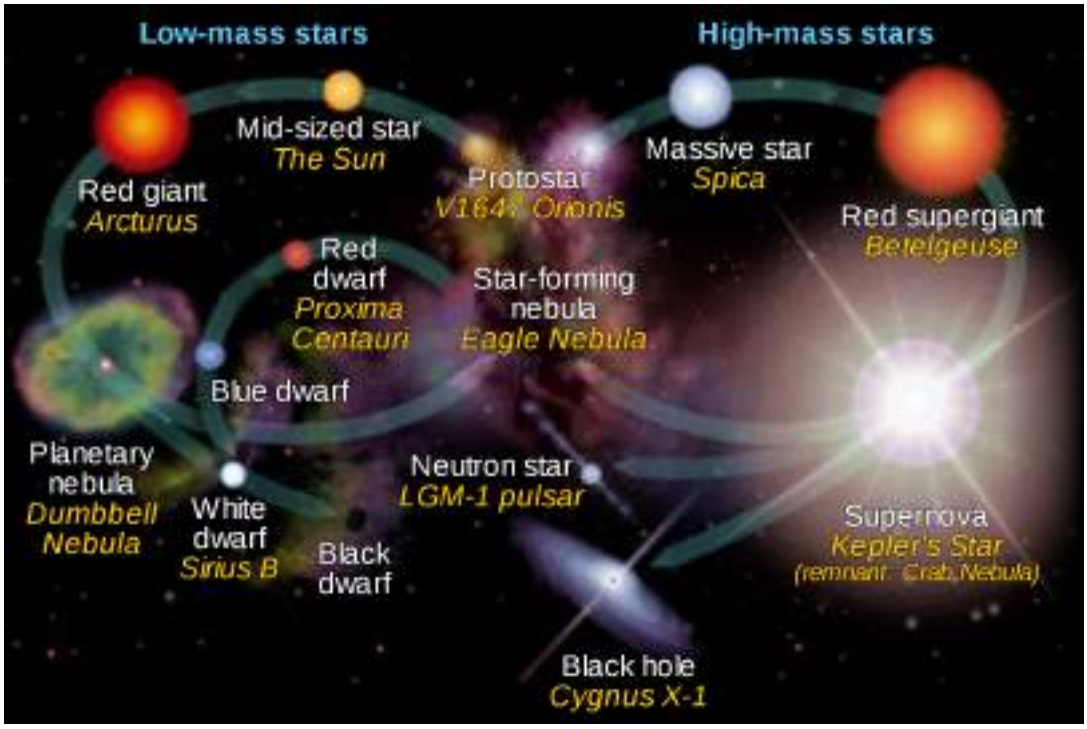

Figure 8. Schematic overview of stellar evolution for low mass and high mass stars with examples. From Wikipedia, by cmglee based on an original image from NASA Goddard Space Flight Center

Once the burgeoning star's temperature is high enough, nuclear reactions will start to take place, with H fusion becoming the major energy source. At this stage, the star is said to be in its main sequence phase.

Along the main sequence, stars are in hydrostatic equilibrium, meaning that the force of gravity is counteracted by the outward pressure fueled by fusion reactions. In this static picture, the structure of the star is described by the following set of equations:

$$\frac{dP}{dr} = -G\frac{M_r\rho}{r^2} \qquad (42)$$

$$\frac{dM_r}{dr} = 4\pi r^2\rho \qquad (43)$$

$$\frac{dL_r}{dr} = 4\pi r^2\rho\epsilon \qquad (44)$$

$$\frac{dT}{dr} = -\frac{3}{4ac}\frac{\bar{\kappa}\rho}{T^3}\frac{L_r}{4\pi r^2} \qquad radiation$$

$$-\left(1-\frac{1}{\gamma}\right)\frac{\mu m_h}{k}\frac{GM_r}{r^2} \qquad (45) \qquad convection$$

The previous idealized set of differential equations describe the pressure (42), mass (43), luminosity (44) and temperature (45) gradients as a function of stellar radius and shows how they are interconnected. From these equations, the Vogt-Russell theorem arises, which states that the mass and composition structure determine the radius, luminosity and internal structure, as well as the evolution of the star.

Although the model has several limitations, it serves as a tool to understand several properties of the star. For instance, the amount of mass determines the rate at which stars will consume its energy, since a larger mass will require a larger pressure coming from the nuclear fusion reactions. As a consequence, massive stars have lifetimes orders of magnitudes shorter than low-mass stars. The lifetime range of main sequence stars can vary from 10^6 years to $5{\cdot}10^{11}$ years. Luminosity and radii are, equivalently, larger for more massive stars. The mass loss rate during this stage of stellar evolution is 10^{-14} $M_\odot/yr$, confirming that through their lifetime stars are effectively static.

Another result of the previous equations is the radial structure of the star. Three main regions dominate the star structure: the core, where H fusion is happening, and the radiative and convective zone, which as the name suggest are characterized by the energy transport mechanism.

Once H fusion is no longer occurring at the core of the star, the core will contract and release potential energy to the outer shells, causing its expansion and a decrease of the effective temperature. This process generates a shell of H fusion surrounding the core, now mainly composed of He. Several processes involving changes in the composition and reignition of layers of H and He fusion causes an even larger expansion of the star and a drop in effective temperature. This brings the star to a stage known as the Asymptotic Giant Branch (AGB), which corresponds to the Red Giant label in Figure 8. During the AGB stage, the structure of the star is described as a shell of Helium fusion, a shell of Hydrogen fusion, an envelope with non-ionized H and He and a core composed of Carbon/Oxygen, with no fusion reactions taking place. The H shell expels mass at an estimated rate between 10^{-7} to 10^{-4} $M_\odot/yr$, which depends on further considerations of the evolutionary stage inside the AGB period. The estimated lifetime of this evolutionary stage is of the order of 10^7 years

and finishes with the formation of a white dwarf and ejection of the remaining shell[21,22]. This phase is called the post-AGB phase. The ejected matter from the stellar envelope will loose its gravitational binding to the star and will travel through the ISM, where eventually will form a new star-forming nebula and start the cycle again.

While the main sequence stars do not eject large quantities of mass through their life, and therefore don't contribute to the return of mass to the ISM, the initial and final stages of star formation (Herbig/T-tauri stars and AGB/post-AGB respectively) contribute to the return budget. Young stellar objects form circumstellar shells that accrete and form protoplanetary disks, and the real estimate of dust return varies from 0.33-0.1 of the accreted material. Hence, the main contributors to the presence of dust in the ISM are thought to be AGB stars and supernovae (i.e., the explosion of a massive post AGB-star)[23]. It must be noted that the initial and final stages of stellar evolution represent 1% of the total evolutionary time of the stellar cycle, which make it less abundant to observe, as can be seen in Table 1. As a consequence, the number of observable stars in such stages is low, and observational data of the processes occurring in such stages is scarce.

Evolutionary stage	Number of entries	Percentage of population
Herbig	151	0.004 %
T-Tauri	3278	0.095 %
AGB	2737	0.089 %
Post-AGB	306	0.009 %
Total star entries	3.442.662	

Table 1. Population of stellar objects relevant to this thesis extracted from the Simbad astronomical database (http://simbad.u-strasbg.fr/simbad/)

The link between stellar death and new star forming regions is the ISM. It is important to note that the ISM is far from being a homogeneous medium. Rather, current theories assume that the ISM can be divided in five different phases: molecular medium (MM), cold neutral medium (CNM), warm neutral medium (WNM), warm ionized medium (WIM) and hot ionized medium (HIM). The main differences between phases correspond to density and strength of the radiation. In terms of density, the variations are as large as $10^3\ \mathrm{H/cm^3}$ in the MM to $10^{-3}\ \mathrm{H/cm^3}$ in HIM. The radiation causes the ionization fraction to vary from non-ionized material in the MM to highly ionized metal elements in the HIM.

Due to different processing mechanism, dust is theoretically expected to be amorphized an destroyed in a time period of $5{\cdot}10^8$ million years, while the replenishment rate is calculated to be $2.5{\cdot}10^9$ million years[19,24,25]. As observation shows the presence of dust in the ISM, the faster destruction rate with respect to replenishment rate seems contradictory. While it has been suggested that dust may grow in the ISM, it is clear that a complete picture of the processes involving dust growth, destruction and formation is still missing.

Nature of dust.

As mentioned in the previous section, AGB stars and supernovae are thought to be the main source of dust in the universe. The conditions of stellar atmospheres are, nevertheless, very harsh for the formation of grains and molecules: the temperature of the outer envelope of AGB stars varies from 10,000 K at the most internal region to 10 K at the most external, where the border with the ISM lies[26]. Simultaneously, pressure also drops significantly, and thus in the region in which temperature is near to 1,000 K the pressure is within the range of 10^{-7} to 10^{-10} bars. Under such environment, only extremely refractory grains -i.e., materials showing great thermal stability and thus strong bonding- can be formed with adequate rates. A first guess of the possible condensates in such environments can be made by using elemental abundances. Table 2 shows the elemental abundances of our sun as reported by Asplund et al[27]. Although the chemical composition changes within the stellar phase and quite likely from source to source, it is expected that the abundances are within similar orders of magnitude among main sequence stars, as well as in the initial stages of AGB stars. From Table 2, the elements with higher abundancies capable of forming refractory materials are C and O, which can form carbonaceous or oxide dust respectively. The nature of the carbonaceous dust is thought to be amorphous material -soot and polycyclic aromatic hydrocarbon (PAH)-, while oxides can be formed of a variety of elements. Again, arguments based on abundances point out that the most copious oxides should be silicates of either Fe or Mg nature.

Element	Solar System abundance
H	$9.09 \cdot 10^{-1}$
He	$8.51 \cdot 10^{-2}$
C	$2.69 \cdot 10^{-4}$
N	$6.76 \cdot 10^{-5}$
O	$4.90 \cdot 10^{-4}$
Mg	$3.98 \cdot 10^{-5}$
Al	$2.82 \cdot 10^{-6}$
Si	$3.24 \cdot 10^{-5}$
Fe	$3.16 \cdot 10^{-5}$
Ti	$8.91 \cdot 10^{-8}$

Table 2. Solar system elemental abundances. It is assumed that, overall, elemental abundances in the sun are similar to other stars and ISM[27]. In astrophysics, the H abundance is referred to X, the He abundance to Y, and the rest of elements as Z, a value also known as metallicity.

Several evidences confirm the composition and presence of both families of dust particles. Two major indications are spectroscopic evidence obtained from observation and the composition of meteors. However, carbonaceous and silicate dust are not expected to form simultaneously. C and O primarily form carbon monoxide due to its very large binding energy of 11.14 eV, which is of the same order of the $\mathrm{N_2}$ molecule and larger than any

precursor to silicate or carbonaceous dust[28]. Formation of CO is much more favorable than either family of dust and thus the less common element of the population of C and O atoms is expected to be completely locked into CO. Therefore, AGB stars will form different kinds of dust according to their composition: carbon rich (C-rich) stars will produce carbon dust, and oxygen rich (O-rich) stars will produce silicate dust. Stars that have O/C ratios ~1 mainly produce SiC grains.

The theoretical prediction of the most abundant dust compositions is supported by observational evidence. Careful analysis of the spectra of AGB stars, regions of the ISM and young stars show features characteristic of both types of grain both in the UV and IR regions. Table 3 provides a list of the strongest emission and absorption features and their corresponding dust assignments. A corresponding IR spectrum obtained from observations toward the center of the galactic plane is shown in Figure 9. The wavelength/frequency of the IR signals correspond to the average wavelength/frequency of the features, as changes in the dust composition shift the wavelength/frequency of the peaks to slightly shorter or longer values.

Wavelength	Frequency	Assigned to
217.5 nm	$1.38 \cdot 10^{15}$ Hz	Carbon/aromatic dust
3.1 μm	3226 cm^{-1}	Ices
3.4 μm	2941 cm^{-1}	Carbon/aliphatic dust
6.2 μm	1492 cm^{-1}	PAHs
7.7 μm	1299 cm^{-1}	PAHs
8.6 μm	1163 cm^{-1}	PAHs
9.7 μm	1031 cm^{-1}	Silicate dust
11.3 μm	885 cm^{-1}	PAHs
18 μm	555 cm^{-1}	Silicate dust

Table 3. Spectroscopic features in wavelength, frequency and their corresponding assignment. PAH is the acronym for Polycyclic Aromatic Hydrocarbon.

The IR signals reported in Table 3 are mainly associated with stretching and bending modes of C-H and Si-O bonds. These IR bands are generally quite broad, especially for the silicate features, therefore implying that it originates from non-crystalline dust. While the previous features are the most prominent, crystalline silicate dust has also been detected in several environments[29–31].

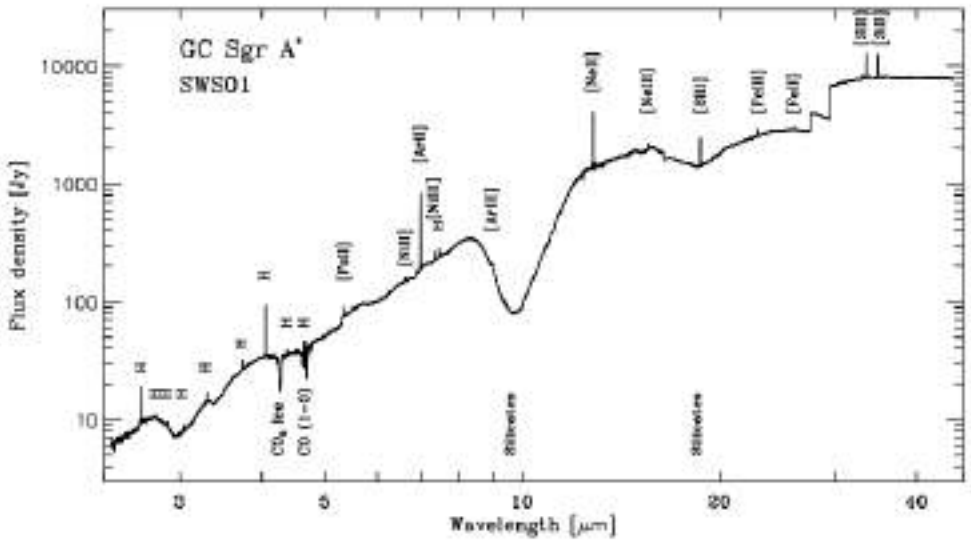

Figure 9. IR spectrum obtained by IRAS from the galactic center (GC). Emission by atomic features are seen as spikes and labelled according to its origin, while absorption due to dust grains and ices correspond to large dips in the spectrum.

General silicate structure

Silicates constitutes the largest family of minerals, where the main structural unit is the silicate tetrahedron $[\mathrm{SiO_4}]^{4-}$, with cations counteracting the silicate tetrahedron charge. The semi-covalent nature of the Si-O bond[32] allows the silicate tetrahedrons to polymerize in a sizeable number of ways, and thus allow a great diversity of crystalline materials. The classification of silicate minerals is based on the degree of polymerization/structure of the silicate tetrahedrons, as can be seen in Table 4.

Major group	Structure	Silicate chemical formula
Nesosilicates	Isolated tetrahedron	$[SiO_4]^{4-}$
Sorosilicates	double tetrahedra	$[Si_2O_7]^{6-}$
Cyclosilicates	Rings	$[Si_nO_{3n}]^{2n-}$
Inosilicates	Chains	$[Si_nO_{3n}]^{2n-}$ or $[Si_{4n}O_{11n}]^{6n-}$
Phyllosilicates	Sheets	$[Si_2nO_{5n}]^{2n-}$
Tectosilicates	3d Frameworks	$[Al_xSi_yO_{(2x+2y)}]^{x-}$

Table 4. Classification of Silicate groups according to the polymerization of the silicate units

For each of major group, several sub-groups exist according to the particular crystal structure, which is determined by the cation that compensates the silicate charge. Fe and Mg are the main elements adjoint with silicates in astronomical environments. Both are divalent cations and have similar cationic radii. Hence, silicates of both metals share the same crystalline structures and can be exchanged in their corresponding minerals by the other cation, therefore forming near ideal solid solutions[33,34] (i.e., the energy of substituting $\mathrm{Mg^{2+}}$ by $\mathrm{Fe^{2+}}$ or vice versa is linear with respect to the concentration of either element in the crystalline system). As a consequence, genuinely pure Mg or Fe silicates are not common in nature and normally contain a large fraction of the other element. Thus, in

general, silicate stoichiometry is better represented by $A_{2-x}B_xSiO_4$ or $A_{1-x}B_xSiO_3$, with A and B being either Fe or Mg.

The most abundant crystalline systems of Mg and Fe stoichiometries contain either isolated tetrahedrons (nesosilicates) for the C_2SiO_4 stoichiometry or chains of tetrahedra (inosilicates) for the $CSiO_3$ stoichiometry, with $C = Mg/Fe$. The C_2SiO_4 composition forms the Olivine group, which has an orthorhombic crystalline structure with the Pbnm space group. Wadsleyite and ringwoodite are polymorphs of the olivine stoichiometry found in meteors and shown to exist in high-pressure regions such as the Earth mantle. The Mg-rich olivine is called Forsterite (Fo) while the Fe-rich olivine is called Fayalite (Fa). As previously mentioned, olivine generally appears containing a substantial fraction of Fe and Mg in either of the "pure" mineral species. A representation of the Olivine structure is displayed in Figure 10 A.

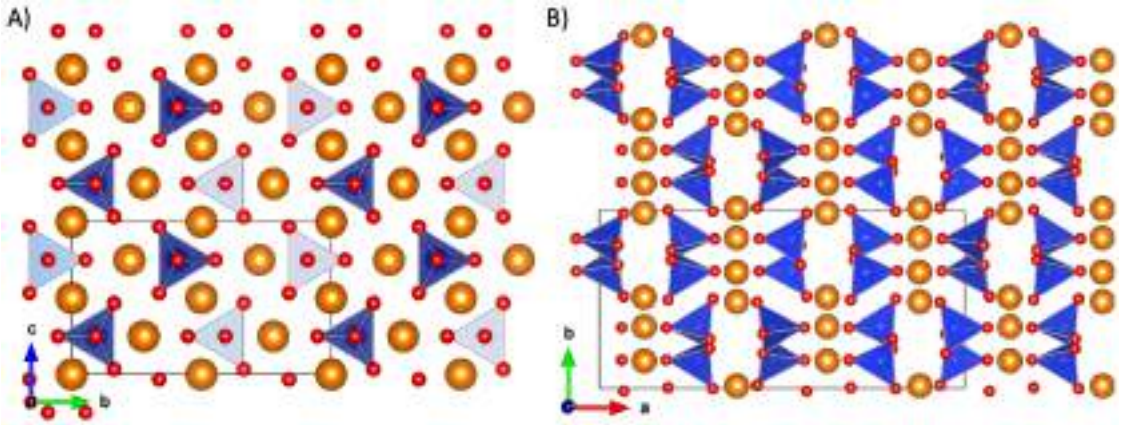

Figure 10. Crystal structures of Olivine (A) and Pyroxene (B), with $[SiO_4]^{4-}$ tetrahedrons in blue, oxygen atoms in red and divalent cations in orange.

On the other hand, the $CSiO_3$ composition forms the Pyroxene group. The Mg-rich end member is called Enstatite (En) while the Fe-rich end member is called Ferrosilite (Fs). Three different polymorphs are largely abundant: two orthorhombic crystal structures with groups Pbca and Pbcn and a monoclinic crystal structure with the space group $P2_1/c$. The ortho-En is the most abundant of the three polymorphs. A representation of the Pyroxene crystal structure can be seen in Figure 10 B.

The exact structure of astrosilicates remains unknown. As pointed out in the previous section, the silicate dust IR bands are attributed to amorphous material due to the broadness of the bands. An accepted definition of amorphous material is given by S.R Elliot, which defines amorphous as a structure that lacks long range order[35]. Glasses are a subset of amorphous structures and are defined as "an amorphous solid which exhibits a glass transition". While silica (SiO_2) generates amorphous structures with ease, the addition of Mg in the structure lowers the ability of the silicate structure to form amorphous states, as described in Zachariasen's theory of glasses[36]. Even when En can form glasses with ease, the large Mg:Si ratio in Forsterite suggested that it could not form glasses. Amorphous materials with the same overall composition of Mg_2SiO_4 were synthesized in 1982 by Nuth et al.[37] by evaporation of Mg and SiO at a temperature of 750K. However, such amorphous particles showed at least some degree of segregation with MgO regions, pure Si and

Mg_2SiO_4 phases. To distinguish such an inhomogeneous particle with a hypothetic pure Mg_2SiO_4 amorphous state, the term silicate-smoke was coined. Some years later, other techniques were devised which allow for a better synthesis of glassy Mg_2SiO_4 samples, based on ion bombardment, ultra-rapid cooling of silicate melts, sol-gel synthesis or vapor deposition of gas-phase precursors[38–41]. However, a small variety of subtle physical-chemical properties such as porosity, compactness of the sample, homogeneity or hydration, some of which arise naturally from the synthesis technique, have an impact on the resulting IR spectra. Therefore, while the IR spectra of amorphous silicates are very similar, small differences with respect to peak positions and broadness of the peaks highlight differences in the physical structure of the samples. Such differences are not easily measured with standard characterization techniques due to the small size of the samples used (between 10 to 100 nm)[42,43]. While we will refer to all the different samples by amorphous material, one must bear in mind that their structure is not clearly determined. Without an understanding of the structure it is not possible to evaluate further properties such as kinetics of growth, adsorption or crystallization.

State of the art into the research of astrosilicates.

As mentioned before, the typical silicate IR features appear at both 9.7 and 18 μm. These silicate IR features, as present in AGB stars, were fitted in 1996 using laboratory spectra from Mg-rich amorphous material of olivine composition[44]. The amorphous material in the ISM was thus determined to likely be of olivine stoichiometry, but in this case, with a quite large contribution of Fe of around 50%[45–47]. Nevertheless, different Fe/Mg ratios can result in similar spectra due to particle effects such as porosity and shape. Thus, pure Mg compositions can also fit the ISM spectrum. In addition, the shape of the 9.7 μm silicate feature is not constant throughout the entirety of the ISM, which suggests slight differences at different phases of the ISM[48]. Finally, IR spectra of Herbig stars are best fitted with Mg-pure amorphous silicate spectra as the main component[49]. Therefore, although silicates are clearly the source of one of the most prominent signals in the IR spectrum of most ISM environments, there is still wide discrepancies on the exact composition and nature of astrosilicate dust particles. This problem arises as amorphous structures can exhibit a great degree of variation in shape, structure and composition that allows one to fit the same IR spectrum with quite different grain types.

With space telescopes such as Spitzer, accurate measures in the far-IR have also revealed some crystalline dust, including crystalline olivines and pyroxenes in circumstellar shells. The 69 μm and 40.5 μm features, which respectively serve to identify olivine and pyroxene crystals, also allows one to partially determine the Fe content of such crystals[50]. From IR analysis it can be concluded that the observed crystalline astrosilicate dust particles are mainly Mg-rich silicate crystals which contain ~15% of the silicate dust mass[30,51,52]. Herbig stars possess similar features as AGB stars, but they can reach higher crystallinity levels of up to 36% (see the entry for HD179218 in table 9 from Juhasz[49]). In the ISM however, no crystalline IR features have been observed, placing upwards limits to the presence of silicates in the ISM of less than ~3%[53]. The difference in the degree of crystallinity between AGB stars and the ISM provides evidence of the dust processing in

the ISM, and two possible mechanisms have been proposed: 1. Complete destruction and reformation of amorphous material[54], or 2. Amorphization of the dust grains by low energy ions[55] or high-energy cosmic rays[56].

Theoretical work on the nucleation and growth of silicates in AGB envelopes was started by Gail, Sedlmayr and Ferrorati. Based purely on thermodynamic arguments of bulk crystalline samples and a simple model for the description of the physical state of AGB stars, their work shows the preferential condensation of forsterite in the circumstellar shells of AGB stars[57,58], even if the Mg/Si ratio is largely displaced toward Si[59]. The main outcomes of such modelling are the predicted proportions of different chemical species and their grain size, assuming the particles are of spherical shape. Overall, the models show that the formed grains should stop growing at radius between 0.04 to 0.14 μm (thus, in the NP regime), with differences related to the chemical stoichiometry. At such sizes, the radiation pressure from the star causes the ejection of the NPs from the star atmosphere[60,61]. Still, a variety of results can be achieved by changing input parameters of the model, such as gas density of elements in the stellar wind, effective temperature of the star, and more importantly, sticking coefficients (i.e, the ability of an incoming atom/molecule to be adsorbed on the surface of a grain[62]). However, an important requirement of the models is the presence of seed nanoclusters of 1nm in radius. The true nature of the seed nanoclusters is still not clear. The main candidates for seed nanoclusters are TiO_2 and Al_2O_3[63], as these compounds are very refractory, and the elemental abundances are large. Surprisingly, observational evidence seems to indicate that TiO/TiO_2 nanoclusters/gas-phase molecules are detectable through a wide range of distances from the parent star, with the amount of Ti trapped in nanoclusters accounting for almost the entirety of Ti[64]. As astrosilicate dust must condensate in the vicinity of the star, the long-range presence of Ti nanoclusters discard it as a seed for astrosilicate dust. Observation of Al-compounds and their distributions seem more in line with the expected distributions if Al-compounds are indeed precursors to astrosilicate dust grains, but clear evidence is still lacking[65]. In addition to these two species, atomistic modelling has shown that the nucleation of silicate nanoclusters is feasible if the precursor $(SiO)_2$ species can be formed[66], highlighting the need to incorporate *ab initio* computed data for nanoclusters of the involved species in order to clearly determine the different routes by which dust can be formed.

While the objective of the former theoretical approaches was to determine the nucleation conditions and rates of astrosilicate NPs, other theoretical approaches are used to describe the physical properties of dust grains. While IR absorption allows one to determine the composition of the dust grains, the UV-vis scattering and the polarization at different wavelengths allows one to introduce constraints on the size and shape of the dust NPs. Using the optical constants of bulk silicates, Mie theory allows one to extrapolate the spectral properties down to the nanometer regime. Using such approximations, Weingartner, Li and Draine[67,68] computed the size population of different grains, providing estimates of up to 20% of the Si elements in nanoclusters with radius below 1.5 nm. It must be noted, however, that Si depletion varies largely along different regions of the ISM -see Figure 2 of the review by Jones[6]-.

The shape of silicate particles is important in the selection of the model used to reproduce the IR spectrum of the dust particles[50,69]. Dust shape is also responsible for the polarization of the received starlight[70], and thus proposed grain models need to adequately fit such observable characteristics. Assuming spheroidal shapes -i.e, two axes being equal in length-, the possible values of axial to equatorial ratio which fit the observed polarization ranges from 3[71] to 1.3[72].

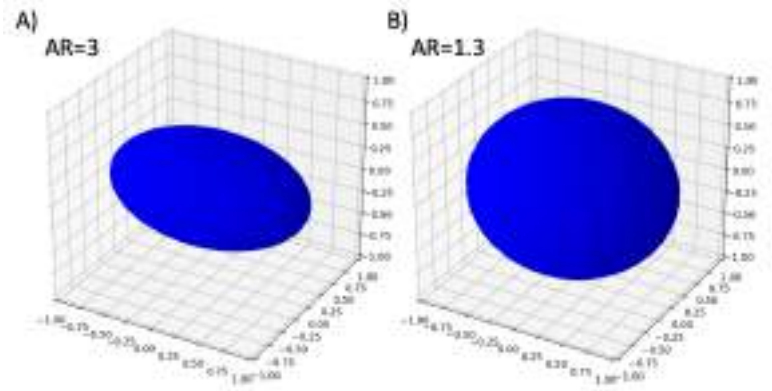

Figure 11. Ellipsoids with aspect ratios (AR) of 3 (A) and 1.3 (B), corresponding to the theoretical shapes of astronomical silicates as obtained from polarization constrains.

The importance of nanosilicates.

Nanoscale and sub-nanoscale silicates are gaining attention in the astrophysics community. The relatively large population of "ultrasmall" dust particles (i.e., nanoclusters and NPs) mentioned before is thought to play a role in the heating of the ISM due to photoelectric emission[67,73]. Thanks to their large surface to bulk ratio, their absorption and scattering cross-sections are much larger than their corresponding bulk materials[74], and thus their interaction with free electrons and other particles is more efficient. In the work of Weingartner and Draine[67], the ionization potentials (IP) and electron affinities (EA) are approximated from bulk parameters for a series of sizes ranging from 5 Å to 1.5 nm in radius. From such parameters, the charged state of the nanoclusters as well as the heating due to incident light was evaluated and its importance to some astronomical environments assessed.

While the top-down methodology used to extrapolate the IP and EA properties is useful as a first order approximation, such electronic properties are prone to be dependent on the detailed atomic/electronic structure of the silicate material down to the nanoscale. The large surface contribution at such sizes means that the properties will be governed primarily by surface effects, and thus bulk extrapolations could be misleading[75]. One of such properties is the IR spectra. Current estimates of the amount of silicate nanoclusters and the amount of crystalline silicates in the ISM is based on the extrapolation of the bulk optical constants by means of Mie theory. The large fraction of surface at the nanoscale cause a deviation of the environment from the ideal bulk case, and thus the force constants on each atomic center will not be the same as in the bulk case. Consequently, the IR spectrum should differ. The size limit at which the IR spectrum of a nanocluster will correspond to that of a bulk sample is unknown.

Silicate NPs and nanoclusters can also be present in the atmosphere of some astronomical objects. Brown Dwarfs -i.e., stellar objects with masses between 0.08 and 0.12 $M_{\odot}$, unable to undergo nuclear fusion- show a colour change in the range of temperatures between 1100K and 1400K, known as the L-T transition. The formation of clouds is the main candidate to explain the colour transition[76]. As in AGB stars, the temperature conditions suggest that the main condensates should be silicates or iron. Yet, the pressure conditions are very different: from 10^{-4} to 10 bars in Brown Dwarfs, -around 10^{-7} for AGB stars-, and thus the structures and compositions are expected to differ from ISM silicates. Another important feature that has been recently related to astrosilicate nanoclusters is an unidentified signal in the microwave region -300 MHz to 300 GHz- of the electromagnetic spectrum. The Anomalous Microwave Emission (AME) refers to an emission feature observed in most ISM environments which appears between 10 to 60 GHz and was first detected as early as 1960. The AME is correlated with the presence of dust[77–79] and therefore dust is regarded as the most likely carrier for such emission. Since the models for AME emission requires particles with radius ranging from 7 Å to 10 nm, the original models relied on PAHs as the most important source of the AME, as PAHs are thought to be the most abundant particles with a molecular size. Yet, further research has recently shown that the intensity of PAHs is not well correlated with AME intensity[80], casting doubts on PAHs as the source of the AME. Since then, silicates have gained attention as likely carriers of the AME emission[81,82]. However, to establish the carrier of the AME it is necessary to know the dipole moments of the parent species. Up to date, no experimental or computational determination of the dipole moments of silicate nanoclusters has been available, and the role of nano-silicates in the AME emission is still under debate.

It is clear that understanding silicate nanoclusters is crucial to further enhance our knowledge of the universe, as they are likely to provide new ways to measure the physical state of a wide range of astronomical objects. Computational chemistry can play an important role in such feat, as several techniques allow to obtain structures in the nano-meter size regime. For the smaller nanoclusters, GO can provide reliable low energy structures based on internal energy. The GO technique can also provide a wide range of isomers which allows one to explore the variations that a given property could have if a range of structures is chosen instead of the lowest energy structure. For the NP regime, faceted particles possessing known bulk crystal structures can serve as a starting point to explore the potential energy landscape by means of thermal annealing. Having reliable structures, properties such as dipole moments -which determine the microwave emission and intensity-, IR spectra and free energies can be computed. Thus, computational chemistry can in principle determine which are the most likely structures for astrosilicate nanocluster and NP species, the observable properties of such particles, and allow us to understand the astronomical environment in which the particles are found. This part of the thesis aims to provide a solid knowledge on the physical properties of astrosilicates as obtained from accurate computational methods, with emphasis on the importance such properties have on our knowledge of astrosilicates in space. Solid evidence is presented in favour of nanosilicates as the main source of AME.

Chapter 9: Objectives

As seen in the previous chapter, silicate NPs and nanoclusters have important roles in a wide variety of environments (ISM, circumstellar shells of both post-AGB stars, young stars, etc) and are likely candidates for several signals in the electromagnetic spectra (e.g. AME). Laboratory measurements of such clusters/NPs is, up to now, still unachieved, and thus properties such as optical constants, dipole moments, IPs or EAs are being derived from top-down models.

Thus, in the present part of this thesis we want to provide a foundational computational study of Mg-rich silicate nanoclusters/NPs with the purpose to serve as reference data for astrophysics research by providing ab-initio determined properties of Mg silicates as well as to provide structures for further investigations. We focus our interest on stoichiometric pure Mg silicate particles $\mathrm{MgSiO_3}$ for pyroxenic stoichiometry and $\mathrm{Mg_2SiO_4}$ for olivinic stoichiometry containing from tens of atoms up to thousands of atoms. Such particles have sizes of several nm in diameter.

In detail, the objectives of this part of the thesis are:

1. Determine/derive the most appropriate IP to perform extensive and accurate GO.
2. Obtain reliable low energy global minima candidate structures for Mg-pure (i.e, $\mathrm{Mg_2SiO_4}$ and $\mathrm{MgSiO_3}$) silicates of sub-nm size.
3. Obtain reliable low energy candidate structures for olivinic stoichiometry NPs with diameter between 1 to 5 nm.
4. Describe the structural properties of such silicates and compare them to their most stable bulk phase.
5. Identify particularly stable structures (i.e. “magic” clusters) that could become good candidates to direct astronomical observations in order to confirm the presence of such nanoclusters.
6. Evaluate whether bulk crystal structure is thermodynamically favoured at the nanoscale.
7. Provide spectroscopic data that can be used to unequivocally detect nanoscale silicates in astronomical environments.
8. Determine whether astrosilicate nanoclusters can indeed be an important source for the AME.

Chapter 10: Structure and Properties of Nanosilicates with Olivine $(Mg_2SiO_4)_N$ and Pyroxene $(MgSiO_3)_N$ Compositions

Introduction

The presence of silicate grains of large sizes is demonstrated by their absorption/emission features in the IR spectrum in a wide range of astronomical environments[31,49,83–85]. The size of such silicate structures can be extrapolated by fitting the light extinction curves with models of dust having a certain size distribution[2,86]. Using the experimental optical constants from different laboratories[44,55,87] and applying Mie theory, the observational IR curve can be fitted considering the particle size as a parameter. The fitting predicts particle sizes from 0.1 μm to 0.005 μm. Since the population density of particles results also from the fitting, the depletion of Si can be traced. The results suggest that almost the entirety of Si is trapped in dust in the cold regions (MM, CNM) of the ISM, assuming that the ISM has a similar composition to our Sun[88].

After the proposal of PAHs as likely carriers of the IR features appearing at 3.3, 6.2, 7.7, 8.6 and 11.3 μm, research has focused on trying to find out the population of such equivalent nanoclusters for astrosilicate dust. The lack of observed signatures of silicates in some regions of the interstellar medium led to the conclusion that astrosilicate nanoclusters were not present in the diffuse interstellar medium[89]. However, further research suggested that astrosilicate nanocluster signatures could be hidden under the large PAH features. In such scenario, a fraction of up to ~15%[68] of the total Si budget could be hidden in astrosilicate nanoclusters if their radii is <1.5 nm. Such conclusion was reached after using experimental optical constants of large grains to extrapolate the IR spectrum of crystalline and amorphous nanoclusters. After computing the IR emission of such nanoclusters, the population limit is determined by not allowing the emission to surpass the observed intensity. While the previous argument does not prove the existence of such small silicates, the fact that silicate dust is largely abundant with reasonable sizes in most sightlines, but almost completely disappears in certain environments is a strong proof of the processing, destruction, and regrowth of silicate grains, which can justify the large presence of astrosilicate nanoclusters. Moreover, the regrowth of silicates in the ISM requires a nucleation route in cold environments. Modelling of such growth is being carried out using binding energies extracted from bulk parameters, but a fair modelling of the growth requires the binding energies of the nanometer species[90,91].

In addition to the destruction processes in the ISM, the formation of silicates in AGB stars is a likely source of freshly generated astrosilicate nanoclusters. Again, large grains of silicates are easily detected through their IR signatures and UV extinction. While thermodynamic arguments and computational models of the structure of AGB stars clearly allow the formation of such silicates, they require seeds where deposition of parent species -i.e, Mg, SiO, and H_2O- allow the growth of silicates. Typically, Al_2O_3 or TiO_2 are generally thought to be the primary seed condensates, but computational chemistry methods have shown that silicate nanoclusters of $Mg_2Si_2O_6$ (P-2) can indeed form steadily and apparently grow in a barrier less manner, at least for a couple of monomeric additions[92,93]. The only

requirement is the formation of the Si_2O_2, whose mechanism of formation has not yet been demonstrated.

The understanding of both grain formation and destruction in the ISM can be further enhanced by computational chemistry research. Deriving the amount of nanoclusters and NPs in the ISM using properties of bulk materials may be erroneous. The proportion of surface atoms in such small clusters is very large, and thus their properties will not correspond to those of bulk materials. The presence of defects and surface reconstruction will affect the bond lengths and angles, and thus modify the IR spectra. The IR spectra of nanoclusters of sizes of up to approximately one hundred atoms can be calculated by *ab initio* methods and thus, if realistic structures are available, IR spectra of astrosilicate nanoclusters can be evaluated and compared to previous assumptions. In terms of the formation of silicates in AGB stars, research requires a number of advances in order to confirm that silicate growth is actually feasible: (i) kinetic models must prove that the growth continues unhampered until nanoclusters of large sizes, (ii) the growth rate must allow one to reach macroscopic particles at the observed rates and (iii), since the observational spectra is fitted with olivine particles, a formation route to the olivine stoichiometry is required.

With respect to nanoclusters, all the previous points require to obtain reliable structures for both olivine and pyroxene stoichiometries. Some authors have already published some structures for these species, but the methodology and objectives of these works is not adequate for understanding astrosilicate nanoclusters. In the work performed by Woodley[94], the main objective was to evaluate a Global Optimization algorithm, and thus the reported structures are not optimized with *ab initio* methods but rather correspond to the directly obtained structures from the GO with the use of IPs. On the other hand, the work of Lazzati et al.[95] did perform DFT optimizations after the GO, but only focused on the olivine stoichiometry. The structures proposed by the two papers are quite different among themselves. Figure 12 shows as an example the structure of $(Mg_2SiO_4)_7$ of both works. The structures shown by Lazzati et al.[95] are segregated structures where a SiO_2 skeleton of completely linked $[SiO_4]^{4-}$ tetrahedra takes the central position, and low coordinated Mg^{2+} cations are grouped around the SiO_2 skeleton in a sandwich-like manner. On the other hand, the structures proposed in Woodley's work are much more compact and several of them appear to be symmetric. Yet, the Olivine structures also appear to be composed of a SiO_2 core and MgO surrounding it.

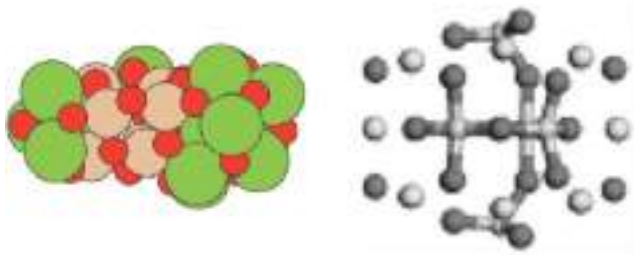

Figure 12. Structures for $(Mg_2SiO_4)_7$ obtained in the work of Lazzati et al.[95] (left) and Woodley et al.[94] (right). The colour code for the left structure is green for Mg, light brown for Si and red for O, for the right structure, black is O, light grey is Si and white is Mg.

GO procedures, while being extremely useful, can provide unrealistic results if not applied with care. One important feature that was not tested in any of the previously published works was the capability of the used IPs to reproduce the relative energies of Mg silicate structures. Optimization of the IP PES can provide unrealistic results if the energetic description of the IP does not correspond to that of the material at the nanoscale. The IPs used both by Woodley and Lazzati et al both are derived from an IP originally devised to describe bulk properties of general silicates[96]. Hence, the IP's ability to provide reasonable structures for clusters cannot be guaranteed.

Our group has published a comparison of two IPs, FFSiOH and ReaxFF, to describe structures and relative stabilities of pure silica and hydroxylated silica nanoclusters compared to the results obtained with DFT calculations using the B3LYP functional[97]. FFSiOH reproduced the structure, energetics and even frequencies of pure and hydroxylated silica up to the point of allowing one to accurately compute free energies[98]. Using the FFSiOH atomic charges as a reference, and the shape of the Mg-O interaction as calculated from an IP published by Walker et al.[99], we included Mg as a species into the FFSiOH IP. The new IP (labelled as Mg-FFSiOH) has the Mg-O interaction manually fine-tuned by trying to obtain the best correlation in relative energy for a sub-set of $(\mathrm{MgSiO_3})_6$ structures against the relative energy derived from DFT calculations using the PBE0 functional. The resulting IP outperforms previous IPs in describing the relative energies of Mg silicate structures, as described by the PBE0 functional, for both Olivinic and Pyroxenic stoichiometries. An example for O-6 structures can be seen in Figure 13.

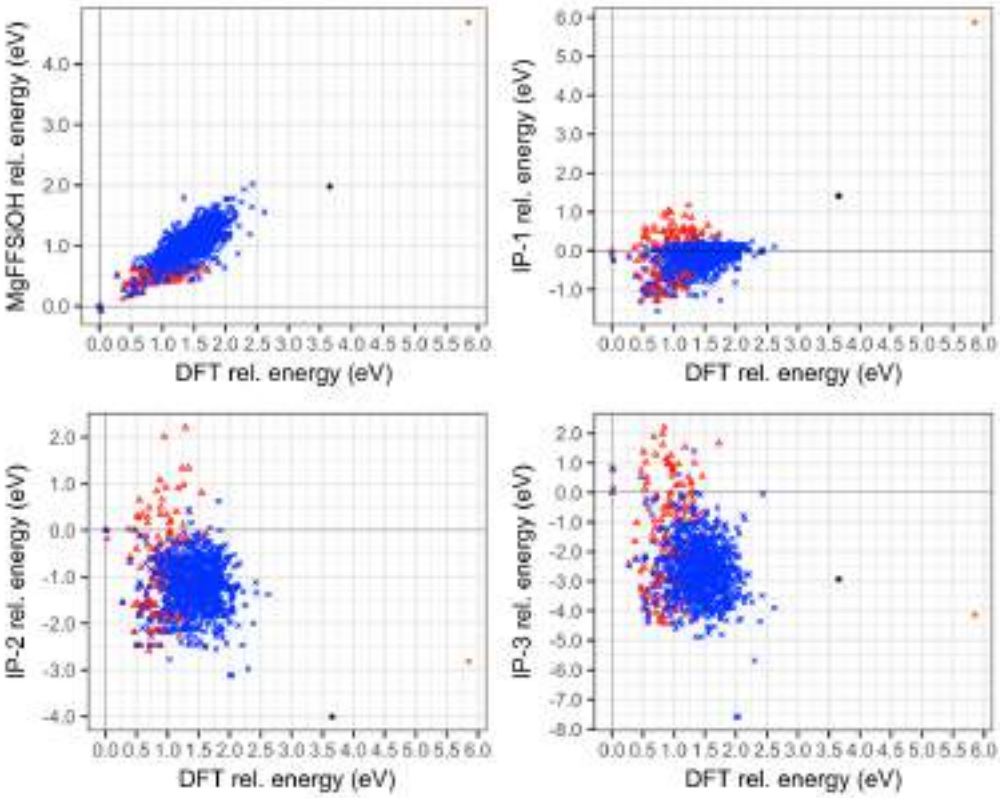

Figure 13. DFT relative energy vs IP relative energy for isomers of the $(Mg_2SiO_4)_6$ structure. IP-1 corresponds to the one defined in Walker et al.[99], IP-2 is the potential defined in Woodley[94], and finally IP-3 is the potential defined in Lazzati et al.[95] the colours represent structures found in GO searches using Woodley IP (blue) and Mg-FFSiOH (red). In orange the structure found by Lazzati, and in black the structure found by Woodley.

The correspondence between DFT and IP relative energy in the Mg-FFSiOH is better than any other reported IP. For the olivine stoichiometry nanoclusters, the previous reported GM candidates of 6 formula units are between 2 to 5.5 eV above our GM candidate. For the pyroxene stoichiometry, the energy difference is quite smaller, of the order of 0.4 eV for the $(MgSiO_3)_7$ cluster -see Figure 1 in results-. The good correlation between Mg-FFSiOH and the DFT energies used as reference allows us to be confident that the obtained structures are good references for energetic studies and extracting information from the structure of the nanoclusters.

The energies and structures obtained through the GO optimization method allows one to determine if some particular nanocluster sizes are intrinsically more stable than others. In cluster beam experiments of MgO, the flow of nanoclusters going through a mass spectrometer shows that the size population of nanoclusters is biased towards certain sizes[100,101]. Computational modelling allows one to rationalize the energetic stability of such nanoclusters by analyzing their structure. This analysis shows that the series of $(MgO)_{3N}$ clusters corresponds to structures that form symmetric tubes or cubes, while nanoclusters not belonging to this series had less stable structures. The energetically stable and abundant nanoclusters are known as “magic” clusters in the literature. If such magic clusters exist in the family of silicates, those nanoclusters should be targeted as main candidates for further studies and astronomical observations, since their presumably large population could lead to detectable signatures of their presence.

The IR spectra of the silicate nanoclusters can be computed by means of the harmonic approximation. The observed astronomical spectrum will be composed of the individual spectrum of each nanocluster, weighted by the density of each individual nanocluster. While currently there is no way to determine the population of each nanocluster size, by adding the spectra of the different silicate nanoclusters we can highlight common features which can be compared to models available in the literature. Such analysis can provide fundamental measures to allow better estimates of silicates nanoclusters. It is important therefore the find out the differences between the IR spectra of silicate nanoclusters and the corresponding IR spectra from extrapolation of bulk parameters.

In collaboration with Dr. Thomas Lazauskas and Dr. Scot Woodley, the following article provides the basis of the work performed on astrosilicate nanoclusters. Their contribution to the article was to apply their advanced GO code Knowledge Lead Master Code (KLMC)[102] in the search of stable structures. In this article, we present low lying energy structures of Mg-pure pyroxene and olivine stoichiometric nanoclusters containing from 1 to 10 formula units. We compare the structure and electronic properties of such silicate nanoclusters with the corresponding most stable bulk crystal structure: En for pyroxene and Fo for olivine. The energetic stability of the nanoclusters has been compared with respect to the bulk structure as well as among themselves, to find out whether magic clusters exists for silicates. The IR spectra of the nanoclusters has also been calculated using the harmonic approximation. Finally, as an exploratory analysis to understand shifts compared to bulk spectra, we generated an IR spectrum by equally weighted sums of all nanocluster spectra.

Results

Article

Cite This: ACS Earth Space Chem. 2019, 3, 2390−2403

http://pubs.acs.org/journal/aesccq

Structure and Properties of Nanosilicates with Olivine $(Mg_2SiO_4)_N$ and Pyroxene $(MgSiO_3)_N$ Compositions

Antoni Macià Escatllar,[†] Tomas Lazaukas,[‡] Scott M. Woodley,*[,‡] and Stefan T. Bromley*[,†,§]

[†]Departament de Ciència de Materials i Química Física & Institut de Química Teòrica i Computacional (IQTCUB), Universitat de Barcelona, E-08028 Barcelona, Spain

[‡]Department of Chemistry, University College, London WC1H 0AJ, U.K.

[§]Institució Catalana de Recerca i Estudis Avançats (ICREA), E-08010 Barcelona, Spain

Supporting Information

ABSTRACT: Magnesium-rich silicates are ubiquitous both terrestrially and astronomically, where they are often present as small particles. Nanosized Mg-rich silicate particles are likely to be particularly important for understanding the formation, processing, and properties of cosmic dust grains. Although astronomical observations and laboratory studies have revealed much about such silicate dust, our knowledge of this hugely important class of nanosolids largely rests on top-down comparisons with the properties of bulk silicates. Herein, we provide a foundational bottom-up study of the structure and properties of Mg-rich nanosilicates based on carefully procured atomistic models. Specifically, we employ state-of-the-art global optimization methods to search for the most stable structures of silicate nanoclusters with olivine $(Mg_2SiO_4)_N$ and pyroxene $(MgSiO_3)_N$ compositions with $N = 1-10$. To ensure the reliability of our searches, we develop a new interatomic potential that has been especially tuned for nanosilicates. Subsequently, we refine these searches and calculate a range of physicochemical properties of the most stable nanoclusters using accurate density functional theory based electronic structure calculations. We report a detailed analysis of structural and energy properties, charge distributions, and infrared vibrational spectra, where in all cases we compare our finding for nanosilicates with those of the corresponding bulk silicate crystals. For most properties considered, we find large differences with respect to the bulk limit, underlining the limitations of a top-down approach for describing these species. Overall, our work provides a new platform for an accurate and detailed understanding of nanoscale silicates.

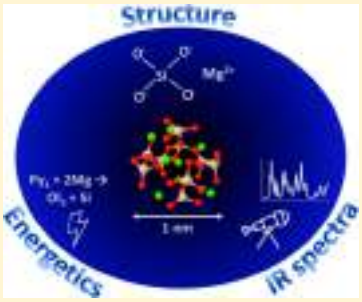

KEYWORDS: *cosmic dust grains, silicates, infrared spectra, nanoclusters, interstellar medium, computational modeling, global optimization, density functional theory*

INTRODUCTION

Silicates constitute the largest fraction of solid matter in the universe. Although bulk silicates form the basis for the geology of the earth's crust and mantle,[1] weathering processes produce mineral nanoparticles which are widely distributed throughout many terrestrial systems.[2] Tonnes of small silicate particles also enter our atmosphere every day in the form of interplanetary dust particles.[3] Indeed, all planetary silicates have their origin in such extraterrestrial silicate dust, which is ubiquitously found in numerous astronomical environments.[4,5] Much of this silicate cosmic dust is formed around evolved oxygen-rich stars where it nucleates from small nanoscale clusters to form micrometer-sized grains, which are then injected into the interstellar medium (ISM).[6] Before their eventual coalescence into larger bodies in protoplanetary disks, these grains follow a long and tumultuous journey through the ISM. During this time the dust is subject to processing by high-energy particles and radiation (e.g., fragmentation, destruction, and reformation), leading to silicates with a range of sizes, shapes, chemical compositions, and structures.[7,8] Largely because of such processes, a significant percentage of silicate cosmic dust grains are likely to be nanosized (i.e., with diameters of between 1 and 100 nm). Using observational constraints, it has been estimated that up to 10% of the mass fraction of silicate grains in the ISM could form a large population of very small nanosilicates with diameters of less than 3 nm.[9] We also note that the modeling of brown dwarf atmospheres also underlines the likely importance of (nano)silicates in cloud formation and the temperatures of such objects.[10,11]

Clues to the chemical structures and composition of silicate dust in astronomical environments largely rely on the fact that silicates tend to absorb and/or emit light at two characteristic infrared (IR) wavelengths around 10 and 20 μm, which are

Received: May 16, 2019
Revised: June 25, 2019
Accepted: July 18, 2019
Published: July 19, 2019

DOI: 10.1021/acsearthspacechem.9b00139
ACS Earth Space Chem. 2019, 3, 2390−2403

associated with vibrational modes associated with Si−O stretching and O−Si−O bending, respectively. A comparison of IR observations with spectra from laboratory silicate samples has generally confirmed that cosmic silicates are probably of pyroxene ($Mg_{1-n}Fe_nSiO_3$) or olivine ($Mg_{2-n}Fe_nSiO_4$) compositions or mixtures thereof and are very Mg-rich.[12] In some specific cases, crystalline grains of these two compositions (i.e., enstatite and forsterite, respectively, for the Mg-rich end members) have been observed; however, in the majority of cases, the observed IR spectra exhibit only two broad silicate peaks, and no detailed chemical structural information can be obtained. As such, the available information on the properties of nanoscale silicates is very limited.

Herein, we provide the structures and properties of stable Mg-rich pyroxene $(MgSiO_3)_N$ and olivine $(Mg_2SiO_4)_N$ nanosilicates for N = 1−10 (∼0.4−1.1 nm diameters) with structures obtained via global optimization searches and properties evaluated using accurate quantum chemical calculations. We analyze how the structure and properties of nano-olivines and nano-pyroxenes evolve with size and how both compare with one another and their respective bulk crystalline limits. For example, by comparing the stabilities of these mixed magnesium silicate nanosystems with those of pure magnesium oxide $(MgO)_N$ and silica $(SiO_2)_N$ nanoclusters, we obtain nanosize-scaled formation energies, which are compared with those of the respective bulk phases. For all of our nanosilicates, we also calculate their IR spectra over a 5−25 μm wavelength range and compare them with typical IR spectra of astronomical silicate dust and of crystalline enstatite and forsterite. In general, our systematic and detailed study reveals a number of significant differences between nanosilicates and bulk silicates and provides a new platform for understanding the stabilities, structures, and properties of silicates from the nanoscale upwards.

METHODOLOGY

For both Mg-rich pyroxene $(MgSiO_3)_N$ and olivine $(Mg_2SiO_4)_N$ compositions, we employed global optimization methods to explore the potential energy surface (PES) of nanosilicate structures to find the lowest-energy isomers for each size for N = 1−10. For these calculations, we developed a specifically tailored interatomic potential (IP) for silicate nanoclusters and performed searches using both the Monte Carlo basin hopping (MCBH)[13] method and a genetic algorithm (GA),[14] as described below. Depending on the system size, 50 to 200 of the lowest-energy nanocluster isomers from the combined global optimization searches for each N and stoichiometry were then optimized without symmetry constraints using quantum chemical density functional theory (DFT)-based calculations. For the latter, we employed all-electron, full potential electronic structure code FHI-aims[15] using the PBE0 hybrid functional[16] and a Tier1/light-atom-centered numerical basis set. We note that the basis set has an accuracy comparable to that of a TZVP Gaussian-type orbital basis set.[17] DFT calculations of this type were used to derive all reported energies, charges, structures, and harmonic IR vibrational frequencies. All results pertain to the best global minimum (GM) candidate nanoclusters as determined by their lowest energy obtained via these DFT-based calculations.

Monte Carlo Basin Hopping (MCBH). Although originally applied to biomolecules,[18] the MCBH algorithm has been shown to be an excellent tool for exploring the low-energy PES of nanoclusters.[13] Our present application of the method follows previous successful work on anhydrous and hydroxylated silica nanoclusters,[19−21] titanosilicate nanoclusters,[22] and the nucleation of silicon monoxide[23] and magnesium silicates.[24] The standard MCBH algorithm moves on the PES of nanocluster configurations through repeated steps of distorting optimized structures, through the application of small random atomic displacements, followed by structural reoptimization. To better explore the PES in our MCBH searches, in addition to atomic displacements, we also set 0.5% of the steps to attempt a Mg ↔ Si cation exchange move to further disrupt the nanocluster structure. After each step, newly optimized nanocluster structures are accepted if they are lower in energy than the previously accepted optimized structure. If they are higher in energy, then a probabilistic Metropolis criterion is employed to determine the outcome. In the latter, the probability of acceptance is lower/higher for a larger/smaller increase in energy. Herein, we employ our cascade MCBH code[25] which was written using the Python-based Atomistic Simulation Environment (ASE)[26] and which uses the General Utility Lattice Package (GULP)[27] code as an externally called nanocluster optimizer. The IPs we employ describe the polarizability of the oxygen anions through the core−shell model.[28] Highly distorted structures possessing polarized ions described in this way can be difficult to optimize. To avoid these difficulties, our cascade MCBH approach first optimizes distorted nanoclusters with a simplified IP without shells, followed by a more refined optimization with shells incorporated. For each nanocluster composition and size, we used 5 MCBH runs of between 10 000 and 250 000 steps depending on the cluster size and with each initialized using a distinct nanocluster structure. During each run, the temperature was dynamically adapted to maintain a target acceptance/rejection ratio of 0.65.

Genetic Algorithm (GA). A Lamarckian GA search of the PES of all nanocluster compositions and sizes was also performed using the Knowledge Led Master Code (KLMC)[14,29] software suite. The KLMC's GA module has previously been proven to efficiently locate low-energy minima for a range different systems.[30−33] Most of the search parameters were kept as defined in ref.[14] Some minor adjustments were, however, introduced in order to ensure a sufficiently intensive search of the PES for magnesium silicate nanoclusters. Namely, depending on the system size under investigation, the population size, number of iterations, and simulation box size were varied from 100 to 200, from 1000 to 2000, and from 10 to 28 Å, respectively. For each nanocluster size and stoichiometry (olivine and pyroxene), we performed five independent GA searches. We stopped our GA simulations when the energy of the lowest-energy structure and the average energy of the 20 lowest energy structures became stable.

Interatomic Potentials (IP). To make the application of both global optimization algorithms efficient and tractable for available computer resources when performing an extensive search of the PES for each nanocluster composition, IPs based on simple analytical expressions were used. Such IPs are computationally very inexpensive to evaluate with respect to quantum mechanical-based electronic structure calculations. Generally, however, IPs are parameterised to describe bulk crystalline systems and are thus often less reliable for describing nanoscale systems where structures can be more varied and disordered. Also, because they possess two types of cations, ternary magnesium silicate nanoclusters have a relatively high degree of configurational structural freedom

DOI: 10.1021/acsearthspacechem.9b00139
ACS Earth Space Chem. 2019, 3, 2390−2403

compared to clusters of binary ionic compounds. For any one nanocluster size with a fixed composition, for example, we can imagine a range of Mg/Si cationic ordering possibilities, ranging from various highly segregated structures (e.g., layered, core−shell, side-by-side) to fully mixed structures. Thus, in order to help our global optimization searches find low-energy isomers of $(Mg_2SiO_4)_N$ and $(MgSiO_3)_N$ nanoclusters we require an IP that provides a reasonably reliable description of the complex PES of these systems.

Herein, we have reparametrized a bulk-parametrized IP to more accurately describe the structures and energetics of nanosilicates. This strategy has previously been shown to work successfully in an IP-based global optimization study of silica nanoclusters.[34] Recently, we showed that FFSiOH[35] is a highly accurate and reliable bulk-parametrized IP for describing the structure and properties of hydroxylated silica nanoclusters.[36] Using the Si−O interaction in FFSiOH as a base, we incorporated new parameters to describe the Mg−O interaction in magnesium silicate nanoclusters based on a modified version of the Mg−O interaction potential used in a previously reported IP.[37] We refer to this new IP as Mg-FFSiOH, which incorporates a short-range Buckingham interaction, long-range electrostatics, and polarization of the oxygen anions:

$$U = \sum_i \sum_{j>i} \frac{q_i q_j}{r} + \frac{1}{2} \sum_{\mathrm{O}} k^{\mathrm{O}}_{\mathrm{C-S}}(r^{\mathrm{O}}_{\mathrm{S}} - r^{\mathrm{O}}_{\mathrm{C}})^2 + \sum_a \left(A_a \exp\left(-\frac{r}{\rho_a}\right) - \frac{C_a}{r^6} \right) + \sum_b D_b[(1 - \exp(-a_b(r - r_b)))^2]$$

The full set of IP parameters for Mg-FFSiOH is provided in Table S1 of the Supporting Information (SI). Although our global optimization searches were mainly carried out using the Mg-FFSiOH IP, we also employed an IP used to model bulk crystalline olivine by Walker et al.[38] (hereafter referred to as IP-1) and an IP based on parameters published in ref 39 for pure Si−O and O−O interactions and parameters reported in a library file of the GULP code[27] for the Mg−O interaction (hereafter referred to as IP-2). The use of multiple IPs helped to provide a greater degree of structural richness to our searches. An example of the ability of Mg-FFSiOH to describe the relative energies of silicate nanoclusters with respect to those calculated by (DFT-based calculations is shown in Figure 1 for the cases of olivine $(Mg_2SiO_4)_6$ nanocluster isomers and $(MgSiO_3)_7$ pyroxene nanocluster isomers. In each case, we plot the Mg-FFSiOH-optimized energies versus the corresponding DFT-optimized energies for over 1000 distinct isomers obtained from global optimization searches. For the $(Mg_2SiO_4)_6$ searches we used Mg-FFSiOH and IP-1, and for the $(MgSiO_3)_7$ searches we used Mg-FFSiOH and IP-2. Clearly, in both cases, the Mg-FFSiOH calculated isomer energies correlate quite well with those from DFT-based calculations. For $(Mg_2SiO_4)_6$, the two lowest-energy isomers according to Mg-FFSiOH are also the lowest in energy for DFT. For $(MgSiO_3)_7$, the best GM candidate according to DFT is the 16th lowest-energy isomer with respect to Mg-FFSiOH. We note that our best GM candidates for both olivine and pyroxene nanoclusters for nearly all cases for $N > 5$ resulted from global optimization searches using Mg-FFSiOH.

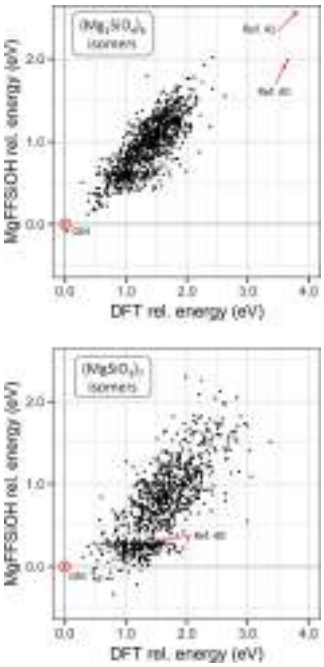

Figure 1. MgFFSiOH IP-optimized energies against DFT-optimized energies with respect to the energy of the lowest-energy DFT structure (GM) for ∼1000 isomers as obtained from global optimization searches described above for $(Mg_2SiO_4)_6$ olivine nanocluster isomers (upper) and $(MgSiO_3)_7$ pyroxene nanocluster isomers (lower). Data points corresponding to the GM candidates obtained in ref 40 are highlighted in each case. Note that the GM $(Mg_2SiO_4)_6$ candidate from ref 41 was found to lie over 5.5 eV higher in energy than our proposed GM isomer (as calculated via DFT) and is outside of the plotted range.

■ RESULTS AND DISCUSSION

Previous work by Woodley[40] using an evolutionary algorithm and a simplified version of IP-2 without polarizable shells on the oxygen anions was the first to report GM candidates for magnesium silicate nanoclusters. In this work, only IP-optimized nanocluster structures were reported (i.e., no DFT-based refinement, as performed in the present work) for $(Mg_2SiO_4)_N$ for $N = 1-7$ and for $(MgSiO_3)_N$ for $N = 1-10$. In ref 40, the GM candidates found for both olivine and pyroxene nanosilicate families were found to exhibit all or most of their Si cations in a single central network of oxygen-bridged SiO_4 tetrahedra decorated by peripherally scattered Mg cations. Only the larger $(Mg_2SiO_4)_N$ olivinic nanoclusters ($N = 4-7$) were found to display one SiO_4 unit separated from the main silica network. For the pyroxene $(MgSiO_3)_N$ GM candidates, the silica networks tended to be quite compact and form a number of $(SiO)_x$ rings with $x = 2-5$. A number of the predicted GM candidates displayed fairly symmetric structures and often displayed five-coordinate Si centers.

A more recent study by Mauney and Lazzati[41] focusing on the nucleation of astrophysical Mg-rich olivinic dust also derived some GM candidates for $(Mg_2SiO_4)_N$ with $N = 2-13$ using an IP (hereafter referred to as IP-3) which was derived from combining parameters from various sources.[34,37,42] The

DOI: 10.1021/acsearthspacechem.9b00139
ACS Earth Space Chem. 2019, 3, 2390−2403

reported Mg-rich olivine nanoclusters, like many of those in ref 40, possess a single ···Si−O··· bonded network. However, in ref 41 the reported lowest-energy nanoclusters have a relatively high degree of segregation. In particular, the silica fraction of the $(Mg_2SiO_4)_N$ nanoclusters was typically found to form highly compact subclusters sandwiched between dense MgO regions.

IP-2 and IP-3 have a number of parameters in common with IP-1. In fact, IP-1, IP-2, and IP-3 have a core set of parameters for O−O and Si−O interactions that can be found in earlier published IPs (e.g., refs 42 and 39). As such, we may expect that the reliabilities of the predicted low-energy isomers using each of these three IPs with respect to DFT-based calculations would be quite similar. In section S1 of the SI, we plot the relative energies of the 1000 $(Mg_2SiO_4)_6$ isomers in Figure 1 calculated using IP-1, IP-2, and IP-3 with respect to those calculated using DFT. Figure S2 shows that the performance of IP-1, IP-2 and IP-3 is rather poor compared to that of Mg-FFSiOH (Figure 1). The energetic stabilities of the candidate GM isomers for $(Mg_2SiO_4)_6$ proposed in ref 40 (using IP-2 without shells) and ref 41 (using IP-3) are also indicated in Figure 1 (upper). These isomers are found to be between 1.5 and 5.5 eV higher in energy (as calculated using DFT) than our GM candidate and to be less energetically stable than many other isomers in our extensive data set. The predicted GM isomer for $(MgSiO_3)_7$ in ref 40 is also highlighted in Figure 1 (lower), confirming the relatively worse performance of IP-2 for pyroxene nanoclusters. A more extensive comparison between IP-2 and DFT relative energies for $(MgSiO_3)_7$ isomers is reported in section S2 of the SI. Clearly, these comparisons raise serious doubts as to the adequacy of IP-1, IP-2, and IP-3 for finding structures of low-energy silicate nanoclusters.

Our newly parametrized Mg-FFSiOH, as employed herein, appears to provide a reasonably accurate and computationally efficient means to search the PES of energetically stable nanosilicate cluster structures. The use of a more accurate IP for our global optimizations with respect to previous searches is also clearly reflected in the structures of the resultant candidate GM nanocluster isomers. For example, in contrast to previous studies, the olivinic $(Mg_2SiO_4)_N$ nanocluster structures from our Mg-FFSiOH-based global optimization searches display increasingly nonsegregated structures with increasing size. This relatively low degree of SiO_4 polymerization in our olivine nanoclusters is consistent with the bulk crystalline phase of Mg_2SiO_4 (i.e., forsterite), where all of the silica tetrahedra are completely isolated. Below we provide a more detailed structural analysis of all of our GM nanocluster candidates followed by an evaluation of their charge distributions, energetics, and IR spectra.

Structure. Figures 2 and 3 show our candidate GM nanocluster structures for Mg-rich olivine $(Mg_2SiO_4)_N$ and pyroxene $(MgSiO_3)_N$ nanoclusters, respectively. Hereafter, we will refer to our olivine and pyroxene nanoclusters with N units by the abbreviations O-N and P-N, respectively. The Cartesian coordinates of the atoms in all nanoclusters are provided in the SI and are also available in the open access HIVE database of atomic structures for nanoclusters (https://hive.chem.ucl.ac.uk/).

Although the majority of the O-N and P-N nanocluster structures are nonsymmetric, a few symmetric and nearly symmetric cases were found. For olivine nanoclusters, symmetry is exhibited only by O-1 (C_{2v}) and O-2 (C_s). The

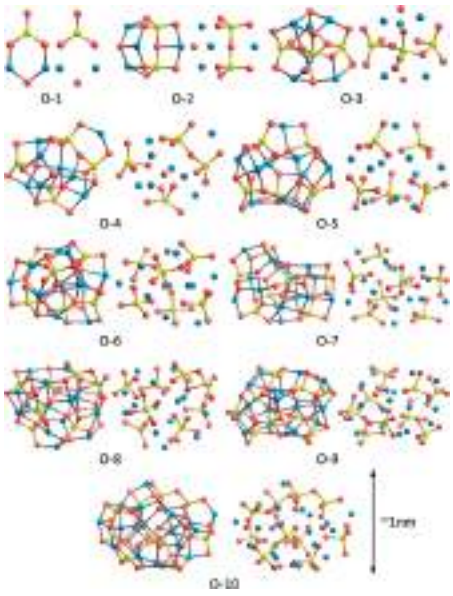

Figure 2. Structures of our GM candidate Mg-rich olivine $(Mg_2SiO_4)_N$ nanoclusters (O-N) for N = 1−10. For each size, we show the bonding connectivity of all atoms (left) and that of only the bonded Si−O skeleton (right). Atom key: Si, yellow; O, red; and Mg, blue.

O-3 nanocluster is also close to having a structure with C_s symmetry that is broken by small distortions. For pyroxene nanoclusters, P-1, P-2, and P-6 have structures with C_{2v}, C_{2h}, and C_i point group symmetries, respectively. A more symmetric C_{2h} version of the P-6 $(MgSiO_3)_6$ structure is also found in a very low energy $(Al_2O_3)_6$ nanocluster isomer.[43] Attempts to optimize our candidate GM $(MgSiO_3)_6$ P-6 structure in this higher symmetry spontaneously relaxed to the more stable C_i structure probably because of the symmetry-breaking influence of the two cation types. The P-3 and P-4 nanoclusters can also be viewed as having structures in which energy-lowering distortions have broken a higher C_{2v} symmetry to form a C_1 structure. We note that the P-4 and O-3 nanoclusters were employed in a previous study modeling the formation and dissociation of H_2 on nanosilicate dust grains.[44,45] The P-4 nanocluster was also used in a study of absorption of water on nanosilicates.[65] All other nanocluster structures are reported herein for the first time.

$[SiO_4]^{4-}$ Polymerization. In the olivine Mg_2SiO_4 composition, two Mg^{2+} cations formally balance the charge of each $[SiO_4]^{4-}$ anion. Indeed, the structure of bulk crystalline forsterite can be viewed as an interacting ordered array of such discrete ionic species. However, if $[SiO_4]^{4-}$ tetrahedra begin to segregate and share oxygen atoms (i.e., $[SiO_3{-}O{-}SiO_3]^{6-}$), then this in turn frees up O^{2-} ions that then can coordinate with Mg^{2+} cations to promote MgO-rich regions (i.e., MgO segregation). Generally, a low degree of ≡Si−O−Si≡ polymerization implies less segregation and vice versa. In bulk systems with the Mg_2SiO_4 composition, such segregation appears to be strongly energetically disfavored and the dimerization of $[SiO_4]^{4-}$ tetrahedra is typically observed only in high pressure phases (e.g., wadsleyite). Consistent with the

DOI: 10.1021/acsearthspacechem.9b00139
ACS Earth Space Chem. 2019, 3, 2390−2403

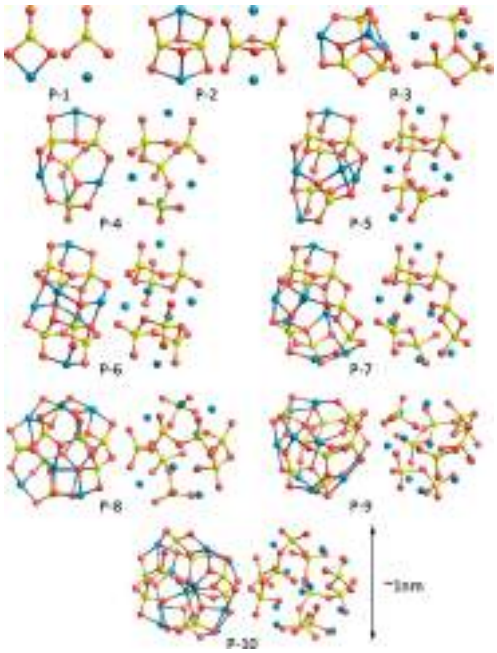

Figure 3. Structures of our GM candidate Mg-rich pyroxene $(MgSiO_3)_N$ nanoclusters (P-*N*) for N = 1−10. For each size, we show the bonding connectivity of all atoms (left) and that of only the bonded Si−O skeleton (right). Atom key: Si, yellow; O, red; and Mg, blue.

structure of low-energy bulk Mg_2SiO_4 crystalline phases under ambient conditions, our candidate GM olivine nanocluster structures have a much lower degree of polymerization than do previously reported nanoclusters.[40,41] With increasing system size, the most energetically stable nanoclusters should approach their respective bulk limit in terms of properties and structure. The size-dependent evolution of oxide nanocluster properties toward the bulk is very system-specific and is typically highly nonmonotonic at small system sizes.[46] However, on average we expect that the degree of polymerization (i.e., number and size of polymers) in our olivine nanoclusters should diminish with increasing size. The smallest olivine nanoclusters, O-2 and O-3, are found to be fully polymerized and exhibit segregated structures containing a $[Si_2O_7]^{6-}$ dimer and a $[Si_3O_{10}]^{8-}$ trimer for O-3. For O-4, half of the four $[SiO_4]^{4-}$ tetrahedra are dimerized, with the other two being isolated. O-5 and O-6 both contain no polymers and are fully mixed systems with all $[SiO_4]^{4-}$ tetrahedra isolated. Surprisingly, a small degree of polymerization appears again for O-7 whereby two of the $[SiO_4]^{4-}$ tetrahedra (<30%) are dimerized. Our best GM candidate for O-8 also exhibits a single dimer, but in this case, two $[SiO_4]^{4-}$ units share two oxygen atoms to form a Si_2O_2 ring. Such strained "two-rings" are not typically found in stable bulk silicates but are known to be high-energy local reconstructions on the surfaces of amorphous pure silica.[47] Two-rings are, however, commonly found in small low energy nanoclusters of pure silica.[20] In the case of O-8, the Si_2O_2 two-ring resides on the surface of the nanocluster, but it is not clear why this particular structure is more stable than many others in our searches that do not display such a ring. The O-9 nanocluster possesses a single oxygen-bridged dimer, meaning that ∼22% of the $[SiO_4]^{4-}$ tetrahedra are polymerized. The O-10 structure possesses two such dimers with six isolated $[SiO_4]^{4-}$ units. Although the trends in the number and length of polymers in our $(Mg_2SiO_4)_N$ GM candidates are not simply monotonically decreasing with increasing N, we note that (i) the highest degree of polymerization (i.e., 100%) is found for O-2 and O-3, (ii) polymerization is mainly limited to dimerization, with only one instance of a trimer polymer in O-3, and (iii) the number of nonpolymerized isolated $[SiO_4]^{4-}$ units tends to increase with size (e.g., 0−2 for O-1−O-4 and 5−7 for O-5−O-10).

Because of the higher Si/O ratio in pyroxene (1:3) relative to that in olivine (1:4), a correspondingly higher degree of polymerization (i.e., oxygen sharing) in pyroxene is necessary to maintain the four-coordination of the $[SiO_4]^{4-}$ units. In the bulk crystalline $MgSiO_3$ enstatite phase, this is achieved through the formation of linear polymers chains in which every $[SiO_4]^{4-}$ tetrahedral unit participates in two single-oxygen bridges with two other units. Similarly, in finite $(MgSiO_3)_N$ nanoclusters a relatively higher degree of polymerization is necessary relative to olivine nanoclusters. In our candidate GM pyroxene nanoclusters, polymerization occurs via the formation of closed rings and/or branched networks. For the very small P-2 and P-3 nanoclusters, the polymerization needed to ensure four-coordination of the $[SiO_4]^{4-}$ units results in the formation of two-rings and/or triply shared oxygen centers. Nanoclusters P-4 and P-5 have more extended branched polymeric networks which exhibit a single $(SiO)_3$ three-ring. P-6 can be seen as a simple structural extension of P-5, which results in a symmetric nanocluster structure with two nonlinked three-rings. Similarly, P-7 can be viewed as an extension of P-6 in which the symmetry is lost and the two distinct three-rings become a dimer and a branched network containing a three-ring and a two-ring, respectively. Nanoclusters P-8 and P-10 contain branched networks containing one three-ring. The P-9 structure is unusual because it contains three silicate groups, one nonpolymerized isolated $[SiO_4]^{4-}$ tetrahedron, a $[Si_2O_7]^{-6}$ dimer, and a six-membered chain which contains three two-rings. Although all of these pyroxene nanoclusters are relatively highly polymerized, often with a single network of $[SiO_4]^{4-}$ tetrahedra, there does not appear to be any simple tendency with respect to the type/degree of polymerization in nanoclusters over the considered size range.

$[SiO_4]^{4-}$ Tetrahedral Distortion. For both the P-*N* and O-*N* nanoclusters, the overall structural distortion of the $[SiO_4]^{4-}$ tetrahedral units, with respect to perfect tetrahedrality, decreases with increasing N. Specifically, in Figure 4 we show how the root-mean-square (rms) O−Si−O angle over all $[SiO_4]^{4-}$ units in each nanocluster relative to the symmetric unstrained angle of 109.47° (i.e., $\Delta_{O-Si-O} = \langle abs(\theta_{O-Si-O} - 109.47)\rangle$) varies with N, as compared with the bulk values of enstatite (4.4°) and forsterite (6.5°). Generally, the overall trend is for Δ_{O-Si-O} values to decrease with increasing N, indicating a corresponding decrease in internal structural strain with increasing nanocluster size. However, the two classes of nanoclusters show differences in their structural evolution with size. For small nanocluster sizes (N < 4), the pyroxene nanoclusters have notably more tetrahedral distortion than olivine nanoclusters. However, for the P-*N* nanoclusters the Δ_{O-Si-O} values also rapidly decrease with increasing size, and for N = 4, the tetrahedral distortion is lower than in the O-4

DOI: 10.1021/acsearthspacechem.9b00139
ACS Earth Space Chem. 2019, 3, 2390−2403

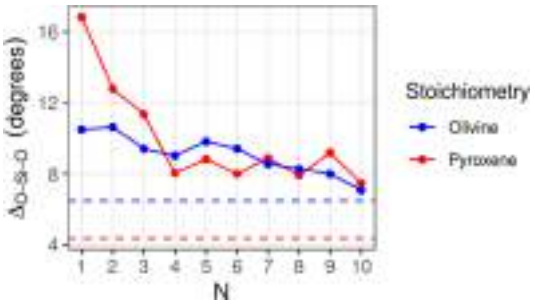

Figure 4. Average tetrahedral distortion of $[SiO_4]^{4-}$ centers ($\Delta_{Si-O-Si}$) with respect to nanocluster size (N) for both the O-N (blue) and P-N (red) series. Dashed lines correspond to the bulk limits of forsterite (blue, 6.5°) and enstatite (red, 4.4°).

nanocluster. For sizes $N \geq 4$, the tetrahedral distortion in the P-N nanoclusters appears to stabilize and exhibits an odd−even oscillation around a value of approximately 8.3°. This result suggests that pyroxene nanoclusters are structurally still far away from the bulk crystalline limit. This can be rationalized by the fact that the inherent spatial confinement of the finite nanoclusters causes the short polymerized $[SiO_4]^{4-}$ chain to be bent and dendritic, unlike the long linear chains in the bulk structure. For O-N nanoclusters with $N \geq 4$, the Δ_{O-Si-O} values tend to keep gradually decreasing with increasing N, and for O-10, they come very close to the bulk limit. This result is in line with the fact that the larger O-N clusters exhibit isolated $[SiO_4]^{4-}$ units as in the bulk forsterite structure.

Mg^{2+} Coordination Number. Silicate polymerization is only one descriptor of the chemical structure of nanosilicates. By examining the changes in the number of bonded neighbors to each Mg^{2+} cation (i.e., the coordination number, CN) throughout the O-N and P-N series, we obtain a complementary perspective on the size-dependent evolution of nanosilicate structure (Figure 5). Generally, for both P-N

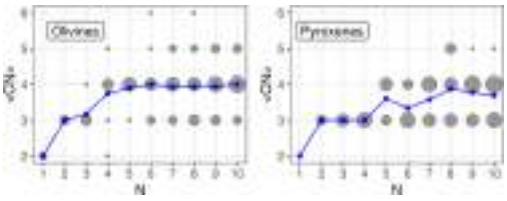

Figure 5. Average coordination numbers of Mg^{2+} cations (i.e., ⟨CN⟩) in O-N (left) and P-N (right) nanoclusters (blue lines). The size of the gray disks corresponds to the number of Mg^{2+} cations with a particular coordination in a nanocluster of a given size. A 2.3 Å Mg−O bond cutoff was applied to calculate the coordination values.

and O-N structures the average CN, ⟨CN⟩, of Mg^{2+} cations tends to increase with increasing nanocluster size. For the O-N nanoclusters, ⟨CN⟩ monotonically increases from 2 (O-1) to 4 (O-6), where it then seems to stabilize for O-7 to O-10 (Figure 5, left). For the P-N nanocluster series, ⟨CN⟩ increases in a more irregular fashion from 2 (P-1) to 3.88 (P-8), where it then remains between 3.8 and 3.9 until P-10. We note, in particular, that the ⟨CN⟩ value for P-5 appears to be rather high relative to its size, leading to a small peak in the ⟨CN⟩ versus size plot in Figure 5 (right). As we will see below, this property is likely related to the anomalous high energy stability of the P-5 nanocluster.

In both sets of nanoclusters, ⟨CN⟩ is still always below the typical bulk value of 6 as found in both forsterite and enstatite bulk crystals. This is unsurprising because many of the Mg^{2+} cations in finite nanoclusters are near the surface and have correspondingly fewer oxygen neighbors than within an extended bulk system. Examining individual contributions to ⟨CN⟩, we can see that there is indeed a heterogeneous mix of CN values for each Mg^{2+} cation within each nanocluster (gray disks in Figure 5). For the P-N series, the lower and upper bounds of the set of exhibited individual CN values {A, B, etc.} follow a monotonically increasing tendency with increasing nanocluster size: P-1, {2}; P-2−P-4, {3}; P-5−P-7, {3, 4}; P-8−P-10, {3, 4, 5}. See Figure 5 (right). Here, a maximum individual CN value of 5 is achieved, clearly confirming the nonbulk chemical environment of all Mg^{2+} cations in all P-N nanoclusters. For the O-N series, the distribution of CN values for individual Mg^{2+} cations in each nanocluster evolves with size in a more complex fashion. For example, O-4 has a broader set of CN values (i.e., {2, 3, 4, 5}) than do O-3 and O-5 (i.e., {3, 4}), with all three nanoclusters having fairly similar ⟨CN⟩ values between 3 and 4. This suggests that O-N nanoclusters can use multiple low-energy structural arrangements of Mg^{2+} cations to compensate for the charge of their $[SiO_4]^{4-}$ anions. This apparent structural freedom is further confirmed by examining the Mg^{2+} CN distributions and overall structures for the largest olivine nanoclusters, O-6−O-10. As in most of the O-N series considered, in these nanoclusters most of the Mg^{2+} cations are four-coordinated. For O-6, unlike for smaller olivine nanoclusters, one finds a centrally located Mg^{2+} cation which allows it to be the first six-coordinated Mg^{2+} in the O-N series. The structures of O-7 and O-8 further exhibit two Mg^{2+} cations linked by two oxygen anions, near their centers. For O-7, both central Mg^{2+} cations are five-coordinated, whereas for the larger O-8 structure one of the central cations is able to attain six-coordination. Although the emergence of six-coordinate Mg^{2+} cations in O-6 and O-8 suggests that the larger O-N nanoclusters are becoming more bulklike, these nanoclusters are still far from having fully bulklike structures. In O-9 and O-10, for example, we see structures that maintain a relatively high ⟨CN⟩ by having fewer three-coordinate Mg^{2+} cations and more with Mg^{2+} cations with five-coordination, but display no six-coordinated centers.

Atomically Partitioned Charges. In mineralogy, the atomic structure of silicates is often described and classified in terms of the ordering and polymerization of silicate anionic species with respect to an arrangement of charge-compensating Mg cations (see above). Although silicates are generally ionic insulators, the degree of charge transfer between anions and cations largely depends on the local environment of the ions in question. In crystalline bulk silicates, the periodic space group symmetry dictates that only a limited number of distinct environments for the ions are possible. However, for our silicate nanoclusters, often possessing no point group symmetry, every ion can have a different coordination environment (Figure 5), thus potentially yielding a different ionic charge.

In Figure 6, we plot the Hirshfeld partitioned charges[48] of oxygen anions and magnesium cations with respect to nanocluster size and distance to the center of mass of each nanocluster for both the O-N and P-N series. We note that

DOI: 10.1021/acsearthspacechem.9b00139
ACS Earth Space Chem. 2019, 3, 2390−2403

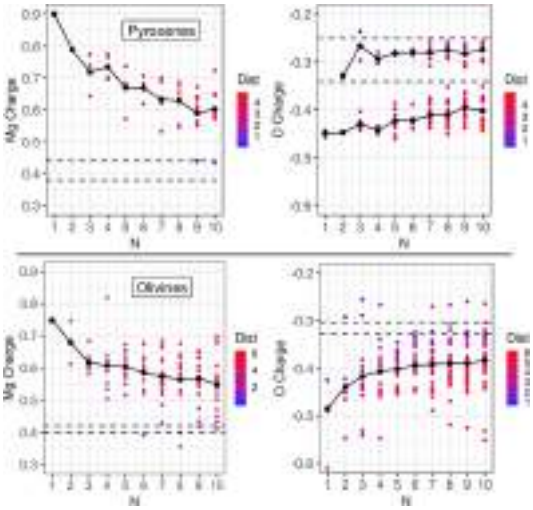

Figure 6. Hirshfeld partitioned charges of Mg cations (left) and O anions (right) in P-*N* (upper) and O-*N* (lower) nanoclusters. Dashed lines correspond to bulk crystalline limiting values (i.e., forsterite for the O-*N* series and enstatite for the P-*N* series), and black data points and the associated black line follow the corresponding average partitioned charge values with respect to size *N*. The colors of other data points indicate the distance (in angstroms) between the charged ion and the center of mass of the respective nanocluster according to the respective legend next to each plot.

these partitioned charges are significantly smaller in magnitude than the formal charge states of the constituent ions and do not reflect any observable quantity. Instead, these partitioned charges should be viewed as a consistent means by which to compare the charge distribution in the nanoclusters with respect to variations in size, structure, and composition.

For the O-*N* nanocluster series, the average partitioned positive Mg charge and the average partitioned negative O charge both decrease in magnitude with increasing nanocluster size. In the bulk olivinic limit of forsterite, Mg cations occupy two crystallographically similar but distinct sites. Atomic charge partitioning reveals these two types of sites to have very slightly different positive charges. The respective bulk limiting values (i.e., for forsterite for the O-*N* series and for enstatite for the P-*N* series) are indicated by dashed lines in Figure 6. A corresponding situation is found for O anions which are found to possess slightly different negative partitioned charges. In both cases, the respective average partitioned charges in the O-*N* clusters are always higher in magnitude than that in the bulk but approach the bulk partitioned charge values with increasing nanocluster size.

In the bulk enstatite crystal, there are two crystallographically distinct oxygen anions with significantly different chemical environments: (i) bridging siloxane oxygen centers (Si−O−Si) and (ii) oxygen centers bonded to a single silicon cation. The former oxygen center is found to have a lower partitioned charge (−0.25 e) than the latter (−0.34 e). Both types of oxygen can be identified in the P-*N* nanoclusters, and as in the bulk, the siloxane bridging oxygen anions are consistently less negative than the remaining oxygen centers on average. As in the O-*N* case, the nanocluster-averaged partitioned charges of these oxygen centers are more negative than their respective bulk counterparts and become progressively less negative with increasing *N*. The nanocluster-averaged partitioned Mg cationic charges in the P-*N* series also follow the general trend found for the O-*N* nanoclusters, whereby the charge magnitude decreases with increasing nanocluster size toward the bulk limits for partitioned Mg cationic charges in forsterite. We note that unlike the Mg and O partitioned charges, the average partitioned silicon charge for all O-*N* nanoclusters remains unchanged at +0.42 e with a standard deviation of 0.02 and a bulk value of +0.46 e. For P-*N* nanoclusters, the average partitioned Si charge is +0.46 e with a standard deviation of 0.03, while for enstatite the value is +0.51 e.

In each plot in Figure 6, we color code each individual O and Mg partitioned charge to indicate its distance from the center of mass of the respective nanocluster. First, this analysis shows that the average partitioned charge values for O anions and Mg cations result from a wide range of charge values which, in some cases, can be lower in magnitude than the corresponding bulk charge values. Such an extreme variation reflects the high structural variety in nanoclusters with respect to the ordered crystalline bulk phases. Second, we observe a tendency for partitioned charges to be smaller in magnitude the closer they are to the center of their respective nanocluster. In the plots in Figure 6 we can see this by an increasing blueness (i.e. toward smaller distances) of the data points closer to the bulk limiting dashed lines. This can be rationalized by noting that atoms in the interior of a nanocluster (i.e., nonsurface) have a chemical environment closer to the bulk, and hence they have correspondingly more bulklike charge. With increasing size, the proportion of interior atoms increases; therefore, the average partitioned charge within a nanocluster for each species comes progressively closer to the bulk limit.

Relative Energies. We employ the normalized relative energy, $E_{rel}(N)$ (eq 1) and first-order and second-order energy differences, $\Delta^1(N)$ and $\Delta^2(N)$ (eqs 2 and 3, respectively) to characterize the relative energetic stability of our O-*N* and P-*N* nanosilicate clusters:

$$E_{rel}(N) = \frac{E_N}{N} - E_{bulk} \quad (1)$$

$$\Delta^1(N) = E_N - E_{N-1} - E_1 \quad (2)$$

$$\Delta^2(N) = E_N - \frac{E_{N-1} + E_{N+1}}{2} \quad (3)$$

Here, E_N is the total energy of a nanocluster containing *N* stoichiometric units, and E_{bulk} is the energy per stoichiometric unit of the respective bulk crystalline structure.

In Figure 7, we plot the normalized relative energies for both the O-*N* and P-*N* nanocluster series. In both cases, $E_{rel}(N)$ decreases monotonically from $N = 1-10$ with increasing size. From a structural point of view olivine nanoclusters seem to be closer than the pyroxene nanoclusters to the most stable bulk phase. However, the largest O-10 nanocluster is 3.55 eV higher in energy per unit than bulk forsterite, whereas for the same number of units pyroxene is 2.56 eV higher in energy than the enstatite bulk. To provide a rough estimate of the size at which the nanosilicates become bulklike, we fit the $E_{rel}(N)$ data with a third-order polynomial in powers of $N^{-1/3}$ (ref 49):

$$E_{rel}(N) = a_1 N^{-1/3} + a_2 N^{-2/3} + a_3 N^{-1} \quad (4)$$

DOI: 10.1021/acsearthspacechem.9b00139
ACS Earth Space Chem. 2019, 3, 2390−2403

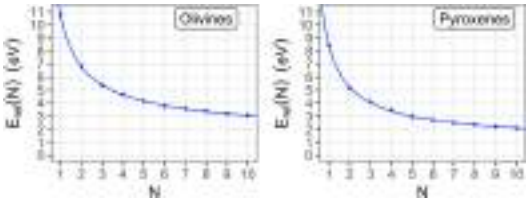

Figure 7. Energy per stoichiometric unit, $E_{rel}(N)$, for the O-N nanoclusters with respect to forsterite (left) and the P-N nanoclusters with respect to enstatite (right). Blue data points indicate the calculated data, and the blue lines show fits to the data following eq 4.

The resulting fitting lines based on the O-N and P-N total energy data are shown in Figure 7. (All fitting parameters are provided in Table S2 of the SI.) Considering, generally, that metastable bulk polymorphs typically lie, at most, within a few tenths of an eV per unit of the most stable bulk phase, we assume that nanoclusters would become bulklike when $E_{rel}(N) - E_{bulk} < \delta$, where we take δ to be 0.1 eV per atom. For olivine, this criterion provides us with an approximate size of $N = 860$ (i.e., 6020 atoms), whereas for pyroxene we obtain a smaller size of $N = 380$ (i.e., 1900 atoms). Although these are relatively crude assessments, it suggests that at least a few thousand atoms are required for nanosilicates to start to exhibit bulklike energy stabilities. Interestingly, these estimates also suggest that pyroxene attains a more bulklike energetic stability at smaller sizes than olivine.

In Figure 8, we plot the first-order energy difference, $\Delta^1(N)$, and the second-order energy difference, Δ^2(N), for both the

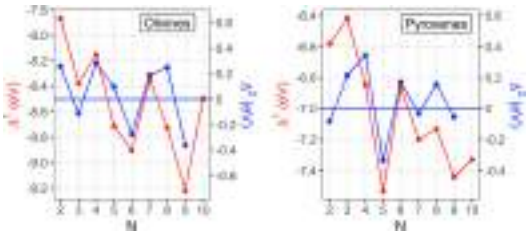

Figure 8. First-order (red line, left vertical axes) and second-order (blue line, right vertical axes) energy differences for the O-N (left) and P-N (right) nanoclusters.

O-N and P-N nanoclusters with respect to nanocluster size. The first-order energy difference provides a measure of stability for a nanocluster with N units with respect to a nanocluster of $N - 1$ units and the $N = 1$ monomer. In this sense, $\Delta^1(N)$ can be thought of as a nucleation energy where more negative values indicate an energetically favored incremental $N - 1 \rightarrow N$ size increase and positive values indicate the converse. The second-order energy difference measures the energy stability of a nanocluster with N units with respect to nanoclusters with both $N - 1$ and $N + 1$ units. For both measures, the appearance of pronounced dips for specific values of N confirms the particularly high relative stability of this nanocluster size with respect to neighboring nanocluster sizes. Values of N with high relative stability as shown by $\Delta^1(N)$ and $\Delta^2(N)$ are referred to as magic numbers. Magic number nanoclusters are found in many systems and are usually found to have relatively high abundances in the distribution of nanocluster sizes in cluster beam experiments.[50] For olivine, the O-3, O-6, and O-9 sequences of nanoclusters exhibit pronounced dips for $\Delta^2(N)$ and, to a lesser extent, for $\Delta^1(N)$. These nanoclusters do not appear to have any common structural features and have no symmetry. Of these three nanoclusters, O-9 has the lowest values for both measures and this is the most magic size for the olivine series. For the pyroxene nanoclusters, although P-7 and P-9 show dips for $\Delta^1(N)$ and $\Delta^2(N)$, the clearest signal of magic number stability is for P-5, which has very pronounced dips for both measures. Although the P-5 nanocluster has no symmetry, its high relative stability may be linked to its relatively high Mg cation coordination for its size (Figure 5).

We note that $\Delta^1(N)$ and $\Delta^2(N)$ are very sensitive measures of the relative energy stability, and it is thus interesting to establish whether the stability trends they predict are also valid at finite temperatures. We note that many dust-containing astrophysical environments (e.g., the ISM) have rather low temperatures ($\lesssim$100 K) and pressures, so the change in our 0 K results will be negligible. However, in circumstellar regions of evolved stars,[6] nanosilicates are thought to start nucleating at temperatures close to 1000 K. One may also consider the standard laboratory conditions to be relatively extreme compared to those of the ISM. In section S3 of the SI, we calculate the $\Delta^1(N)$ and $\Delta^2(N)$ values for our P-N and O-N nanoclusters based on their finite temperature free energies under standard terrestrial conditions (298 K and 101 300 Pa) and circumstellar conditions (1000 K and 0.0005 Pa). From this analysis, we can see that the general tendencies predicted by our energetics calculated at 0 K are maintained for all O-N nanoclusters. For the P-N nanoclusters, we see little difference under standard conditions, but under circumstellar conditions, the changes are more significant. In particular, we note that the P-5 nanocluster loses its magic stability status and P-9 becomes more magic.

Energies of Formation. The enthalpy of formation of a bulk magnesium silicate from the binary oxides (MgO rock salt and SiO_2 quartz) (ΔH_f^{oxides}) can be derived from

$$\Delta H_f^{oxides}[\text{silicate}] = \Delta H_f[(MgO)_a(SiO_2)_b] - (a\Delta H_f[MgO] + b\Delta H_f[SiO_2]) \quad (5)$$

where $\Delta H_f[(MgO)_a(SiO_2)_b]$ is the enthalpy of formation of the magnesium silicate in question and $\Delta H_f[MgO]$ and $\Delta H_f[SiO_2]$ are the enthalpies of formation of the oxides, all relative to the elements. For forsterite (Mg_2SiO_4), stoichiometric coefficients $a = 2$ and $b = 1$ are used, whereas for enstatite ($MgSiO_3$), one should employ $a = b = 1$. Using extrapolated 0 K values from the NIST-JANAF tables of experimental thermodynamic data[51] for the three terms on the right-hand side of eq 5, we obtain ΔH_f^{oxides}[forsterite] = −0.66 eV and ΔH_f^{oxides}[enstatite] = −0.38 eV. We note that these values are within 0.01 eV of directly measured values obtained at 970 K.[52] Using the same level of DFT theory as for the nanoclusters, we find ΔH_f^{oxides}[forsterite] = −0.77 eV and ΔH_f^{oxides}[enstatite] = −0.42 eV, which are in quite good agreement with the experimental values, thus confirming the adequacy of our DFT calculations for silicate energetics. Note that in these theoretical values the calculated internal energies are assumed to be a good approximation to the enthalpies (i.e., pV contributions are taken to be negligible). Because of the fact that both of these silicates have distinct stoichiometries, a direct comparison of these two values is not very informative.

DOI: 10.1021/acsearthspacechem.9b00139
ACS Earth Space Chem. 2019, 3, 2390−2403

For each silicate family considered, we would like to have a method for comparing the formation energies with their respective bulk values which takes into account the finite size of both the nanosilicate and the oxide components. One way to do this is to find appropriately sized low-energy nanoclusters of MgO and SiO_2 which, when brought together, form a system with the same size and stoichiometry as for a particular silicate nanocluster. Formally, we can describe this energy difference (per stoichiometric unit) by

$$\Delta H^{\text{oxides}}_{f(\text{reactive})}[\text{nanosilicate}] \approx \Delta E^{\text{oxides}}_{f(\text{reactive})}[\text{nanosilicate}] = \frac{E[(\text{Mg}_a\text{Si}_b\text{O}_{a+2b})_N] - (E[(\text{MgO})_{aN}] + E[(\text{SiO}_2)_{bN}])}{N} \quad (6)$$

where N is the number of stoichiometric units in the silicate nanocluster and, as in eq 1, we have $a = 2$ and $b = 1$ for the olivine case and $a = b = 1$ for the pyroxene case. Note that in this case we compare the internal energies of a combined system with $(a + 2b)N$ oxygen anions with two smaller systems containing aN and $2bN$ oxygen anions, respectively. In this sense, we refer to these energies as reactive formation energies (RFEs).

Although nanocluster RFEs can be difficult to obtain experimentally, they can be easily evaluated using the calculated energies of our candidate GM nanosilicates and the corresponding GM nanoclusters for $(\text{MgO})_N$[53,54] and $(\text{SiO}_2)_N$.[20] In Figure 9, we plot the RFEs of the P-N and O-N

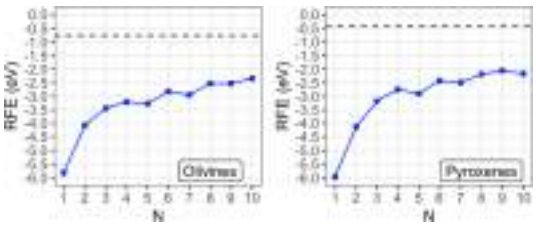

Figure 9. Reactive formation energies (RFEs) for the O-N (left) and P-N (right) silicate nanoclusters with respect to the number of stoichiometric units. In each case, the calculated limiting value of the calculated enthalpy of formation of the respective bulk crystalline silicate is indicated by a dashed line (i.e., forsterite, left; enstatite, right).

nanoclusters (blue lines) with respect to the number of units in each nanocluster. In both cases, the RFE is initially relatively negative because of the high energy stabilization gained from the addition of the smallest and least stable monomeric pure oxide species. With increasing nanocluster size, the internal energies per unit of nanosilicates and the respective pure oxide nanoclusters tend to increasingly stabilize toward the corresponding bulk values. Note that, unlike the simple normalization used to obtain the energy per unit (Figure 7) for the nanoclusters, the RFE energies are dependent on the stabilities of different smaller subclusters for each nanocluster size and thus show some size-dependent fluctuations. However, with increasing size these fluctuations will subside and the RFE values for the P-N series and the O-N nanocluster series will become progressively closer to the calculated bulk enthalpies of formation for enstatite and forsterite, respectively (dashed horizontal lines in Figure 9). Taking the largest O-10 and P-10 nanoclusters, we note that their RFE values are both still >1.5 eV more negative than the respective bulk $\Delta H^{\text{oxides}}_f$ values.

An alternative way to calculate silicate nanocluster formation energies is with respect to the proportions of pure oxide nanoclusters which contain the same number of oxygen anions as in the silicate nanocluster in question. In such a formulation, silicate nanoclusters are compared with oxide nanoclusters of a similar size, thus mirroring the calculation of $\Delta H^{\text{oxides}}_f$ for bulk silicates. The equation for calculating such a "mixing" formation energy (MFE) for nanosilicates is given in eq 7.

$$\Delta H^{\text{oxides}}_{f(\text{mixing})}[\text{nanosilicate}] \approx \Delta E^{\text{oxides}}_{f(\text{size-consistent})}[\text{nanosilicate}] = \frac{E(\text{Mg}_a\text{Si}_b\text{O}_{a+2b})_N - \left(\frac{a}{a+2b}E[(\text{MgO})_{(a+2b)N}] + \frac{2b}{a+2b}E[(\text{SiO}_2)_{\left(\frac{a}{2}+b\right)N}]\right)}{(a+2b)N} \quad (7)$$

The results of the MFE are shown for both pyroxene and olivine systems in Figure 10. As for the RFE values, the MFE

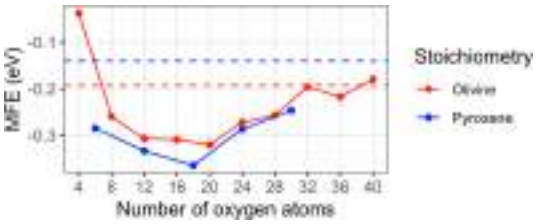

Figure 10. Mixing formation energies (MFEs) of the O-N (red) and P-N (blue) silicate nanoclusters with respect to oxygen content. The dashed lines indicate the calculated bulk enthalpy of formation for forsterite (red) and enstatite (blue) per oxygen atom.

equation implies that with increasing size the MFE will approach the respective enthalpy of formation (per oxygen) of the corresponding bulk. The MFE compares the energy of any particular silicate nanocluster with that of a proportional mix of pure oxide nanoclusters possessing the same number of oxygen cations. As such, the MFE values are not dominated by the energy liberated in a reaction of smaller pure oxide nanoclusters and, unlike the RFE values, do not simply tend to increase monotonically with increasing silicate nanocluster size. Instead, starting from the smallest considered nanoclusters, the MFE values for both pyroxene and olivine nanoclusters initially decrease with increasing size. For nanosilicates with more than approximately 18 oxygen cations, the MFE values in both cases tend to then increase toward their respective bulk limits. Curiously, although the bulk enthalpy of formation per oxygen atom (and thus the bulk MFE) is more negative for forsterite than for enstatite, for the range of oxygen content considered for the nanosilicates the MFE values are more negative for pyroxene than for olivine. This inversion of the MFE values for small sizes has implications for the relative stabilities of nanosilicates. For example, if we take two silicate nanoclusters with the same oxygen content in this inverted MFE regime, we can calculate the total energies of the following Si/Mg exchange reactions and compare with the corresponding bulk case (in square brackets we also include the bulk reaction energy calculated from data in the JANAF tables[51]):

$$(\text{Mg}_2\text{SiO}_4)_3 + \text{Si} \rightarrow (\text{MgSiO}_3)_4 + 2\text{Mg}, \quad \Delta E = -0.59 \text{ eV}$$

DOI: 10.1021/acsearthspacechem.9b00139
ACS Earth Space Chem. 2019, 3, 2390−2403

$$(Mg_2SiO_4)_6 + 2Si \rightarrow (MgSiO_3)_8 + 4Mg, \quad \Delta E = -0.53 \text{ eV}$$

$$(Mg_2SiO_4)_{\text{forsterite}} + Si \rightarrow (MgSiO_3)_{\text{enstatite}} + 2Mg, \quad \Delta E = +1.11[+1.84 \text{ eV}]$$

These reactions imply that under nonoxidizing conditions (i.e., limited availability of oxygen), it is energetically favorable to convert olivine nanoclusters to pyroxene nanoclusters via the replacement of Mg by Si, while the analogous bulk process is not energetically viable. In astrophysical environments, atomic Si is often depleted into silicate dust and/or SiO molecules, tending to reduce its availability for such processes. At low-enough temperatures, the latter can condense into $(SiO)_N$ nanoclusters[55] which tend to segregate into O-rich (i.e., silica-like) and Si-rich (i.e., silicon-like) subclusters.[23] Because Si−Si bonds are much weaker than Si−O bonds, dust processing in the ISM (e.g., shocks, sputtering) could potentially then lead to the release of Si from the Si-rich parts of such nanograins. We further note that careful estimates of observed Si depletions in various regions of the ISM have recently been incorporated into dust evolution models. This modeling leads to predictions of the sufficient availability of atomic Si for high silicate dust formation rates, especially in a cold neutral medium.[56] Our mechanism provides one possible route whereby such available Si could then be (re)depleted onto olivinic nanograins, leading to the sputtering of Mg to produce pyroxenic species. In particular, the nanoscale thermodynamic preference for pyroxene could provide an additional route for the observed presence of pyroxene dust,[57,58] where bulk thermodynamics would suggest the favored formation of olivine.[59]

IR Vibrational Spectra. Typical IR spectra from amorphous astronomical silicates have two broad peaks centered around 10 μm and 18−20 μm.[4,60] The more intense 10 μm peak is associated with Si−O stretching modes, and the weaker, longer-wavelength peak is linked to O−Si−O bending modes. Like all silicate grains, nanosilicates will absorb infrared (IR) radiation, and because of their ultrasmall size, they are also subject to single-photon heating and thus are likely to produce well-defined IR emission signatures.[60] Under the assumption that the IR wavelengths at which nanosilicates absorb/emit are the same as those typically associated with bulk laboratory silicates, observational spectra can place some limitations on the potential abundance of nanosilicate species. Assuming a single-sized population of spherical grains, for example, the IR emission intensity with respect to wavelength can thus be estimated for different ultrasmall grain sizes. In this way, without violating any observational IR emission constraints, it has been proposed that up to 15% of the silicon in the diffuse ISM could reside in amorphous nanosilicate grains having diameters ≤1 nm.[9] Such approaches to estimate the IR spectra of nanosilicates are based on approximate top-down methods in that they employ simple geometric representations of grain shapes without atomic detail and dielectric responses derived from those of bulk silicates. Our DFT-based calculations allow us to directly and accurately calculate the oscillatory atomic motions associated with IR-active vibrational modes in our atomistically detailed silicate structures. Herein, we use such an approach to calculate the IR vibrational spectra for our O-*N* and P-*N* nanoclusters which all lie in the ≤1-nm-diameter size regime.

A study comparing various functionals for DFT-based calculations of the bulk forsterite crystal using a 28-atom unit cell showed PBE0 to be particularly accurate for capturing silicate atomic structure (differences with respect to experimental parameters are typically <1%) and also for accurately reproducing relative experimental IR oscillator strengths.[61] Reference 62 also showed that the DFT-calculated vibrational frequencies of bulk forsterite using PBE0 were consistently slightly overestimated with respect to experimentally measured values (by 12.3 cm^{-1} on average). To compare our DFT-calculated results more easily with published IR spectra of silicate dust from astronomical observations, we convert the frequencies directly obtained from our calculations to wavelengths in micrometers and add a small amount of Gaussian broadening. We note that an average corrective frequency downshift of 12.3 cm^{-1} would correspond to small corrective wavelength upshifts of only ∼0.1 μm for features close to 10 μm and ∼0.3 μm for features close to 20 μm. In Figures 11 and 12, we show the uncorrected DFT-calculated IR spectra for the O-*N* and P-*N* nanoclusters, respectively. In these figures, we highlight the wavelength range associated with Si−O stretching modes for the respective bulk crystal (gray area) and the wavelengths of the corresponding main crystalline bands within this region (red lines). With respect to the calculated spectra of the corresponding crystalline bulk systems, in the

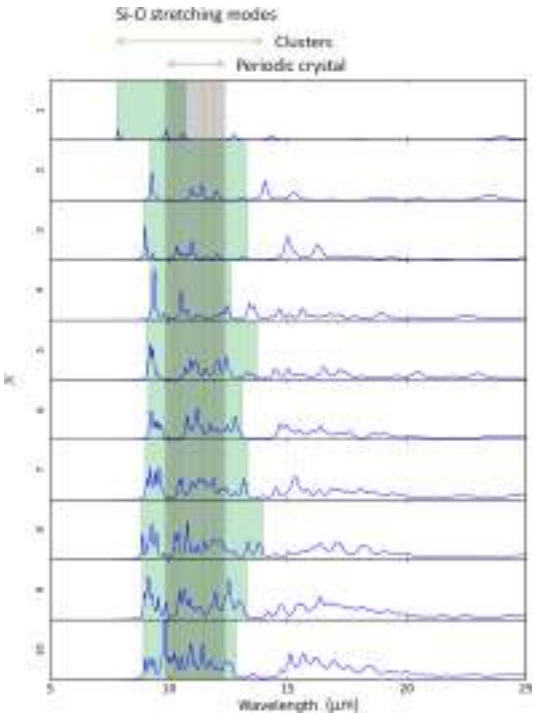

Figure 11. Calculated harmonic IR spectra for the O-*N* nanoclusters with respect to wavelength (blue line). The gray shaded region spans the wavelength range corresponding to Si−O stretching modes calculated for the bulk forsterite crystal (where vertical orange lines correspond to experimental peak positions of the IR reflection spectra[62]). The green shaded regions show the corresponding wavelength range where Si−O stretching modes can be identified for each nanocluster (note that O−Si−O bending modes can also be found in these regions). The overlap of green and gray regions is indicated by dark-green shading.

DOI: 10.1021/acsearthspacechem.9b00139
ACS Earth Space Chem. 2019, 3, 2390−2403

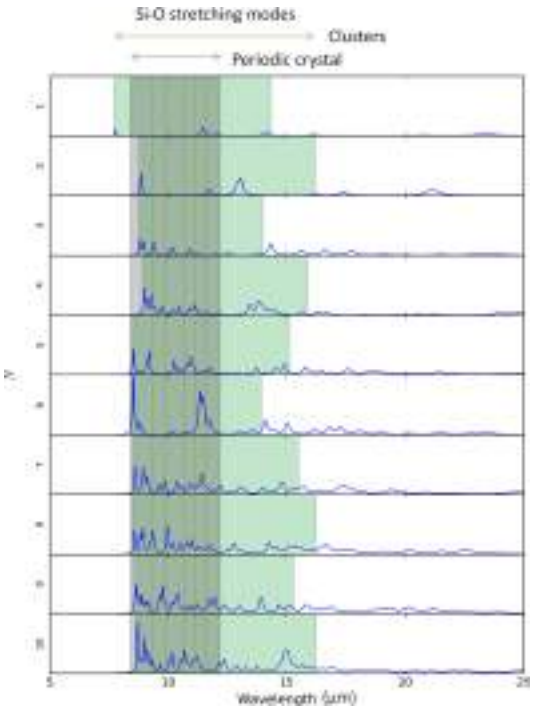

Figure 12. Calculated harmonic IR spectra for P-*N* nanoclusters with respect to wavelength (blue line). The gray shaded region spans the wavelength range corresponding to Si−O stretching modes calculated for the bulk clinoenstatite crystal (where vertical orange lines correspond to experimental peak positions of the mass absorption coefficients[63]). The green shaded regions show the corresponding wavelength range where Si−O stretching modes can be identified for each nanocluster. (Note that O−Si−O bending modes can also be found in these regions.) The overlap of green and gray regions is indicated by dark-green shading.

nanoclusters the lower-wavelength peaks corresponding to Si−O asymmetric stretching tend to cover a broader wavelength range (green shading in Figures 11 and 12). These regions tend to be reasonably symmetrically broadened in the O-*N* nanoclusters with respect to that for forsterite. For the pyroxene nanoclusters, however, the region of Si−O stretching modes starts at a very similar wavelength to that in bulk enstatite but then extends to much longer wavelengths (often to >15 μm as compared to the bulk enstatite upper limit of ∼12 μm). Such differences are likely due to the distinct size-induced atomic structure of the nanoclusters (see above) relative to the periodic atomic order found in crystalline bulk systems.

Unlike typical IR spectra from astronomical silicate sources, the calculated IR spectra of the individual nanoclusters clearly have a great deal of discernible detail because of the fact that these small nanoclusters possess a relatively small number of vibrational degrees of freedom. This molecular-like character is clearly more evident in the smaller clusters than in the larger nanosilicates, where individual peaks start to overlap to form broader features. Even for the larger nanosilicate clusters considered, however, there are a number of significant distinct peaks in the 8−12 μm region. It is of note that very few of the individual nanocluster spectra have significant IR oscillator strengths at or very close to 10 μm (e.g., O-10). As such, it is not clear to what extent silicate nanoclusters would contribute to the observed 10 μm Si−O stretching feature. We also note that, generally, the well-defined peaks in the Si−O stretching regions of the nanocluster spectra do not coincide with those of the corresponding bulk crystal. In those few cases where there is a match between nanocluster and bulk IR Si−O peaks (e.g., for O-8 and P-8), this is clearly not due to a structural correspondence between the two systems and is likely just a coincidence.

For longer wavelengths, none of the pyroxene clusters exhibit significant IR peaks beyond 15−17 μm. For the olivine clusters, some discernible IR peaks can be found at up to 18 to 19 μm. The double-peaked spectra observed for noncrystalline astronomical silicates are best matched by the spectra for O-*N* nanoclusters, especially for $N \geq 6$. For this set of nanoclusters, two main regions of the spectra can be distinguished: (i) a Si−O stretching region between approximately 8 and 14 μm and (ii) a longer-wavelength region between 14 and 21 μm. In the latter region, the more intense peaks tend to be found in the 15−18 μm range and are thus at shorter wavelengths than usually observed for astronomical silicate dust (i.e., 18−20 μm).

We note that our reported spectra correspond only to the lowest-energy GM silicate nanoclusters and do not currently consider contributions from metastable nanosilicate isomers in the size range considered. A comparison of DFT-derived IR spectra with spectra from cluster beam experiments indicates that the contributions from the lowest-energy cluster isomers often dominate the measured spectra.[64] However, in astrophysical environments, various processing phenomena could yield distributions of nanoclusters that are not dominated by thermodynamics and that have contributions from large ensembles of dust particles with diverse structures. To begin to see the effect of mixing spectra from nanosilicate grains with different structures and sizes, in Figure 13 we show

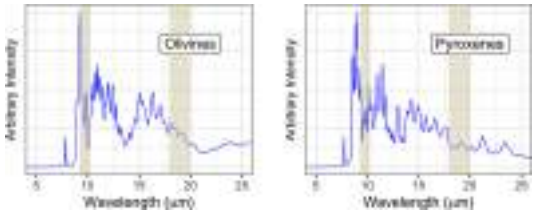

Figure 13. Spectra resulting from equally weighted sums of (i) all spectra from O-*N* nanoclusters in Figure 11 (left) and (ii) all spectra from P-*N* nanoclusters in Figure 12 (right). Shaded bars indicate typical wavelength ranges for the two main features assigned to noncrystalline silicate dust.

the spectra resulting from equally weighted sums of all O-*N* spectra (left) and of all P-*N* spectra (right). In Figure 13, we also highlight wavelength regions typical of astronomical silicate IR spectra with gray areas at 9.7 ± 0.5 μm and at 18−20 μm. Consistent with the above discussion of IR spectra of individual nanoclusters, in both summed spectra in Figure 13 we find that the 18−20 μm region is relatively weak and instead we have greater intensity in the 14−18 μm range. In both spectra we also find two main peaks on either side of 10 μm rather than a single feature peaking at around 10 μm. In

DOI: 10.1021/acsearthspacechem.9b00139
ACS Earth Space Chem. 2019, 3, 2390−2403

both cases, we also find a sharp feature at around 9.1 μm and a broader set of less intense peaks spanning a wavelength range approximately between 10.2 and 12.5 μm.

The clear difference between our calculated IR nanosilicate spectra and those typically observed and assigned to silicate dust raises some questions. For example, the poor match between our calculated IR spectra and those observed in circumstellar outflows of evolved stars (where the nucleation of nanosilicates is thought to occur) could provide evidence that nucleation predominantly occurs on other seed species rather than on nanosilicates forming directly. Another possibility could be that nanosilicates in such environments are present but are very short-lived species (because of growth into larger grains) and thus their net populations are very small. Generally, our accurate calculated data for silicate nanoclusters in the $\leq$1-nm-diameter size regime show that the assumption that nanosilicates display IR spectra analogous to those of bulk silicates is not always valid. As such, much care should be taken when assessing the astronomical abundances of nanosilicates based on bulk silicate interpretations of observed IR spectra.[9]

■ CONCLUSIONS

Through the development of an IP that has been specifically tuned for describing the structures and energetics of nanosilicates, we perform extensive global optimization searches to find new candidate GM isomers for olivine $(Mg_2SiO_4)_N$ and pyroxene $(MgSiO_3)_N$ nanoclusters for N = 1−10. Using quantum chemical DFT calculations, we refine our search results to obtain more accurate energies, structures, and properties of our obtained nanosilicates. In particular, we track the evolution of chemical structure, relative energies, energies of formation, ionic charge distributions, and IR spectra with nanocluster size and composition. Whenever possible we compare these results with those from analogous accurate calculations on bulk silicate crystals (i.e., enstatite and forsterite).

Both O-*N* and P-*N* nanoclusters tend to have rather irregular structures with only a few exhibiting symmetric or nearly symmetric atomic arrangements. Although there is no indication of crystalline structure, in all cases, some of the larger O-*N* nanoclusters have all of their $[SiO_4]^{4-}$ units as nonpolymerized isolated species and also begin to exhibit occasional six-coordinate Mg^{2+} cations, as found in the corresponding bulk forsterite crystal. The sizes and structures of our reported nanoclusters are also strongly linked to their ionic charge distributions. We find that the magnitude of the average atomically partitioned charges of the oxygen anions and magnesium cations decreases with increasing size of both O-*N* and P-*N* nanoclusters toward their respective bulk values. However, in line with their rather irregular structures there is a large scattering of cationic and anionic charges in all nanoclusters.

Within the set of nanoclusters studied, we find that some have relatively high energy stabilities with respect to other nanoclusters of the same composition and similar size (e.g., O-9 and P-5) and are thus predicted to be magic number clusters at low temperatures. For larger nanoclusters, extrapolating how the energy stability per unit of the O-*N* and P-*N* series evolves with increasing size, we roughly estimate that a crossover to bulklike crystalline stability would require having silicate nanoparticles with at least ∼2000 atoms (pyroxene) and ∼6000 atoms (olivine). The energies of formation of our magnesium silicate nanoclusters with respect to the reaction from constituent subclusters of MgO and SiO_2 (i.e., the RFE values) approach the corresponding bulk crystal energies of formation from below in a nearly monotonically increasing fashion. The energies of formation of our silicate nanoclusters were also calculated with respect to a normalized mixture of MgO and SiO_2 nanoclusters, both with the same oxygen content as the silicate nanocluster under consideration, (i.e., the MFE values). With increasing size the silicate nanocluster MFE values should converge to the energy of formation values per oxygen atom of the respective bulk silicate. Unlike for RFE values, the MFE values pass through a minimum (for nanoclusters containing 18−20 oxygen anions) before approaching toward bulk values for larger nanocluster sizes. For sizes near this minimum, the MFE values for pyroxene nanoclusters are lower than those for olivine nanoclusters, which is the inverse of the situation for the bulk energies of formation per oxygen atom for enstatite and forsterite, respectively. This unexpected higher stability for small pyroxene nanoclusters relative to olivine nanoclusters, under conditions when oxygen availability is limited, has potential implications for astrophysical dust processing and/or formation (e.g., circumstellar environments, the ISM, and exoplanetary atmospheres).

Finally, we report the calculated harmonic IR spectra of all considered silicate nanoclusters. As expected from their small size, all spectra have a number of discernible peaks. However, in line with their noncrystalline structures, few of the peaks in the nanosilicate spectra have wavelengths which match those of the IR spectra from bulk silicate crystals. For the Si−O stretching region, the O-*N* and P-*N* nanoclusters typically have IR peaks with both longer and shorter wavelengths than those found for forsterite and enstatite, respectively. The O−Si−O bending band of typical IR spectra for astronomical silicates typically covers an 18−20 μm range. In the P-*N* nanoclusters, we find very little intensity for the O−Si−O bending modes. For the O-*N* nanoclusters, we find more significant peaks for these modes but with the highest intensity concentrated over a 15−18 μm interval. A sum of spectra for each respective nanosilicate family confirms this general picture and also highlights that the 10 μm Si−O bending feature for our nanosilicates tends to be split into two components above and below 10 μm.

Overall, we provide a systematic bottom-up study of the structure, energetics, and properties of stable Mg-rich nanosilicates with both olivine and pyroxene stoichiometries. Our results, based on accurate electronic structure calculations of atomically detailed nanoclusters, highlight clear differences between nanosilicates and bulk silicates and how the former approaches the latter with increasing size. Our analyses thereby underline the limitations of trying to understand and rationalize the properties of ultrasmall nanosilicate grains by using traditional top-down approaches extrapolating from bulk silicate properties. Overall, we provide a new platform for an accurate and detailed understanding of nanoscale silicates which we hope will be of use in both earth and space sciences.

■ ASSOCIATED CONTENT

Supporting Information

The Supporting Information is available free of charge on the ACS Publications website at DOI: 10.1021/acsearthspacechem.9b00139.

DOI: 10.1021/acsearthspacechem.9b00139
ACS Earth Space Chem. 2019, 3, 2390−2403

Parameters for the MgFFSiOH IP, parameters used for fitting energy versus size data, IP versus DFT relative energy correlation plots using different IPs for $(Mg_2SiO_4)_6$ and $(MgSiO_3)_7$ isomers, free-energy-corrected $\Delta^1(N)$ and $\Delta^2(N)$ values for all O-*N* and P-*N* nanoclusters, and Cartesian coordinates for all O-*N* and P-*N* nanoclusters (PDF)

AUTHOR INFORMATION

Corresponding Authors

*E-mail: Scott.Woodley@ucl.ac.uk

*E-mail: s.bromley@ub.edu

ORCID

Tomas Lazaukas: 0000-0002-8351-9857

Scott M. Woodley: 0000-0003-3418-9043

Stefan T. Bromley: 0000-0002-7037-0475

Notes

The authors declare no competing financial interest.

ACKNOWLEDGMENTS

S.T.B. and A.M.E. acknowledge financial support from the Spanish MINECO/FEDER CTQ2015-64618-R research project, the Ministerio de Ciencia, Innnovación y Universidades (MCIU) Spanish Structures of Excellence María de Maeztu program through grant MDM-2017-0767, and, in part, by Generalitat de Catalunya (grants 2017SGR13 and XRQTC). The Red Española de Supercomputación (RES) is also acknowledged for the provision of supercomputing time. We also acknowledge EU COST Action (CM1401) "Our Astro-Chemical History". S.M.W. and T.L. acknowledge support from EPSRC grants (EP/I03014X and EP/K038958) and computer facilities from UCL, and, via membership in the UK's HEC Materials Chemistry Consortium (which is funded by EPSRC (EP/L000202 and EP/R029431)), the ARCHER UK National Supercomputing Service (http://www.archer.ac.uk) and the UK Materials and Molecular Modelling Hub for computational resources (MMM Hub, which is partially funded by EPSRC (EP/P020194)). We also acknowledge help from Ms. Clara Aler Tubella for graphic arts design.

REFERENCES

(1) Lutgens, F. K.; Tarbuck, E. J.; Tasa, D. *Essentials of Geology*, 11th ed.; Pearson Prentice Hall, 2012.

(2) Hochella, M. F.; Lower, S. K.; Maurice, P. A.; Penn, R. L.; Sahai, N.; Sparks, D. L.; Twining, B. S. Nanominerals, Mineral Nanoparticles, and Earth Systems. *Science (Washington, DC, U. S.)* **2008**, *319* (5870), 1631−1635.

(3) Plane, J. M. C. Cosmic Dust in the Earth's Atmosphere. *Chem. Soc. Rev.* **2012**, *41* (19), 6507.

(4) Henning, T. Cosmic Silicates. *Annu. Rev. Astron. Astrophys.* **2010**, *48* (1), 21−46.

(5) Molster, F. J.; Kemper, C. Crystalline Silicates. *ISO Science Legacy*; Springer-Verlag: Berlin, 2005; Vol. *119*, pp 3−28. .

(6) Gail, H.-P.; Sedlmayr, E. *Physics and Chemistry of Circumstellar Dust Shells*; Cambridge University Press: Cambridge, 2013. .

(7) Bringa, E. M.; Kucheyev, S. O.; Loeffler, M. J.; Baragiola, R. A.; Tielens, A. G. G. M.; Dai, Z. R.; Graham, G.; Bajt, S.; Bradley, J. P.; Dukes, C. A.; et al. Energetic Processing of Interstellar Silicate Grains by Cosmic Rays. *Astrophys. J.* **2007**, *662* (1), 372−378.

(8) Kemper, F.; Vriend, W. J.; Tielens, A. G. G. M. The Absence of Crystalline Silicates in the Diffuse Interstellar Medium. *Astrophys. J.* **2004**, *609* (2), 826−837.

(9) Li, A.; Draine, B. T. On Ultrasmall Silicate Grains in the Diffuse Interstellar Medium. *Astrophys. J.* **2001**, *550* (2), L213−L217.

(10) Charnay, B.; Bézard, B.; Baudino, J.-L.; Bonnefoy, M.; Boccaletti, A.; Galicher, R. A Self-Consistent Cloud Model for Brown Dwarfs and Young Giant Exoplanets: Comparison with Photometric and Spectroscopic Observations. *Astrophys. J.* **2018**, *854* (2), 172.

(11) Burrows, A.; Sharp, C. M. Chemical Equilibrium Abundances in Brown Dwarf and Extrasolar Giant Planet Atmospheres. *Astrophys. J.* **1999**, *512* (2), 843−863.

(12) Jäger, C.; Dorschner, J.; Mutschke, H.; Posch, T.; Henning, T. Steps toward Interstellar Silicate Mineralogy. *Astron. Astrophys.* **2003**, *408* (1), 193−204.

(13) Wales, D.; Doye, J. P. K. Global Optimization by Basin-Hopping and the Lowest Energy Structures of Lennard-Jones Clusters Containing up to 110 Atoms. *J. Phys. Chem. A* **1997**, *101* (97), 5111−5116.

(14) Lazauskas, T.; Sokol, A. A.; Woodley, S. M. An Efficient Genetic Algorithm for Structure Prediction at the Nanoscale. *Nanoscale* **2017**, *9* (11), 3850−3864.

(15) Blum, V.; Gehrke, R.; Hanke, F.; Havu, P.; Havu, V.; Ren, X.; Reuter, K.; Scheffler, M. Ab Initio Molecular Simulations with Numeric Atom-Centered Orbitals. *Comput. Phys. Commun.* **2009**, *180* (11), 2175−2196.

(16) Adamo, C.; Barone, V. Toward Reliable Density Functional Methods without Adjustable Parameters: The PBE0 Model. *J. Chem. Phys.* **1999**, *110* (13), 6158−6170.

(17) Lamiel-Garcia, O.; Ko, K. C.; Lee, J. Y.; Bromley, S. T.; Illas, F. When Anatase Nanoparticles Become Bulklike: Properties of Realistic TiO_2 Nanoparticles in the 1−6 nm Size Range from All Electron Relativistic Density Functional Theory Based Calculations. *J. Chem. Theory Comput.* **2017**, *13* (4), 1785−1793.

(18) Li, Z.; Scheraga, H. A. Monte Carlo-Minimization Approach to the Multiple-Minima Problem in Protein Folding. *Proc. Natl. Acad. Sci. U. S. A.* **1987**, *84* (19), 6611−6615.

(19) Bromley, S. T.; Flikkema, E. Columnar-to-Disk Structural Transition in Nanoscale $(SiO_2)_N$ Clusters. *Phys. Rev. Lett.* **2005**, *95*, 185505.

(20) Flikkema, E.; Bromley, S. T. Dedicated Global Optimization Search for Ground State Silica Nanoclusters: $(SiO_2)_N$ (N = 6−12). *J. Phys. Chem. B* **2004**, *108* (28), 9638−9645.

(21) Jelfs, K. E.; Flikkema, E.; Bromley, S. T. Hydroxylation of Silica Nanoclusters $(SiO_2)_M(H_2O)_N$, M = 4, 8, 16, 24: Stability and Structural Trends. *Phys. Chem. Chem. Phys.* **2013**, *15* (47), 20438−20443.

(22) Cuko, A.; Calatayud, M.; Bromley, S. T. Stability of Mixed-Oxide Titanosilicates: Dependency on Size and Composition from Nanocluster to Bulk. *Nanoscale* **2018**, *10* (2), 832−842.

(23) Bromley, S. T.; Gómez Martín, J. C.; Plane, J. M. C. Under What Conditions Does $(SiO)_N$ Nucleation Occur? A Bottom-up Kinetic Modelling Evaluation. *Phys. Chem. Chem. Phys.* **2016**, *18* (38), 26913−26922.

(24) Goumans, T. P. M.; Bromley, S. T. Efficient Nucleation of Stardust Silicates via Heteromolecular Homogeneous Condensation. *Mon. Not. R. Astron. Soc.* **2012**, *420* (4), 3344−3349.

(25) Cuko, A.; Macía, A.; Calatayud, M.; Bromley, S. T. Global Optimisation of Hydroxylated Silica Clusters: A Cascade Monte Carlo Basin Hopping Approach. *Comput. Theor. Chem.* **2017**, *1102*, 38−43.

(26) Hjorth Larsen, A.; Jørgen Mortensen, J.; Blomqvist, J.; Castelli, I. E.; Christensen, R.; Dułak, M.; Friis, J.; Groves, M. N.; Hammer, B.; Hargus, C.; et al. The Atomic Simulation Environment—a Python Library for Working with Atoms. *J. Phys.: Condens. Matter* **2017**, *29* (27), 273002.

(27) Gale, J. D.; Rohl, A. L. The General Utility Lattice Program (GULP). *Mol. Simul.* **2003**, *29* (5), 291−341.

(28) Dick, B. G.; Overhauser, a. W., Jr; BG Dick; Overhauser, A. Theory of the Dielectric Constants of Alkali Halide Crystals. *Phys. Rev.* **1958**, *112* (1), 90−103.

(29) Woodley, S. M. Knowledge Led Master Code Search for Atomic and Electronic Structures of LaF_3 Nanoclusters on Hybrid

DOI: 10.1021/acsearthspacechem.9b00139
ACS Earth Space Chem. 2019, 3, 2390−2403

Rigid Ion−Shell Model−DFT Landscapes. *J. Phys. Chem. C* **2013**, *117* (45), 24003−24014.
(30) Mora-Fonz, D.; Lazauskas, T.; Farrow, M. R.; Catlow, C. R. A.; Woodley, S. M.; Sokol, A. A. Why Are Polar Surfaces of ZnO Stable? *Chem. Mater.* **2017**, *29* (12), 5306−5320.
(31) Escher, S. G. E. T.; Lazauskas, T.; Zwijnenburg, M. A.; Woodley, S. M. Structure Prediction of $(BaO)_n$ Nanoclusters for $n \leq 24$ Using an Evolutionary Algorithm. *Comput. Theor. Chem.* **2017**, *1107*, 74−81.
(32) Lazauskas, T.; Sokol, A. A.; Buckeridge, J.; Catlow, C. R. A.; Escher, S. G. E. T.; Farrow, M. R.; Mora-Fonz, D.; Blum, V. W.; Phaahla, T. M.; Chauke, H. R.; et al. Thermodynamically Accessible Titanium Clusters Ti_N, N = 2−32. *Phys. Chem. Chem. Phys.* **2018**, *20* (20), 13962−13973.
(33) Mora-Fonz, D.; Lazauskas, T.; Woodley, S. M.; Bromley, S. T.; Catlow, C. R. A.; Sokol, A. A. Development of Interatomic Potentials for Supported Nanoparticles: The Cu/ZnO Case. *J. Phys. Chem. C* **2017**, *121* (31), 16831−16844.
(34) Flikkema, E.; Bromley, S. A New Interatomic Potential for Nanoscale Silica. *Chem. Phys. Lett.* **2003**, *378* (5−6), 622−629.
(35) Pedone, A.; Malavasi, G.; Menziani, M. C.; Segre, U.; Musso, F.; Corno, M.; Civalleri, B.; Ugliengo, P. FFSiOH: A New Force Field for Silica Polymorphs and Their Hydroxylated Surfaces Based on Periodic B3LYP Calculations. *Chem. Mater.* **2008**, *20* (7), 2522−2531.
(36) Macià Escatllar, A.; Ugliengo, P.; Bromley, S. T. Modeling Hydroxylated Nanosilica: Testing the Performance of ReaxFF and FFSiOH Force Fields. *J. Chem. Phys.* **2017**, *146* (22), 224704.
(37) Lewis, G V; Catlow, C R A Potential Models for Ionic Oxides. *J. Phys. C: Solid State Phys.* **1985**, *18* (6), 1149−1161.
(38) Walker, A. M.; Wright, K.; Slater, B. A Computational Study of Oxygen Diffusion in Olivine. *Phys. Chem. Miner.* **2003**, *30* (9), 536−545.
(39) Schröder, K.-P.; Sauer, J.; Leslie, M.; Richard, C.; Catlow, A.; Thomas, J. M. Bridging Hydrodyl Groups in Zeolitic Catalysts: A Computer Simulation of Their Structure, Vibrational Properties and Acidity in Protonated Faujasites (H-Y Zeolites). *Chem. Phys. Lett.* **1992**, *188* (3−4), 320−325.
(40) Woodley, S. M. Structure Prediction of Ternary Oxide Sub-Nanoparticles. *Mater. Manuf. Processes* **2009**, *24* (3), 255−264.
(41) Mauney, C. M.; Lazzati, D. The Formation of Astrophysical Mg-Rich Silicate Dust. *Mol. Astrophys.* **2018**, *12*, 1−9.
(42) Sanders, M. J.; Leslie, M.; Catlow, C. R. A. Interatomic Potentials for SiO_2. *J. Chem. Soc., Chem. Commun.* **1984**, *19*, 1271.
(43) Li, R.; Cheng, L. Structural Determination of $(Al_2O_3)_n$ (N = 1−7) Clusters Based on Density Functional Calculation. *Comput. Theor. Chem.* **2012**, *996*, 125−131.
(44) Oueslati, I.; Kerkeni, B.; Bromley, S. T. Trends in the Adsorption and Reactivity of Hydrogen on Magnesium Silicate Nanoclusters. *Phys. Chem. Chem. Phys.* **2015**, *17* (14), 8951−8963.
(45) Kerkeni, B.; Bromley, S. T. Competing Mechanisms of Catalytic H_2 Formation and Dissociation on Ultrasmall Silicate Nanocluster Dust Grains. *Mon. Not. R. Astron. Soc.* **2013**, *435* (2), 1486−1492.
(46) Bromley, S. T.; Moreira, I. D. P. R. R.; Neyman, K. M.; Illas, F. Approaching Nanoscale Oxides: Models and Theoretical Methods. *Chem. Soc. Rev.* **2009**, *38* (9), 2657−2670.
(47) Chiang, C. M.; Zegarski, B. R.; Dubois, L. H. First Observation of Strained Siloxane Bonds on Silicon Oxide Thin Films. *J. Phys. Chem.* **1993**, *97* (27), 6948−6950.
(48) Hirshfeld, F. L. Bonded-Atom Fragments for Describing Molecular Charge Densities. *Theor. Chim. Acta* **1977**, *44* (2), 129−138.
(49) Viñes, F.; Lamiel-Garcia, O.; Illas, F.; Bromley, S. T. Size Dependent Structural and Polymorphic Transitions in ZnO: From Nanocluster to Bulk. *Nanoscale* **2017**, *9* (28), 10067−10074.
(50) Aguado, A.; López, J. M. Structures and Stabilities of CaO and MgO Clusters and Cluster Ions: An Alternative Interpretation of the Experimental Mass Spectra. *J. Phys. Chem. B* **2000**, *104* (35), 8398−8405.
(51) Malcolm, W.; Chase, J. *NIST-JANAF Thermochemical Tables*; 4th ed.; American Chemical Society: Washington, D.C., 1998.
(52) Zaitsev, A. I.; Arutyunyan, N. A.; Shaposhnikov, N. G.; Zaitseva, N. E.; Burtsev, V. T. Experimental Study and Modeling of the Thermodynamic Properties of Magnesium Silicates. *Russ. J. Phys. Chem.* **2006**, *80* (3), 335−344.
(53) Dong, R.; Chen, X.; Wang, X.; Lu, W. Structural Transition of Hexagonal Tube to Rocksalt for $(MgO)_{3n}$, $2 \leq n \leq 10$. *J. Chem. Phys.* **2008**, *129* (4), 044705.
(54) Chen, M.; Felmy, A. R.; Dixon, D. A. Structures and Stabilities of $(MgO)_n$ Nanoclusters. *J. Phys. Chem. A* **2014**, *118* (17), 3136−3146.
(55) Krasnokutski, S. A.; Rouillé, G.; Jäger, C.; Huisken, F.; Zhukovska, S.; Henning, T. Formation of Silicon Oxide Grains at Low Temperatures. *Astrophys. J.* **2014**, *782* (1), 15.
(56) Zhukovska, S.; Dobbs, C.; Jenkins, E. B.; Klessen, R. S. Modeling Dust Evolution in Galaxies with a Multiphase, Inhomogeneous ISM. *Astrophys. J.* **2016**, *831* (2), 147.
(57) Molster, F. J.; Waters, L. B. F. M.; Tielens, A. G. G. M. G. M.; Barlow, M. J. Crystalline Silicate Dust around Evolved Stars. *Astron. Astrophys.* **2002**, *382* (1), 222−240.
(58) Chiar, J. E.; Tielens, A. G. G. M. Pixie Dust: The Silicate Features in the Diffuse Interstellar Medium. *Astrophys. J.* **2006**, *637* (2), 774−785.
(59) Gail, H.-P. Chemical Reactions in Protoplanetary Accretion Disks. IV. Multicomponent Dust Mixture. *Astron. Astrophys.* **1998**, *332*, 1099−1122.
(60) Draine, B. T. Interstellar Dust Grains. *Annu. Rev. Astron. Astrophys.* **2003**, *41* (1), 241−289.
(61) De La Pierre, M.; Orlando, R.; Maschio, L.; Doll, K.; Ugliengo, P.; Dovesi, R. Performance of Six Functionals (LDA, PBE, PBESOL, B3LYP, PBE0, and WC1LYP) in the Simulation of Vibrational and Dielectric Properties of Crystalline Compounds. The Case of Forsterite Mg_2SiO_4. *J. Comput. Chem.* **2011**, *32* (9), 1775−1784.
(62) Suto, H.; Sogawa, H.; Tachibana, S.; Koike, C.; Karoji, H.; Tsuchiyama, A.; Chihara, H.; Mizutani, K.; Akedo, J.; Ogiso, K.; et al. Low-Temperature Single Crystal Reflection Spectra of Forsterite. *Mon. Not. R. Astron. Soc.* **2006**, *370* (4), 1599−1606.
(63) Jäger, C.; Molster, F. J.; Dorschner, J.; Henning, T.; Mutschke, H.; Waters, L. B. F. M.; Jäger, C.; Molster, F. J.; Dorschner, J.; Henning, T.; Mutschke, H.; Waters, L. B. F. M.; Jäger, C.; Molster, F. J.; Dorschner, J.; et al. Steps toward Interstellar Silicate Mineralogy. IV. The Crystalline Revolution. *Astron. Astrophys.* **1998**, *916*, 904−916.
(64) Haertelt, M.; Fielicke, A.; Meijer, G.; Kwapien, K.; Sierka, M.; Sauer, J. Structure Determination of Neutral MgO Clusters—Hexagonal Nanotubes and Cages. *Phys. Chem. Chem. Phys.* **2012**, *14* (8), 2849.
(65) Goumans, T. P. M.; Bromley, S. T. Hydrogen and oxygen adsorption on a nanosilicate − a quantum chemical study. *Mon. Not. R. Astron. Soc.* **2011**, *414*, 1285−1291.

DOI: 10.1021/acsearthspacechem.9b00139
ACS Earth Space Chem. 2019, 3, 2390−2403

Conclusions

1. We developed a new IP (Mg-FFSiOH) tailored to perform GO for Mg-silicate stoichiometries. From the scatter plots of the relative energy, as calculated with DFT using the PBE0 functional, versus the relative energy, as calculated with Mg-FFSiOH, we find that there is a reasonable correlation between the two sets of energies: r^2=0.57 for $(MgSiO_3)_7$ and r^2=0.68 for $(Mg_2SiO_4)_6$. The results for this IP outperform all commonly used IPs and gives us confidence that our presented results are accurate
2. With the exception of P-1, P-2 and P-6, the rest of the P-N nanoclusters do not present symmetry.
3. As with the P-N nanoclusters, the O-N nanoclusters do not show symmetry with the exception of O-1 and O-2. The nanoclusters show some degree of polymerization of the silica part, which is contrary to the known bulk phase Fo. Overall, the tendency is to decrease the degree of polymerization as the nanocluster size increases. Mg^{2+} cations tend to be placed close to the center of the nanocluster to increase their coordination.
4. The atomic charges calculated within the Hirshfeld partition scheme, the average O-Si-O angle, and the Mg coordination, all show values larger than bulk ones. The importance of each of the structural descriptors in stabilizing the energy is not clear. Although in many silicate systems the O-Si-O angle is thought to be one of the most important factors to describe the energetic stability of the nanoclusters, the presence of four-member rings indicate that other energetic contributions (e.g., Mg coordination, Mg coordination shape, surface effects…) that we have not been able to identify can play a more important role. The O-N nanoclusters are closer to the corresponding bulk value than the P-N nanoclusters
5. In the P-N series, the first and second order energy differences as defined in the paper show that the P-5 cluster is particularly stable, and thus corresponds to a magic cluster. For the O-N nanoclusters, there is a series of magic clusters following the 3N sizes.
6. Although the structural parameters seem to suggest that O-N clusters are closer to the bulk, in terms of energy the P-N clusters are slightly closer to the bulk limit. This is a rather surprising result since (i) Fo is thermodynamically more stable than En and (ii) for the same number of formula units, the O-N clusters have more atoms, and therefore it would be expected to be closer to the bulk values. If the energy comparison is done with respect to oxygen content, we find that the P-N nanoclusters have lower energy per oxygen atom than the O-N nanoclusters, as opposed to the bulk system.
7. In terms of IR spectra, although the nanoclusters are amorphous and thus would generally be fitted with the broad 10 μm feature, we show that, due to the small number of atoms in the clusters, the IR spectrum of each individual nanocluster is

composed of a wide distribution of signals with no visual correspondence to those typical of astronomical silicates. Adding together the IR spectrum for each stoichiometry separately we can highlight the most important features and test whether the resulting spectra would appear as a gaussian distribution. Even the added spectra of the particles show large deviations from the expected behavior, with several strong features appearing. The 10 μm feature is shifted to lower wavelengths and a strong wide feature at 11.5 μm appears. On the other hand, we don't find features in the 18 to 20 μm range, but rather at quite smaller wavelengths around ~15 μm. Such results point towards the inadequacy of the usage of bulk parameters to extrapolate the IR spectra of nanoclusters and highlights the need to reevaluate the presence of silicates in the ISM as calculated with IR spectroscopy.

Chapter 11: Assessing the viability of silicate nanoclusters as carriers of the anomalous microwave emission: A quantum mechanical study

Introduction

The Microwave radiation (i.e, from 300 MHz to 300GHz) received by radio telescopes is composed of two main components: i) a background component, the cosmic microwave background (CMB), assigned to echoes of early stages of the universe, and ii) foreground components, which can be ascribed to different mechanisms: thermal emission by dust grains, synchrotron radiation and free-free emission. However, observations in the late 90s showed the existence of a bump in the region between 10 to 60 GHz[78,79]. Some controversy over the existence of such bump followed until its clear detection in the Perseus[103] and the ρ-Ophiuchus[104] molecular clouds. As the mechanism that caused the emission is not yet clear, this feature has been named the Anomalous Microwave Emission (AME). Since then, studies trying to localize the AME have shown that such emission is ubiquitous[105,106] in the ISM. Furthermore, the importance of the AME was highlighted in at least two studies which showed that AME accounts for 25 to 45% of the radiation emitted at 23 GHz in the direction of the galactic plane[107,108]. Moreover, the AME has been recently detected in Herbig stars[109] and nearby galaxies[110].

While several hypothesis have been put forward as for which mechanism is responsible for the AME[111,112], the mechanism that better fits the observations is the spinning dust mechanism proposed by Draine and Lazarian[113,114]. The spinning dust mechanism uses classical mechanics to describe the emission and intensity of rotational emission from "ultra-small dust particles" -i. e nanoclusters having radii between ~5 Å to 20 Å- subject to a large number of torques arising from the conditions of the ISM, such as plasma-drag or collision with H and He ions. This mechanism is supported by several factors. First, spatial correlation of the intensity of the AME with dust emission in the IR links these two emissions in some manner[105,106]. Second, the model predicts that the H column density, a trace of dust growth, should be inversely proportional to the intensity of AME, as a consequence of the coalescence of nanoclusters in large grains[104,115,116]. Third, the polarization of the AME is consistent with that of dust nanoclusters[117]. Finally, the studies done with the space telescope Planck showed that the maximum intensity of the feature is not constant, but rather appears to be displaced towards higher frequencies, which can be described by rotation of smaller, faster nanoclusters[116].

Although the spinning dust model fit observations particularly well, two important caveats prevent the use of the AME to obtain properties of the environment in which it is found. To emit radiation due to rotation, the nanoclusters require to have sufficiently large permanent dipole moment, which is required to be larger as the size increases. Second, the shape of the particle and the orientation of the dipole moment with respect to the principal moments of inertia plays an important role on the intensity of the emission. The

spinning dust model can thus work well with almost any particle type provided that the combination of abundance-permanent dipole moment allows for large enough emissivity.

The detection of IR features associated with C-H and C-C stretching and bending modes of polyaromatic hydrocarbons (PAHs) -i.e, the features at 3.3, 6.2, 7.7, 8.6, 11.2 μm- brought the confirmation of the presence of molecules with radius as small as 5 Å[118,119], which could have an abundance of 5 to 10% of the C mass[120]. Thus, PAHs have been regarded as the main ultra-small species and the most likely candidate for the AME emission. Other candidates based on carbon-based species are nanodiamonds, as proposed by Greaves et al.[109]

Instead of the dipole moment, the astrophysics community use the parameter β, defined as $\beta = \frac{\mu}{\sqrt{N}}$, with μ being the dipole moment in Debyes, and N the number of atoms, to describe the average dipole moment need by PAH molecules to have the required emission. In the work of Draine[114], the value of β was set to 0.4, and such value has been implemented in the results of the Planck Collaboration[108].

β = 0.4				
N	Dipole moment	Selected Molecules	N	Dipole moment (β)
10	1.26	Benzonitrile[121]	13	4.18 (1.15)
15	1.54	Ethylbenzene[122]	18	0.59 (0.14)
20	1.79	Azulene[123]	18	0.8 (0.19)
50	2.82	Fluorene[123]	23	0.56 (0.02)
100	4	Coronene[123]	36	0 (0)
150	4.5	N-Coronene[124]	36	5.48 (0.91)

Table 5. Left: approximate dipole moment of molecules with selected N values assuming $\beta = 0.4$, and right, dipole moment of some astronomically relevant PAH with the calculated β values.

However, it is still not clear that PAHs are the carriers of the AME. PAHs are mainly non-polar molecules as they are mostly constituted by non-polar C-H and C-C bonds. In addition, most of the molecules are symmetric. Hence, most of the studied PAHs have very small or even no dipole moment. In Table 5 we report the dipole moment of some pure PAH molecules and some which contain N in their structure, as well as a list of the dipole moment particles of size N should have in order to comply with $\beta = 0.4$. Some arguments have been put forward in order to justify the possible large dipole moment in such grains, such as the possibility of having radicals, charged states, or N substituted PAHs. As can be seen in the table, N substitution allows for large values of dipole moment, but it does not seem likely that the combination of abundance and dipole moment of such species allows one to explain the entirety of AME emission. An important observational result is also contrary to the PAHs as the carriers of the AME. If PAHs were indeed the source of the AME, the emission in the IR should be correlated with the AME emission. However, a recent study[80] has shown that this is not the case, but still found excellent correlation between dust IR emissivity and AME emissivity.

As PAHs are questioned as being the source of AME, research is going back to investigate other dust species as carriers of the AME. The similar dust population between carbonaceous and silicate dust has brought forward the possible contribution of silicates to the AME. Since there is no experimental measure of the dipole moment of silicate nanoclusters, two separate works[81,82] have tried to determine the required values of dipole moment of silicates nanoclusters in order to account for the entirety of the AME. The two studies arrive to similar conclusions: if the fraction of nanosilicates (Y_{Si}) is between 0.04 to 0.14, silicates could account for the entirety of the AME if $\beta \approx 0.3 - 0.4$ without violating any other observational constraint. The presence of the dipole moment is justified by random orientation of Si-O bonds. However, such justification does not seem likely, as SiO_4 tetrahedrons are fairly rigid.

Dipole moments can be readily obtained with *ab initio* quantum chemical methods for any particular structure in its ground state or in other electronic states. Thus, we have used the results from the previous GO study to evaluate the dipole moment of our silicate nanocluster global minima candidates. While Mg-rich silicates are generally thought to be the most abundant silicon bearing species, molecular SiO is detected in large quantities and in a wide variety of environments. Moreover, the SiO molecule can condense in cold environments, as shown in the literature[125], which appears to be the most viable route to the formation of silicates in the ISM. Hence, $(SiO)_N$ is another potential viable carrier of the AME. As GO of the $(SiO)_N$ molecule are readily available in the literature[66], we also included $(SiO)_N$ nanoclusters in our study.

Even if thermodynamic arguments suggest that the most stable structure should be the most abundant, the conditions at which silicates form in different astronomical conditions could be controlled by kinetic effects rather than thermodynamics. Thus, in addition to the size evolution of the dipole moment we evaluate the dipole moment of a range of 150 structures up to 1.5 eV higher in energy than the global minima candidate for the O-6 and P-6 sizes. This test allows us to both obtain a view of the energetic distribution of dipole moments as well as check the robustness of our results in the event that our structures are not the global minima or in the case that astrosilicate nanoclusters are composed of several high-lying isomers. As astrosilicates could contain $\mathbf{Fe^{2+}}$ we evaluate the effect of substituting one $\mathbf{Mg^{2+}}$ cation for a $\mathbf{Fe^{2+}}$ cation in all positions of the P-4 structure in order to explore the possible variations due to $\mathbf{Fe}$ incorporation. Finally, we also evaluated the differences in dipole moment caused by the formation of anions (Z=-1) and cations (Z=1), which are expected to be in abundance in some astronomical environments[67].

Polarization of the AME and IR requires the grains to be non-spherical and some authors[71,72,126] have tried to obtain plausible axial ratios of the particles based on the observed polarization. From our calculations, the ratios of the moments of inertia can be evaluated, and assuming ellipsoidal shapes of homogeneous density the ellipsoids semi-axis can be calculated.

The moments of inertia, obtained directly from the structure, are also a requirement to compute the rotational constants of the nanoclusters, which correspond to the most

fundamental value required to evaluate the rotational spectra of molecules/nanoclusters[127]. In this work we provide the rotational constants for all the studied nanoclusters. The calculation of the rotational spectra of rigid-rotor diatomic/linear molecules can be computed analytically, but for asymmetric top rotors this is not the case. Yet, the spectra of asymmetric top rotors can be computed by assuming that the rotational wavefunction can be described as a linear combination of symmetric rotor functions[128]. Free codes are available to diagonalize the rotational Hamiltonian. In this work, we used the ASROT code from the PROSPE website[129] to compute the rigid-rotor energy levels and Einstein coefficient of spontaneous emission of our nanoclusters. With the Einstein coefficient of spontaneous emission between two states (A_{ij}), the transition frequencies, and the population of each rotational level obtained from Boltzmann statistics, we compute the emissivity of our nanoclusters in every wavelength for typical MC conditions, and compare this model with existing models based on classical mechanics. As we used the rigid-rotor approximation to describe our spectra, in Appendix 4 we provide an estimate of the order of magnitude difference due to the inclusion of centrifugal terms. The centrifugal constants for the P-1, O-1 and P-2 nanoclusters are determined by anharmonic frequency calculations as described in the paper of Barone[130], using the Gaussian code[131].

Finally, the vertical ionization potential ($\mathrm{IP_V}$) and the vertical electron affinity ($\mathrm{EA_V}$) are reported. These parameters are required to determine the charge state of the particles and can also determine the interaction and temperature -through photoelectron emission- of the environment in which the nanoclusters are[67].

Results

A&A 634, A77 (2020)
https://doi.org/10.1051/0004-6361/201936419

Astronomy & Astrophysics

Assessing the viability of silicate nanoclusters as carriers of the anomalous microwave emission: a quantum mechanical study

A. Maciá Escatllar[1] and S. T. Bromley[1,2]

[1] Departament de Ciència de Materials i Química Física Institut de Química Teòrica i Computacional, Universitat de Barcelona, C/Martí i Franquès 1, 08028 Barcelona, Spain
[2] Institució Catalana de Recerca i Estudis Avançats (ICREA), 08010 Barcelona, Spain
e-mail: s.bromley@ub.edu

Received 31 July 2019 / Accepted 10 January 2020

ABSTRACT

Nanosized silicate dust is likely to be abundant in many astronomical environments and it is a prime candidate for being the source of the anomalous microwave emission (AME). To assess the viability of silicate nanoclusters as AME carriers, their detailed properties need to be established. Using quantum chemical calculations, we compute the accurate chemical and electronic structures of three families of nanoclusters with astrophysically relevant compositions: Mg-rich olivine $(Mg_2SiO_4)_N$, Mg-rich pyroxene $(MgSiO_3)_N$, and silicon monoxide $(SiO)_N$, all in the the ≤1 nm diameter size regime and for neutral and ±1 charge states. From these fundamental data, we directly derive the shapes, ionization potentials, electron affinities, and dipole moments of all nanoclusters. The aspect ratio of the nanoclusters fluctuates significantly with N for small sizes, but especially for the olivine and pyroxene nanoclusters, it tends to stabilize towards ~1.3 for the largest sizes considered. These latter two nanocluster families tend to have mass distributions consistent with approximately prolate ellipsoidal shapes. Our calculations reveal that the dipole moment of all our nanoclusters can be substantially affected by changes in chemical structure (i.e. different isomers for a fixed N), ionisation, and substitution of Mg by Fe. Although all these factors are important, the dipole moments of our Mg-rich nanoclusters are always found to be large enough to account for the observed AME. However, $(SiO)_N$ nanoclusters are only likely to be potential AME contributors when they are both charged and their chemical structures are anisotropically segregated. We also model the emissivity per H of a representative $(Mg_2SiO_4)_5$ nanocluster by directly calculating the quantum mechanical rotational energy levels and assuming a distribution of occupied levels in accordance with equilibrium Boltzmann statistics. We compare our bottom-up results with previously published classical models and show that a population of silicate nanoclusters containing only 1% of the total Si budget can reproduce the AME emissivity.

Key words. dust, extinction – ISM: lines and bands – radio continuum: ISM – radiation mechanisms: general – astrochemistry – molecular data

1. Introduction

The anomalous microwave emission (AME) is detected as a foreground feature which typically peaks between 20 and 30 GHz and extends over a 10–60 GHz range (Dickinson et al. 2018). The AME has been observed in many astrophysical environments including the diffuse ISM (Hildebrandt et al. 2007) and galactic clouds (Watson et al. 2005). It is also likely that AME is fundamentally related to the excess microwave emission observed in circumstellar environments (Ubach et al. 2017; Hoang et al. 2018; Greaves et al. 2018). Nanosized dust grains, hereafter referred to as nanoclusters, are expected to be the origin of the AME due to the spatial correlation of AME with regions of dust infrared (IR) emission (Ade et al. 2011; Casassus et al. 2006; Finkbeiner et al. 2002). In the case of circumstellar shells, a theoretical study by Rafikov (2006) showed that with our current understanding of emission mechanisms, the excess microwave emission observed in circumstellar shells should have a large contribution from spinning dust. Several mechanisms could, in principle, explain the AME depending on the type of grain that produces it. For example, iron-containing nanoclusters could contribute due to their magnetic properties (Draine & Lazarian 1999), while silicate and carbonaceous nanoclusters could emit due to thermal emission (Agladze et al. 1996) and/or rapid spinning (Ali-Haïmoud et al. 2009; Draine & Lazarian 1999, 1998; Erickson 1957; Jones 2009). A recent review of available observational evidence and astrophysical modelling concluded that spinning dipolar nanoclusters are the most likely cause of the AME (Dickinson et al. 2018). As the grain rotation rate must be rather high to account for the AME, studies have focused on nanoclusters with typical diameters of ≤1 nm.

Initially, spinning polycyclic aromatic hydrocarbons (PAHs) were proposed as candidates for the source of the AME (Draine & Lazarian 1998). However, it has since been shown that there is no correlation between the observed IR intensities of PAHs and AME intensities (Hensley et al. 2015), which implies that the AME likely originates from other nanograin carriers (Hensley et al. 2015; Tibbs et al. 2011; Vidal et al. 2011). Although large quantities of both silicate and carbonaceous dust can be verified through their characteristic IR spectra, as yet, there is no clear observational evidence to support any one particular type of nanograin as the general source of the AME. Recently, carbon nanodiamonds have been put forward as a possible source of AME in protoplanetary disks (Greaves et al. 2018). From a bottom-up chemical perspective, one potential problem with this proposal is the origin of the necessary dipoles in such species. As carbon is inherently a non-polar covalently bonded material, one must also provide evidence of

A&A 634, A77 (2020)

an astrophysically feasible process via which a sufficiently high dipole is produced in such potential carriers. Recently, silicate nanoclusters have been proposed as possible general carriers of the AME (Hoang et al. 2016; Hensley & Draine 2017). Here, as the chemical bonding in silicates is more ionic, nanosilicates will intrinsically tend to be polar without the need for invoking external processes for dipole creation.

Currently employed models of microwave emission from spinning nanoclusters allow any type of nanograin to contribute to the AME as long as it is sufficiently abundant and has a large enough dipole moment (Ali-Haïmoud 2013; Dickinson et al. 2018). The work of Draine & Lazarian (1998) established the foundations on how to compute the rotational energy distribution from nanoclusters taking into account the effect of several processes such as grain-gas collisions, photon absorption/emission, H_2 formation on the surface of the grain, interactions with the plasma, etc. Later models developed refinements such as including grain wobbling and precession (Hoang et al. 2010), testing the effect of asymmetric grains (Hoang et al. 2011) or using the Fokker-Planck equation to obtain more accurate rotational energy distributions (Ali-Haïmoud et al. 2009). All these approaches are based on detailed attempts to describe relevant (astro)physical phenomena and how they could affect rotational energy distributions. In such works, estimates of the magnitudes of nanograin dipole moments are based on largely qualitative top-down arguments (i.e. from general considerations of properties of bulk materials). The dipole moments derived by such means may be quite reasonable, however, the lack of a more quantitative and accurate basis for such estimates hinders our ability to test the validity of various potential nanograin sources of AME. In principle, however, the microwave emission from spinning nanoclusters can be derived directly in a more bottom-up manner (i.e. from their detailed chemical/structural/electronic properties) and thus the potential contributions to the AME from different nanocluster types could be calculated and compared theoretically.

Ideally, to obtain the accurate dipole moment of a nanocluster, one requires its atomistically detailed chemical structure, the associated electronic charge distribution and its overall charge. In order to find stable chemical structures of nanoclusters one can employ global optimisation structure searches (Catlow et al. 2010). Further, by using quantum chemical modelling one can then derive the electronic structure of such nanoclusters and various astronomically relevant properties (e.g. dipole moments, IR spectra, heat capacities...). Recently, following such an approach, we reported low energy structures of silicate nanoclusters of both Mg-rich olivine $(Mg_2SiO_4)_N$ and pyroxene $(MgSiO_3)_N$ stoichiometries with $N = 1-10$ (Escatllar et al. 2019), and $(SiO)_N$ nanoclusters with $N = 1-20$ (Bromley et al. 2016). In all cases, the largest considered nanocluster size was of the order of 1 nm diameter. As judged by detections of characteristic IR bands at 10 and 18 μm, Mg-rich silicate dust particles are commonly found in a wide range of astrophysical environments (Fogerty et al. 2016; Kessler-Silacci et al. 2006; Molster et al. 2002; Waelkens et al. 1996). Based only on this high abundance, silicate nanoclusters are a potential candidate source for the AME. Assuming that silicate nanoclusters contain 15% of the total Si budget in the ISM (Li & Draine 2001), Hoang et al. (2016) estimated that silicate nanoclusters may be able to explain the entirety of the observed AME. Molecular SiO is also present in large quantities in the ISM, and its condensation into nanosized species in the cold environment of the ISM has been shown to be viable experimentally (Krasnokutski et al. 2014). As such, $(SiO)_N$ nanoclusters could also be considered as a possible contributor to the AME.

Herein, we derive accurate dipole moments (μ), ionization potentials (IP) and electron affinities (EA) directly from accurate quantum chemical calculations of stable nanoclusters of olivine $(Mg_2SiO_4)_N$, pyroxene $(MgSiO_3)_N$ and $(SiO)_N$ silicon monoxide for neutral, and ±1 charge states and for sizes up to 1 nm in diameter. Where possible we compare our bottom-up derived data with previous reported top-down modelling studies. Although we show that some assumptions in the top-down derivation of nanosilicate properties are inaccurate, we confirm that nearly all our considered olivine and pyroxene nanoclusters do possess dipole moments with magnitudes that are sufficient to lead to significant contributions to the AME. For all our nanoclusters we provide the rotational constants and dipole moments in Appendix B.

To compute the emissivity of our nanoclusters, we employ an alternative approach to the one generally used in the literature. Herein, due to the fact that we have calculated the atomic and electronic structure of a range of stable silicate nanoclusters, we use this information to directly calculate the rotational energy levels in a bottom-up fashion using quantum mechanics. In this respect, our approach is similar to the one used for PAHs as reported by Ysard & Verstraete (2010). In the present work, we apply statistical thermodynamics to compute the population of each rotational level. In effect, this approach assumes that all the physical processes described in the above works act together to bring the nanocluster rotational energy distribution to local thermodynamic equilibrium (LTE). As such, the current methodology should be most accurate in conditions where LTE is likely to be fulfilled, such as molecular clouds or dark clouds, and then only requires an effective rotational temperature. In a future work, we plan to consider non-equilibrium conditions for more accurately modelling other astrophysical environments.

Here we show that quantum chemical modelling can be a powerful and accurate tool for investigating detailed astrophysically relevant properties of silicate nanoclusters. Together with constraints from observation and laboratory studies, our bottom-up approach can complement more traditional top-down modelling approaches. In particular, we aim to provide more secure underpinnings for assessing the properties, abundance and astrophysical relevance of nanosized silicate dust.

2. Methodology

The detailed atomistic structures of all considered Mg-pure Olivine $(Mg_2SiO_4)_N$, Mg-pure Pyroxene $(MgSiO_3)_N$ and silicon monoxide $(SiO)_N$ nanoclusters (hereafter referred to as O-N, P-N and SiO-N, respectively) were obtained from extensive searches of low energy isomers as reported in Escatllar et al. (2019) and Bromley et al. (2016). In each case, the atomistic and electronic structure of all considered nanoclusters were optimised using all-electron density functional theory (DFT) based quantum chemical calculations using the hybrid PBE0 (Adamo & Barone 1999) functional. The calculations were performed using the all-electron FHI-AIMS code (Blum et al. 2009) using a Tier1/light atom-centred numerical basis set which has an accuracy comparable to a TZVP Gaussian-type orbital basis set (Lamiel-Garcia et al. 2017).

From the masses of each atomic species and the optimized atomistic structures of the nanoclusters we can calculate the moments of inertia I_n where $n \in x, y, z$ and where we take: $I_z \geq I_y \geq I_x$. The ratios between moments of inertia allow us to determine the approximate shape of the nanoclusters. Although the moments of inertia are rigorously defined, as we are dealing with species that contain only a few tens of atoms, the derived

measure of nanograin spheroidal shape should be carefully interpreted as being associated with a mass-weighted spatial distribution of different atom types. If $I_z = I_y = I_x$, then $I_x/I_z = 1$ and the mass distribution can be associated with a sphere. When $I_z > I_y$ and $I_y/I_x = 1$, the nanocluster can be described by an oblate spheroid, with the degree of oblateness given by the magnitude of I_z/I_y. Alternatively, the case where $I_y > I_z$ and $I_z = I_y$ corresponds to a prolate spheroid, with the degree of prolateness given by the magnitude of I_y/I_z. In all other cases where the three moments of inertia are different the nanocluster shape can be classed as being between the two limiting oblate and prolate cases.

The dipole moment (μ) of each nanocluster was directly computed from its calculated electron density and nuclear positions. The full electron density ($\rho(r)$) is readily obtained from DFT calculations, allowing to compute μ by:

$$\mu = \int r\rho(r)dr + \sum_A Z_A R_A, \tag{1}$$

where the left-hand integral term corresponds to the electron contribution to μ, and the right-hand term sums over all nuclei A, with nuclear charge Z_A and position R_A. Specifically, we report μ values for P-N and O-N for N = 1–10 and SiO-N for N = 2–20 in their neutral state and ±1 charged states. The IP and EA values were also calculated for all neutral nanoclusters. The IP is defined as the energy required to extract an electron from the highest occupied molecular orbital (HOMO), therefore:

$$\mathrm{IP} = \Delta E_{\mathrm{M}\rightarrow\mathrm{M}^+} = E(\mathrm{M}^+) - E(\mathrm{M}), \tag{2}$$

where E(M) is the total calculated energy of a neutral nanocluster, M, and $E(\mathrm{M}^+)$ is the energy of nanocluster, M, with one electron removed. The EA is defined as the energy released upon attachment of a free-electron onto a nanocluster, with positive sign meaning a release in energy, and negative sign meaning that electron attachment requires energy (Zhan et al. 2003). Hence, it is calculated as:

$$\mathrm{EA} = -\Delta E(\mathrm{M}\rightarrow\mathrm{M}^-) = E(\mathrm{M}) - E(\mathrm{M}^-), \tag{3}$$

where E(M) is the total calculated energy of a neutral nanocluster, M, and $E(\mathrm{M}^-)$ is the energy of nanocluster, M, with one electron added. This definition is consistent with that reported in Weingartner & Draine (2001a). We note that the values reported in this work correspond to vertical EA and IP values (i.e. where the nanocluster structure in its charged and neutral state is unchanged).

The rotational spectrum of a nanocluster can be computed quantum mechanically by calculating the eigenvalues of the rotational Hamiltonian (H_r). For symmetric nanoclusters, the angular momentum operators (P^2: square of the total angular momentum, P_Z: space-fixed angular momentum projection on the Z-axis, and P_z: body-fixed angular momentum projection on the z-axis) commute with H_r and thus the energies can be found easily (Ysard & Verstraete 2010). However, for asymmetric top species, such as most of the nanoclusters in this work, the P_z operator does not commute with H_r. In such cases, the rotational wavefunction can be described as linear combinations of symmetric top wavefunctions, after which the rotational Hamiltonian is diagonalized. For a complete description of the calculation of such rotational spectra, we refer the reader to more detailed sources (Gordy & Cook 1984). Here, we use the ASROT software (Kisiel 2001) from the PROSPE website (Kisiel 2019) to compute the frequencies (ν) in MHz and line intensities (I) in nm^2 MHz at a given temperature (T) of each allowed transition using the rotational constants (B_x). From the two former quantities and using T = 300 K, we can obtain the Einstein coefficient of spontaneous emission for the $i \rightarrow j$ transition (A_{ij}) (Pickett et al. 1998) as:

$$A_{ji} \simeq I_{ji}(T)\nu_{ji}[Q_{rs}(T)/g']e^{E'/kT} \cdot 1.748\times10^{-9}, \tag{4}$$

where ν_{ij} is the transition frequency between the states i and j in MHz, $Q_{rs}(T)$ is the rotational partition function at T = 300 K, g' is the degeneracy of the upper-state ($g' = 2J+1$), E' is the upper state energy in cm^{-1}, k is the Boltzmann constant and 1.748×10^{-9} converts the resulting units to s^{-1}. Q_{rs} can be approximated as:

$$Q_{rs} = \frac{\pi^{1/2}}{\sigma_r}\frac{T^{3/2}}{(\Theta_{r,x}\Theta_{r,y}\Theta_{r,z})^{1/2}}, \tag{5}$$

where $\Theta_{r,n}$ as the rotational temperature for the x, y or z axis. The former approximation of Q_{rs} is valid as long as Θ_r/T is smaller than unity. For our nanoclusters, the values never exceed 0.001 even with T = 10 K. As in the work of Ysard & Verstraete (2010), the total power emitted by a specific transition is calculated as:

$$P(j) = A_{ji}E_{ji}\,J/s. \tag{6}$$

To obtain the power emitted in a given astronomical environment it is further required to add the population fraction of the upper state j ($\frac{N_j}{N_g}$), the total number of nanoclusters in that environment (N_g) and divide by 4π to obtain the power emitted per steradian:

$$P(j) = A_{ij}\cdot\nu_{ij}\cdot h\cdot\frac{N_j}{N_g}\cdot N_g\cdot\frac{1}{4\pi}\,J/s\,sr^{-1}, \tag{7}$$

where h is the Planck constant. Finally, the emissivity is obtained by dividing the given P by the number of hydrogen atoms (n_{H}) in the given environment ($\mathcal{J}/n_{\mathrm{H}} = P/n_{\mathrm{H}}$). From this approach, the only free parameters are the number of nanoclusters, the fraction of nanoclusters in a given energy state j and the number of hydrogen atoms. Most available models compute the population of each rotational level by a detailed description of the physics of each environment (Draine & Lazarian 1998; Ali-Haïmoud et al. 2009; Ysard & Verstraete 2010), including gas-grain collisions, plasma-drag, H_2 formation on the surface of the nanoclusters, energy transfer between vibrational and rotational states and several other mechanisms. Gas-grain interactions and energy transfer between vibrational and rotational states should in principle allow reaching a stationary distribution of the rotational energy. We thus expect that in some dense environments, such as molecular clouds (MC), dark clouds (DC) and reflection nebulas (RN), the populations of each rotational energy level can be approximated by statistical mechanics. The fraction of particles in the state j can then be computed by:

$$\frac{N_j}{N_g} = \frac{g'e^{-E'/kT}}{Q_r(T)}, \tag{8}$$

where T is the rotational temperature of the grain. While the dust T values in Draine & Lazarian (1998) correspond to total grain temperatures, here we take them to be nanocluster rotational temperatures. In Appendix A we show how our results compare with results from Draine & Lazarian (1998) and Ali-Haïmoud et al. (2015) for a fictitious asymmetric PAH with

A&A 634, A77 (2020)

a number of atoms (N_{atoms}) equal to 20 and $\mu = 1.8D$ in selected astronomical environments, confirming that rotational energy in thermal equilibrium can reproduce AME calculations.

The final parameter required is the number of silicate nanoclusters N_c. The works of Weingartner & Draine (2001b) and Li & Draine (2001) provide the basis for most distributions employed in other theoretical studies of AME (Hoang et al. 2010; Draine & Hensley 2016; Ali-Haïmoud et al. 2009). The work of Li & Draine (2001) provides upper abundance limits of silicate nanoclusters with radii ≤1 nm to be <15% of the total Si budget, based on extrapolated IR properties. The study of Weingartner & Draine (2001b) provides a size distribution function capable of reproducing the observed extinction in the Milky Way and Magellanic Clouds. However, the work of Hensley & Draine (2017) and Hoang et al. (2016) suggests that the fraction of small nanosilicate grains could be limited by microwave emission observations. For example, if silicate nanoclusters have large dipole moments, fewer nanoclusters would be needed to reproduce the observed emissivities. In this work, we tentatively explore this possibility by taking a representative nanosilicate containing 21 atoms with Mg_2SiO_4 composition (i.e. O-3) and computing the required abundance of such nanoclusters needed to qualitatively reproduce the results of other reported studies for an MC environment. The population of our representative nanosilicate grain is defined as the total Si atoms per H nucleon (3.65×10^{-5}) as in Weingartner & Draine (2001b), times the fraction of Si atoms contained in nanoclusters (Y_{gr}), divided by the number of Si atoms in each nanocluster (3):

$$N_c = 3.65 \times 10^{-5} \cdot Y_{gr}/3. \quad (9)$$

With our accurate chemical structures, the rotational constants B_n are directly available from:

$$B_n = \frac{h}{8\pi^2 I_n}, \quad (10)$$

where I_n is the moment of inertia corresponding to the one of three orthogonal rotational axes $n \in x, y, z$. In Appendix B we report B_n values for all our nanoclusters.

The spectra derived in this work correspond to rigid-rotor spectra under thermodynamic equilibrium and thus have some intrinsic bias towards longer wavelengths as we do not incorporate the effect of centrifugal distortion. The addition of centrifugal distortion terms is beyond the scope of the present paper as their calculation generally requires significant extra computational effort (Puzzarini et al. 2010). Nevertheless, to estimate the possible effect of distortion constants, we computed the distortion coefficients from anharmonic frequency calculations as described in Barone (2005) for the P-1 and P-2 nanoclusters using the Gaussian16 code (Frisch et al. 2016), employing DFT based calculations with the PBE0 functional and a 6-31G* basis set. In Appendix B we provide an estimate of spectral change due to the inclusion of centrifugal distortion, which ranges from 0.2 to 3% with increasing size, from the P-1 to O-10 nanocluster, respectively.

3. Nanocluster shape

In Fig. 1A and B, we plot I_y/I_x versus I_z/I_x for all considered nanocluster structures in order to provide an overview of their shape distribution. In principle, amorphous grains (i.e. with no long-range crystalline atomic order) should not have any preferred growth directions. As such, in the absence of external anisotropic factors, the intrinsic average shape of amorphous grains is expected to be spherical. In contrast, for example, crystalline grains tend to exhibit facetted morphologies and are thus intrinsically non-spherical (Zamirri et al. 2019). The nanocluster structures presented in our work are clearly not crystalline and hence it may be expected that they would become spherical as their size increases. Interestingly, we actually find that many of our silicate nanoclusters are still far away from being spherically symmetric for the size range we consider. In general, a large fraction of nanoclusters is found inside the prolate area of the plot. The largest O-N nanoclusters are prolate with two moments of inertia 40% larger than the smallest one. On the other hand, the largest P-N nanoclusters are slightly oblate but relatively closer to the spherical limit. Conversely, the largest SiO nanoclusters are largely prolate. The elongation of SiO nanoclusters is a consequence of the side-by-side segregated nature of such species, containing silica-rich (SiO_2) and silicon-rich (Si) fractions respectively, which causes an elongation of the nanocluster structure (Bromley et al. 2016).

In Fig. 1C and D we report the shapes of two large sets of silicate nanoclusters with fixed sizes and compositions but variable chemical structures. Specifically, we plot I_y/I_x versus I_z/I_y for a set of 180 P-6 isomers (C) and 180 O-6 isomers (D). In these plots, the colour code represents the relative energy of each isomer with respect to the lowest energy structure in each set. The random distribution of colours in both plots confirms the lack of correlation between energetics and shape. The P-6 structures cover a wide range of I_y/I_x and I_z/I_y values with both ratios reaching up to 3 and with respective median values of 1.51 and 1.78. For P-6 these two ratios are correlated with each other such that the plotted data follow a fairly narrow band that lays close and parallel with the limiting prolate shape line. Only for I_z/I_x values lower than ~1.6 do we find a few P-6 structures that are dominantly oblate. Overall, only 20% of the particles appear to be below the line that separates the prolate from oblate particles.

The O-6 structures cover a smaller range of shape variability than the P-6 set with all I_y/I_x and I_z/I_x values being less than 2 and respective median values of 1.17 and 1.37. As in the P-6 set, the majority of the O-6 structures have shapes which tend to be more prolate. Here, however, the tendency is slightly less pronounced with the O-6 set, and the fraction of particles in the oblate region is 37%.

Several studies have tried to obtain dust grain shapes by calculating the polarization caused by differently shaped particles and comparing it to observation. Most models rely on spheroidal particles, where the free parameter is the axial to equatorial ratio, also known as aspect ratio (AR = a/b) with $a > b$. Several works have reproduced observed polarizations using grains with AR values of 1.33 (Gupta et al. 2005) or between 1 and 2 (Draine & Fraisse 2009). The largest AR values are reported by Das et al. (2010) to be between 2 and 3. Although these studies tend to address the shape of relatively large grains (i.e. size ~ 0.1 μm), the evolution of AR values with increasing size from the nanocluster scale upwards can potentially help us understand the origin of the shape of larger grains. The ultrasmall nanoclusters considered herein can be thought of as nucleation seeds for dust growth, as considered in the works of Gobrecht et al. (2016) and Goumans & Bromley (2012), and are thus likely to influence the shape of larger grains. In Fig. 2 we report the change in the AR values of our nanoclusters with respect to the number of atoms. For very small nanocluster sizes there is a high degree of fluctuation in the AR values for all considered nanocluster species. For the SiO-N nanoclusters this behaviour persists for all sizes. However, for the O-N and P-N set of nanosilicates the AR values

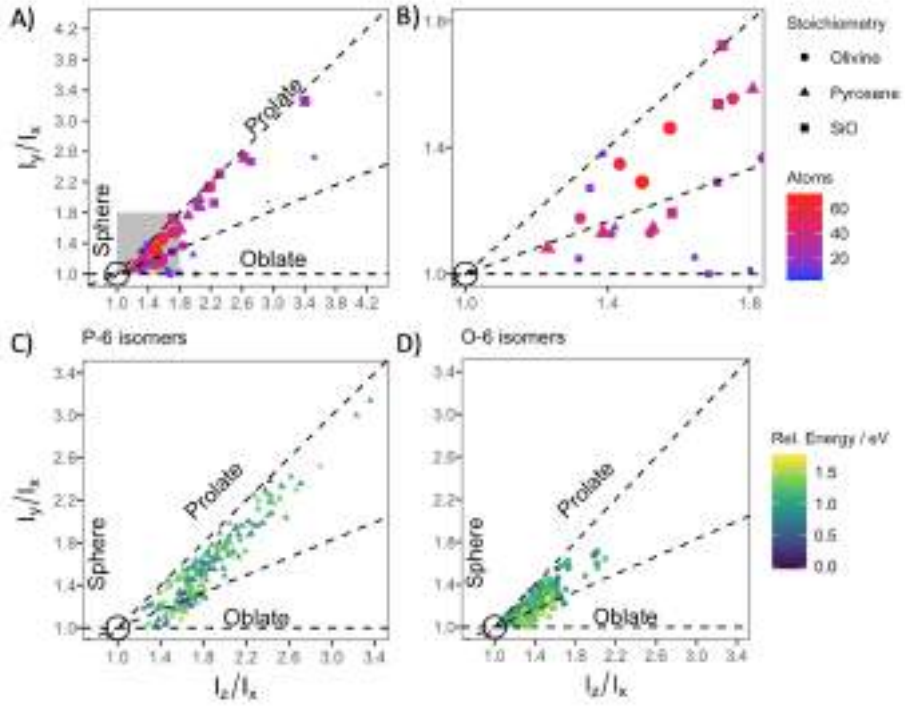

Fig. 1. Ratio between the largest and smallest moment of inertia (I_z/I_x) with respect to the ratio between the intermediate moment of inertia to the smallest one (I_y/I_x) for three selected sets of nanoclusters. The black circle indicates the ratio that defines a perfect sphere ($I_y/I_x = I_z/I_x = 1$), while the dashed lines show the prolate ($I_z = I_y > I_x$) and oblate ($I_z = I_y < I_x$) limits. (*A*) Lowest energy O-*N* and P-*N* nanoclusters for $N = 1$–10 and SiO-*N* nanoclusters for $N = 1$–20, grey area corresponds to the plotted area in (*B*). (*B*) Zoom of the plot in (*A*) over a 1.0–1.8 range for both axes. (*C*) 180 P-6 nanocluster isomers. (*D*) 180 O-6 nanocluster isomers.

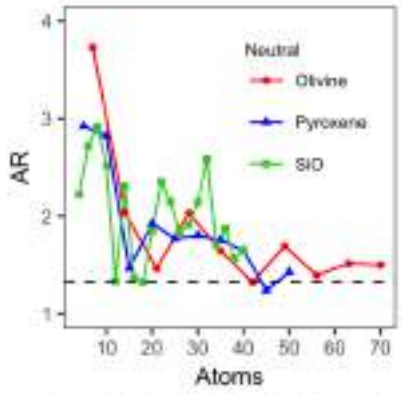

Fig. 2. Aspect ratio (AR) of O-*N* , P-*N* and SiO-*N* nanoclusters with respect to the number of atoms in each nanocluster. The dashed line corresponds to AR = 1.33 as determined by Gupta et al. (2005).

seem to be stabilizing at larger sizes to lay in a range between 1.7 and 1.3 in line with the values used by Gupta et al. (2005) and Draine & Fraisse (2009). We note that these results are tentative as they correspond to a tendency derived from only a few nanoclusters over a small size range.

4. Dipole moments

The proposal for nanosilicates being the source of the AME was established in the works of Hoang et al. (2016) and Hensley & Draine (2017). Using an expected fraction of silicate nanoclusters relative to the total Si abundance in the ISM of between 0.06 and 0.14, they concluded that nanosilicates could explain the entirety of the observed AME in the ISM. In order to reach this conclusion it was necessary that the silicate nanoclusters should comply with:

$$\beta = \mu / \sqrt{N_{\text{atoms}}} \geq 0.3, \tag{11}$$

where N is the number of atoms in the nanocluster and μ is the dipole moment in Debyes. Without detailed accurate data pertaining to such nanosilicates, the compliance with the above criterion was justified by the following hypothesis: since the Si-O bond is polar and the structure of the nanosilicates is assumed to be amorphous, random orientations of the Si-O bonds will lead to the formation of a permanent dipole in the nanosilicate. Assuming a simple near-spherical volume dependence on N_{atoms} (using a bulk silicate density) and a fixed value for the dipole moment of the Si-O bond, a random walk can be used to estimate values of μ for different values of N_{atoms} (Hoang et al. 2016).

In the present work, the dipole moments of our nanoclusters are calculated directly from their charge distributions (see above). In Fig. 3 we show the chemical structures and charge

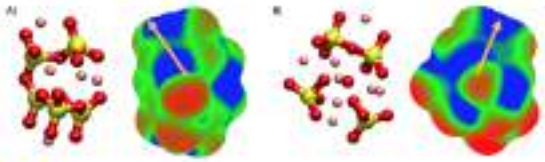

Fig. 3. Chemical structure (left) and electrostatic potential projected upon the electron density (right) for most stable $(MgSiO_3)_5$ P-5 nanocluster isomer (*A*), and the most stable $(Mg_2SiO_4)_4$ O-4 nanocluster isomer (*B*). Atom colour key: Si – yellow, O – red, Mg – pink. The charge density isosurface value is 0.1 e/Å^3. The electrostatic potential ranges from −0.07 (blue) to 0.07 (red) in AU. The orange arrows indicate the direction of the dipole moment vector.

density distributions for the P-5 and O-4 nanoclusters. Here, the charge density is bounded by a surface which follows a fixed charge density value (i.e. a charge density isosurface) typical for the outer region of an atom. Such isosurfaces provide a visual means to appreciate the detailed atomistic shape of a nanocluster. The colouring of the isosurfaces is proportional to the electrostatic potential at each point (i.e. a measure of the energy required to take an electron from zero electric field to a point on the isosurface). The blue (negative) regions correspond to regions for which it is more energetically favourable to place an electron (i.e. indicating local excess positive charge), and red (positive) regions correspond to where it is more energetically costly to place an electron (indicating local excess negative charge). Green regions correspond to more neutral areas. Overall, the presence of a dipole in a nanocluster is compatible with spatial asymmetries of the electrostatic potential on an isosurface which surrounds the nanocluster. Clearly, in the cases of P-5 and O-4, the blue and red areas do not symmetrically cover the isosurfaces of each nanocluster and thus a dipole is expected in both cases. The direction of the dipole in each case is shown by an arrow.

We note that the Si cations always sit centrally with respect to four tetrahedrally bonded O anions and are thus always inside the nanoclusters. Perfectly symmetric $[SiO_4]^{4-}$ tetrahedra possess no dipole moment (as the dipoles of the four Si-O bonds cancel each other) and thus would not contribute to the overall dipole moment of a nanocluster. In our small nanoclusters, these silica tetrahedra only display small deviations from their ideal structure (Escatllar et al. 2019) and thus do not tend to make a significant contribution to the overall calculated dipole moments. We also note that, although the structures of silicate nanoclusters are non-crystalline, often we find some $[SiO_4]^{4-}$ tetrahedra that are orientationally aligned (see atomistic structures in Fig. 3). Overall, the presence of large dipole moments in nanosilicates is clearly not simply due to random orientations of Si-O bonds as suggested by other authors (Hoang et al. 2016).

Inspecting the atomistic structures of our nanoclusters and their associated electrostatic potential we find that generally the regions with largest negative electrostatic potential correspond to surface Mg^{2+} cations positions, while areas of positive electrostatic potential are associated with surface oxygen anions locations. This tendency can be understood from the lower number of neighbours for ions at the nanocluster surface and a resultant lowering of the shielding of the electrostatic field for these ions in directions away from the nanocluster. Asymmetries in the positions of anions and cations near a nanocluster surface will thus tend to produce an overall nanocluster dipole. Conversely, the short-range dipoles due to alternating charges of cations and anions within the nanocluster will tend to be both counteracted by dipoles of neighbouring ion pairs and/or be shielded by the polarisation of the surrounding charge density. The energetic stability of a silicate nanocluster mainly depends on the number and strength of interactions due to ionic bonding. Although asymmetric arrangements of cations and anions tend to give rise to dipoles, generally in a small nanocluster the energetic cost to maintain an overall dipole is outweighed by the sum of bonding interaction energies. Overall, we find that only very few nanocluster isomers have symmetric atomistic structures which naturally lead to a zero overall dipole. In our set of lowest energy nanoclusters, the P-6 nanocluster is an example of a symmetric structure with no dipole. To highlight this is not a typical situation, in Fig. 4A we plot the relative energetic stabilities against the dipole moments of 180 low energy $(MgSiO_3)_6$ isomers, clearly showing the anomalously low dipole of the P-6 structure. Similarly, for olivine nanoclusters in Fig. 4B we show the analogous plot for 180 low energy $(Mg_2SiO_4)_6$ isomers where the lowest energy O-6 nanocluster has a finite dipole and where only two metastable isomers have dipole moments close to zero. In both cases, we note that there is no correlation between relative energetic stability and dipole moment, confirming that the energetic cost of maintaining a dipole in nanosilicates is small compared to the internal bonding energy.

While the lowest energy nanocluster structure would be the most populated in thermodynamic equilibrium, processing in astronomical environments could generate metastable isomers which can be kinetically trapped for long periods of time. As such, rather than the dipole moment of only the lowest energy nanocluster, a better overall estimate of the dipole possessed by astronomical nanosilicates may be to take an average dipole moment over a set of nanocluster isomers. In Figs. 4A and B the vertical red dashed lines indicate the median of the dipole moment all corresponding isomers. In both cases, the median dipole value is found to be larger than the dipole moment of the respective lowest energy nanocluster. Although this result is expected for the P-6 case for which the dipole moment is zero, the dipole moment the O-6 nanocluster is also significantly lower than the median value. These results indicate that our calculated dipole moments for the lowest energy nanocluster for each size is likely to be a lower bound estimate with respect to an average value taken with respect to many nanocluster isomers for that size. In Fig. 4C we compare the μ (Debye) values against number of atoms (N_{atoms}) for all our O-*N*, P-*N* and SiO-*N* nanoclusters in their neutral state. The grey shaded area in the plot highlights the region for which nanosilicates would not significantly contribute to the AME (i.e. $\mu(N_{atoms}) < \beta\sqrt{N_{atoms}}$ for $\beta = 0.3$), as estimated in previous studies (Hensley & Draine 2017; Hoang et al. 2016). The black dashed lines indicate the previously estimated upper and lower limits for dipole moments (i.e., $\beta = 1.0$ and $\beta = 0.3$) for nanosilicates in the two previous references. These upper and lower limits are also indicated in Figs. 4A and B by vertical black dashed lines. Overall, the $\mu(N_{atoms})$ values of the olivine and pyroxene nanoclusters show little regularity with respect to size. The $\mu(N_{atoms})$ values of the smaller P-*N* and O-*N* nanoclusters have some tendency to fluctuate more at smaller sizes probably due to the greater proportion of surface to interior atoms in such species. The O-4 nanocluster has a particularly large dipole moment for its size, which is even larger than that of the O-1 nanocluster. As noted above, the origin of such large dipole moment seems to be the presence of a low coordinated surface Mg cation (see Fig. 3) which is not counteracted by any other ion. Generally, the majority of O-*N* and P-*N* nanoclusters (except for the symmetric P-2 and P-6 nanoclusters) possess μ values,

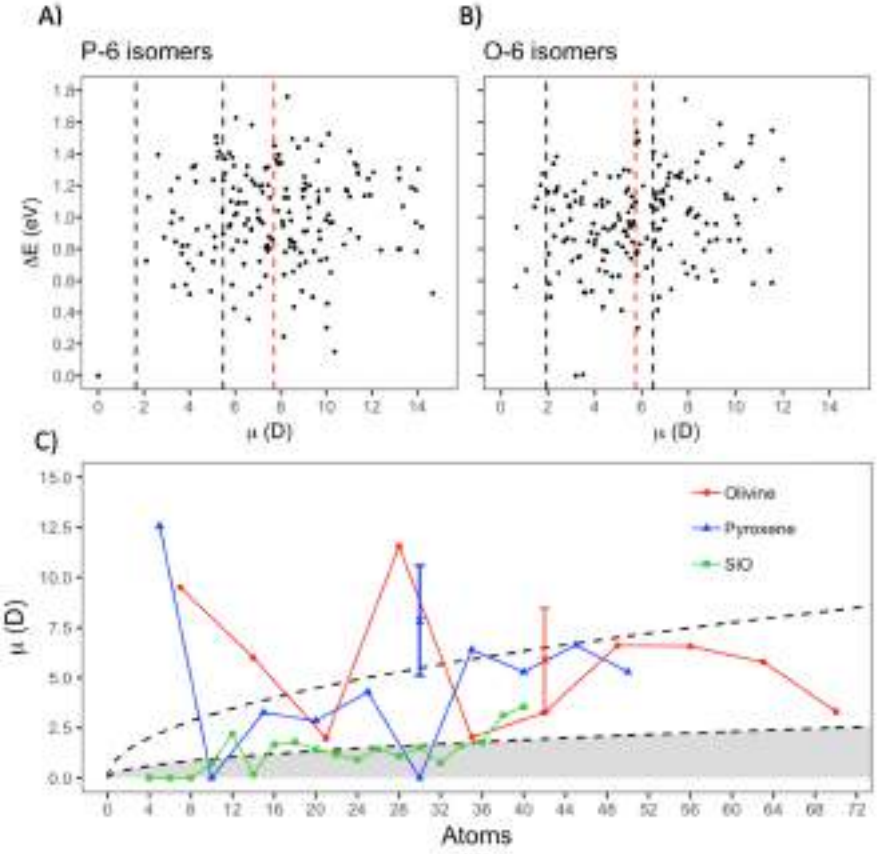

Fig. 4. *Top*: values of μ (Debye) against relative energy (eV) of nanocluster isomer with respect to the lowest energy structure for P-6 isomers (*A*) and O-6 isomers (*B*). In each plot, the black dashed lines indicate the lowest and highest previously estimated dipole moments for nanosilicates (Hoang et al. 2016), while the red dashed lines mark the median value calculated for each data set. (*C*) Dipole moments μ for O-*N* (red circles), P-*N* (blue triangles) and SiO-*N* (green squares) nanoclusters with respect to the number of atoms N_{atoms}. The blue and red crosses correspond to the average dipole μ values for the P-6 and O-6 isomer shown in (*A*) and (*B*) with the error bars indicating the variance in μ values for each set. The grey shaded area corresponds to the region where the dipole moment is too small for nanosilicates to contribute substantially to the AME. The two dashed lines correspond to the limits in (*A*) and (*B*).

which, although varying in a rather irregular manner, are above the lower value deemed significant for contributing to the AME (i.e. $\beta = 0.3$). Many of these nanoclusters have dipole moments that are close to, and sometimes above, the upper estimated limit (i.e. for $\beta = 1.0$) for nanosilicates. As noted above, as our μ values are calculated for the lowest energy nanoclusters, this means that they are likely lower estimates of median dipole moments for each size and composition. In Fig. 4C we also include median and variance of the set of μ values for $(MgSiO_3)_x$ (N_{atoms} = 30) and $(Mg_2SiO_4)_x$ (N_{atoms} = 42) isomers plotted in Figs. 4A and B. In both cases, the dipole moment of the original lowest energy nanocluster would be shifted to near or above the notational upper limit line. Clearly, however, whether we take median μ values or not, our Mg-rich olivine and pyroxene nanoclusters have dipoles that are sufficiently large to significantly contribute to the AME.

In contrast to the O-*N* and P-*N* species, the neutral SiO-*N* nanoclusters generally display significantly lower dipole moments making them less likely to contribute to the AME. For many of the SiO-*N* nanoclusters the μ values are on, or below, the lower limit for AME significance. Only five of the nineteen SiO-*N* nanoclusters considered have sufficiently large dipole moments to be above this limit. The zero dipole of the first few SiO-*N* nanoclusters can be ascribed to their symmetric structures. However, for larger sizes $(SiO)_N$ nanoclusters tend to structurally segregate into oxygen-rich (i.e. SiO_2-like) and silicon-rich regions in a side-by-side fashion (Bromley et al. 2016). Although, such structures are suitably asymmetric for possessing a large dipole, in the neutral state charge does not tend to localise on either segregated region. As such the only ionic charge imbalance come from the formation of Si-O bonds in the oxygen-rich regions which, in the absence of network disrupting Mg^{2+} ions, tend to form symmetric $(SiO)_z$ rings and $(SiO_4)^{4-}$ tetrahedra, both of which possess very low dipole moments.

As noted above, ISM silicates are likely to contain a small fraction of Fe^{2+} in their chemical structure, which has been

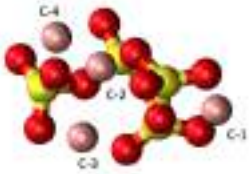

Fig. 5. Structure of the P-4 nanocluster with the different cation positions labelled.

Table 1. Dipole moment variation of the P-4 structure by substituting one Mg^{2+} by one Fe^{2+} in each of the four different sites (C-1 to C-4).

Structure	μ (D)	$\Delta\mu$ (D)
Original P-4	2.83	0.00
Fe C-1	3.55	+0.72
Fe C-2	1.56	−1.27
Fe C-3	3.06	+0.23
Fe C-4	2.34	−0.49
Fe mean	2.63	−0.2

assumed to explain the polarization of starlight and polarized emission from aligned dust grains (Hoang et al. 2010). Although the present work does not deal with polarisation, the inclusion of Fe^{2+} could nevertheless affect the calculated dipole moments of the nanoclusters. As a test case we evaluate the change in the dipole moment induced by substituting one Mg^{2+} cation by a Fe^{2+} cation in the P-4 nanocluster in all four symmetrically inequivalent positions, C-1 to C-4 (see Fig. 5). We note that the energetic stability of Fe^{2+} substitution in each of the positions is very similar (difference of <0.2 eV) and thus all could be occupied in a population of Fe^{2+}-substituted P-4 nanoclusters. In Table 1 we show the dipole moments of the P-4 nanocluster with each C Mg^{2+} cation substituted by a Fe^{2+} cation. The results show that the dipole moment of the Fe-substituted small P-4 nanocluster can both increase and decrease with respect to the Mg-pure original P-4 structure. In this case, we find a maximum variation of −1.27 Debyes. Although in this extreme case the dipole reduction is significant, the total dipole moment is still 1.56 Debyes and thus the nanocluster would still be a viable carrier of the AME. Overall, in this test case, the range and average change of dipole moment due to Fe-substitution would not be significant compared to the dipole variation expected due to structural isomerisation (see Figs. 4A and B).

Charging of nanoclusters will also affect their electronic structure and hence their corresponding dipole moment. In addition, an excess charge can significantly affect the interaction between a nanocluster and its environment, influencing, for instance, the collisional cross-section or the grain temperature. In Draine & Lazarian (1998), the effect of grain charging on the dipole is modelled by assuming that the extra charge is localized over a region of the grain with the charge centroid displaced from the centre of mass by 1% of the grain radius (see also Purcell 1975). Such a localized charge would then add to the intrinsic dipole moment by $\Delta\mu = \epsilon a_1 Ze$, with $\epsilon = 0.01$ being the displacement of the charge centroid with respect to the centre of mass, a_1 the grain radius and Ze the grain charge. The overall predicted effect is that charging a grain increases its dipole moment by a small amount. In Fig. 6 we report the difference in dipole

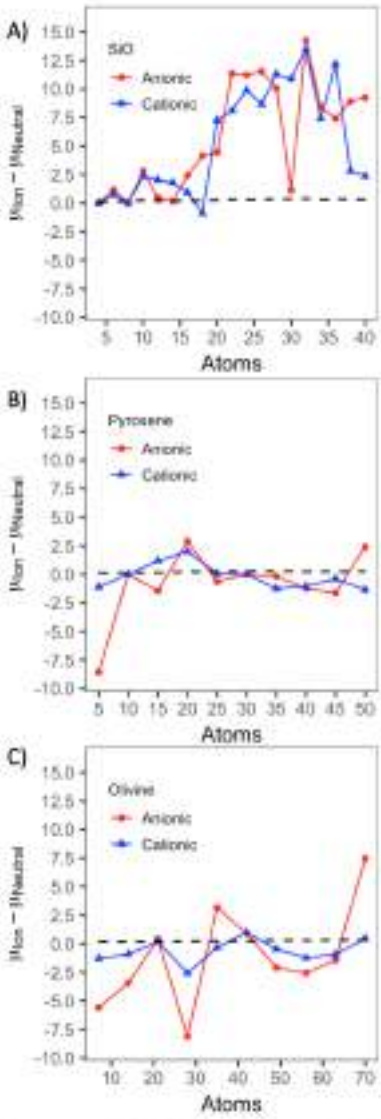

Fig. 6. Dipole moment (Debye) difference between ionic (red circles: anionic, blue triangles: cationic) and neutral states for the SiO, pyroxene and olivine nanoclusters. The dashed line correspond to the increase of dipole moment using the model of Draine & Lazarian (1998) and using the largest nanocluster axis to project the displacement.

moment in the ±1 anionic/cationic states of our nanoclusters with respect to that of corresponding neutral nanoclusters where the dashed lines indicate the increase in dipole predicted by classical top-down modelling (Draine & Lazarian 1998). Clearly, in nearly all cases the changes in dipole we observe in our quantum chemical calculations are significantly larger and less regular in magnitude with respect to size and composition than the classical estimates. Typical changes in the dipole moment for the classical model are of the order of 0.2 D. Thus, due to the large

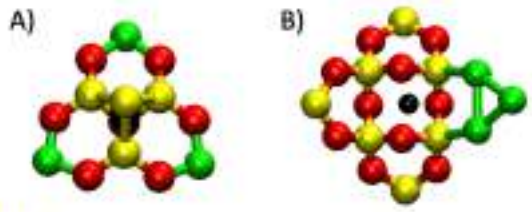

Fig. 7. Chemical structures of anionic nanoclusters for: (*A*) $(SiO)_7$ and (*B*) $(SiO)_{10}$ nanoclusters. The black dots correspond to the centres of mass. Oxygens are shown as red, while silicon is shown as yellow or green. The green colour indicates that the Si centre in question charge possesses a larger than average negative charge.

range in the difference of dipole moments in Fig. 6 the prediction of classical model appears as a horizontal line close to zero. Even though it seems intuitive that adding a charge to a nanocluster would increase its dipole moment, the results of our accurate electronic structure calculations show that this is not necessarily the case. In fact, for most of the O-*N* and P-*N* nanoclusters a change in the charge state results in a diminished dipole moment, suggesting that the added charge allocates itself to counteract the existing dipole of the neutral nanocluster. This is most clearly exhibited for the O-4 nanocluster which, as a neutral nanocluster, has a large dipole moment. However, once the O-4 nanocluster becomes charged most of the dipole moment is counteracted. Conversely, charged SiO-*N* nanoclusters with $N \geq 10$ exhibit large and consistent increases in their dipole moments. The reason for such behaviour in these nanoclusters is their asymmetric segregated nature. Although in the neutral charge-balanced state these segregated nanoclusters have low dipole moments (see above) excess charge localizes on either the O-rich or Si-rich side of the nanocluster giving rise to a spatially asymmetric charge distribution and the generation of a significant dipole moment. We note that for $N < 10$ the SiO-*N* nanoclusters have a more symmetric structure and the additional charge is distributed in a more balanced way, thus not leading to large dipole increases. In Fig. 7 we show structures of the $(SiO)_7$ and $(SiO)_{10}$ nanoclusters, where we colour in green the atoms that receive most of the electron density from an added electron. The $(SiO)_7$ cluster distributes the electron density on three peripheral Si atoms in a symmetric fashion that leads to little change in the overall dipole moment. However, in the $(SiO)_{10}$ nanocluster the added electron is completely localized on the Si-rich region which generates a large difference between the centre of mass and centre of charge, dramatically increasing the dipole moment.

5. Ionization potentials and electron affinities

From our quantum chemical calculations we can also extract the electron affinity (EA) and the ionization potential (IP) of our nanoclusters. These two parameters can be used to help understand the charge state of the nanoclusters in various astrophysical environments as well as to determine the temperature of the ISM (Weingartner & Draine 2001a). Figure 8 provides the IP and EA values of the O-*N*, P-*N* and SiO-*N* nanoclusters versus their radius in Å. Here we calculate the radius using the average of the moments of inertia (i.e. modelling the nanocluster as a sphere with homogeneous density). Although our nanoclusters are not perfectly spherical (see above) we convert them to a spherical shape in order to better compare our IP and EA values with values calculated using the classical electrostatic based equations reported in Weingartner & Draine (2001a). For the IP values, the discrepancies between our quantum chemical calculations and classical electrostatic estimates are largest for both the smallest O-1 and P-1 nanoclusters (>3.5 eV). With increasing nanocluster size our calculated IP values for the O-*N* and P-*N* series gradually decrease linearly with respect to the nanocluster radius whereas the classical electrostatic values decrease proportionally to the inverse nanocluster radius. For the P-*N* set of nanoclusters, our calculated values meet the classical estimated tendency at a radius of ~4.0 Å and match well up to a radius of ~4.7 Å. For the O-*N* nanoclusters, the IP values as predicted by our quantum chemical calculations tend to be approximately 0.5 eV lower than those of the P-*N* nanoclusters. As such, the IP values for the O-*N* nanoclusters would likely match the classical prediction at nanocluster size larger than of those considered in this study (for the P-10 nanocluster the difference is ~0.5 eV). For the SiO-*N* nanoclusters our calculated IP values are always significantly below the classical approximation, where, even for the largest seven SiO-*N* nanoclusters, the difference is >3 eV.

The quantum chemically calculated EA values for both O-*N* and P-*N* nanoclusters appear to follow a similar gradually decreasing tendency with respect to increasing radius, with both sets of values seeming to reach a plateau at 0.86 eV for the largest sizes. Conversely, the classical electrostatic values follow a negative inverse radius relationship with respect to nanocluster radius which crosses the limiting plateau EA value over a radius range of ~3–5 Å. Moving above and below this nanocluster size range the discrepancy between the classical electrostatic predicted EA values and the quantum chemical values increases. For the SiO-*N* nanoclusters the general tendency is for the EA values to increase in a fairly consistent fashion with respect to the classical approximation. Generally, the magnitudes of the calculated EA values for smaller SiO-*N* nanoclusters tend to be higher than those predicted by the classical estimates. However, for the larger SiO-*N* nanoclusters, for $N = 10$–19, the calculated EA values oscillate above and below the classical prediction.

The IP and EA values reported by Weingartner & Draine (2001a) are used for silicate nanocluster sizes with a >3.5 Å (see solid portion of black lines in Fig. 8). Comparing our calculated IP values with those of Weingartner & Draine (2001a) in this region for the O-*N* and P-*N* nanoclusters we obtain maximal differences of ~1 eV for nanoclusters of 3.5 Å radius and ~0.5 eV for a 5 Å radius. However, for the SiO-*N* nanoclusters the respective energetic differences are ~6 and ~4 eV. For the EA values, the corresponding energy differences for the O-*N* and P-*N* nanoclusters are <0.5 eV for nanoclusters of 3.5 Å radius, and ~0.8 eV for 5 Å radius nanocluster. For the SiO-*N* nanoclusters the respective energy differences are ~3 and ~0.5 eV.

In general, the size dependence of the values of the IP and EA as predicted by classical electrostatic arguments is not in very good overall agreement with that of more accurate quantum chemical calculations. However, for O-*N* and P-*N* silicate nanoclusters with a radius close to ~4 Å the match between the EA and IP values from the two types of calculations is quite reasonable. For the IP values this match is fairly well maintained for larger nanocluster sizes, whereas for the EA values the correspondence deteriorates. For the SiO-*N* nanoclusters our quantum chemically calculated IP values are always significantly below those predicted by the classical approximation although for larger sizes the EA values predicted by both methods tend to be in closer agreement.

A&A 634, A77 (2020)

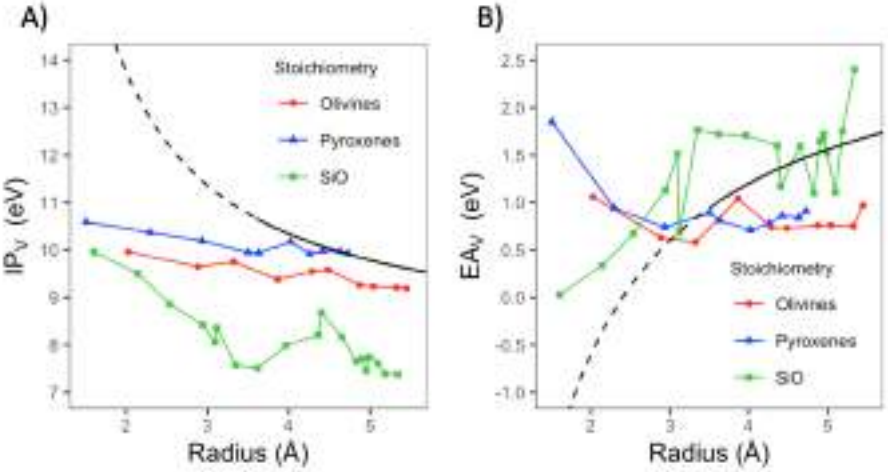

Fig. 8. IP$_V$ (*A*) and EA$_V$ (*B*) for the O-*N* (red circles), P-*N* (blue triangles) and SiO-*N* (green squares) nanoclusters. The dashed and solid black line corresponds to the classically derived equations used in Weingartner & Draine (2001a). Note that only the solid part of the black line corresponds to values applied to nanosized grains in Weingartner & Draine (2001a).

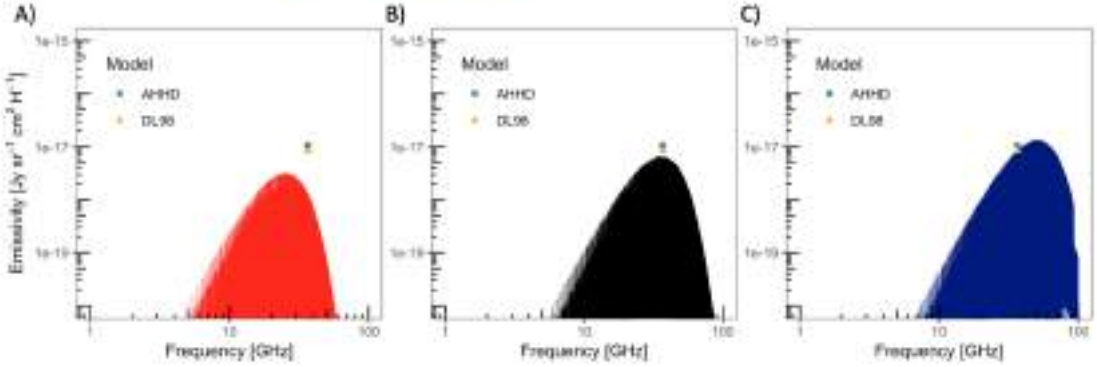

Fig. 9. Emissivity of a representative grain of $(MgSiO_4)_1$ containing 1% of the total Si budget at rotational temperatures of T=10 (red, *left*), 20 (black, *middle*) and 40 (dark blue, *right*) K under MC conditions as described in Draine & Lazarian (1998). The maximum emisoivity of the models of Ali-Haïmoud et al. (2009, AHHD) and Draine & Lazarian (1998, DL98) are also plotted.

6. Microwave emission

The quantum mechanical derived data in this work allows us to derive the microwave emission of our nanosilicates. Figure 9 shows the predicted emissivity of a population of representative O-3 nanoclusters under general assumed conditions of MCs as described in Draine & Lazarian (1998), using three rotational temperatures of $T_{rot} = T_{kin}$ = 10, 20 and 40 K and containing a fraction of 1% of total Si. Thus, the only difference in the three models corresponds to changes in temperature. As expected, an increase in temperature causes an increase of emissivity and peak frequency. For the temperature of 20 K, both peak position and emissivity are in very good agreement with the models of Draine & Lazarian (1998, model DL98) and Ali-Haïmoud et al. (2009, model AHHD). Again, we highlight that both cited methodologies compute the rotational distribution of the grains by estimating the influence of numerous physical processes involved in accelerating and decelerating grain rotation. Thus, such models can be applied to a wide range of environments where rotation may be above or below the thermal rotation rate. Several parameters are required for such models, both for the environment and the grain. Nevertheless, in some circumstances, the rotational energy distribution will still follow the Boltzmann distribution. In Appendix A we show that, under general MC conditions, the present study under the assumption of LTE slightly overestimates the emission in comparison with the detailed models of DL98 and AHHD by ~40%. On the other hand, the O-3 nanocluster possesses one of the lowest non-zero dipoles moments in our considered set of nanocluster isomers. In Fig. 4 we show that the average dipole moments of a population of P-6 and O-6 nanocluster isomers is larger than that of the lowest energy P-6 and O-6 nanocluster isomer. Assuming this is a general tendency, we should then use a larger dipole moment value for a representative average O-3 nanocluster. Doing so would cause the calculated emission to be larger than shown in Fig. 9 and would imply that a lower

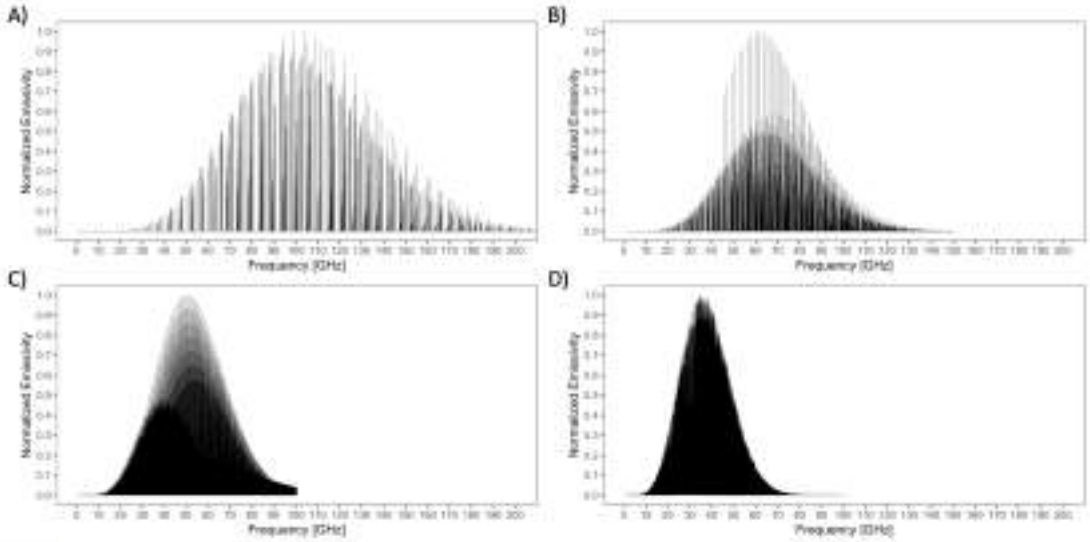

Fig. 10. Calculated microwave emission spectra of the P-1 (*A*), O-1 (*B*), O-2 (*C*) and O-3 (*D*) nanoclusters at $T = 20$ K normalized so that the most intense peak has unit intensity. For P-1 no clear separation between lines is found. For O-1, the most intense lines are separated by a line spacing of 1.85 GHz, which lowers to 1.3 Ghz for O-2. For O-3 the density of states becomes too large to identify a line-spacing, although some individual lines appear.

abundance of nanoclusters would be required to produce this emission.

Li & Draine (2001) argued that silicate nanoclusters with diameters $\lesssim$1.0 nm radii could not contain more than 15% of Si in the ISM based on the lack of IR signatures attributed to silicates. Based on this constraint, Hensley & Draine (2017) and Hoang et al. (2016) argued that the entirety of the AME could be attributed to such silicate nanoclusters as long as they possess sufficiently large dipole moments. We note that such constraints should be viewed with caution as the IR spectra of silicate nanoclusters can not generally be extrapolated from those of bulk silicates (Zamirri et al. 2019; Escatllar et al. 2019). Herein, having access to the silicate nanocluster dipole moment, we can, instead, find the appropriate population of nanoclusters that would be required to account for the observed AME. Our modelling requires only 1% of the total Si budget to reproduce AME predictions of other models in MCs. In this way, we have an alternative bottom-up constraint on silicate nanocluster abundances based on microwave observation.

As noted in Draine & Lazarian (1998), the use of classical mechanics to describe the microwave emission can be justified if a grain is above a certain size or temperature. However, several of our grains are small enough to be effectively considered molecules, such as P-1, O-1 and a fraction of the smaller SiO_N species. In addition, the high resolution achievable by radio telescopes (e.g. 0.4 MHz, Ali-Haïmoud et al. 2015) requires us to evaluate the possibility that, even if the overall spectral shape of the emission can be described by classical mechanics, at such high resolutions some hint of structure could also be found. Although a full analysis of the microwave spectra of the nanoclusters is beyond the scope of the present work, in Fig. 10 we show the calculated normalized (i.e, strengths are relative to the most intense signal) microwave spectra for the small P-1, O-1, O-2 and O-3 nanoclusters at MC conditions (20 K rotational temperature). P-2 was not considered as its high symmetry leads to a zero dipole moment, and thus no emission. We find that the P-1 spectrum shows a complicated pattern of well-separated peaks (see Fig. 10A) with no clear constant line-separation. The O-1 nanocluster also shows molecular-like emission spectrum, but in this case the main peaks are much more consistent showing a spacing of ~1.8 GHz. With increasing nanocluster size, the density of states increases and the peak separation becomes smaller and the spectra become an almost continuous (see Fig. 10D).

In Fig. 11, we compare the microwave emission spectra of Mg-pure olivine and pyroxene nanoclusters with three sizes (small: one monomeric unit of olivine and pyroxene, medium: P-4 and O-3 nanoclusters containing 20 and 21 atoms respectively, and large: P-10 and O-10 nanoclusters, containing 50 and 70 atoms respectively) in conditions representative of MCs (T = 20 K). The fraction of the total Si budget in the nanoclusters is taken to be 1% for the medium and large nanoclusters and 10^{-5} for the smallest ones. With increasing size we find that the emissivity rapidly decreases. The plots in Fig. 11 show that, as expected, an increase in mass is correlated with a decrease in the magnitude of the rotational constants (see Table B.1), and thus a smaller spacing of the rotational levels. Hence, the spectral peaks are displaced towards lower frequencies with an increasing number of atoms. It is clear from Fig. 11 that the microwave emission from all the nanoclusters in the size range we consider overlaps with the observed frequency range of the AME at T= 20 K. The smallest nanoclusters have emission covering most of the observable AME frequency range but tend to peak at higher frequencies than those observed. At 20 K, we find that the emissivity of the smallest P-1 and O-1 nanoclusters peaks at a frequency close to 100 GHz. As AME observations generally have a maximum emissivity in the range between 20 and 30 GHz, it follows that the population fraction of the O-1 and P-1 nanoclusters must

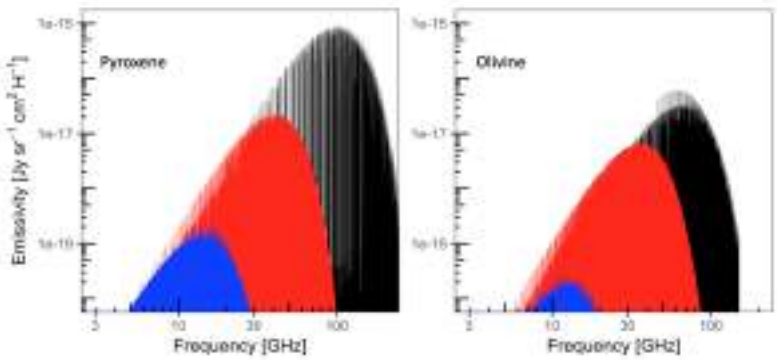

Fig. 11. Calculated microwave emission spectra for the O-N and P-N for small (i.e. N = 1 for O-N and P-N , black), large (i.e. N = 10 for O-N and P-N, blue) and medium-sized nanocluster containing ~20 atoms (N = 3 for O-N, N = 4 for P-N and N = 10 for SiO-N , red) under MC (T = 20 K) conditions. The emissivity is calculated using a fraction of 0.01 of Si in the medium and large nanoclusters and 1e-5 for the smallest nanoclusters.

be smaller than the 10^{-5} used in our modelling. Conversely, from Figs. 9 and 11 it can be seen that Mg-rich silicate nanoclusters containing 20 to 30 atoms can best account for the observed AME spectral shape in MC conditions. Since larger rotational temperatures imply emission at higher frequencies, larger nanoclusters (~50 to 70 atoms) could also then be significant contributors to the AME. With respect to observation, the monomeric species P-1 and O-1 would appear as the most easily detectable species due to the large separation between their spectral peaks and their large emissivities.

7. Conclusions

While the evidence that small spinning dust grains are the source of the AME seems to be well established, the nature of the potential nanosized carriers is still under discussion. In this work we perform accurate bottom-up quantum chemical calculations of the properties of astronomically relevant silicate clusters of Mg_2SiO_4 (olivine), $MgSiO_3$ (pyroxene) and SiO (silicon monoxide) with diameters ≤1 nm, with the main aim of clarifying their importance as carriers of the AME. Our results provide strong evidence that silicate nanoclusters, if present, would be a major component of the AME. Specifically, our results show that:

1. Mg-rich olivine and pyroxene silicate nanoclusters are mainly prolate shaped, with no clear tendency to become spherical with increasing size.
2. The size dependency of IP and EA values calculated by classical electrostatic estimates are generally not in good agreement with those from quantum chemical calculations. However, for olivine and pyroxene nanoclusters with radii close to 4 Å the agreement between both approaches is reasonable.
3. The dipole moments of neutral Mg-rich silicate clusters of both olivine (Mg_2SiO_4) and pyroxene ($MgSiO_3$) compositions are large and well above the estimated minimum for silicates to contribute to the AME. Our statistical analysis of dipole moments for over 180 nanocluster isomer structures for two sizes, $(Mg_2SiO_4)_5$ and $(MgSiO_3)_{10}$, shows less than 4% have a dipole moment below the required values. SiO clusters on the other hand tend to have much lower dipole moments and are less likely to be significant contributors to the AME.
4. Changing the charge state of the nanoclusters can significantly increase or decrease the dipole moment of a neutral nanocluster. For O-N and P-N nanoclusters and the smallest SiO-N particles (with N < 10) ionisation generally lowers the dipole moment of the particle, although the resulting dipoles are still large enough to significantly contribute to the AME. For the segregated SiO-N particles (N > 10) the charge is generally localized in the Si-rich part of the nanocluster, generating a large separation between the centre of mass and centre of charge, thus increasing the dipole moment. In such circumstances, charged SiO-N nanoclusters have larger dipole moments than similar sized magnesium silicate nanoclusters.
5. Substituting a small fraction of Mg^{2+} cations by Fe^{2+} cations can both increase or decrease the dipole moment of a magnesium silicate nanocluster. Although this effect can be fairly large for individual substitutions, it appears that the overall effect does not tend to significantly diminish the magnitude of nanocluster dipole moments. In particular, consideration of Fe^{2+} is very unlikely to affect our overall confirmation that silicate nanoclusters have sufficiently large dipole moments to be carriers of the AME.
6. Using a Boltzmann distribution to describe the population of the rotational levels we find that we only require 1% of the total Si abundance to be contained in Mg-rich silicate nanoclusters in order to reproduce the results of previously published AME models. Thus, we find that the abundance of silicate nanoclusters is better constrained by microwave spectra than IR spectra.
7. By virtue of their detailed and, in principle, resolvable microwave emission spectra, smaller silicate nanoclusters (e.g. P-1, O-1, O-2 and any isomer having <20 atoms) are primary candidates that could provide direct observable evidence of silicate nanoclusters in different ISM phases as well as to allow determine dust temperatures.

Acknowledgements. We acknowledge financial support from the Spanish MINECO/FEDER CTQ2015-64618-R and MICIUN RTI2018-095460-B-100 research projects, the Ministerio de Ciencia, Innovación y Universidades (MCIU) Spanish Structures of Excellence María de Maeztu program through grant MDM-2017-0767 and the Generalitat de Catalunya (grants 2017SGR13 and XRQTC). The Red Española de Supercomputación (RES) is also acknowledged for the provision of supercomputing time. We also acknowledge the EU COST Action (CM1401) – Our Astro-Chemical History. We also thank an anonymous referee and Prof. Miguel Gonzalez for their helpful and constructive comments.

References

Adamo, C., & Barone, V. 1999, J. Chem. Phys., 110, 6158
Ade, P. A. R., Aghanim, N., Arnaud, M., et al. 2011, A&A, 536, A20
Agladze, N. I., Sievers, A. J., Jones, S. A., Burlitch, J. M., & Beckwith, S. V. W. 1996, ApJ, 462, 1026
Ali-Haïmoud, Y. 2013, Adv. Astron., 2013, 1
Ali-Haïmoud, Y., Hirata, C. M., & Dickinson, C. 2009, MNRAS, 395, 1055
Ali-Haïmoud, Y., Pérez, L. M., Muñoz-Idrobo, R. J., & Roshi, D. A. 2015, MNRAS, 447, 315
Barone, V. 2005, J. Chem. Phys., 122, 014108
Blum, V., Gehrke, R., Hanke, F., et al. 2009, Comput. Phys. Commun., 180, 2175
Bromley, S. T., Gómez Martín, J. C., & Plane, J. M. C. 2016, Phys. Chem. Chem. Phys., 18, 26993
Cazaux, S., Cabrera, G. F., Forster, F., et al. 2006, ApJ, 639, 951
Catlow, C. R. A., Bromley, S. T., Hamad, S., et al. 2010, Phys. Chem. Chem. Phys., 12, 786
Das, H. K., Voshchinnikov, N. V., & Il'in, V. B. 2010, MNRAS, 404, 265
Dickinson, C., Ali-Haïmoud, Y., Barr, A., et al. 2018, New Astron. Rev., 80, 1
Draine, B. T., & Fraisse, A. A. 2009, ApJ, 696, 1
Draine, B. T., & Hensley, B. S. 2016, ApJ, 831, 59
Draine, B. T., & Lazarian, A. 1998, ApJ, 508, 157
Draine, B. T., & Lazarian, A. 1999, ApJ, 512, 740
Ericksen, W. C. 1957, ApJ, 126, 480
Escatllar, A. M., Lazauskas, T., Woodley, S. M., & Bromley, S. T. 2019, ACS Earth Space Chem., 3, 2390
Finkbeiner, D. P., Schlegel, D. J., Frank, C., & Heiles, C. 2002, ApJ, 566, 898
Fogerty, S., Forrest, W., Watson, D. M., Sargent, B. A., & Koch, I. 2016, ApJ, 830, 71
Frisch, M., Trucks, G., Schlegel, H., et al. 2016, Gaussian 16 Revision C.01 (Wallingford CT: Gaussian Inc.)
Gobrecht, D., Cherchneff, I., Sarangi, A., Plane, J. M. C., & Bromley, S. T. 2016, A&A, 585, A6
Gordy, W., & Cook, R. L. 1984, Microwave Molecular Spectra, 3rd edn. (Hoboken: Wiley-Interscience Publication), 747
Goumans, T. P. M., & Bromley, S. T. 2012, MNRAS, 420, 3344
Greaves, J., Scaife, A., Frayer, D., et al. 2008, Nat. Astron., 2, 662
Gupta, R., Mukai, T., Vaidya, D. B., Sen, A. K., & Okada, Y. 2005, A&A, 441, 555
Hensley, B. S., & Draine, B. T. 2017, ApJ, 836, 179
Hensley, B., Murphy, E., & Staguhn, J. 2015, MNRAS, 449, 809
Hildebrandt, S. R., Rebolo, R., Rubiño-Martín, J. A., et al. 2007, MNRAS, 382, 594
Hoang, T., Draine, B. T., & Lazarian, A. 2010, ApJ, 715, 1462
Hoang, T., Lazarian, A., & Draine, B. T. 2011, ApJ, 741, 87
Hoang, T., Vinh, N.-A., & Lan, N. Q. 2016, ApJ, 824, 18
Hoang, T., Lan, N.-Q., Vinh, N.-A., & Kim, Y.-I. 2018, ApJ, 862, 116
Jones, A. P. 2009, A&A, 506, 797
Kessler-Silacci, J., Augereau, J.-c., Dullemond, C. P., et al. 2006, ApJ, 639, 275
Kisiel, Z. 2001, Spectroscopy from Space (Dordrecht: Springer Netherlands), 91
Kisiel, Z. 2019, PROSPE - Programs for Rotational SPEctroscopy
Krasnokutski, S. A., Rouillé, G., Jäger, C., et al. 2014, ApJ, 782, 15
Lamiel-Garcia, O., Ko, K. C., Lee, J. Y., Bromley, S. T., & Illas, F. 2017, J. Chem. Theory Comput., 13, 1785
Li, A., & Draine, B. T. 2001, ApJ, 550, L213
Molster, F. J., Waters, L. B. F. M., Tielens, A. G. G. M., & Barlow, M. J. 2002, A&A, 382, 222
Pickett, H., Poynter, R., Cohen, E., et al. 1998, J. Quant. Spectr. Rad. Transf., 60, 883
Purcell, E. M. 1975, The Dusty Universe (New York: Neale Watson Academic Publications), 155
Puzzarini, C., Stanton, John. F., Gauss, J., et al. 2010, Int. Rev. Phys. Chem., 29, 273
Rafikov, R. R. 2006, ApJ, 646, 288
Tibbs, C., Flagey, N., Paladini, R., et al. 2011, MNRAS, 418, 1889
Ubach, C., Maddison, S. T., Wright, C. M., et al. 2017, MNRAS, 466, 4083
Vidal, M., Casasson, S., Dickinson, C., et al. 2011, MNRAS, 414, 2424
Waelkens, C., Waters, L. B. F. M., de Graauw, M. S., et al. 1996, A&A, 315, 245
Watson, R. A., Rebolo, R., Rubiño-Martín, J. A., et al. 2005, ApJ, 624, L89
Weingartner, J. C., & Draine, B. T. 2001a, ApJS, 134, 263
Weingartner, J. C., & Draine, B. T. 2001b, ApJ, 548, 296
Yurd, N., & Verstraete, L. 2010, A&A, 509, A12
Zamirri, L., Maciá Escatllar, A., Martínez Guiu, J., Ugliengo, P., & Bromley, S. T. 2019, ACS Earth Space Chem., 3, 2323
Zhan, C.-G., Nichols, J. A., & Dixon, D. A. 2003, J. Phys. Chem. A, 107, 4184

Conclusions

1. Mg-rich silicate nanoclusters of up to 1 nm in diameter are mainly prolate, with no tendency to become spherical with increasing size. The aspect ratio of these nanoclusters seems to evolve towards a value of 1.33 as their size increases.
2. The IP and EA values of Mg-rich silicate nanoclusters differ substantially from values calculated from classical electrostatics assuming perfectly spherical clusters. For clusters having a radius of 4 Å the agreement between the values calculated by quantum and classical methods is reasonably good.
3. The dipole moments calculated from DFT methods from all considered Mg-rich silicate nanoclusters are in line with the required values to account for the entirety of the observed AME. Only some nanoclusters with high symmetry have zero dipole moment. $(SiO)_N$ on the other hand do not appear to have the appropriate dipole moments for small sizes, and only the largest segregated $(SiO)_N$ nanoclusters could play some role in accounting for the AME.
4. An analysis of large sets of nanoclusters (~180 isomers) of O-6 and P-6 shows that the variability in dipole moment with respect to nanocluster structure is large. However, only a small fraction (4%) of these nanoclusters have dipole moments that are below the value required to contribute to the AME. We also show the lack of correlation between dipole moment and energetic stability of these nanoclusters, implying that even if the nanoclusters presented in this thesis do not correspond to global minima, it is very likely that more stable nanoclusters would also have large dipole moments.
5. A change in the charge state does not always increase the dipole moment, as previously assumed. For very dipolar nanoclusters, the added charge tends to allocate itself to lower the dipole moment of the neutral nanocluster. Overall, for the P-N, O-N and the smallest SiO-N (N<10) nanoclusters, the dipole moment slightly lowers, although not enough to change the conclusions reached from neutral nanoclusters. For the large SiO-N nanoclusters (N>10), the segregated nature of the particle causes the excess electronic charge to be localized in the Si pure region, bot for anions and cations. As a consequence, a large dipole moment arises from the large difference between the position of the center of mass and the center of charge. Ionic SiO-N nanoclusters could therefore contribute to the AME.
6. Fe incorporation is the main compositional variation that silicate nanoclusters would likely possess. Based on calculations on an example nanocluster we obtained a first order estimate of the effects of substitution of Mg by Fe. We conclude that Fe does not greatly affect the dipole moment of our candidate Mg-rich silicate nanocluster structures.
7. We report the rotational constants of all our nanoclusters. Together with the structures provided in Chapter 10, more precise calculations of the rotational spectrum can be evaluated.

8. We calculate the emissivity of silicate nanoclusters in several astronomical environments by using Boltzmann statistics to evaluate the population of each rotational level. We find that astrosilicate nanoclusters would require 1% of the Si budget in order to account for the entirety of the AME, ten times less than previously assumed.

Chapter 12: What can infrared spectra tell us about the crystallinity of nano-sized interstellar silicate dust grains?

Introduction

The presence of dust in the ISM is essential to allow the cooling of interstellar clouds through gas-surface reactions and, as a consequence, dust is linked to the chemical evolution of interstellar clouds[132,133]. Thus, understanding the types of dust present in the ISM and their efficiency in adsorbing gas-phase molecules and elements is important to further refine evolutionary models of interstellar clouds, galaxies and even the universe[25]. Unfortunately, our knowledge of the evolution of dust grains in the ISM is far from complete. One of the most critical issues in our understanding of dust in the ISM is the discrepancy between injection rates of dust (10^9 yrs to produce all observed dust) and dust destruction rates (10^8 yrs to destroy all observed dust)[19]. The ongoing debate as whether these two rates can be accurately determined with current knowledge[25] highlight the limitations of our knowledge of the critical processes in the ISM.

The IR spectra of astrosilicate dust show differences between the regions where dust is produced (e.g. AGB stars), where it is reprocessed (e.g. the different phases of the ISM) and where it is finally incorporated (e.g. protoplanetary disks). As described in Chapter 8 the main evidence for the presence of silicates in astronomical environments is the IR signatures of the Si-O stretching (~9.7 μm) and O-Si-O bending modes (~18 μm) in silicate tetrahedra. The silicate component expelled from AGB stars is mainly amorphous, but a considerable fraction (from ~20 to 60% in Si mass) could be present as crystalline silicates, as identified by features at 40 and 60 μm[85]. However, IR spectra observed from the ISM indicate that the structure of the dust is amorphous in nature, with an estimated maximum fraction of crystalline dust of 2.4%[134]. Even though the IR spectra of silicates in the ISM clearly points to amorphous dust, the position and width of the two main silicate features varies for different sources[48], which has been suggested to be related to the growth of dust grains or differences in composition. The disappearance of crystalline spectral features suggests that processing occurs in the ISM. There is debate as whether this processing leads to complete destruction of silicates and regrowth into amorphous grains[54] or, instead, that amorphization (without destructions) of crystalline grains is fast enough to produce the observed IR spectra[135]. Current models appear to favour a complete destruction and regrowth scenario.

In addition to IR observations, a novel method has been devised to obtain new information about astrosilicates. Stars that emit strong radiation in the X-ray region of the spectrum can be used to analyse the X-ray absorption spectra of astrosilicates if the original star is located behind a significant dust-containing region of the ISM. Using an extensive set of experimental X-ray absorption fine structure (XAFS) spectra as reference, including amorphous and crystalline materials from several silicate stoichiometries, the XAFS spectra from astronomical observations can be fitted. Preliminary data obtained from the fitting of nine X-ray sources by Zeegers et. al. [136] appear to be at odds with the analysis of IR spectra

with respect to the fraction of crystalline silicates. This work indicates that the minimum fraction of crystalline dust in the ISM is at least 4%, with the largest fraction being 12%. It must be taken into account that the fine structure that appears in a XAFS spectrum is a result of the atomic neighbourhood of the irradiated atom and is thus very sensitive to short range order. It is also possible that the amorphous structures generated either in the ISM or in the outflows of AGB stars does not correspond to that of the amorphous samples synthesized in the laboratory. Hence, a plausible conclusion may be that X-ray observations show that silicates in the ISM, although amorphous at long length scales, possess larger degree of local order than expected from amorphous samples synthesized on Earth. It can also be argued that crystalline grains of up to tens of nanometres in diameter, while not being detectable in the IR, can be detected in XAFS spectra and thus could increase the observed crystalline fraction in the ISM.

Another issue with the determination of the crystalline fraction of the ISM and even the amount of astrosilicate NPs present in the ISM comes from the IR data used to fit observations. Due to the lack of spectroscopic data on nano-sized crystals, astronomers extrapolate IR optical constants of large grains down to the nanocluster regime[68]. While extrapolations have been necessary, the large fraction of surface area to bulk fractions in nanometer sized dust grains can cause the extrapolated values to be erroneous. For example, the optical constants for large grains will be dominated by a bulk environment which is different to a nanoscale object with a large fraction of surface atoms. In Chapter 10 we have shown that the IR spectra of the GM silicate nanocluster candidates are composed of a wide range of individual peaks, some of which are discernible even after summation of spectra from nanoclusters of several different sizes. As size increases, the spectra of amorphous particles must become identical to that of the corresponding micrometer particles. The cross-over size at which the IR spectra of nanoclusters will converge towards that of micrometer-sized particles is not known, but it is required in order to confirm the validity of the extrapolations used in the literature. Likewise, the shape of the IR spectra of crystalline astrosilicate NPs may not be well determined by extrapolation from that of the bulk crystalline material.

Finally, the lack of symmetry of our GM silicate nanoclusters candidates shows that the bulk crystalline structure is not stable at the nanoscale. For other systems, the dependency of stability on size is rationalized by the competition between bulk and surface energy. Several examples of such transitions have been experimentally determined for compositions of TiO_2[137–139], ZnO[140,141] and ZrO_2[142]. If a cross-over between amorphous and crystalline phases exists at the nanoscale, it may play a fundamental role in understanding the growth of silicates in the ISM and around AGB stars, as well as understanding the dynamics of the ISM.

In the following article, we develop different dust models of astrosilicate NPs of an Mg-pure olivinic composition $(Mg_2SiO_4)_N$ and explore whether structural differences can be appreciated in their IR spectra. The model particles are generated with three different methods for sizes of 14, 30, 50, 60, 80, 92, 104 and 116 formula units (N). The methods by which such models are generated attempt to mimic the different mechanisms by which

astronomical grains could form and grow. For crystalline particles, we follow the Wulff construction, while for amorphous materials two methods are employed: i) amorphization of crystalline particles by MD simulations which allow one to generate reconstructed grains without any memory of the original crystal structure, and ii) aggregation of SiO, Mg and O atoms onto a small seed nanocluster, mirroring gas-phase dust grain nucleation at a temperature of 1000K using MD simulations. The particles that results from gas-phase aggregation are non-spherical, and very structurally inhomogeneous, with some regions having a large degree of SiO_2 polymerization, and others showing the presence of aggregates of pure MgO. Using DFT calculations the structures are refined, and their internal energies evaluated. This allows us to more accurately differentiate the three models based on energetic stability grounds, as well as structurally. We indicate measures that allow us to unequivocally determine the structural differences between the amorphous, nucleated and crystalline NPs, and try to relate them to global and local structural order, in an attempt to classify different degrees of amorphicity in the NPs. The energetical stability of each of these models has been determined and the size of stability cross-over estimated. As the most studied observable of interstellar silicate grains is their IR spectra, the main objective of this study is to identify whether the three different structural phases can be discerned throughout their IR spectra. For the smaller grain models the IR spectra could be calculated directly using DFT calculations, whereas for the larger models the use of IPs was mandatory due to the increase in computational cost. While we have shown that our newly developed Mg-FFSiOH IP can reproduce DFT relative energies better than previously reported IPs, IR spectra obtained from using Mg-FFSiOH do not accurately reproduce DFT IR spectra as well as the IP used in Walker et al[99]. For this reason, we evaluated the IR spectra of large grains using the former IP rather than Mg-FFSiOH.

This work is a collaboration with Professor Piero Ugliengo and PhD student Lorenzo Zamirri. The author of this thesis wrote the codes to perform the gas-phase aggregation of silicate grains, performed the amorphization of the crystalline structures, the RMSD-Si analysis, the tetrahedral distortion analysis and the harmonic spectra calculated with IPs. The discussion of size dependent amorphous/crystallinity cross-over, as well as the astrophysical implications of the calculated amorphous and crystalline IR spectra were also mainly written by the author.

Results

ACS EARTH AND SPACE CHEMISTRY

Article

Cite This: ACS Earth Space Chem. 2019, 3, 2323−2338

http://pubs.acs.org/journal/aesccq

What Can Infrared Spectra Tell Us about the Crystallinity of Nanosized Interstellar Silicate Dust Grains?

Lorenzo Zamirri,[†,∥] Antoni Macià Escatllar,[‡,∥] Joan Mariñoso Guiu,[‡] Piero Ugliengo,*[,†] and Stefan T. Bromley*[,‡,§]

[†]Dipartimento di Chimica and Nanostructured Interfaces and Surfaces (NIS) Centre, Università degli Studi di Torino, via P. Giuria 7, IT-10125 Torino, Italy

[‡]Departament de Ciència de Materials i Química Física and Institut de Química Teòrica i Computacional (IQTCUB), Universitat de Barcelona, C/Martí i Franquès 1, ES-08028 Barcelona, Spain

[§]Institució Catalana de Recerca i Estudis Avançats (ICREA), ES-08010 Barcelona, Spain

Supporting Information

ABSTRACT: Infrared (IR) spectroscopy is the main technique used to identify and characterize silicate dust grains in astronomical environments. From IR spectra, the fraction of crystalline dust particles can be estimated and used to help understand the processing of dust occurring in different astronomical environments such as the interstellar medium (ISM) and circumstellar shells. Narrow spectral lines are assigned to crystalline grains, while broad signals are usually assumed to originate from amorphous material. Herein, we accurately calculate the IR spectra and energetic stabilities of several amorphous and crystalline silicate nanograins with an astronomically common Mg-rich olivinic (Mg_2SiO_4) stoichiometry and with sizes ranging from hundreds to thousands of atoms. First, unlike at larger length scales, crystalline forsterite-like grains at the nanoscale are found to be energetically metastable with respect to amorphous grains. However, from our careful analysis, we further show that the IR spectra of such nanosilicate grains cannot be unambiguously used to identify their structural nature. In particular, our work indicates that amorphous and crystalline silicate nanograins both exhibit broad IR spectra typical of noncrystalline grains, raising potential issues for estimates of the fraction of crystalline silicate dust in the ISM.

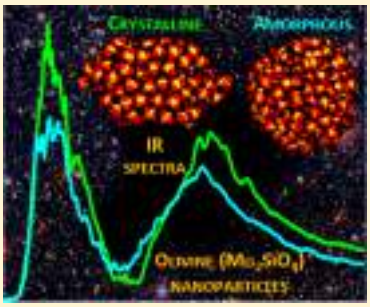

KEYWORDS: *Forsterite nanoparticles, cosmic dust, amorphous silicates, crystalline silicates, density functional theory, force fields, interstellar medium, vibrational IR spectra*

1. INTRODUCTION

Silicates are a fundamental constituent of the solid matter in the universe and are abundantly and ubiquitously detected as dust particles in several environments, e.g., dense molecular clouds (MCs), circumstellar shells (CS) of young and old stars, comets, and the interstellar medium (ISM).[1−5] The lifecycle of silicate dust is very complex and involves newly generated dust in the CS of old dying stars, destruction, regeneration, and processing in the ISM and subsequent incorporation in MCs and protoplanetary disks.[1,2] Silicate dust is affected to a greater or lesser degree by the astrophysical conditions encountered throughout its journey. Knowledge of the structure and crystallinity of silicate dust can thus provide a diagnostic tool to help understand the physical and chemical conditions in a range of astronomical environments.

Infrared (IR) spectra provide the primary source of information regarding the atomistic structure of astronomical silicate dust grains. Observations where well-defined IR peaks can be discerned give strong support for the presence of highly crystalline grains (e.g., in some CSs).[6] In such cases, comparison with laboratory IR spectra from carefully prepared samples can help deduce the crystal structures and chemical compositions of the observed dust grain populations. From such studies, it has been confirmed that crystalline silicate dust is very magnesium-rich and primarily of either pyroxene ($MgSiO_3$) and/or olivine (Ol, Mg_2SiO_4) composition.[7,8] IR spectra from the ISM are dominated by two broad peaks at around 10 and 18 μm that are attributed to silicate vibrational Si−O bond stretching and O−Si−O bond bending modes, respectively. Such spectra are usually interpreted as originating from amorphous silicates.[1] This assignment is supported by noting the strong similarity of such observed IR spectra with those from experimentally prepared bulk amorphous silicates.[9−12] Spectral analyses of carefully prepared laboratory samples have revealed that the position and width of these two characteristic IR peaks of dense glassy amorphous silicates vary, to an extent, with respect to the chemical composition,[1,9] and the degree of thermal anneal-

Received: June 3, 2019
Revised: July 24, 2019
Accepted: August 19, 2019
Published: August 19, 2019

DOI: 10.1021/acsearthspacechem.9b00157
ACS Earth Space Chem. 2019, 3, 2323−2338

ing.[9−11] Interestingly, it has also been shown that experiments irradiating crystalline silicates with high energy ions, thus mirroring the environment of the ISM, can induce atomic disorder and porosity.[13] Although these irradiated samples spectroscopically appear to be very similar to dense amorphous silicates, they likely retain residual pockets of the original crystal order. By fitting observed IR spectra using various combinations of laboratory spectra, a number of investigations have attempted to gain insights into the properties and structure of amorphous silicate dust from the positions and shapes of the 10 and 18 μm silicate features.[11,14,15] Since the lifecycle of silicate dust involves different types and degrees of energetic processing, insights into the evolutionary history of grain populations and how processed they are can be gained from knowing their crystallinity. By fitting the observed 10 μm absorption feature using laboratory IR spectra from both amorphous and crystalline silicate samples, an upper bound on the fraction of crystalline silicate in the ISM of 2.2% by mass was derived,[16,17] consistent with other more recent measurements.[18] Although such studies clearly point to a strong lack of crystalline dust grains in the diffuse ISM, we explore the possibility that observational IR spectra from putative amorphous grain populations could have contributions from a population of quasi-crystalline nanosized silicate grains.

In this work, we developed atomistic models of nanoparticles (NPs) with diameters varying between ∼1.2 and ∼4.6 nm and with a pure Mg_2SiO_4 olivinic composition. It has been estimated that such small NP grains could form up to 10% of the mass of the silicates in the ISM without violating observational constraints and, if so, could form the largest population of ISM silicate dust grains by number.[19] Indirect support for the existence of such a population of nanosilicate grains also comes from their potential role in explaining the anomalous microwave emission (AME) in the ISM.[20−22] We employ both quantum mechanical (QM) and classical mechanical (CM) calculations to model our nanograins with varying degrees of crystallinity and provide a detailed analysis of their structure and relative energetic stabilities. Our main focus is on how the crystallinity of such nanograins is reflected in their IR spectra. In order to assess this, we derive reliable IR spectra directly from accurately modeling the vibrational modes in our atomistically detailed silicate NP structures. Through this approach, we explicitly show that, unlike for larger grains, IR spectra do not provide a clear measure of crystallinity for nanograins. The possible implications of our results for estimating the crystallinity of astronomical silicate dust are discussed.

2. COMPUTATIONAL DETAILS

For all QM calculations, we used the CRYSTAL package,[23] while for CM calculations we used the GULP[24] and LAMMPS[25] codes.

2.1. Relative Energies. For all calculations, the relative energies per Mg_2SiO_4 formula unit with respect to bulk crystalline forsterite of our Ol NPs, ΔE^*, have been computed according to eq 1

$$\Delta E^* = \frac{1}{N}E_{NP} - \frac{1}{4}E_{bulk} \quad (1)$$

where E_{NP} is the energy of an Ol NP with N formula units and E_{bulk} is the energy corresponding to a unit cell of crystalline forsterite containing four Mg_2SiO_4 units.

2.2. QM Calculations. For the QM modeling, we used the CRYSTAL package, which can perform *ab initio* density functional theory (DFT) and Hartree−Fock calculations of periodic (e.g., crystals, surfaces, polymers) as well as nonperiodic (e.g., molecules, NPs) systems. The wave function is expressed as a linear superposition of crystalline/molecular orbitals, which in turn are expanded as linear superpositions of Gaussian-type functions centered on all atoms, constituting the basis set. All calculations were performed within the DFT framework, using the Perdew−Burke−Ernzerhof (PBE) functional,[26] and a specific basis set consisting of the following contraction: (8s)-(61sp), (6s)-(6211sp)-(1d), and (6s)-(31sp)-(1d) for the Mg, Si and O atoms, respectively. In the following, we will refer to this basis set as "OlBS". A detailed description of the OlBS is provided in the Supporting Information (SI).

Default thresholds parameters were adopted for all energy calculations, geometry optimizations and IR frequency and intensity calculations. To evaluate the electron density, we used a pruned (75, 974) grid, consisting of 75 radial points and a maximum number of 974 angular points. At these points, Coulomb and exchange integrals were computed. All other technical details regarding these DFT calculations are reported in the SI.

2.3. CM Calculations. We used the CM-based GULP code to perform the preliminary optimizations of bulk cut NPs, to amorphize the PBE-optimized NPs through molecular dynamics (MD) simulations, and to simulate IR spectra for all NPs. Specifically, for some preliminary optimizations, we used the general Reax force-field (FF),[27] while for all other GULP calculations we used the FF used by Walker et al.,[28] which is based on previously reported FFs developed by Price et al.[29] and Catlow et al.[30] All the parameters controlling the numerical accuracy of the GULP calculations were kept constant to default values. For geometry optimizations, we used either the standard Broyden−Fletcher−Goldfarb−Shanno (BFGS) algorithm or, when necessary, the Rational Function Optimization (RFO) algorithm.[31,32] IR intensities were computed from the Born effective charge tensor.[33] All MD simulations used in the amorphization of bulk cut NPs were performed at either 1800 or 2400 K within the canonical ensemble (NVT) using a 1 fs time step and with initial velocities randomly generated at 800 K.

For preparing the nucleated NPs, we used MD-based simulations using the CM-based LAMMPS code (see Subsection 3.1.3 below). Here we progressively built NPs by the addition of monomeric species (SiO, O, and Mg) following the heteromolecular homogeneous nucleation route proposed by Goumans and Bromley.[34] Each monomeric addition step was performed within the microcanonical ensemble (NVE) with a time step of 0.5 fs and using the Berendsen thermostat to maintain the temperature between 1000 and 800 K, typical for dust nucleation in CS environments.

We checked the reliability of the PBE/OlBs and Walker FF methodologies by comparing the simulated structural (lattice parameters) and spectroscopic IR features of crystalline forsterite with those from experimental measurements. Figure 1 shows the comparison of IR spectra (the experimental spectrum from a sample of amorphous Mg_2SiO_4 olivine material is also included), while Table S2 shows the structural details in terms of the forsterite cell parameters. Experimental spectra are taken from a recent work and reproduced with the authors' permission.[35] Structural data are in excellent agreement with the experimental ones (errors are within ∼1%, Table S2) for both CM and QM based methodologies. The simulated spectra are generally in good agreement with the experimental IR spectrum for forsterite. In particular, both the QM-based (PBE/OlBS) and the CM-based (Walker FF) show two distinct Si−O

DOI: 10.1021/acsearthspacechem.9b00157
ACS Earth Space Chem. 2019, 3, 2323−2338

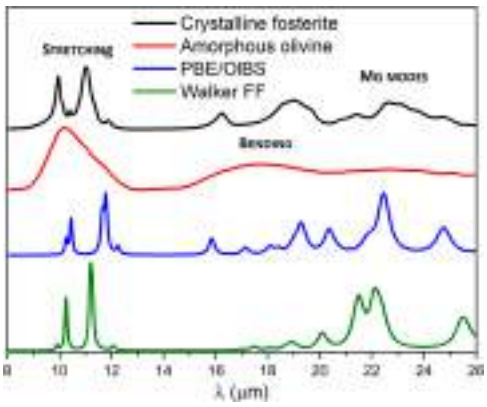

Figure 1. Experimental spectra (from ref 35) for crystalline forsterite (in black) and amorphous Mg_2SiO_4 olivine (in red) compared with calculated IR spectra using CRYSTAL at PBE/OlBS level (in blue) and GULP with the Walker FF (in green). Intensity is in arbitrary units, and spectra are vertically shifted for ease of comparison.

stretching peaks between 10 and 12 μm with similar relative intensities as in the experimental spectrum. Also, both simulated spectra exhibit a characteristic feature at ~22−23 μm. The PBE/OlBS spectrum also shows peaks between 16 and 19 μm in agreement with the experimental spectrum. These peaks are not so evident in the Walker FF spectrum, indicating that this CM-based method may find it more difficult to reproduce O−Si−O bending modes. For the purpose of the present work, we are predominantly interested in the relative amount of discernible detail in the IR spectra for our different sets of Ol NPs. As such, the two methods we employed are clearly able to provide well-defined IR spectra with narrow characteristic peaks of crystalline material, and this is sufficient for our purposes.

3. RESULTS AND DISCUSSION

In this Section, we explain the procedures we followed to generate our different NP models (Subsection 3.1), then we present and analyze the results from an energetic and structural point of view (Subsection 3.2), and finally, we show and discuss the simulated IR spectra of the NPs (Subsection 3.3). Figure 2 schematically summarizes the methods we followed to produce our atomistic NP models, the calculations performed within this work, and the methods used to define the initial geometries of our Ol NPs. Figures 3−6 show the initial and PBE/OlBS-optimized structures of some selected NPs.

3.1. Generation of NPs. To simulate Ol NPs, we developed three different sets of NP models, namely bulk cut (BC) or crystalline, amorphized (A), and nucleated (N) NPs. Hereafter we label our NPs as "*Ny Z*" where *N* represents the number of formula-units, *Z* = BC, A, or N (i.e., it indicates the set which the NP belongs to), and *y* can be any additional information necessary to identify the NP in question.

3.1.1. Bulk Cut (BC) Crystalline NPs. BC NPs were generated following the top-down methodology, starting from the Wulff construction (i.e., following the shape of a macroscopic, perfect crystal, Figure 2, panel A, top-right corner) of forsterite. We note that this method has already been successfully used to model NPs of binary oxide systems such as titania and ceria.[36,37]

The main steps we followed in this top-down approach were:

- Using CRYSTAL, we first optimized the crystallographic structure of the forsterite unit cell using DFT calculations at a PBE/OlBS level of theory (top-left corner of panel A of Figure 2).[38]
- Using the VESTA software,[39] we replicated the unit cell several times and then cut along the crystallographic directions representing the most energetically stable surfaces of forsterite crystals,[40] as derived from previous DFT calculations.[41] During this phase, the initial choice of the unit cell origin can play a fundamental role in the final shape and stability of the resulting NP, thus we also studied bulk cuts after translating the forsterite unit cell. NPs generated after this translation have been labeled with "trasl". For more details, see the SI.

The NPs generated after this top-down method represent our initial set (Figure 3). After some *a posteriori* structural modifications and preoptimizations using Reax FF, we finally fully optimized the NPs at a PBE/OlBS level of theory (see resulting structures in Figure 4). All the details concerning the top-down procedure, the *a posteriori* NP modifications and the Reax FF optimizations are reported in the SI. For the largest BC NP studied in this work (418 formula-units), as the PBE/OlBS optimization was very computationally demanding, we only employed CM-based calculations. For all reported energetic and structural results concerning this NP, refer to the calculations using the Walker FF (right-hand side of Figure 2 B). For the details, please see the SI.

3.1.2. Amorphized (A) NPs. Using the GULP code, PBE/OlBS-optimized BC NPs were heated using classical MD simulations at 1800 K with the aim of amorphizing their structures. For one NP only (30a BC) we also tested a higher temperature of 2400 K to check for temperature effects on the final structure and morphology of the NP (see Sections 3.2 and 3.3 for details). For most NPs, after a 10 ps equilibration, we ran MD simulations for 20 ps of production time. For the largest 418 formula unit NP, a significantly longer 200 ps production time was found to be necessary to amorphize the NP. Further details about these MD runs are available in the SI. These amorphized particles were then optimized at a PBE/OlBS level of theory using CRYSTAL (see Figure 2, panel B). The final optimized NP structures are shown in Figure 5.

3.1.3. Nucleated (N) NPs. Since the A NPs were generated by thermal annealing of BC NPs, it is possible that they can still retain geometric similarities with the original crystalline structures. As silicates in the ISM may form by condensation from the gas-phase under nonequilibrium conditions, amorphous silicate grains, however, can be completely unrelated to bulk crystal structures. Therefore, we also constructed NPs using a bottom-up procedure through monomeric addition ensuring no relationship with the forsterite crystal structure and then ran MD at 1800 K simulations using the LAMMPS code. These N NPs were then finally optimized at PBE/OlBS level of theory using CRYSTAL (see resulting NP structures in Figure 6).

It is worth noting that, as a consequence of the way they are generated, these N NPs often appear to display as a mixture of MgO, pyroxenes (−Si−O− chains), and pure olivine, although their stoichiometries are the same as that of pure forsterite. This differentiation of phases is particularly evident for the smaller NPs (see, for example, the 30 N NP of Figure 6) where the structures are quite distinct to that of forsterite (the forsterite unit cell structure is reported in the top-left corner of Figure 2, panel A).

DOI: 10.1021/acsearthspacechem.9b00157
ACS Earth Space Chem. 2019, 3, 2323−2338

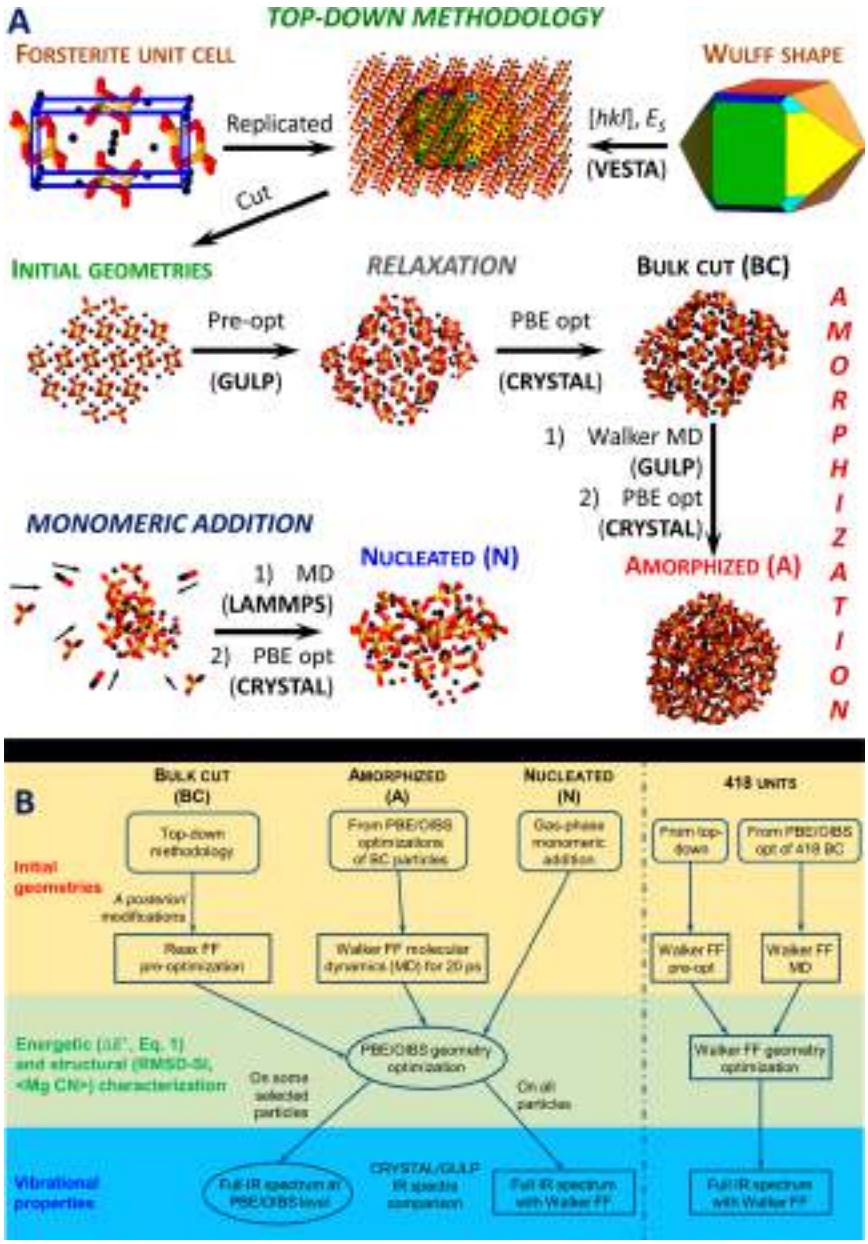

Figure 2. A: Graphical representation of the procedures followed to obtain our three types of Ol NPs. *i*) bulk cut (BC) NPs (top-down methodology, followed by structural relaxation using the GULP code at Reax FF level), *ii*) amorphized (A) NPs (MD-based amorphization at high temperatures using the GULP code with the Walker FF), and *iii*) nucleated (N) NPs (from gas-phase monomeric addition). Atom color code: Si, yellow; O, red; Mg, black. B: schematic representation of the methods employed in the work. In rounded rectangles we outline the methods we used to define the initial geometries of our NPs (panel A). Square rectangles represent FF calculations (GULP), while ellipses represent PBE/OlBS calculations (CRYSTAL). The scheme on the right-hand side of the straight dot-dashed line refers only to the 418 formula-units NP, for which slight modifications of the NP-generation procedure were necessary (see Sections 3.1.1 and 3.1.2) and for which all properties were calculated exclusively with FFs.

3.2. Energetic and Structural Features. *3.2.1. Energetics and Stability.* The relative energetic stability of our PBE/OlBS-optimized NPs per Mg_2SiO_4 formula unit with respect to the forsterite bulk (ΔE^*) has been computed according to eq 1. ΔE^* values (in kJ mol^{-1}) for all NPs are reported in Table 1, together with other structural properties. We have grouped the

DOI: 10.1021/acsearthspacechem.9b00157
ACS Earth Space Chem. 2019, 3, 2323−2338

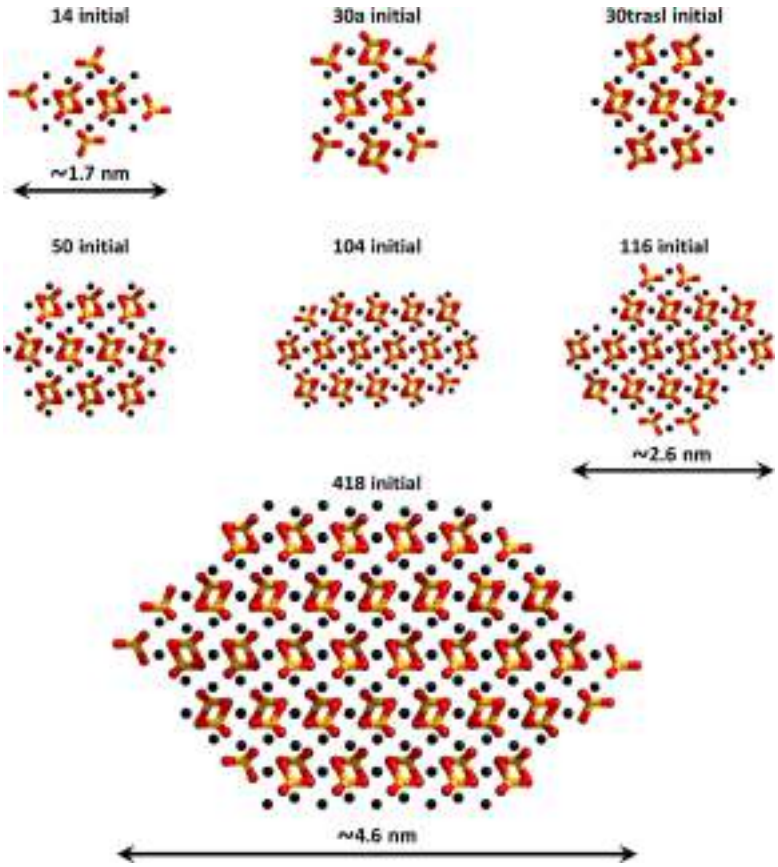

Figure 3. Selected structures of the set of initial unrelaxed Ol NPs (see Subsection 3.1.1), i.e., with structures frozen to those of the original forsterite crystal. Color code: same as Figure 2. Note that the relative NP sizes are not to scale. See Figure S1 for the full set of initial NP structures.

data with respect to the number of formula units N in order to facilitate a comparison between NP models of the same size. The NPs containing 30 formula units are used as a test case to show the effect of different methods to generate the crystal cuts as well as different annealing temperatures. 30a BC and 30b BC NPs correspond to two different crystalline cuts for the 30 formula unit nontranslated NP (Figures 3 and 4). The 30a A at 1800 K and 30a A at 2400 K NPs have been amorphized using two MD runs at 1800 and 2400 K, respectively (Figure 5).

The overall energetic stability is clearly affected by the different processes involved in the generation of a given NP, which highlights the importance of carefully generating such NPs in order to estimate the amorphous vs crystalline stability crossover size regime. For example, the difference in energy per formula unit between the 30a BC and 30trasl BC NPs is 23.6 kJ mol^{-1} (Table 1). This energy difference is close to that between forsterite and the energetically metastable wadsleyite Mg_2SiO_4 crystal polymorph (~32 kJ mol^{-1}).[42] This result highlights the importance of generating top-down BC NPs from unit cells with different translated origins. Generally, this can also be seen from the fact that the lowest lying BC NP structure (highlighted in bold in Table 1) is neither consistently in the translated ("trasl") nor in the nontranslated series. Conversely, different amorphization temperatures (1800 vs 2400 K) do not appear to significantly affect the final results, at least from an energetic stability (ΔE^*) point of view.

Figure 7 provides the ΔE^* values as a function of $N^{-1/3}$, following the spherical cluster approximation (SCA) that relates the energy of a NP with the ratio between its surface and bulk atoms.[43] We note that the SCA is only a first order geometric approximation that does not take into account the atomic/electronic degrees of freedom (e.g., surface stress) in realistic NPs, which roughly correspond to higher order terms.[36] We find that the lowest energy structures of each family of crystalline, amorphous, and nucleated NPs follow well a simple fitted $N^{-1/3}$ dependence, with R^2 values of 0.982, 0.986, and 0.979, respectively. Hence, even if some of the NP structures do not correspond to the lowest energy minima for that family of NPs, these simple fits can provide a tentative estimate of the size-dependent energetic trends for each of the NP families.

We first note that the A NPs are the most energetically stable NPs for all considered sizes. Although A NPs are always more stable that N and BC NPs, we note that the largest A NPs of 104 and 116 formula units are higher in energy per unit than the smaller 92 unit A NP. This result clearly indicates that the 104 and 116 unit A NP models are not the most stable amorphous NPs for their size. As found in other NP systems,[36] the BC NP structures are more energetically unstable relative to the A NPs

DOI: 10.1021/acsearthspacechem.9b00157
ACS Earth Space Chem. 2019, 3, 2323−2338

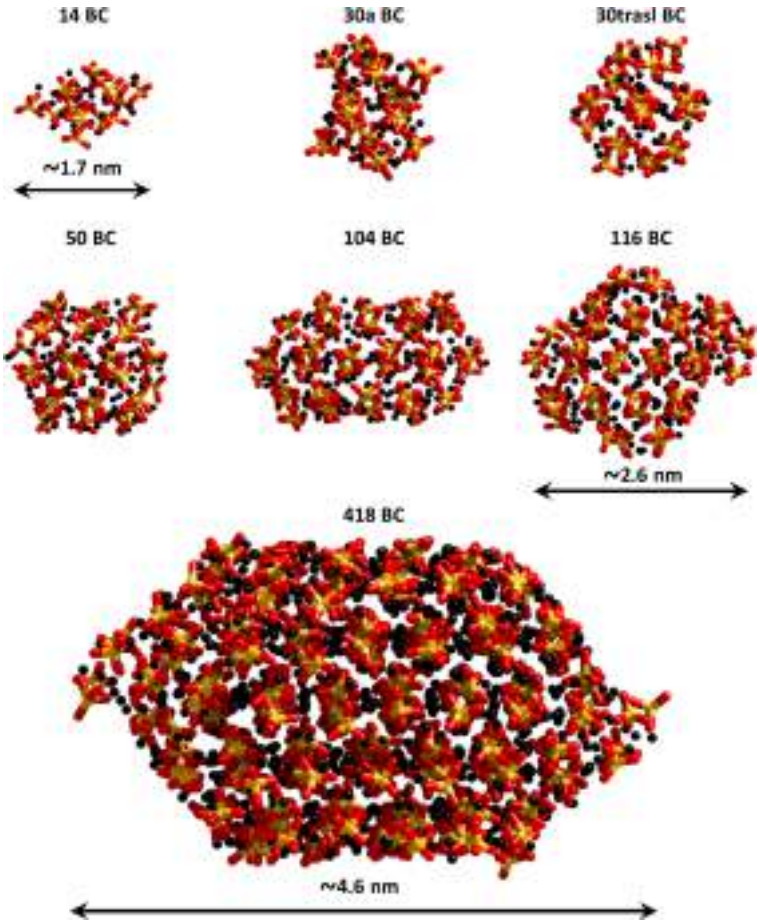

Figure 4. Selected structures of the set of optimized PBE/OlBS bulk cut (BC) NPs particles (Subsection 3.1.1), i.e., NPs resulting from energy-lowering relaxation of the NP structures in Figure 3. Color code: same as Figure 2. Note that the relative NP sizes are not to scale. See Figure S2 for the full set of BC NPs.

for the smallest sizes but converge faster to the bulk limit (i.e., the fitting line for BC NPs has a steeper slope than that for A NPs), as expected by the fact that crystalline forsterite is the most stable bulk phase of the Mg-rich olivine family. This implies that any process that generates small crystalline NPs will be generating metastable particles, which will, upon annealing, evolve toward amorphous structures. Although the exact energy evolution for each family is not precise due to the use of the SCA and the fact that not all NPs are the lowest energy for their type and size, we can extrapolate the fitted lines to roughly estimate the energetic crossover point between amorphous and crystalline NPs. Following a previous study,[44] we convert the number of formula units to the radius of an NP assuming a spherical shape and a volume per Mg_2SiO_4 unit extracted from bulk forsterite. With the current available data, the crossover between A and BC NPs appears to occur at a diameter of ∼12 nm, which is quite far away from the NP sizes explored within this work. Finally, the N NPs appear to be the most energetically unfavorable species, typically being ∼50 kJ mol^{-1} less stable than the BC NPs. It is reasonable to suggest that the large metastability of N NPs arises from their "glass-like" silicate disorder and the suboptimal mixing of MgO units into their structure. There is still an ongoing debate on the formation mechanisms of silicate dust in the envelopes of asymptotic giant branch (AGB) stars. Observational evidence seem to show the preferential formation of amorphous material with respect to crystalline NPs,[45] while thermodynamics based on extended systems always assume the formation of the most stable bulk phase, which is crystalline Ol.[46] The results in this work highlight the necessity to consider the formation of amorphous Ol NPs as a possible route for the condensation of silicate species in CS, probably aiding to bridge the discrepancy between purely thermodynamic arguments and observational evidence. It must also be considered that, although on thermodynamics grounds, the smallest silicate grains should be amorphous, the actual structure of dust particles of such dimension in CSs and the ISM will not depend only on the energetics but also on several processes like accretion from nucleation centers, temperature-related kinetics effects, high- and low-energy collisional events involving cosmic rays, and/or other dust particles.[1,2,6,47,48]

3.2.2. Structural Descriptors and Characterization. The energetic analysis performed in Subsection 3.2.1 suggests the

DOI: 10.1021/acsearthspacechem.9b00157
ACS Earth Space Chem. 2019, 3, 2323−2338

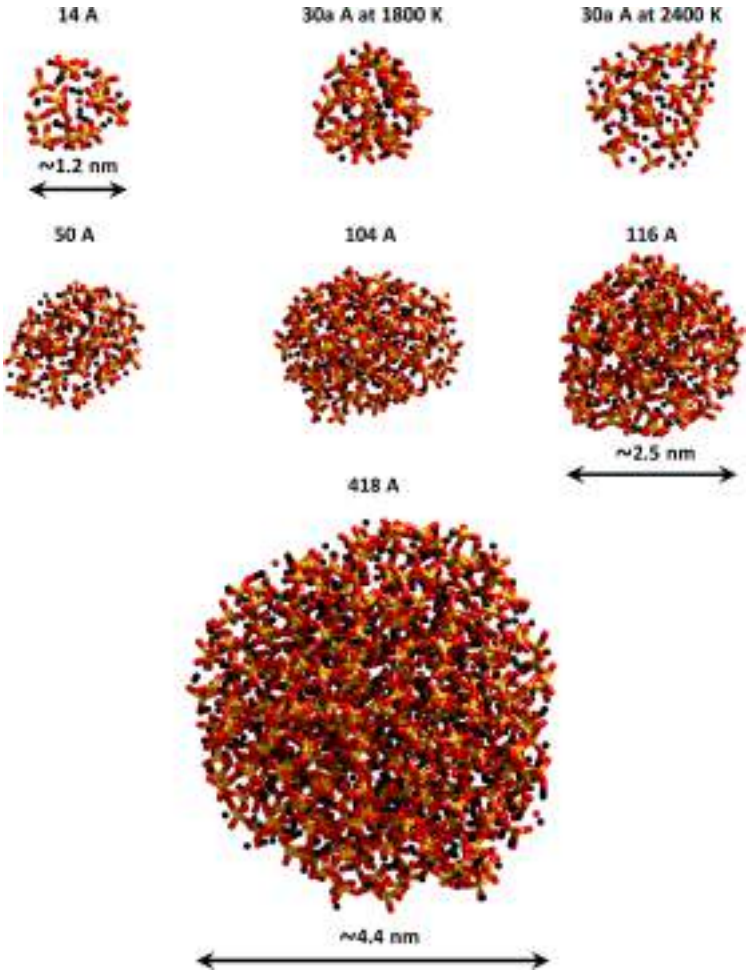

Figure 5. Selected structures of the set of amorphized (A) NPs, after PBE/OlBS optimization (Subsection 3.1.2). Color code: same as Figure 2. Note that the relative NP sizes are not to scale. See Figure S3 for the full set of A NPs.

existence of at least three energetically distinguishable phases of small Ol NPs: amorphous material with mainly isolated $[SiO_4]^{4-}$ tetrahedra, crystalline forsterite, and glass-like NPs with some segregated pockets of MgO and more polymerized silicate units. From an energetic point of view, these three phases are represented by our three sets of A, BC, and N NPs, respectively. Experimental characterization of these phases at such a small scale would be extremely challenging. Theoretically, however, with direct access to the detailed atomistic structure, we can begin to quantitatively analyze the structural differences among these three NP families.

Silicates are structurally complex inorganic materials due to the presence of both ionic (Mg−O) and semicovalent (Si−O) bonds, with the former being weaker than the latter. The difference in bond energy causes Mg cations to be more mobile, while the SiO_4 anionic units are more rigid but can create complex polymerized networks with little energetic cost. In order to structurally characterize our NPs, we first take the crystalline forsterite phase as a crystalline benchmark, which we describe in terms of tetrahedral units of SiO_4 that are regularly interspaced by octahedrally coordinated Mg cations. Second, we assume that the degree of crystallinity of NPs can be described by two structural measures that we take to be optimal in the Ol bulk crystal: *i*) short-range structural order, which is related to the orientation and distortion of SiO_4 tetrahedra and MgO_6 octahedra, at their fixed lattice sites, and *ii*) long-range periodic order, which is related to the repeated presence of the SiO_4 and MgO_6 units along the crystal lattice vectors.[38,40] In this work, we use the average Mg-coordination number ($\langle$Mg CN$\rangle$) and the structural distortion of SiO_4 tetrahedra to describe short-range order, while the root-mean-square-displacement of silicon atoms (RMSD-Si) is used to describe long-range order. The use of $\langle$Mg CN$\rangle$ as a short-range order descriptor is justified by the fact that reorientation of silicate tetrahedra and displacement of Mg cations from their equilibrium geometries will cause changes in the Mg−O distances and, hence, to the coordination numbers. It is reasonable to assume that amorphization using mild temperatures will involve small changes in the orientation

DOI: 10.1021/acsearthspacechem.9b00157
ACS Earth Space Chem. 2019, 3, 2323−2338

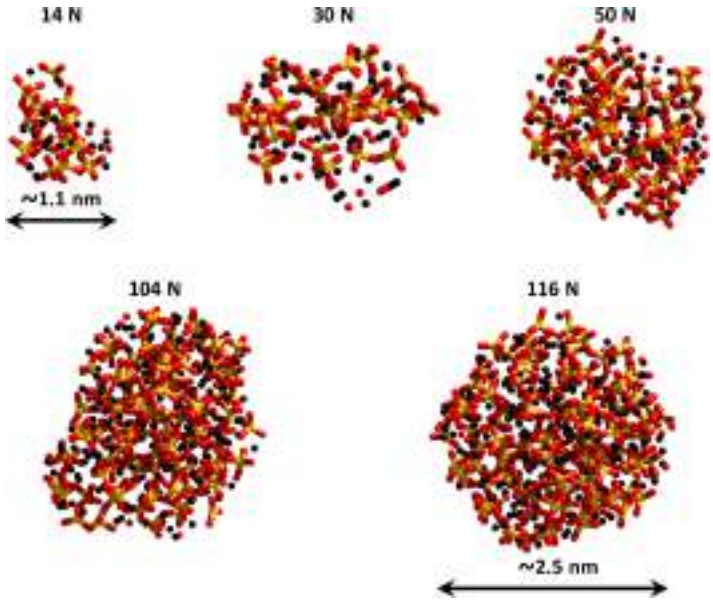

Figure 6. Selected structures of the set of nucleated (N) NPs, after PBE/OlBS optimization (Subsection 3.1.3). Color code: same as Figure 2. Note that the relative NP sizes are not to scale. See Figure S4 for the full set of N NPs.

and/or distortion of the different units, especially for the lower coordinated (i.e., least well bound) atoms at the surface. Surface relaxation of a NP can thus be seen as a local amorphization taking place at the outermost layers of the NP, which should be reflected in the ⟨Mg CN⟩ values and the spatial distribution of SiO_4 structural distortion. However, a higher temperature amorphization should cause a strong displacement of the different SiO_4 units, with the possibility of inducing polymerization of the silicate skeleton. The displacement of the SiO_4 units can be analyzed through the RMSD-Si. Although the RMSD-Si is a natural way in which to compute the displacement in the MD amorphized NPs with respect to the corresponding parent BC NP, the comparison with the nucleated NPs is not straightforward, as the atomic assignment cannot be unequivocally matched to an original crystalline structure. We therefore only provide RMSD-Si values for the A NPs in order to compare MD amorphized NP structures with the BC NPs.

In Figure 8, we show illustrative examples of crystalline (left), locally amorphized (center), and globally amorphized (right) Ol structures. In the left panel, the perfect periodic structure of crystalline forsterite can be easily recognized, with the oxygen atoms of the isolated silicate tetrahedra coordinating to the Mg cations. In the center panel, a mild amorphization has partially altered the original crystalline structure, but some crystalline features are evidently retained, while in the right panel, a higher temperature amorphization results in a structure lacking any clear remnants of crystallinity. Although the structures in the right and center panels of Figure 8 both represent amorphous Ol, both RMSD-Si and ⟨Mg CN⟩ structural descriptors can help us to analyze whether they have some intrinsic structural features that allow one to distinguish them in our NPs.

In the left panel of Figure 9 we graphically report the RMSD-Si data for all the PBE/OlBS-optimized NPs (data for the 418 formula unit NPs are omitted for a clearer representation; see Table 1 for the values). The RMSD-Si values for BC particles are low even for the smallest considered NP sizes. For A NPs, the RMSD-Si values are several times larger and spread over a wider range. These data show that BC NPs preserve a high degree of periodic crystalline order, while the relatively lower crystallinity of the A NPs is clear.

Finally, we note that the RMSD-Si value for the 30a A NP after a 2400 K MD run is almost double that of the corresponding NP after a 1800 K MD run (3.24 Å versus 6.44 Å, Table 1), with the latter value being the highest among all PBE/OlBS optimized particles. This indicates that the use of higher temperatures could produce an even more amorphized NPs. However, as we will show in the next Section, this large difference in the RMSD-Si value does not produce significant differences in the simulated IR spectra.

In the right panel of Figure 9, we graphically show the ⟨Mg CN⟩ values as a function of the number of formula units *N* for our three sets of NPs, plotting the average when we have more than one NP for a given *N*. In this figure, the ⟨Mg CN⟩ values of the initial NPs (Figure 3) are also incorporated in order to compare the values with respect to the perfect crystalline structure for every NP size (see Table 1 for values). From Figure 9, it can be seen that the initial unrelaxed cut NPs have the largest ⟨Mg CN⟩ values of all considered NPs, corresponding to the fact that, by construction, they are structurally most like the bulk crystal. However, even for this family of NPs, the largest initial cut NP has a ⟨Mg CN⟩ value of 5.28, which is still significantly different from the bulk crystal limiting value of 6 due to the lower coordination of Mg cations near the NP surface. From the other three families of NPs, as expected, BC NPs have ⟨Mg CN⟩ values, which are the closest to those of the initial cut NPs. Here, the largest BC has a lower ⟨Mg CN⟩ value of 5.04 indicating that the initial cut NPs preferentially relax to lower energy structures with slightly lower crystallinities. The lowering of ⟨Mg CN⟩ values going from the perfect initial cut NPs to relaxed BC NP structures points to the fact that even the most

DOI: 10.1021/acsearthspacechem.9b00157
ACS Earth Space Chem. 2019, 3, 2323−2338

Table 1. Summary of Energetic and Structural Data for All PBE/OlBS-Optimized Olivinic NPs[a]

NP model	n	N	$N^{-1/3}$	ΔE^*	⟨Mg CN⟩	RMSD-Si
14 BC	98	14	0.415	**420.1**	4.25	1.12
14 A				**382.0**	4.14	3.95
14 N				474.2	4.04	-
30a BC	210	30	0.322	357.9	4.35	0.95
30b BC				346.4	4.48	1.05
30trasl BC				**334.3**	4.55	0.90
30a A at 1800 K				331.1	4.37	3.24
30a A at 2400 K				340.5	4.30	6.44
30trasl A				**327.0**	4.50	3.40
30 N				417.5	4.18	-
50 BC	350	50	0.271	**298.7**	4.64	0.78
50trasl BC				311.5	4.61	0.98
50 A				282.0	4.56	2.86
50trasl A				**280.2**	4.64	2.04
50 N				350.7	4.31	-
60 BC	420	60	0.255	304.3	4.53	1.09
60trasl BC				**301.0**	4.55	0.85
60 A				281.6	4.56	3.32
60trasl A				**273.6**	4.54	1.70
60 N				350.1	4.43	-
80 BC	560	80	0.232	**287.0**	4.71	1.04
80trasl BC				294.2	4.68	0.73
80 A				272.4	4.61	3.72
80trasl A				**255.4**	4.65	2.26
80 N				323.4	4.38	-
92 BC	644	92	0.222	**263.3**	4.72	0.67
92trasl BC				281.5	4.71	0.77
92 A				264.9	4.58	3.45
92trasl A				**246.8**	4.65	2.15
92 N				329.3	4.39	-
104 BC	728	104	0.213	267.4	4.78	0.55
104trasl BC				**259.9**	4.72	0.64
104 A				262.7	4.53	2.94
104trasl A				**249.0**	4.67	2.18
104 N				318.5	4.45	-
116 BC	812	116	0.205	**255.9**	4.84	0.83
116trasl BC				272.2	4.71	0.94
116 A				250.6	4.63	3.04
116trasl A				**235.5**	4.69	2.15
116 N				308.3	4.49	-
418 BC[b]	2926	418	0.13	**82.9**	5.04	0.97
418 A[b]				**86.0**	4.74	9.21

[a] n is number of atoms; N the number of Mg_2SiO_4 formula units. Relative energies with respect to forsterite bulk (ΔE^*, eq 1) are in kJ mol^{-1} per formula unit. ⟨Mg CN⟩ values correspond to the overall average coordination numbers of Mg ions. Root-mean-square-displacements of the silicon atoms (RMSD-Si) are given in Å. ΔE^* values for the most stable bulk cut and amorphized NP for each N are highlighted in bold. [b]Data from Walker FF-optimizations only (see Figure 2, panel B, right-hand side).

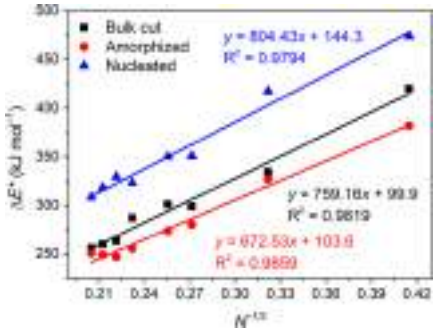

Figure 7. Relative energies with respect to forsterite bulk per formula unit (ΔE^*) for the most stable NPs we found for each size, as a function of the number of formula units (N): the linear correlation fitting parameters and R^2 values are also reported close to each respective line.

crystalline material at the nanoscale cannot be described as completely crystalline. Visual inspection of the NPs suggests that the BC NPs should be considered as being core−shell structures (i.e., with highly crystalline cores and slightly disordered near surface shells). For the largest A NP, the ⟨Mg CN⟩ value is equal to 4.74, while for a hypothetical 418 N NPs it can be predicted from the trends of the existing data to be even smaller (~4.60). These lower ⟨Mg CN⟩ values correspond to a higher degree of local structural disorder and thus even lower crystallinities. These data strengthen our above analysis concerning the structural (and energetic) distinguishability of BC, A, and N NPs.

The ⟨Mg CN⟩ and RMSD-Si values are averages over the whole structure of a NP and thus do not spatially differentiate regions of more or less local structural change within a NP. Changes in both O−Si−O angle and Si−O bond distances are typical ways in which local structural relaxation can take place. Although separated in IR spectra, relaxations of these structural features combine to distort the $[SiO_4]^{4-}$ tetrahedra in NPs. From our discussion above, we should expect that in a relaxed BC NP the relaxation of $[SiO_4]^{4-}$ tetrahedral should be mainly close to the surface, whereas for an amorphous NP we should expect all $[SiO_4]^{4-}$ tetrahedral to be fairly equally distorted. In Figure 10, we show two cuts through the relaxed 116 BC NP (left) and a cut through the 116 A NP (right) showing only the Si atoms. The degree of local $[SiO_4]^{4-}$ tetrahedral disorder (i.e., of the surrounding four oxygen atoms, which are not shown) is related to the color of the Si atom in question. We take the tetrahedral arrangement of oxygen atoms around the Si atoms in forsterite as our benchmark for the highest tetrahedrality. We measure the degree of distortion of each $[SiO_4]^{4-}$ center by taking the RMSD of the atom positions with those of a rotationally aligned $[SiO_4]^{4-}$ center from the forsterite crystal. In Figure 10, we give the lightest color to Si atoms with associated $[SiO_4]^{4-}$ centers having structures very close to those in forsterite and progressively darker shading to more distorted tetrahedrons. For the amorphized 116 formula unit NPs (right, Figure 10), the darker shading of all Si atoms shows that all $[SiO_4]^{4-}$ centers have significantly distorted structures. However, for the BC (left, Figure 10), it is clear that significant tetrahedral distortion only occurs at the surface of the NP (i.e., due to surface relaxation).

In summary, from our average measures (i.e., ⟨Mg CN⟩ and RMSD-Si values) we find that BC NPs preserve a higher degree of periodic crystallinity than A NPs, while BC, A, and N NPs all show some degree of local structural distortion, which increases with the level of amorphization. We note that our BC NP structures correspond to the most crystalline possible morphologies for their size (i.e., relaxed crystal cuts), even though our structural measures show that they do not possess the full structural order of the perfect, infinite crystal. In principle, average local structural measures such as our ⟨Mg

DOI: 10.1021/acsearthspacechem.9b00157
ACS Earth Space Chem. 2019, 3, 2323−2338

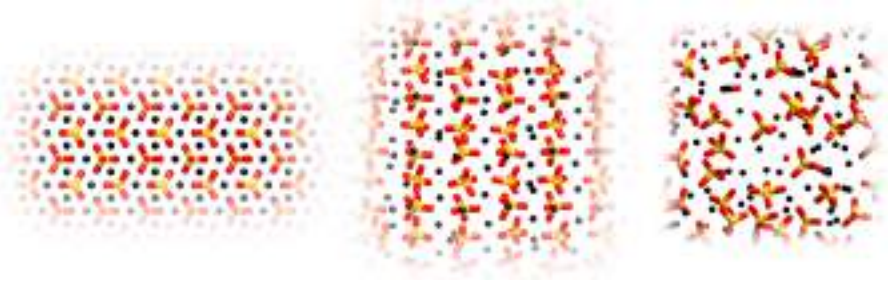

Figure 8. Left: periodic structure of perfectly crystalline forsterite. Center: structure for a noncrystalline olivinic material, preserving a partial long-range order (Si and Mg atoms are disposes in "column and rows", but silicate tetrahedra are partially distorted and rotated). Right: structure for a noncrystalline bulk material with a forsterite stoichiometry with no local and periodic order (highly distorted and partially polymerized SiO_4 tetrahedra, with some formation of MgO units). Color code: same as Figure 2.

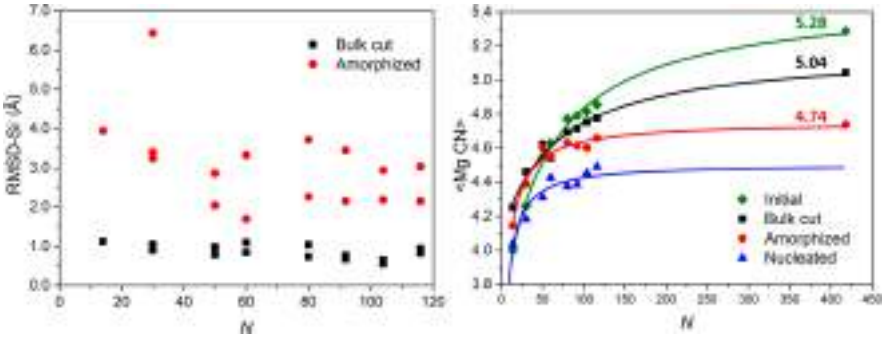

Figure 9. Left panel: Root-mean-square-displacements of the silicon atoms (RMSD-Si) in Å with respect to the initial cuts of Figure 3 as a function of the size of the particles, N (data for the 418 formula unit NPs are not shown; see Table 1 for the numerical values). Right panel: Average Mg coordination numbers, ⟨Mg CN⟩, as a function of the size of the particles (N). See Table 1 for the numerical values. The numerical values correspond to the largest 418 formula unit NPs. Lines are added as a guide to the eye.

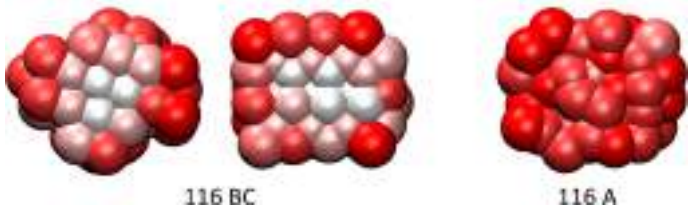

Figure 10. Cuts through 116 NPs showing only Si atoms with the degree of local tetrahedral distortion of the associated $[SiO_4]^{4-}$ centers indicated by shading (lighter, less distortion; darker, more distortion). Left: two perpendicular cuts through the 116 BC NP. Right: a single cut through the 116 A NP.

CN⟩ values could be measured and/or observed from X-ray absorption spectra. Interestingly, preliminary estimates of the proportion of crystalline dust in the ISM based on such X-ray observations have placed tentative upper limits, which are significantly in excess of those derived from IR observations.[49] From our spatially resolved maps of tetrahedral distortion of individual $[SiO_4]^{4-}$ centers, we can further confirm that, although A NPs are distorted fairly homogeneously throughout their structure, the main contribution to local structural disorder in BC NPs is through surface relaxation.

3.3. Full IR Spectra. *3.3.1. Simulated Full IR Spectra.* Besides structural identification, it is important to establish whether our Ol NPs can be characterized by IR spectroscopy, as this corresponds to the main astronomical observable for silicate dust grains. Consequently, we employed frequency calculations to obtain the full IR spectra of all optimized NPs. All IR spectra, calculated using GULP for the larger NPs and CRYSTAL for the smaller NPs, as well as the comparisons between the two, are reported in the SI.

The PBE/OlBs full IR harmonic spectra with CRYSTAL were simulated only for a few NPs, i.e., all the 14 and 30 formula units NPs and the 50 BC NP. For all NPs, we also simulated the full IR spectra with the GULP code at the Walker FF level (Figure 2, panel B). In all cases, the line shapes of the IR spectral peaks were obtained from sums of Gaussian functions centered at the computed IR frequencies with heights adjusted to the

DOI: 10.1021/acsearthspacechem.9b00157
ACS Earth Space Chem. 2019, 3, 2323−2338

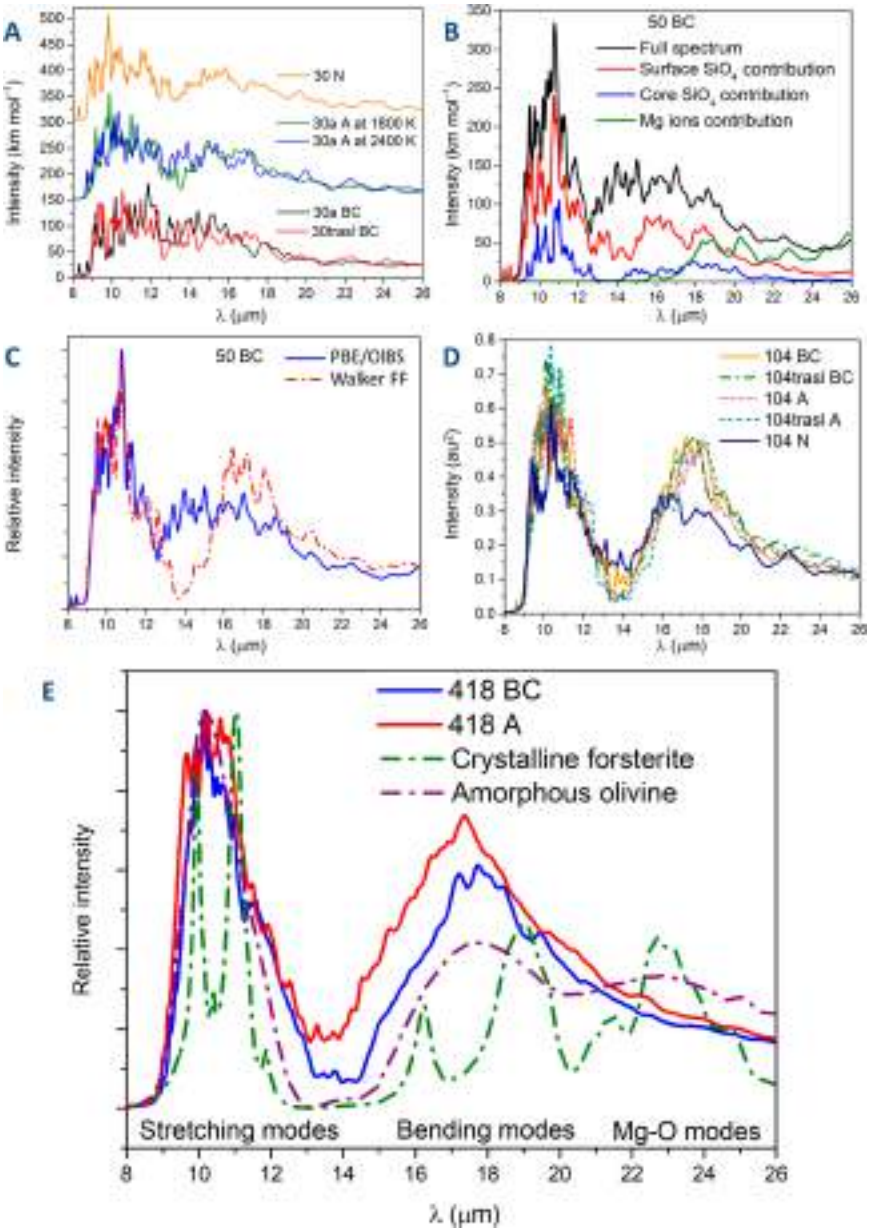

Figure 11. Simulated IR spectra for some selected NPs: A: Some selected 30 formula unit NPs calculated with DFT (spectra for A and N NPs have been vertically transposed by 150 and 300 km mol^{-1}, respectively, for the sake of clarity). B: 50 BC NP IR spectrum calculated with DFT. Contributions from subsets of atoms are also reported (see Subsection 3.3.1). C: 50 BC NP IR spectrum as calculated using DFT and using the Walker FF. D: All 104 NPs IR spectra calculated with the Walker FF. E: 418 unit BC and 418 unit A NPs IR spectra calculated using the Walker FF. The spectra for experimentally synthesized crystalline forsterite and amorphous olivine are also reported for comparison.[35] These experimental spectra have been reproduced with the authors' permission.

corresponding absolute IR intensities. The full width at half-maximum (fwhm) for the Gaussian functions was set equal to 10 cm^{-1}. This choice is justified below (see Subsection 3.3.2). In Figure 11, A–E panels, we report the full IR spectra for some selected particles in the 8–26 μm (1250–385 cm^{-1}) region. See Figures 4–6 for the corresponding structures. The full set of IR frequencies and intensities for all NPs computed with either CRYSTAL or GULP are available in the SI. The reliability of the

DOI: 10.1021/acsearthspacechem.9b00157
ACS Earth Space Chem. 2019, 3, 2323–2338

IR spectra from both CRYSTAL and GULP calculations is confirmed through a comparison with experimental data for both amorphous and crystalline Ol (Figure 1).

Figure 11 panel A reports the IR spectra of a wide selection of 30 formula unit NPs including examples of BC (both translated and nontranslated), A (amorphized at 1800 and 2400 K), and N families. At such a small NP size, and using 10 cm^{-1} as fwhm, clearly we do not have only two distinct peaks typical of amorphous silicates.[1,2,50,51] Indeed, many individual small narrow peaks extending over a wide range of wavelengths can be easily distinguished. However, even though the individual peaks of the spectra for each NPs differ in their position, the overall profile of all spectra is quite similar. In particular, the IR spectral profiles of these NPs are broadly characterized by two distinct regions, namely, the Si−O stretching between 8 to 12 μm and the O−Si−O bending between 13 to 18 μm. Silicate NPs at these sizes tend to show sharp spectral features due to the limited number of atoms, irrespectively of the amorphous/crystalline nature of the specific NP in question. Calculated IR spectra of even smaller olivine and pyroxene silicate nanoclusters have also been reported showing a similar behavior.[52] The comparison of all the spectra in Figure 11 panel A suggests that small crystalline and amorphous silicate NPs with an olivinic Mg_2SiO_4 composition are indistinguishable by IR spectroscopy irrespective of their origin. Generally, the large number of distinct peaks can be attributed to the effect of the high surface to core ratio of these NPs and the subsequent effect that surface relaxation exerts on the core of the NP. This is well underlined by Figure 11 panel B, which shows the contribution to the IR spectrum of the 50 BC NP with respect to different chemical species (i.e., "surface shell" and "core" silicates and Mg cations). In the surface shell, SiO_4 units contribute to the whole spectrum, while Mg ions in this region involve modes from $\lambda > 17$ μm (~590 cm^{-1}). The contributions from bulk SiO_4 units are also present throughout the 8−20 μm (~1250−500 cm^{-1}) range, but to a minor extent.

As IR calculations using DFT are computationally expensive for NPs larger than 50 formula units, the IR spectra of larger NPs were analyzed by means of CM calculations. The IR spectra of these NPs were calculated using the Walker FF, which provides a reasonable account of the IR peak positions of silicate NPs (see also Figures S8−S17). Figure 11 panel C shows a comparison between the IR spectrum of the 50 BC NP as calculated using the Walker FF and DFT at a PBE/OlBS level. The IR spectrum from a CM-based FF calculation can only provide an approximation to the more accurate QM-based DFT-calculated spectrum; however, the overall FF description of the IR spectrum appears to still be fairly well captured. In particular, the spectrum of the 50 formula units NP in both cases comprises a wide range of features with two main regions: the Si−O stretching region around 10 μm and the O−Si−O bending region. While the FF calculation reproduces the 10 μm features very well, intensity at the O−Si−O region (i.e., ~13−16 μm) are less well captured and seems to be shifted toward longer wavelengths with respect to the DFT-calculated IR spectrum. This behavior mirrors that shown in the comparison of the Walker FF calculated spectrum of forsterite with the corresponding DFT-calculated spectrum and that from experiment (see Figure 1) and is thus perhaps a systematic feature of IR spectra calculated using the Walker FF. Nevertheless, the qualitative broad and double-peaked IR spectrum is well reproduced in both calculations, which in both cases clearly do not provide evidence for a highly crystalline NP.

Figure 11 panel D shows the full IR spectra for all the 104 formula unit NPs calculated using the Walker FF as illustrative examples. As for the 50 BC NP in Figure 11 panel B, the characteristic broad double-peaked silicate profile is reproduced for all BC, A, and N NPs. In particular, the spectra from the two BC and the two A NPs are almost identical, with very similar absolute intensities for the two main peaks. As the sizes are increased, the O−Si−O bending region appears to be less sharp and more featureless and becomes more similar to the typical features observed in the spectra of astrosilicates. This similarity is even more clear for the spectra of the largest 418 formula unit NPs, depicted in Figure 11 panel E, shown together with two experimental IR spectra for crystalline forsterite and amorphous olivine.[35] At this size, which corresponds to a NP diameter of ~4.6 nm, the BC NP IR spectrum is still dominated by the two broad silicate peaks and thus, like the A NP, spectroscopically noncrystalline. As previously discussed, the effects of surface relaxation are up to at least a size of ~4 nm, clearly large enough to prevent the appearance of crystalline features in the IR spectra.

The N NPs show slight changes from the BC and A particles. The first noticeable change corresponds to the decreases of the intensities of both peaks. In addition, the O−Si−O peak is arguably shifted toward lower values. This effect is found in the spectra of all the N NPs (see Figures S18−S26) and is probably the result of the formation of silicate polymerization and MgO segregation. The displacement of the O−Si−O band has previously been linked to the progressive change of silicate structure along the mineral series olivine−pyroxene−silica.[9,10,53]

The broadened IR peaks exhibited by our NPs is a direct consequence of the (partial) loss of local and periodic crystalline order. For BC NPs, which maintain much of their periodic crystalline order with respect to amorphous NPs (see Figure 9, left), the local structural disorder mainly occurs at the surface (i.e.. surface relaxation) as shown in Figure 10. For BC NPs the proportion of surface to core atoms could be a useful indicator of the extent of surface relaxation. We may assume, for example, that a necessary condition for a NP to exhibit a crystalline-like IR spectrum would be that it has at least 50% of its atoms to be in relatively undisturbed crystalline positions. Using the SCA (see Subsection 3.2.1), we predicted that the energetic stability crossover size between amorphous and crystalline NPs is ~12 nm diameter. For this NP size, the SCA provides us with an estimate of the ratio of surface to core atoms of only 24%. This is a lower bound, as in real NPs the surface area is typically larger than that of a sphere, and surface reconstruction of the outermost atoms can also disrupt subsurface atomic ordering. Nevertheless, at this crossover size and above, it is highly probable that olivinic NPs have crystalline cores and that the reconstructed surface atom proportion is <50%, and thus, we would more likely expect a crystalline-like IR spectrum. Conversely, for the largest NPs considered in our study the SCA predicts a significantly higher lower bound proportion of surface atoms of 60.5% for the 418 NPs and 79.3% for the 116 formula unit NPs. The high proportion of surface atoms in each case and the associated surface reconstruction are consistent with the noncrystalline IR spectra for these NPs. We also note that atoms in the NP interiors also appear to contribute to peak broadening. This is evidenced by the absence in the IR spectra from all NP models of significant features at wavelengths larger than ~24 μm, usually assigned to modes involving Mg cations in perfect crystalline silicates.[6] As such, even in the NP core, the positions of Mg and O atoms in the largest considered BC NPs

DOI: 10.1021/acsearthspacechem.9b00157
ACS Earth Space Chem. 2019, 3, 2323−2338

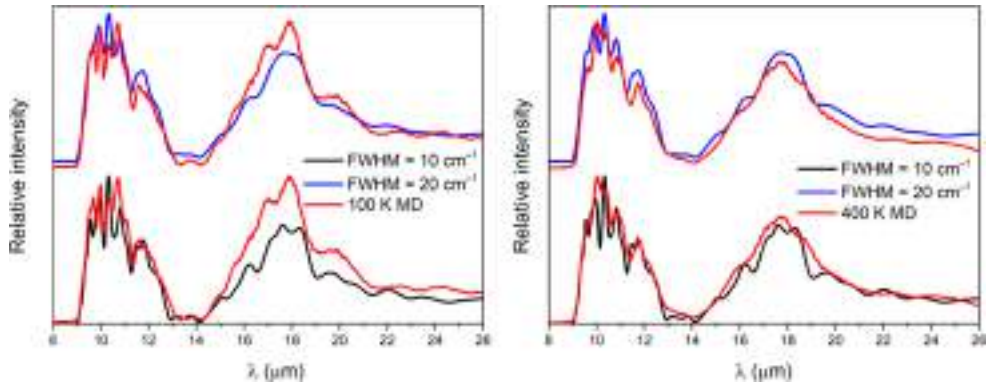

Figure 12. Comparison of the harmonic IR spectra for the 104 BC NP applying two different broadenings (fwhm = 10 cm^{-1} in black and fwhm = 20 cm^{-1} in blue), with the MD-based IR spectra (red). The MD simulation temperature is set equal to 100 K (left) and 400 K (right).

cannot be considered as fully mirroring those of crystalline forsterite.

Overall, the IR spectra of our larger NPs of all types are dominated by two broad features associated with Si−O stretching and O−Si−O bending modes. The peak wavelength, width and strength of these bands are related to the distribution of Si−O bond lengths and O−Si−O angles in each NP. For very narrow distributions of these quantities (as in crystalline forsterite), the associated IR bands will also be very narrow. For noncrystalline systems, the associated IR peaks will be related to the properties of the distributions of Si−O bonds and O−Si−O angles (e.g., broadness, maximum values). Clearly, we have similar types of 10 and 18 μm bands (i.e., position, width, and intensity) for both relaxed BC NPs and amorphized NPs, and we should thus expect that their Si−O bond lengths and O−Si−O angle distributions are similar. In Figures S27−S32 we show these distributions for the BC, A, and N 116 formula unit NPs clearly demonstrating their similarity, thus helping to underpin the similarity of the resultant IR peaks. We also note that the width of the Si−O stretching peak in our larger NPs ranges from 1.7 to 2.0 μm, which is in line with typical ISM 10 μm peak widths.[54] Although consistent with observation, our calculations only deal with a very small selection of NP structures, sizes, and compositions, and the possible significance of this match should not be overstated.

As a consequence of the above-mentioned effects, the simulated NP spectra for all our larger NPs closely resemble those assumed to arise from amorphous cosmic silicates. Thus, contrary to the spectroscopic distinguishability of large crystalline and amorphous dust grains, Mg-rich olivinic nanograins (at least in the size range considered herein) cannot be classified as being in an amorphous or crystalline state only from their IR spectra, despite the fact that they can be explicitly and measurably shown to be structurally and energetically distinguishable.

3.3.2. Temperature Effect on Simulated IR Spectra. To justify the extent of broadening applied to the individual harmonic frequencies in our computed IR spectra above, we also computed the IR spectra for the 104 BC and 80 BC NPs (as test cases) directly from finite temperature MD simulations at temperatures of 100 and 400 K. As these calculations would be extremely computationally expensive to perform at a QM level, we employed the CM-based GULP codes for this analysis. Such calculations inherently incorporate anharmonic effects and thus provide a realistic measure of the temperature-induced broadening of spectral features. Details on the theoretical background to calculate such spectra can be found in the SI. The results for the 104 BC NP only are shown in Figure 12.

At a temperature of 100 K, the MD-based IR spectra show at least five discernible peaks in the 10−12 μm Si−O stretching region and three peaks in the 15−22 μm O−Si−O bending region. This corresponds well to the respective number of distinct peaks in each corresponding region of the 10 cm^{-1} broadened harmonic spectrum (see lower spectra in Figure 12, left). Conversely, the 400 K MD-derived anharmonic spectrum has fewer discernible peaks in the Si−O wavelength region and only a single broad peak with two shoulders in the O−Si−O bending region. This spectrum better corresponds to a 20 cm^{-1} broadened harmonic spectrum (see upper spectra in Figure 12, right).

From these results, we can conclude that when computing the IR spectra of NPs using the harmonic approximation, the applied broadening can be tuned to simulate temperature-induced anharmonic effects. Here, we find that a harmonic IR spectrum broadened by 10 cm^{-1} provides a good approximation to the inherent broadening of an IR spectrum of an NP at ∼100 K. All our harmonic spectra in Figure 11 are broadened by 10 cm^{-1} and thus roughly correspond to the temperatures that could be encountered in a number of astrophysical environments (e.g., CS, protoplanetary disks, exoplanetary atmospheres, and diffuse interstellar clouds). We further note that this analysis only corresponds to the effect of temperature on the IR spectrum of a single NP. A more detailed analysis should take into account large ensembles of NPs with different sizes and structures, which will also tend to affect the discernible details in an observed IR spectrum.

We note that the small amount of broadening applied to our calculated harmonic frequencies results in a corresponding broadening of the wavelength peaks of ∼0.1 μm. As such, the applied broadening mainly affects the number of resolved peaks in a spectrum but does not significantly affect the overall broadness of features comprising many summed peaks (as clearly seen in Figure 12). As such, the widths of our calculated Si−O and O−Si−O features are hardly affected by the choice of individual peak broadening.

DOI: 10.1021/acsearthspacechem.9b00157
ACS Earth Space Chem. 2019, 3, 2323−2338

4. CONCLUSIONS

In this work we provide a comprehensive study of the energetic, structural, and IR spectroscopic properties of crystalline and noncrystalline Mg-rich olivine (Mg_2SiO_4) NPs possessing 10s to 1000s of atoms (from ∼1 to ∼5 nm in diameter). Bulk cut (BC) crystalline-like NPs were modeled using the top-down Wulff construction, while two kinds of noncrystalline NPs were studied: thermally annealed (amorphized, A) NPs based on the Wulff constructed cuts and nucleated (N) particles grown by monomeric addition. While the A and BC NPs share some structural features similar to bulk crystalline forsterite (e.g., isolated SiO_4 units), the N NPs show the presence of pyroxene-like chains and small MgO regions and thus can be seen as partial solid mixtures. In terms of energetics, BC NPs are metastable with respect to A NPs, while N NPs are higher in energy than both other NP types. In the bulk phase, however, crystalline forsterite is the most energetically stable phase. From the size-dependent energetic trends of the A and BC NPs, we tentatively estimate that the energetic stability crossover size between these two NP families will occur for a NP size of ∼12 nm diameter.

We have analyzed the structures of our NPs in detail in order to evaluate the effects of amorphization by comparing three measures of crystallinity to assess local and periodic order. The displacements of silicon atoms were used to characterize the periodic order and demonstrated that the A NPs are easily structurally differentiated as more disordered with respect to the crystalline BC NPs. From the analysis of the "average Mg coordination number" ⟨Mg CN⟩, our local order descriptor, we show that the BC NPs have lower than bulk values due to surface effects, which cause a lowering of the Mg coordination. However, the A and N NPs show even lower ⟨Mg CN⟩ values due to their more disordered structures. By examining the spatially resolved local structural distortion of tetrahedral SiO_4 units in BC and A NPs we also confirm that *i*) A NPs show a homogeneous distribution of disorder throughout the whole NP and that *ii*) BC NPs show only significant local structural distortion at their surfaces. Due to the large surface to core atom proportions (>50%) in the considered NPs, the effect of surface relaxation on the IR spectra of BC NPs is found to be relatively large.

The IR spectra of the smallest NPs are composed of a large collection of distinct signals. As the NP size increases, the IR spectra of all NP families show broader peaks in the characteristic ∼10 and ∼18 μm regions, in accordance with typical astronomical silicate IR spectra. Surprisingly, both thermally annealed structurally amorphous NPs and NPs relaxed from bulk crystalline cuts (with only significant disorder at their surfaces) show similar double-peaked broad spectra. Indeed, from the calculated IR spectra, our larger BC and A NPs would be clearly judged as spectroscopically amorphous. This result implies that it would be very difficult to accurately estimate the degree of crystallinity of nanosilicate grains in the ∼1−5 nm diameter regime using IR spectroscopy alone. In contrast, the IR spectra from nucleated NPs arising from gas phase monomeric addition show some features that make them distinguishable from the A and BC NPs.

There are several astronomical implications to our results. First, the higher energetic stability of amorphous NPs with respect to their crystalline counterparts highlight the necessity to include such considerations in theoretical studies of the formation of silicates in different environments. Here, however, further work is necessary to provide a more accurate estimate of the crossover NP size for the amorphous to crystalline transition. Second, the IR spectra of maximally crystalline nanograins (i.e., BC NPs) having diameters of ∼4.5 nm cannot be distinguished from the corresponding spectra of amorphous nanograins (i.e., A NPs). This surprising result may cast some doubts on the currently established upper limits of the fraction of crystalline silicate dust in the ISM based on observed IR spectra. If a large population of crystalline nanograins exists in the ISM, a traditional analysis would lead to their observed IR spectra being interpreted as showing the presence of amorphous grains. Generally, the existence of many highly crystalline nanograins could be hidden in IR spectra that are usually taken to indicate only amorphous silicates. Although further studies are needed to evaluate the size regime where the IR spectra of crystalline and amorphous NPs eventually becomes distinguishable, our results may also provide support for preliminary results from X-ray absorption observations,[49,55] which indicate a relatively large fraction of crystalline silicate dust in the ISM as compared to estimates based on analyses of IR spectra.[16]

■ ASSOCIATED CONTENT

Supporting Information

The Supporting Information is available free of charge on the ACS Publications website at DOI: 10.1021/acsearthspacechem.9b00157.

S1: Description of computational details. S2: Technical details about the procedure we followed to generate bulk cut and amorphized NPs. S3: Details of the calculations used to derive a realistic value of the full width at half-maximum for the IR spectra. S4: Plots of the harmonic IR spectra for all NPs. S5: Si−O bond distance and O−Si−O angle distributions for the 116 formula-unit BC, A, and N NPs (PDF)

IR spectra (ZIP)

Cartesian coordinates of all optimized NPs where we report the structure of each Ol NP in XMOL format (ZIP)

Input and output files of our CRYSTAL (DFT) and GULP (Walker FF) calculations containing the computed IR intensities and frequencies of all NPs (ZIP)

■ AUTHOR INFORMATION

Corresponding Authors

*(S.T.B.) E-mail: s.bromley@ub.edu. Telephone: +34 93 403 9732.

*(P.U.) E-mail: piero.ugliengo@unito.it. Telephone: +39 011 670 4596.

ORCID

Lorenzo Zamirri: 0000-0003-0219-6150

Piero Ugliengo: 0000-0001-8886-9832

Stefan T. Bromley: 0000-0002-7037-0475

Author Contributions

‖These authors contributed equally to this work.

Notes

The authors declare no competing financial interest.

■ ACKNOWLEDGMENTS

L.Z. and P.U. acknowledge financial support from the Italian MIUR (Ministero dell'Istruzione, dell'Università e della Ricerca) and from Scuola Normale Superiore (project PRIN 2015, STARS in the CAOS - Simulation Tools for

DOI: 10.1021/acsearthspacechem.9b00157
ACS Earth Space Chem. 2019, 3, 2323−2338

Astrochemical Reactivity and Spectroscopy in the Cyberinfrastructure for Astrochemical Organic Species, cod. 2015F59J3R). A.M.E., J.M.G., and S.T.B. acknowledge support from the Spanish MINECO/FEDER CTQ2015-64618-R research project, the Ministerio de Ciencia, Innnovación y Universidades (MCIU) Spanish Structures of Excellence María de Maeztu program through grant MDM-2017-0767, and, in part, by Generalitat de Catalunya (grants 2017SGR13 and XRQTC). The Red Española de Supercomputación (RES) and the Italian CINECA consortium are also acknowledged for the provision of supercomputing time for part of this project. We also acknowledge Dr. Daiki Yamamoto from Hokkaido University, Sapporo, and Dr. Shogo Tachibana from University of Tokyo for having provided us the raw IR data for bulk crystalline forsterite and amorphous Mg_2SiO_4 olivine shown in Figure 1 and Figure 11E.

REFERENCES

(1) Henning, T. Cosmic Silicates. *Annu. Rev. Astron. Astrophys.* **2010**, *48*, 21−46.
(2) Henning, T. Cosmic Silicates - A Review. In *Solid State Astrochemistry*; Pirronello, V., Krelowski, J., Manicò, G., Eds.; Proceedings of the NATO Advanced Study Institute on Solid State Astrochemistry, 2000; pp 85−103.
(3) Malfait, K.; Waelkens, C.; Waters, L. B. F. M.; Vandenbussche, B.; Huygen, E.; de Graauw, M. S. The Spectrum of the Young Star HD 100546 Observed with the Infrared Space Observatory. *Astron. Astrophys.* **1998**, *332*, L25−L28.
(4) Hanner, M. S. The Silicate Material in Comets. *Space Sci. Rev.* **1999**, *90*, 99−108.
(5) Waters, L. B. F. M.; Molster, F. J.; de Jong, T.; Beintema, D. A.; Waelkens, C.; Boogert, A. C. A.; Boxhoorn, D. R.; de Graauw, T.; Drapatz, S.; Feuchtgruber, H.; Genzel, R.; Helmich, F. P.; Heras, A. M.; Huygen, R.; Izumiura, H.; Justtanont, K.; Kester, D. J. M.; Kunze, D.; Lahuis, F.; Lamers, H. J. G. L. M.; Leech, K. J.; Loup, C.; Lutz, D.; Morris, P. W.; Price, S. D.; Roelfsema, P. R.; Salama, A.; Schaeidt, S. G.; Tielens, A. G. G. M.; Trams, N. R.; Valentijn, E. A.; Vandenbussche, B.; van den Ancker, M. E.; van Dishoeck, E. F.; van Winckel, H.; Wesselius, P. R.; Young, E. T. Mineralogy of Oxygen-Rich Dust Shells. *Astron. Astrophys.* **1996**, *315*, L361−L364.
(6) Molster, F. J.; Kemper, C. Crystalline Silicates. *Space Sci. Rev.* **2005**, *119*, 3−28.
(7) Jäger, C.; Molster, F. J.; Dorschner, J.; Henning, T.; Mutschke, H.; Waters, L. B. F. M. Steps toward Interstellar Silicate Mineralogy. IV. The Crystalline Revolution. *Astron. Astrophys.* **1998**, *339*, 904−916.
(8) Molster, F. J.; Waters, L. B. F. M.; Tielens, A. G. G. M. Crystalline Silicate Dust around Evolved Stars II. The Crystalline Silicate Complexes. *Astron. Astrophys.* **2002**, *240*, 222−240.
(9) Jäger, C.; Dorschner, J.; Mutschke, H.; Posch, T.; Henning, T. Steps toward Interstellar Silicate Mineralogy VII. Spectral Properties and Crystallization Behaviour of Magnesium Silicates Produced by the Sol-Gel Method. *Astron. Astrophys.* **2003**, *408*, 193−204.
(10) Speck, A. K.; Whittington, A. G.; Hofmeister, A. M. Disordered Silicates in Space: A Study of Laboratory Spectra of "Amorphous" Silicates. *Astrophys. J.* **2011**, *740*, 17.
(11) Hallenbeck, S. L.; Nuth, J. A., III; Nelson, R. N. Evolving Optical Properties of Annealing Silicate Grains: From Amorphous Condensate to Crystalline Mineral. *Astrophys. J.* **2000**, *535*, 247−255.
(12) Thompson, S. P.; Parker, J. E.; Tang, C. C. The 10 μm Band in Amorphous $MgSiO_3$: The Influence of Medium-Range Structure, Defects and Thermal Processing. *Astron. Astrophys.* **2012**, *545*, A60.
(13) Demyk, K.; D'Hendecourt, L.; Leroux, H.; Jones, A. P.; Borg, J. IR Spectroscopic Study of Olivine, Enstatite and Diopside Irradiated with Low Energy H^+ and He^+ Ions. *Astron. Astrophys.* **2004**, *420*, 233−243.
(14) Chiar, J. E.; Tielens, A. G. G. M. Pixie Dust: The Silicate Features in the Diffuse Interstellar Medium. *Astrophys. J.* **2006**, *637*, 774−785.
(15) Fogerty, S.; Forrest, W.; Watson, D. M.; Sargent, B. A.; Koch, I. Silicate Composition of the Interstellar Medium. *Astrophys. J.* **2016**, *830*, 71.
(16) Kemper, F.; Vriend, W. J.; Tielens, A. G. G. M. The Absence of Crystalline Silicates in the Diffuse Interstellar Medium. *Astrophys. J.* **2004**, *609*, 826−837.
(17) Kemper, F.; Vriend, W. J.; Tielens, A. G. G. M. The Absence of Crystalline Silicates in the Diffuse Interstellar Medium. *Astrophys. J.* **2005**, *663*, 534−534.
(18) Li, M. P.; Zhao, G.; Li, A. On the Crystallinity of Silicate Dust in the Interstellar Medium. *Mon. Not. R. Astron. Soc.: Lett.* **2007**, *382*, L26−L29.
(19) Li, A.; Draine, B. T. On Ultrasmall Silicate Grains in the Diffuse Interstellar Medium. *Astrophys. J.* **2001**, *550*, L213−L217.
(20) Kogut, A.; Banday, a. J.; Bennett, C. L.; Gorski, K.; Hinshaw, G.; Smoot, G. F.; Wright, E. L. Microwave Emission at High Galactic Latitudes. *Astrophys. J.* **1996**, *464*, L5−L9.
(21) Draine, B. T.; Lazarian, A. Diffuse Galactic Emission from Spinning Dust Grains. *Astrophys. J.* **1998**, *494*, L19−L22.
(22) Draine, B. T.; Lazarian, A. Electric Dipole Radiation from Spinning Dust Grains. *Astrophys. J.* **1998**, *508*, 157−179.
(23) Dovesi, R.; Saunders, V. R.; Roetti, C.; Orlando, R.; Pascale, F.; Civalleri, B.; Doll, K.; Harrison, N. M.; Bush, I. J.; D'Arco, P.; Llunel, M.; Causà, M.; Noël, Y.; Maschio, L.; Erba, A.; Rérat, M.; Casassa, S.. *CRYSTAL17 User's Manual*, 2018.
(24) Gale, J. D. GULP - A Computer Program for the Symmetry Adapted Simulation of Solids. *J. Chem. Soc., Faraday Trans.* **1997**, *93*, 629.
(25) Plimpton, S. Fast Parallel Algorithms for Short-Range Molecular Dynamics. *J. Comput. Phys.* **1995**, *117*, 1−19.
(26) Perdew, J. P.; Burke, K.; Ernzerhof, M. Generalized Gradient Approximation Made Simple. *Phys. Rev. Lett.* **1996**, *77*, 3865−3868.
(27) van Duin, A. C. T.; Dasgupta, S.; Lorant, F.; Goddard, W. A., III ReaxFF: A Reactive Force Field for Hydrocarbons. *J. Phys. Chem. A* **2001**, *105*, 9396−9409.
(28) Walker, A. M.; Wright, K.; Slater, B. A Computational Study of Oxygen Diffusion in Olivine. *Phys. Chem. Miner.* **2003**, *30*, 536−545.
(29) Price, G. D.; Parker, S. C.; Leslie, M. The Lattice Dynamics and Thermodynamics of the Mg2SiO4 Polymorphs. *Phys. Chem. Miner.* **1987**, *15*, 181−190.
(30) Catlow, C. R. A.; Price, G. D. Computer Modelling of Solid-State Inorganic Materials. *Nature* **1990**, *347*, 243−247.
(31) Simons, J.; Joergensen, P.; Taylor, H.; Ozment, J. Walking on Potential Energy Surfaces. *J. Phys. Chem.* **1983**, *87*, 2745−2753.
(32) Banerjee, A.; Adams, N.; Simons, J.; Shepard, R. Search for Stationary Points on Surfaces. *J. Phys. Chem.* **1985**, *89*, 52−57.
(33) Baroni, S.; de Gironcoli, S.; dal Corso, A.; Giannozzi, P. Phonons and Related Crystal Properties from Density-Functional Perturbation Theory. *Rev. Mod. Phys.* **2001**, *73*, 515−562.
(34) Goumans, T. P. M.; Bromley, S. T. Efficient Nucleation of Stardust Silicates via Heteromolecular Homogeneous Condensation. *Mon. Not. R. Astron. Soc.* **2012**, *420*, 3344−3349.
(35) Yamamoto, D.; Tachibana, S. Water Vapor Pressure Dependence of Crystallization Kinetics of Amorphous Forsterite. *ACS Earth Space Chem.* **2018**, *2*, 778−786.
(36) Lamiel-Garcia, O.; Cuko, A.; Calatayud, M.; Illas, F.; Bromley, S. T. Predicting Size-Dependent Emergence of Crystallinity in Nanomaterials: Titania Nanoclusters versus Nanocrystals. *Nanoscale* **2017**, *9*, 1049−1058.
(37) Bromley, S. T.; Moreira, I. D. P. R. R.; Neyman, K. M.; Illas, F. Approaching Nanoscale Oxides: Models and Theoretical Methods. *Chem. Soc. Rev.* **2009**, *38* (9), 2657−2670.
(38) Bostrom, D. Single-Crystal X-Ray Diffraction Studies of Synthetic Ni-Mg Olivine Solid Solution. *Am. Mineral.* **1987**, *72*, 965−972.
(39) Momma, K.; Izumi, F. VESTA 3 for Three-Dimensional Visualization of Crystal, Volumetric and Morphology Data. *J. Appl. Crystallogr.* **2011**, *44*, 1272−1276.

DOI: 10.1021/acsearthspacechem.9b00157
ACS Earth Space Chem. 2019, 3, 2323−2338

(40) Bruno, M.; Massaro, F. R.; Prencipe, M.; Demichelis, R.; De La Pierre, M.; Nestola, F. Ab Initio Calculations of the Main Crystal Surfaces of Forsterite (Mg_2SiO_4): A Preliminary Study to Understand the Nature of Geochemical Processes at the Olivine Interface. *J. Phys. Chem. C* **2014**, *118*, 2498−2506.
(41) Zamirri, L.; Corno, M.; Rimola, A.; Ugliengo, P. Forsterite Surfaces as Models of Interstellar Core Dust Grains: Computational Study of Carbon Monoxide Adsorption. *ACS Earth Space Chem.* **2017**, *1*, 384−398.
(42) Jacobs, M. H. G.; de Jong, B. H. W. S. An Investigation into Thermodynamic Consistency of Data for the Olivine, Wadsleyite and Ringwoodite Form of $(Mg,Fe)_2SiO_4$. *Geochim. Cosmochim. Acta* **2005**, *69*, 4361−4375.
(43) Johnston, R. L. *Atomic and Molecular Clusters*; CRC Press, Taylor & Francis Group, 2002.
(44) Viñes, F.; Lamiel-Garcia, O.; Illas, F.; Bromley, S. T. Size Dependent Structural and Polymorphic Transitions in ZnO: From Nanocluster to Bulk. *Nanoscale* **2017**, *9*, 10067−10074.
(45) Suh, K. W. Crystalline Silicates in the Envelopes and Discs around Oxygen-Rich Asymptotic Giant Branch Stars. *Mon. Not. R. Astron. Soc.* **2002**, *332*, 513−528.
(46) Gail, H.-P.; Sedlmayr, E. Mineral Formation in Stellar Winds. I. Condensation Sequence of Silicate and Iron Grains in Stationary Oxygen Rich Outflows. *Astron. Astrophys.* **1999**, *347*, 594−616.
(47) Molster, F. J.; Yamamura, I.; Waters, L. B. F. M.; Nyman, L.-A.; Kaufl, H.-U.; de Jong, T.; Loup, C. IRAS 09425−6040: A Carbon Star Surrounded by Highly Crystalline Silicate Dust. *Astron. Astrophys.* **2001**, *366*, 923−929.
(48) Gail, H. P.; Sedlmayr, E. Inorganic Dust Formation in Astrophysical Environments. *Faraday Discuss.* **1998**, *109*, 303−319.
(49) Zeegers, S. T.; Costantini, E.; de Vries, C. P.; Tielens, A. G. G. M.; Chihara, H.; de Groot, F.; Mutschke, H.; Waters, L. B. F. M.; Zeidler, S. Absoption and Scattering by Interstellar Dust in the Silicon K-Edge of GX5−1. *Astron. Astrophys.* **2017**, *599*, A117.
(50) Meeus, G.; Waters, L. B. F. M.; Bouwman, J.; van den Ancker, M. E.; Waelkens, C.; Malfait, K. ISO Spectroscopy of Circumstellar Dust in 14 Herbig Ae/Be Systems: Towards an Understanding of Dust Processing. *Astron. Astrophys.* **2001**, *365*, 476−490.
(51) Draine, B. T. Interstellar Dust Grains. *Annu. Rev. Astron. Astrophys.* **2003**, *41*, 241−289.
(52) Macià Escatllar, A.; Lazaukas, T.; Woodley, S.; Bromley, S. T. Structure and Properties of Nanosilicates with Olivine $(Mg_2SiO_4)_N$ and Pyroxene $(MgSiO_3)_N$ Compositions. *ACS Earth Space Chem.* **2019**, DOI: 10.1021/acsearthspacechem.9b00139.
(53) Ossenkopf, V.; Henning, T.; Mathis, J. S. Constraints on Cosmic Silicates. *Astron. Astrophys.* **1992**, *261*, 567−578.
(54) Shao, Z.; Jiang, B. W.; Li, A.; Gao, J.; Lv, Z.; Yao, J. Probing the 9.7 μm Interstellar Silicate Extinction Profile through the Spitzer/IRS Spectroscopy of OB Stars. *Mon. Not. R. Astron. Soc.* **2018**, *478*, 3467−3477.
(55) Zeegers, S. T.; Costantini, E.; Rogantini, D.; de Vries, C. P.; Mutschke, H.; Mohr, P.; de Groot, F.; Tielens, A. G. G. M. Dust Absorption and Scattering in the Silicon K-Edge. *Astron. Astrophys.* **2019**, *627*, A16.

DOI: 10.1021/acsearthspacechem.9b00157
ACS Earth Space Chem. 2019, 3, 2323−2338

Conclusions

1. Several olivinic $(Mg_2SiO_4)_N$ NP models have been generated in order to compare different possible structures that olivine dust grains may have in astronomical environments. These models correspond to crystalline cuts using the Wulff construction, amorphized NPs generated from simulated annealing using the crystal particles as initial seeds, and gas-phase aggregated (nucleated) NPs.

2. The calculated energetic stability of our Mg-silicate model NPs show that crystalline structures are metastable with respect to amorphous NPs, as generated by simulated annealing. The energetic stability of amorphous NPs has been computed by DFT methods for particles with sizes of up to 2.5 nm in diameter (almost 1000 atoms). Extrapolation of the energetic curves using the spherical cluster approximation suggest that the cross-over from amorphous to crystalline grains could occur at a size of ~12 nm in diameter. The nucleated NPs are generally >50 kJ/mol per formula unit less energetically stable than the amorphous NPs.

3. We confirm that the three different NP models are structurally differentiable by providing two measures of order: the <Si-RMSD> and the <Mg-CN>. From the average Mg coordination value, we find that a larger amorphicity implies lower coordination <Mg-CN>: nucleated NPs have the lowest <Mg-CN> values of the set, while crystalline NPs have the largest values, with the annealed NPs having values which lay in between. The crystalline NPs do not show the bulk value of <Mg-CN>, likely because the fraction of surface atoms is still too large.

4. Using DFT calculations, we computed the IR spectra for the three types of model NPs for a size of 30 units, showing, in all cases, numerous distinguishable features. As such these IR spectra are similar to those of the nanoclusters possessing 1 to 10 units. No structural differentiation seems feasible by IR spectra alone for such sized species.

5. We show that MD IR spectra as calculated with the Walker IP is able to accurately reproduce the DFT IR features of the Si-O bonding region for a 50-unit olivinic NP. The features at longer wavelengths, corresponding to the O-Si-O bending and the Mg-O stretching are much more compressed than those from the DFT calculations, and thus precise characteristic features cannot be extracted. In the comparison between experimental IR spectra and DFT-based and/or IP-based IR spectra, both computed methods show similar results. We conclude that the crystalline spectral features should be well reproduced by the Walker FF, allowing us to differentiate between crystalline and non-crystalline IR spectra for all NP sizes.

6. We model the IR spectra of nanoclusters up to a size of ~5nm in diameter using the Walker FF. As the system size increases, the IR peaks start to resemble those of amorphous astrosilicate peaks, (i.e. composed of two main regions: the 9.7 mm feature and the 18 mm feature). Nucleated particles seem to show the 18 mm feature displaced to lower wavelengths, but further analysis is needed.

7. The IR spectra of crystalline and amorphous NPs for the larger size range considered are extremely similar and both resemble a typical amorphous astrosilicate spectrum. We rationalize this finding by virtue of the large proportion of surface atoms that these NPs have, (e.g. largest grain considered has 60.5% of its atoms on the surface)

Chapter 13: Conclusions on Astronomical silicates and Outlook

The work performed in this thesis provides a solid basis for extending our knowledge on the importance of silicate nanoclusters and NPs in the universe.

The first major result of the thesis is the complete characterization of olivinic and pyroxenic Mg-pure stoichiometric nanoclusters by tailoring an IP for GO searches. Analysis of the energetics showed that some nanoclusters can be regarded as magic, and thus they should be targeted as candidates for detection. The structure of the nanoclusters is far from their corresponding bulk crystal structure, and thus they should be regarded as amorphous. However, the IR spectrum of the clusters is far from what is considered the standard amorphous IR spectrum. As nanoclusters only contain up to hundreds of atoms, the number of oscillators is small enough so that no gaussian distribution can be generated. The spectrum of the nanoclusters is composed of single signals with varying degrees of oscillator strengths. Hence, we cast doubt on the use of the standard amorphous spectrum to identify the presence of astrosilicate nanoclusters.

The second major result from this thesis is the theoretical confirmation that silicate nanoclusters have large enough dipole moments to contribute to the AME. We find that with only 1% of the silicate mass in nanoclusters, the entirety of the AME can be explained.

Finally, the energetic stability of crystalline structures with respect to amorphous ones is studied and reveals that crystalline NPs could be more stable in the region of 12nm. The IR spectrum of small NPs (up to 4nm) show that it is not possible to distinguish crystalline NPs from amorphous ones. We attribute the lack of crystalline signals to the large proportion of surface atoms, close to 60%.

The characterization of olivinic and pyroxenic nanocluster structure, energetic stability, IR spectra and MW spectra allows for several future research pathways to be followed which could involve computational and astrophysical modelling, astronomical observation and laboratory studies. A clear follow-up study involving the nanocluster structures, energies and harmonic frequencies derived in this thesis is related to the growth of nanoclusters under a range of astrophysically relevant conditions. In AGB stars, kinetic models have determined the condensation zone of silicate monomers and dimers[93] and assumed grain growth by condensation following the equation formulated by Jacobson[143]. Such models could be easily extended to include our new nanoclusters, which may provide faster rates than previously considered, as well as provide insight into whether the magic clusters identified in this work are indeed more abundant than other sizes in stellar wind conditions. Incorporation of non-stoichiometric species into kinetic models would also allow a better estimate on the pyroxene/olivine ratios under different conditions. The mechanisms and growth rate of silicates under ISM conditions could also be improved thanks to our models. The current view on grain growth in the ISM involves the adsorption of atoms on the grain surface and diffusion on the grain until reaching an active site[91]. Several parameters are needed for such calculations, such as binding energies and active site densities for each of the possible incoming species (Si, O, Mg and Fe). Growth of

nanoclusters by deposition of elements can be studied by trajectory studies which can provide more accurate measures of grain growth under the extremely cold conditions of the ISM.

In terms of IR spectroscopy, it is required to analyze the quantity of nanoclusters needed in order for their individual signals to appear in IR spectroscopy. As for NPs larger than 4 nm, we have shown the crystalline/amorphous indistinguishability of isolated NPs with respect to IR spectroscopy. In light of this finding, current estimates of the crystalline fraction of silicate dust in the ISM may require revision. In this context, it is important to evaluate the overall IR spectra of a multiphasic dust population with different fractions of crystalline components to identify the maximum degree of crystallinity that could be hidden in amorphous grains. In relation to the crystalline/amorphous fraction, annealing MD simulations could help understand the diffusion processes which cause the formation of crystalline material. In turn, such simulations could also help in determining the required timespan to obtain certain degrees of crystallization, which could be confirmed against observable evidence.

With respect to the AME, silicate nanoclusters possess very large dipole moments even in their neutral state, largely thanks to their ionic nature. Hence, it is clear that as long as silicate nanoclusters are present in the ISM, they are likely to be an important source of the AME. A reasonable next step is to confirm or discard the presence of such nanoclusters through microwave observations by: (I) providing more accurate predictions of spectral lines for the smallest silicate nanoclusters and (II) performing observations in the ranges where we have found such silicates nanoclusters to emit. The smallest monomeric and dimeric silicate nanoclusters have large numbers of MW features appearing in a range between 10 to 150 GHz, and up to even larger frequencies if the rotational temperature is larger than 20 K. MW observations can reach resolutions in the range of kHz to few MHz[144]. We note that most of the MW spectra presented in this thesis are calculated under the rigid rotor approximation, thus having errors in the range of MHz or even some GHz for the largest frequencies and highest J-levels. The data provided for P-1 includes centrifugal distortion coefficients which allow more precise calculations of MW spectral lines, but the effect of vibrations have not been taken into account. More explicitly, the rotational constants in the vibrational ground state (B_0^α) should be provided, which can be calculated as:

$$B_0^\alpha = B_e^\alpha + \Delta B_{vib}^\alpha + \Delta B_{el}^\alpha \quad (46)$$

Where ΔB_{vib}^α is the vibrational correction and ΔB_{el}^α is the electronic correction, which is usually neglected[127]. Once the vibrational contribution is taken into account, the predicted MW spectra can be used to search for identifiable lines in astronomical environments. Another related study would be to estimate of the population of rotational levels under non-equilibrium conditions. Collisions with ions, H atoms and H_2 molecules are a major source of energy transfer in MC and DC environments. Understanding attachment of H/H_2 on the grain surface and the rotational energy distribution after interaction would allow one to better characterize the rotational levels in such environments. Again, trajectory studies would shed light on such processes.

References

[1] R.J. Trumpler, Lick Obs. Bull. **14**, 154 (1930).
[2] J.S. Mathis, W. Rumpl, and K.H. Nordsieck, Astrophys. J. **217**, 425 (1977).
[3] R.A. Bernstein, W.L. Freedman, and B.F. Madore, Astrophys. J. **571**, 107 (2002).
[4] G. Lagache, J.-L. Puget, and H. Dole, Annu. Rev. Astron. Astrophys. **43**, 727 (2005).
[5] M.J. Barlow, Mon. Not. R. Astron. Soc. **183**, 417 (1978).
[6] A.P. Jones, J. Geophys. Res. Sp. Phys. **105**, 10257 (2000).
[7] R.C. Kennicutt, Annu. Rev. Astron. Astrophys. **36**, 189 (1998).
[8] K.L. Adelberger and C.C. Steidel, Astrophys. J. **544**, 218 (2000).
[9] E.F. Bell and R.C. Kennicutt, Jr., Astrophys. J. **548**, 681 (2001).
[10] E.F. Bell, Astrophys. J. **586**, 794 (2003).
[11] A.P. Boss, Science (80-.). **276**, 1836 (1997).
[12] H.-P. Gail, Astron. Astrophys. **332**, 1099 (1998).
[13] S. Cazaux and A.G.G.M. Tielens, Astrophys. J. **575**, L29 (2002).
[14] J. Navarro-Ruiz, M. Sodupe, P. Ugliengo, and A. Rimola, Phys. Chem. Chem. Phys. **16**, 17447 (2014).
[15] B. Kerkeni and S.T. Bromley, Mon. Not. R. Astron. Soc. **435**, 1486 (2013).
[16] T.P.M. Goumans, C. Richard, A. Catlow, and W.A. Brown, Mon. Not. R. Astron. Soc. **393**, 1403 (2009).
[17] M. Nuevo, U.J. Meierhenrich, L. D'Hendecourt, G.M. Muñoz Caro, E. Dartois, D. Deboffle, W.H.-P. Thiemann, J.-H. Bredehöft, and L. Nahon, Adv. Sp. Res. **39**, 400 (2007).
[18] W. Schutte, L. Allamandola, and S. Sandford, Science (80-.). **259**, 1143 (1993).
[19] A.P. Jones and J.A. Nuth, Astron. Astrophys. **530**, A44 (2011).
[20] E. Dwek, Astrophys. J. **501**, 643 (1998).
[21] P.A. Bernasconi and A. Maeder, Astron. Astrophys. **307**, 829 (1996).
[22] D. Engels, *AGB and Post-AGB Stars,* in arXiv: astro-ph/0508285 (2005).
[23] E. Dwek, in *AIP Conf. Proc.* (AIP, 2005), pp. 103–122.
[24] A.P. Jones, A.G.G.M. Tielens, D.J. Hollenbach, and C.F. McKee, Astrophys. J. **433**, 797 (1994).
[25] B.T. Draine, Annu. Rev. Astron. Astrophys. **41**, 241 (2003).
[26] B. Rodgers and A.E. Glassgold, Astrophys. J. **382**, 606 (1991).
[27] M. Asplund, N. Grevesse, A.J. Sauval, and P. Scott, Annu. Rev. Astron. Astrophys. **47**, 481 (2009).
[28] B.D. Darwent, Natl. Stand. Ref. Data Syst. Natl. Bur. Stand. (1970).
[29] C.S. Cundy and P. a. Cox, Microporous Mesoporous Mater. **82**, 1 (2005).
[30] F.J. Molster, L.B.F.M. Waters, A.G.G.M.G.M. Tielens, and M.J. Barlow, Astron. Astrophys. **382**, 222 (2002).
[31] K. Malfait, C. Waelkens, L.B.F.M.F.M. Waters, B. Vandenbussche, E. Huygen, and M.S. De Graauw, Astron. Astrophys. **332**, L25 (1998).
[32] A. Kirfel, T. Lippmann, P. Blaha, K. Schwarz, D.F. Cox, K.M. Rosso, and G. V. Gibbs, Phys. Chem. Miner. **32**, 301 (2005).
[33] J.D. Birle, G. V Gibbs, P.B. Moore, and J. V Smith, Am. Mineral. J. Earth Planet. Mater. **53**, 807 (1968).
[34] B.. Wood and O.. Kleppa, Geochim. Cosmochim. Acta **45**, 529 (1981).
[35] S.R. Elliot, *Physics of Amorphous Solids* (Longman Inc, New York, 1984).
[36] W.H. Zachariasen, J. Am. Chem. Soc. **54**, 3841 (1932).
[37] J.A. Nuth and B. Donn, Astrophys. J. **257**, L103 (1982).
[38] W. Kraetschmer and D.R. Huffman, Astrophys. Space Sci. **61**, 195 (1979).
[39] K.L. Day, Astrophys. J. **234**, 158 (1979).
[40] C. Jäger, H. Mutschke, B. Begemann, J. Dorschner, and T. Henning, Astron. Astrophys. **292**, 641 (1994).
[41] A. Tsuchiyama, in *Orig. Evol. Interplanet. Dust* (Springer, 1991), pp. 83–86.

[42] A. Tamanai, H. Mutschke, J. Blum, and G. Meeus, Astrophys. J. **648**, L147 (2006).
[43] A.K. Speck, A.G. Whittington, and A.M. Hofmeister, Astrophys. J. **740**, 17pp (2011).
[44] J. Dorschner, B. Begemann, T. Henning, C. Jaeger, H. Mutschke, J. Dorschner, B. Begemann, T. Henning, C. Jaeger, and H. Mutschke, Astron. Astrophys. **300**, 503 (1995).
[45] A. Li and B.T. Draine, Astrophys. J. **554**, 778 (2001).
[46] U.J. Sofia and D.M. Meyer, Astrophys. J. **554**, L221 (2001).
[47] M. Min, L.B.F.M. Waters, A. de Koter, J.W. Hovenier, L.P. Keller, and F. Markwick-Kemper, Astron. Astrophys. **462**, 667 (2007).
[48] Z. Shao, B.W. Jiang, A. Li, J. Gao, Z. Lv, and J. Yao, Mon. Not. R. Astron. Soc. **478**, 3467 (2018).
[49] A. Juhász, J. Bouwman, T. Henning, B. Acke, M.E. van den Ancker, G. Meeus, C. Dominik, M. Min, A.G.G.M. Tielens, and L.B.F.M. Waters, Astrophys. J. **721**, 431 (2010).
[50] D. Fabian, T. Henning, C. Jäger, H. Mutschke, J. Dorschner, and O. Wehrhan, Astron. Astrophys. **378**, 228 (2001).
[51] C. Jäger, F.J. Molster, J. Dorschner, T. Henning, H. Mutschke, L.B.F.M. Waters, L.B.F.M. Jäger, C., Molster, F. J., Dorschner, J., Henning, T., Mutschke, H., & Waters, C. Jäger, F.J. Molster, J. Dorschner, T. Henning, H. Mutschke, and L.B.F.M. Waters, Astron. Astrophys. **916**, 904 (1998).
[52] L.B.F.M. Waters, F.J. Molster, T. de Jong, D.A. Beintema, C. Waelkens, A.C.A. Boogert, D.R. Boxhoorn, T. de Graauw, S. Drapatz, H. Feuchtgruber, R. Genzel, F.P. Helmich, A.M. Heras, R. Huygen, H. Izumiura, K. Justtanont, D.J.M. Kester, D. Kunze, F.. Lahuis, H.J.G.L.M. Lamers, K.J. Leech, C. Loup, D. Lutz, P.W. Morris, S.D. Price, P.R. Roelfsema, A. Salama, S.G. Schaeidt, A.G.G.M. Tielens, N.R. Trams, E.A. Valentijn, B. Vandenbussche, M.E. van den Ancker, E.F. van Dishoeck, H. Van Winckel, P.R. Wesselius, and E.T. Young, Astron. Astrophys. **315**, L361 (1996).
[53] F. Kemper, W.J. Vriend, and A.G.G.M. Tielens, Astrophys. J. **609**, 826 (2004).
[54] B.T. Draine, in *Cosm. DUST—NEAR FAR*, edited by J.S. Th. Henning, E. Grun (2009), pp. 453–472.
[55] C. Jäger, J. Dorschner, H. Mutschke, T. Posch, and T. Henning, Astron. Astrophys. **408**, 193 (2003).
[56] E.M. Bringa, S.O. Kucheyev, M.J. Loeffler, R.A. Baragiola, A.G.G.M. Tielens, Z.R. Dai, G. Graham, S. Bajt, J.P. Bradley, C.A. Dukes, T.E. Felter, D.F. Torres, and W. van Breugel, Astrophys. J. **662**, 372 (2007).
[57] H.-P. Gail and E. Sedlmayr, Astron. Astrophys. **347**, 594 (1999).
[58] A.S. Ferrarotti and H.-P.P. Gail, Astron. Astrophys. **447**, 553 (2006).
[59] A.S. Ferrarotti and H.P. Gail, Astron. Astrophys. **382**, 133 (2002).
[60] S. Höfner, Astron. Astrophys. **491**, L1 (2008).
[61] S. Höfner and H. Olofsson, Astron. Astrophys. Rev. **26**, 1 (2018).
[62] P. Ventura, F. Dell'Agli, R. Schneider, M. Di Criscienzo, C. Rossi, F. La Franca, S. Gallerani, and R. Valiante, Mon. Not. R. Astron. Soc. **439**, 977 (2014).
[63] T. Kamiński, Proc. Int. Astron. Union **14**, 108 (2018).
[64] T. Kamiński, H.S.P. Müller, M.R. Schmidt, I. Cherchneff, K.T. Wong, S. Brünken, K.M. Menten, J.M. Winters, C.A. Gottlieb, and N.A. Patel, Astron. Astrophys. **599**, A59 (2017).
[65] L. Decin, A.M.S. Richards, L.B.F.M. Waters, T. Danilovich, D. Gobrecht, T. Khouri, W. Homan, J.M. Bakker, M. Van de Sande, J.A. Nuth, and E. De Beck, Astron. Astrophys. **608**, A55 (2017).
[66] S.T. Bromley, J.C. Gómez Martín, and J.M.C. Plane, Phys. Chem. Chem. Phys. **18**, 26913 (2016).
[67] J.C. Weingartner and B.T. Draine, Astrophys. J. Suppl. Ser. **134**, 263 (2001).
[68] A. Li and B.T. Draine, Astrophys. J. **550**, L213 (2001).
[69] J.E. O'Donnell, Astrophys. J. **437**, 262 (1994).
[70] C.H. Smith, C.M. Wright, D.K. Aitken, P.F. Roche, and J.H. Hough, Mon. Not. R. Astron. Soc. **312**, 327 (2000).
[71] H.K. Das, N. V. Voshchinnikov, and V.B. Il'in, Mon. Not. R. Astron. Soc. **404**, 265 (2010).
[72] R. Gupta, T. Mukai, D.B. Vaidya, A.K. Sen, and Y. Okada, Astron. Astrophys. **441**, 555 (2005).
[73] J. Spitzer, Lyman, Astrophys. J. **107**, 6 (1948).

[74] W.D. Watson, Astrophys. J. **176**, 103 (1972).
[75] S.T. Bromley, I.D.P.R.R. Moreira, K.M. Neyman, and F. Illas, Chem. Soc. Rev. **38**, 2657 (2009).
[76] T. Tsuji, K. Ohnaka, and W. Aoki, Astron. Astrophys. **305**, L1 (1996).
[77] A. de Oliveira-Costa, A. Kogut, M.J. Devlin, C.B. Netterfield, L.A. Page, and E.J. Wollack, Astrophys. J. **482**, L17 (1997).
[78] E.M. Leitch, A.C.S. Readhead, T.J. Pearson, and S.T. Myers, Astrophys. J. **486**, L23 (1997).
[79] A. Kogut, A.J. Banday, C.L. Bennett, K.M. Górski, G. Hinshaw, G.F. Smoot, and E.L. Wright, Astrophys. J. **464**, L5 (1996).
[80] B.S. Hensley, B.T. Draine, and A.M. Meisner, Astrophys. J. **827**, 45 (2016).
[81] T. Hoang, N.-A. Vinh, and N.Q. Lan, Astrophys. J. **824**, 18 (2016).
[82] B.S. Hensley and B.T. Draine, Astrophys. J. **836**, 179 (2017).
[83] J.E. Chiar and A.G.G.M. Tielens, Astrophys. J. **637**, 774 (2006).
[84] E. Hatziminaoglou, A. Hernán-Caballero, A. Feltre, and N.P. Ferrer, Astrophys. J. **803**, 110 (2015).
[85] C. Gielen, J. Bouwman, H. Van Winckel, T. Lloyd Evans, P.M. Woods, F. Kemper, M. Marengo, M. Meixner, G.C. Sloan, and A.G.G.M. Tielens, Astron. Astrophys. **533**, A99 (2011).
[86] T. Nozawa and M. Fukugita, Astrophys. J. **770**, 27 (2013).
[87] H. Sogawa, C. Koike, H. Chihara, H. Suto, S. Tachibana, A. Tsuchiyama, and T. Kozasa, Astron. Astrophys. **451**, 357 (2006).
[88] B.T. Draine and A. Li, Astrophys. J. **657**, 810 (2007).
[89] F.X. Desert, F. Boulanger, A. Leger, J.L. Puget, and K. Sellgren, Astron. Astrophys. **159**, 328 (1986).
[90] S. Zhukovska, C. Dobbs, E.B. Jenkins, and R.S. Klessen, Astrophys. J. **831**, 147 (2016).
[91] S. Zhukovska, T. Henning, and C. Dobbs, Astrophys. J. **857**, 94 (2018).
[92] T.P.M. Goumans and S.T. Bromley, Mon. Not. R. Astron. Soc. **420**, 3344 (2012).
[93] D. Gobrecht, I. Cherchneff, A. Sarangi, J.M.C. Plane, and S.T. Bromley, Astron. Astrophys. **585**, A6 (2016).
[94] S.M. Woodley, Mater. Manuf. Process. **24**, 255 (2009).
[95] C.M. Mauney and D. Lazzati, Mol. Astrophys. **12**, 1 (2018).
[96] M.J. Sanders, M. Leslie, and C.R.A. Catlow, J. Chem. Soc. Chem. Commun. 1271 (1984).
[97] A. Macià Escatllar, P. Ugliengo, and S.T. Bromley, J. Chem. Phys. **146**, 224704 (2017).
[98] A. Macià Escatllar, P. Ugliengo, and S.T. Bromley, Inorganics **5**, 41 (2017).
[99] A.M. Walker, K. Wright, and B. Slater, Phys. Chem. Miner. **30**, 536 (2003).
[100] A. Aguado and J.M. López, J. Phys. Chem. B **104**, 8398 (2000).
[101] M. Haertelt, A. Fielicke, G. Meijer, K. Kwapien, M. Sierka, and J. Sauer, Phys. Chem. Chem. Phys. **14**, 2849 (2012).
[102] T. Lazauskas, A.A. Sokol, and S.M. Woodley, Nanoscale **9**, 3850 (2017).
[103] R.A. Watson, R. Rebolo, J.A. Rubiño-Martín, S. Hildebrandt, C.M. Gutiérrez, S. Fernández-Cerezo, R.J. Hoyland, and E.S. Battistelli, Astrophys. J. **624**, L89 (2005).
[104] M. Vidal, S. Casassus, C. Dickinson, A.N. Witt, P. Castellanos, R.D. Davies, R.J. Davis, G. Cabrera, K. Cleary, J.R. Allison, J.R. Bond, L. Bronfman, R. Bustos, M.E. Jones, R. Paladini, T.J. Pearson, A.C.S. Readhead, R. Reeves, J.L. Sievers, and A.C. Taylor, Mon. Not. R. Astron. Soc. **414**, 2424 (2011).
[105] R.D. Davies, C. Dickinson, A.J. Banday, T.R. Jaffe, K.M. Górski, and R.J. Davis, Mon. Not. R. Astron. Soc. **370**, 1125 (2006).
[106] T. Ghosh, A.J. Banday, T. Jaffe, C. Dickinson, R. Davies, R. Davis, and K. Gorski, Mon. Not. R. Astron. Soc. **422**, 3617 (2012).
[107] A. Kogut, D.J. Fixsen, S.M. Levin, M. Limon, P.M. Lubin, P. Mirel, M. Seiffert, J. Singal, T. Villela, E. Wollack, and C.A. Wuensche, Astrophys. J. **734**, 4 (2011).
[108] P.A.R. Ade, N. Aghanim, M. Arnaud, M. Ashdown, J. Aumont, C. Baccigalupi, A. Balbi, A.J. Banday, R.B. Barreiro, J.G. Bartlett, E. Battaner, K. Benabed, A. Benoît, J.-P. Bernard, M. Bersanelli, R. Bhatia, J.J. Bock, A. Bonaldi, J.R. Bond, J. Borrill, F.R. Bouchet, F. Boulanger, M.

Bucher, C. Burigana, P. Cabella, B. Cappellini, J.-F. Cardoso, S. Casassus, A. Catalano, L. Cayón, A. Challinor, A. Chamballu, R.-R. Chary, X. Chen, L.-Y. Chiang, C. Chiang, P.R. Christensen, D.L. Clements, S. Colombi, F. Couchot, A. Coulais, B.P. Crill, F. Cuttaia, L. Danese, R.D. Davies, R.J. Davis, P. de Bernardis, G. de Gasperis, A. de Rosa, G. de Zotti, J. Delabrouille, J.-M. Delouis, C. Dickinson, S. Donzelli, O. Doré, U. Dörl, M. Douspis, X. Dupac, G. Efstathiou, T.A. Enßlin, H.K. Eriksen, F. Finelli, O. Forni, M. Frailis, E. Franceschi, S. Galeotta, K. Ganga, R.T. Génova-Santos, M. Giard, G. Giardino, Y. Giraud-Héraud, J. González-Nuevo, K.M. Górski, S. Gratton, A. Gregorio, A. Gruppuso, F.K. Hansen, D. Harrison, G. Helou, S. Henrot-Versillé, D. Herranz, S.R. Hildebrandt, E. Hivon, M. Hobson, W.A. Holmes, W. Hovest, R.J. Hoyland, K.M. Huffenberger, T.R. Jaffe, A.H. Jaffe, W.C. Jones, M. Juvela, E. Keihänen, R. Keskitalo, T.S. Kisner, R. Kneissl, L. Knox, H. Kurki-Suonio, G. Lagache, A. Lähteenmäki, J.-M. Lamarre, A. Lasenby, R.J. Laureijs, C.R. Lawrence, S. Leach, R. Leonardi, P.B. Lilje, M. Linden-Vørnle, M. López-Caniego, P.M. Lubin, J.F. Macías-Pérez, C.J. MacTavish, B. Maffei, D. Maino, N. Mandolesi, R. Mann, M. Maris, D.J. Marshall, E. Martínez-González, S. Masi, S. Matarrese, F. Matthai, P. Mazzotta, P. McGehee, P.R. Meinhold, A. Melchiorri, L. Mendes, A. Mennella, S. Mitra, M.-A. Miville-Deschênes, A. Moneti, L. Montier, G. Morgante, D. Mortlock, D. Munshi, A. Murphy, P. Naselsky, P. Natoli, C.B. Netterfield, H.U. Nørgaard-Nielsen, F. Noviello, D. Novikov, I. Novikov, I.J. O'Dwyer, S. Osborne, F. Pajot, R. Paladini, B. Partridge, F. Pasian, G. Patanchon, T.J. Pearson, M. Peel, O. Perdereau, L. Perotto, F. Perrotta, F. Piacentini, M. Piat, S. Plaszczynski, P. Platania, E. Pointecouteau, G. Polenta, N. Ponthieu, T. Poutanen, G. Prézeau, P. Procopio, S. Prunet, J.-L. Puget, W.T. Reach, R. Rebolo, W. Reich, M. Reinecke, C. Renault, S. Ricciardi, T. Riller, I. Ristorcelli, G. Rocha, C. Rosset, M. Rowan-Robinson, J.A. Rubiño-Martín, B. Rusholme, M. Sandri, D. Santos, G. Savini, D. Scott, M.D. Seiffert, P. Shellard, G.F. Smoot, J.-L. Starck, F. Stivoli, V. Stolyarov, R. Stompor, R. Sudiwala, J.-F. Sygnet, J.A. Tauber, L. Terenzi, L. Toffolatti, M. Tomasi, J.-P. Torre, M. Tristram, J. Tuovinen, G. Umana, L. Valenziano, J. Varis, L. Verstraete, P. Vielva, F. Villa, N. Vittorio, L.A. Wade, B.D. Wandelt, R. Watson, A. Wilkinson, N. Ysard, D. Yvon, A. Zacchei, and A. Zonca, Astron. Astrophys. **536**, A20 (2011).

[109] J.S. Greaves, A.M.M. Scaife, D.T. Frayer, D.A. Green, B.S. Mason, and A.M.S. Smith, Nat. Astron. **2**, 662 (2018).

[110] E.J. Murphy, G. Helou, J.J. Condon, E. Schinnerer, J.L. Turner, R. Beck, B.S. Mason, R.-R. Chary, and L. Armus, Astrophys. J. **709**, L108 (2010).

[111] C.L. Bennett, R.S. Hill, G. Hinshaw, M.R. Nolta, N. Odegard, L. Page, D.N. Spergel, J.L. Weiland, E.L. Wright, M. Halpern, N. Jarosik, A. Kogut, M. Limon, S.S. Meyer, G.S. Tucker, and E. Wollack, Astrophys. J. Suppl. Ser. **148**, 97 (2003).

[112] C. Dickinson, R.D. Davies, and R.J. Davis, Mon. Not. R. Astron. Soc. **341**, 369 (2003).

[113] B.T. Draine and A. Lazarian, Astrophys. J. **508**, 157 (1998).

[114] B.T. Draine and A. Lazarian, Astrophys. J. **494**, L19 (1998).

[115] C.T. Tibbs, R. Paladini, K. Cleary, S.J.C. Muchovej, A.M.M. Scaife, M.A. Stevenson, R.J. Laureijs, N. Ysard, K.J.B. Grainge, Y.C. Perrott, C. Rumsey, and J. Villadsen, Mon. Not. R. Astron. Soc. **456**, 2290 (2016).

[116] P.A.R. Ade, N. Aghanim, M.I.R. Alves, M. Arnaud, F. Atrio-Barandela, J. Aumont, C. Baccigalupi, A.J. Banday, R.B. Barreiro, E. Battaner, K. Benabed, A. Benoit-Lévy, J.-P. Bernard, M. Bersanelli, P. Bielewicz, J. Bobin, A. Bonaldi, J.R. Bond, J. Borrill, F.R. Bouchet, F. Boulanger, C. Burigana, J.-F. Cardoso, S. Casassus, A. Catalano, A. Chamballu, X. Chen, H.C. Chiang, L.-Y. Chiang, P.R. Christensen, D.L. Clements, S. Colombi, L.P.L. Colombo, F. Couchot, B.P. Crill, F. Cuttaia, L. Danese, R.D. Davies, R.J. Davis, P. de Bernardis, A. de Rosa, G. de Zotti, J. Delabrouille, F.-X. Désert, C. Dickinson, J.M. Diego, S. Donzelli, O. Doré, X. Dupac, T.A. Enßlin, H.K. Eriksen, F. Finelli, O. Forni, E. Franceschi, S. Galeotta, K. Ganga, R.T. Génova-Santos, T. Ghosh, M. Giard, J. González-Nuevo, K.M. Górski, A. Gregorio, A. Gruppuso, F.K. Hansen, D.L. Harrison, G. Helou, C. Hernández-Monteagudo, S.R. Hildebrandt, E. Hivon, M. Hobson, A. Hornstrup, A.H. Jaffe, T.R. Jaffe, W.C. Jones, E. Keihänen, R. Keskitalo, R. Kneissl, J. Knoche, M. Kunz, H. Kurki-Suonio, A. Lähteenmäki, J.-M. Lamarre, A. Lasenby, C.R. Lawrence, R. Leonardi,

M. Liguori, P.B. Lilje, M. Linden-Vørnle, M. López-Caniego, J.F. Macías-Pérez, B. Maffei, D. Maino, N. Mandolesi, D.J. Marshall, P.G. Martin, E. Martínez-González, S. Masi, M. Massardi, S. Matarrese, P. Mazzotta, P.R. Meinhold, A. Melchiorri, L. Mendes, A. Mennella, M. Migliaccio, M.-A. Miville-Deschênes, A. Moneti, L. Montier, G. Morgante, D. Mortlock, D. Munshi, P. Naselsky, F. Nati, P. Natoli, H.U. Nørgaard-Nielsen, F. Noviello, D. Novikov, I. Novikov, C.A. Oxborrow, L. Pagano, F. Pajot, R. Paladini, D. Paoletti, G. Patanchon, T.J. Pearson, M. Peel, O. Perdereau, F. Perrotta, F. Piacentini, M. Piat, E. Pierpaoli, D. Pietrobon, S. Plaszczynski, E. Pointecouteau, G. Polenta, N. Ponthieu, L. Popa, G.W. Pratt, S. Prunet, J.-L. Puget, J.P. Rachen, R. Rebolo, W. Reich, M. Reinecke, M. Remazeilles, C. Renault, S. Ricciardi, T. Riller, I. Ristorcelli, G. Rocha, C. Rosset, G. Roudier, J.A. Rubiño-Martín, B. Rusholme, M. Sandri, G. Savini, D. Scott, L.D. Spencer, V. Stolyarov, D. Sutton, A.-S. Suur-Uski, J.-F. Sygnet, J.A. Tauber, D. Tavagnacco, L. Terenzi, C.T. Tibbs, L. Toffolatti, M. Tomasi, M. Tristram, M. Tucci, L. Valenziano, J. Valiviita, B. Van Tent, J. Varis, L. Verstraete, P. Vielva, F. Villa, B.D. Wandelt, R. Watson, A. Wilkinson, N. Ysard, D. Yvon, A. Zacchei, and A. Zonca, Astron. Astrophys. **565**, A103 (2014).
[117] J.A. Rubiño-Martín, C.H. López-Caraballo, R. Génova-Santos, and R. Rebolo, Adv. Astron. **2012**, 1 (2012).
[118] a. Leger and J.L. Puget, Astron. Astrophys. **500**, 279 (1984).
[119] L.J. Allamandola, A.G.G.M. Tielens, and J.R. Barker, Astrophys. J. **290**, L25 (1985).
[120] A.G.G.M. Tielens, EAS Publ. Ser. **46**, 3 (2011).
[121] J.H.S. Green and D.J. Harrison, Spectrochim. Acta Part A Mol. Spectrosc. **32**, 1279 (1976).
[122] R.D. Nelson, D.R. Lide, and A.A. Maryott, *Selected Values of Electric Dipole Moments for Molecules in the Gas Phase* (Gaithersburg, MD, 1967).
[123] G. Malloci, C. Joblin, and G. Mulas, Chem. Phys. **332**, 353 (2007).
[124] D.M. Hudgins, C.W. Bauschlicher, Jr., and L.J. Allamandola, Astrophys. J. **632**, 316 (2005).
[125] S.A. Krasnokutski, G. Rouillé, C. Jäger, F. Huisken, S. Zhukovska, and T. Henning, Astrophys. J. **782**, 15 (2014).
[126] B.T. Draine and A.A. Fraisse, Astrophys. J. **696**, 1 (2009).
[127] C. Puzzarini, J.F. Stanton, and J. Gauss, Int. Rev. Phys. Chem. **29**, 273 (2010).
[128] W. Gordy and R.L. Cook, *Microwave Molecular Spectra*, 3rd ed. (A Wiley-Interscience publication, 1984).
[129] Z. Kisiel, PROSPE http://info.ifpan.edu.pl/~kisiel/prospe.htm.
[130] V. Barone, J. Chem. Phys. **122**, 014108 (2005).
[131] M.J. Frisch, G.W. Trucks, H.B. Schlegel, G.E. Scuseria, M.A. Robb, J.R. Cheeseman, G. Scalmani, V. Barone, G.A. Petersson, H. Nakatsuji, X. Li, M. Caricato, A. V Marenich, J. Bloino, B.G. Janesko, R. Gomperts, B. Mennucci, H.P. Hratchian, J. V Ortiz, A.F. Izmaylov, J.L. Sonnenberg, D. Williams-Young, F. Ding, F. Lipparini, F. Egidi, J. Goings, B. Peng, A. Petrone, T. Henderson, D. Ranasinghe, V.G. Zakrzewski, J. Gao, N. Rega, G. Zheng, W. Liang, M. Hada, M. Ehara, K. Toyota, R. Fukuda, J. Hasegawa, M. Ishida, T. Nakajima, Y. Honda, O. Kitao, H. Nakai, T. Vreven, K. Throssell, J.A. Montgomery Jr., J.E. Peralta, F. Ogliaro, M.J. Bearpark, J.J. Heyd, E.N. Brothers, K.N. Kudin, V.N. Staroverov, T.A. Keith, R. Kobayashi, J. Normand, K. Raghavachari, A.P. Rendell, J.C. Burant, S.S. Iyengar, J. Tomasi, M. Cossi, J.M. Millam, M. Klene, C. Adamo, R. Cammi, J.W. Ochterski, R.L. Martin, K. Morokuma, O. Farkas, J.B. Foresman, and D.J. Fox, Gaussian16b (2016).
[132] D. Hollenbach and E.E. Salpeter, Astrophys. J. **163**, 155(1971).
[133] E.F. van Dishoeck and G.A. Blake, Annu. Rev. Astron. Astrophys. **36**, 317 (1998).
[134] F.J. Molster and C. Kemper, in *ISO Sci. Leg.* (Springer-Verlag, Berlin/Heidelberg, 2005), pp. 3–28.
[135] K. Demyk, P. Carrez, H. Leroux, P. Cordier, A.P. Jones, J. Borg, E. Quirico, P.I. Raynal, and L. D'Hendecourt, Astron. Astrophys. **368**, L38 (2001).
[136] S.T. Zeegers, E. Costantini, C.P. de Vries, A.G.G.M. Tielens, H. Chihara, F. de Groot, H. Mutschke, L.B.F.M. Waters, and S. Zeidler, Astron. Astrophys. **599**, A117 (2017).
[137] H. Zhang and J.F. Banfield, J. Phys. Chem. B **104**, 3481 (2000).

[138] O. Khatim, M. Amamra, K. Chhor, A.M.T. Bell, D. Novikov, D. Vrel, and A. Kanaev, Chem. Phys. Lett. **558**, 53 (2013).
[139] K. Okada, N. Yamamoto, Y. Kameshima, A. Yasumori, and K.J.D. MacKenzie, J. Am. Ceram. Soc. **84**, 1591 (2004).
[140] Y. Ding, Z.L. Wang, T. Sun, and J. Qiu, Appl. Phys. Lett. **90**, 153510 (2007).
[141] L. Lazzarini, G. Salviati, F. Fabbri, M. Zha, D. Calestani, A. Zappettini, T. Sekiguchi, and B. Dierre, ACS Nano **3**, 3158 (2009).
[142] T. Chraska, A.H. King, and C.C. Berndt, Mater. Sci. Eng. A **286**, 169 (2000).
[143] M.Z. Jacobson, in (Cambridge University Press, 2005).
[144] Y. Ali-Haïmoud, L.M. Pérez, R.J. Maddalena, and D.A. Roshi, Mon. Not. R. Astron. Soc. **447**, 315 (2015).

Chapter 14: Thesis conclusions

While the most applied results of the research presented in his thesis have been described in the corresponding subchapters and the overall advances in the field in chapters at the end of each part, some general considerations that applies to both studies can be drawn.

First of all, we emphasize the importance that computational methodologies can have in advancing fields of study where nanoscale objects are of primary importance. We have shown that bottom-up methodologies can offer new insights of nanometer sized species which cannot be easily measured by experimental set-ups.

Another valuable point of the present thesis is the importance of IPs as pre-optimizers as well as to explore the PES of a chemical system, allowing to fasten more accurate calculations and allowing to extract reliable properties afterwards with *ab initio* methodologies. However, the use of IPs comes with the necessity of assessing whether a particular IP is capable to mimic the structure and relative energy of high accuracy methods.

Finally, we have shown the importance of amorphous structures for both TiO_2 and astronomical silicates. In this regard, it must be noted the large difference in size at which crystalline structures become the most thermodynamically favored structure: for $TiO_2$the size cross-over happens at ~2.5 nm in diameter, while for Mg_2SiO_4 the cross-over is estimated to happen at ~12 nm in diameter. The differences which make silicates become crystalline at much larger sizes should be analyzed in the future.

Appendix

1. Parameters of most important Interatomic Potentials used in this work.

Table A1: Parameters of the TiO_2 IPs used in both Chapters 5 and 6. Units of the parameters are: A_{ij}in eV,ρ_0 in Å and C_{ij} in eV·Å^6

	MA			NanoTiO		
Charge						
Ti	2.196			2.4		
O	-1.098			-1.2		
	A_{ij}	ρ_0	C_{ij}	A_{ij}	ρ_0	C_{ij}
Ti- Ti	31120.2	0.154	5.25	69000.0	0.210	500
Ti-O	16957.53	0.194	12.59	22054.2	0.185	5.05
O-O	11782.76	0.234	30.22	3328.5	0.297	16.48

Table A2: Parameters of the Mg silicate IPs used in Chapters 10 and 12. Units of the parameters are: A_{ij}in eV,ρ_0 in Å and C_{ij} in eV·Å^6

	Walker			MgFFSiOH		
Charge						
Si	4.0			2.7226		
O core	0.848190			1.91981		
O shell	-2.848190			-3.28111		
Mg	2.0			1.3613		
	A_{ij}	ρ_0	C_{ij}	A_{ij}	ρ_0	C_{ij}
Si- O	1283.90734	0.32052	10.66158	8166.2632	0.193884	0.0
Mg-O	1428.5	0.29453	0.29453	3100	0.247732	35.0
O-O	22764.0	0.149	27.88	15039.909	0.227708	0.0
			Core-shell spring constant			
			74.92038			256.71027
	Three body*					
	θ_0		k			
O-Si-O	109.47		2.097			

*: The three-body potential is modeled with harmonic function using:

$$E = \frac{1}{2}k(\theta - \theta_0)^2$$

With θ being the angle between the three atoms.

2. Comparison of the AME model from Chapter 11 with respect to currently used models.

A&A 634, A77 (2020)

Appendix A: Rotational emission for a PAH: comparison with other models

Using the equations described in the Sect. 2, in this appendix we compare the results of our model with those from the works of Ali-Haïmoud et al. (2009) and Draine & Lazarian (1998). The parameters of each environment can be found in Draine & Lazarian (1998), where we have used the dust grain temperature as the rotational temperature of our grains. The number of grains for our particle containing $N_C = 20$ atoms is extracted from the FORTRAN code in Weingartner & Draine (2001b) using a radius of ≈3.5. Dust particles of this size are likely to be the most important contributors to the AME, although larger particles also contribute to the emission. Figure A.1 shows a comparison of the results between our model and the results from Draine & Lazarian (1998) and Ali-Haïmoud et al. (2009). In CNM conditions, where the densities are extremely low and there is a large discrepancy between dust and gas temperature (T_d = 20 K, T_g = 100 K) we find a large discrepancy between published models and our model. Here our calculated emissivities are larger than expected and can not be reconciled by lowering the rotational temperature. For the MC environment, our result is 1.4 times larger than other published models. Surprisingly, for DC our model provides lower emissivities than those previously estimated. In DC, the densities are sufficiently large to expect a distribution dominated by collision interactions, which would cause the rotational temperature to be equal to the gas kinetic temperature. For RN, while $T_d \neq T_g$, the emissivity is reduced by 60% compared to other models.

From Fig. A.1 both the emissivity and peak position obtained in our model is in good agreement for the MC, DC and RN cases. Taking into account that the reported data from DL98 and AHHD correspond to total microwave emissivities for all PAHs and our data corresponds to a single particle, it is expected that our results should appear close to or below the reported data points in terms of emissivity, and at slightly larger frequencies in terms of peak position. The MC case shows larger emissivity in our model than expected, while the best case scenarios correspond to DC and RN conditions.

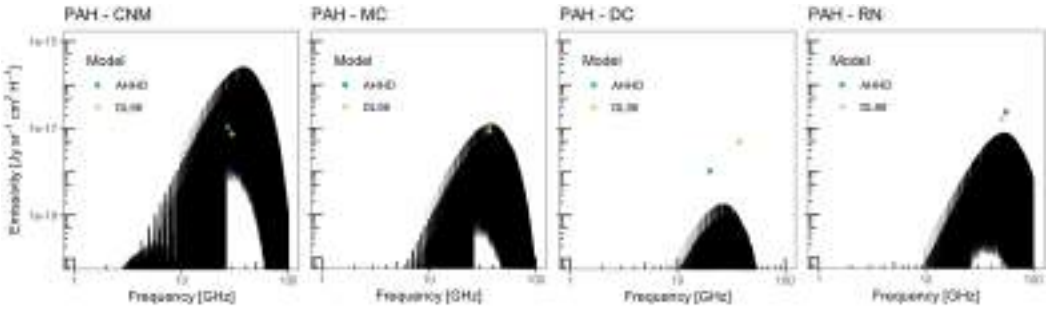

Fig. A.1. Microwave emission from fictitious PAH with the rotational constants A = 432 B = 370 and C = 344 MHz under several astronomical environments: Cold Neutral Medium, Molecular Cloud, Dark Cloud and Reflection Nebula.

Appendix B: Rotational constants and dipole moments of silicate nanoclusters

Table B.1. Rotational (B_α) constants (MHz) for the nanoclusters in this work.

Molecule	B_x (MHz)	B_y (MHz)	B_z (MHz)
O-1	3260.983	1291.755	925.244
O-2	614.676	583.865	373.861
O-3	312.054	277.278	221.305
O-4	196.153	143.527	106.91
O-5	114.285	101.138	75.222
O-6	85.73	72.891	64.873
O-7	73.928	47.551	42.208
O-8	54.536	40.455	38.061
O-9	45.888	31.399	29.14
O-10	37.203	28.814	24.862
P-1	9876.871	2947.067	2269.802
P-2	1472.618	1176.786	746.653
P-3	565.57	492.799	398.548
P-4	391.274	210.07	189.036
P-5	279.393	158.611	146.333
P-6	201.405	101.628	98.244
P-7	137.455	86.734	76.038
P-8	94.832	82.928	62.082
P-9	71.393	66.017	58.03
P-10	64.729	57.262	46.684
SiO-2	11267.036	5809.04	3832.887
SiO-3	2590.916	2590.65	1295.392
SiO-4	1224.702	1209.03	680.397
SiO-5	1408.354	430.413	416.801
SiO-6	614.419	445.02	442.944
SiO-7	467.093	467.05	277.431
SiO-8	352.59	336.434	267.523
SiO-9	289.786	227.942	214.823
SiO-10	229.872	178.145	134.59
SiO-11	242.421	98.354	89.432
SiO-12	196.505	101.967	87.743
SiO-13	155.539	82.323	76.655
SiO-14	148.656	64.472	64.22
SiO-15	133.012	52.728	50.781
SiO-16	158.38	48.654	46.506
SiO-17	81.492	68.293	51.566
SiO-18	90.666	42.475	41.509
SiO-19	86.865	50.438	50.425
SiO-20	72.194	46.981	42.23

Table B.2. Total dipole moments (μ) in Debyes (D) for olivine (O-N), pyroxene (P-N) and silicon monoxide (SiO-N) nanoclusters.

Molecule	μ (D)
O-1	9.50
O-2	6.00
O-3	1.99
O-4	11.60
O-5	2.03
O-6	3.28
O-7	6.60
O-8	6.56
O-9	5.79
O-10	3.27
P-1	12.60
P-2	0.00
P-3	3.28
P-4	2.83
P-5	4.28
P-6	0.00
P-7	6.39
P-8	5.29
P-9	6.61
P-10	5.29
SiO-2	0.00
SiO-3	0.00
SiO-4	0.00
SiO-5	0.73
SiO-6	2.20
SiO-7	0.18
SiO-8	1.68
SiO-9	1.79
SiO-10	1.41
SiO-11	1.19
SiO-12	0.92
SiO-13	1.44
SiO-14	1.08
SiO-15	1.52
SiO-16	0.76
SiO-17	1.63
SiO-18	1.78
SiO-19	3.13
SiO-20	3.55

4. Error estimation from the use of the Rigid-Rotor approximation.

A&A 634, A77 (2020)

Appendix C: Estimate of changes due to centrifugal distortion

The frequencies at which a linear rotor would emit are calculated as:

$$\nu_R(J) = 2B(J+1) - 4D(J+1)^3. \quad \text{(C.1)}$$

In general, the difference in orders of magnitude between B and D is of the order of 4 to 6. As stated in the text, the Gaussian16 package can calculate centrifugal constants. In Table C.1 we compare the smallest rotational constant (B_z) with the centrifugal constants (D_j) for P-1 and P-2 nanoclusters.

The difference in orders of magnitude are 6 for P-1 and 7 for P-2. We can estimate the importance of the centrifugal term by calculating the fraction $4D(J+1)^3/2B(J+1)$ using $J = 400$, $B = 1$ and two values of $D_1 = 10^{-6}$ and $D_2 = 10^{-7}$. For D_1, the fraction is 0.32, which means that the frequencies can be shifted up to 32%, while for D_2, the fraction lowers down to 3.2%.

Table C.1. Rotational (MHz) and Wilson centrifugal distortion constants (kHZ) for P-1 and P-2 nanoclusters.

Molecule	B_z (MHz)	D_j (kHz)	D_jk (kHz)	D_k (kHz)
P-1	2269.802	0.4145	1.7794	6.3816
P-2	746.653	0.0531	−0.102	0.0357

We remind the reader that $J = 400$ may only be accessible for the largest O-10 nanocluster, while the smallest particles should achieve maximum J values of the order of ∼50 to ∼100. For the P-1 nanocluster, we find that using the reported data in Table C.1 the difference is of the order of 0.2%. The centrifugal distortion term will likely reduce as size increases, thus the most likely value for the O-10 is D_2 rather than D_1. Hence, we expect our results to have a typical error of approximately 3% with respect to the real spectra.

5. Link to developed codes and electronic supplementary information (ESI) of the chapters.

ESI for Chapter 5:
https://doi.org/10.1063/1.5095071%23suppl

ESI for Chapter 6:
http://www.rsc.org/suppdata/c9/nr/c9nr00812h/c9nr00812h1.pdf

ESI for Chapter 10:
https://pubs.acs.org/doi/abs/10.1021/acsearthspacechem.9b00139#notes1

ESI for Chapter 12:
https://pubs.acs.org/doi/abs/10.1021/acsearthspacechem.9b00157#notes1

Code for evaluating mixing energies
https://gitlab.com/a.macia/MixingEnergies

6. List of Publications participated by the author of this thesis.

1. Escatllar, A. M., & Bromley, S. T. (2020). Assessing the viability of silicate nanoclusters as carriers of the anomalous microwave emission: a quantum mechanical study. *Astronomy & Astrophysics*, *634*, A77.

2. Zamirri, L., Macià Escatllar, A., Mariñoso Guiu, J., Ugliengo, P., & Bromley, S. T. (2019). What Can Infrared Spectra Tell Us about the Crystallinity of Nanosized Interstellar Silicate Dust Grains?. *ACS Earth and Space Chemistry*, *3*(10), 2323-2338.

3. Escatllar, A. M., Lazaukas, T., Woodley, S. M., & Bromley, S. T. (2019). Structure and Properties of Nanosilicates with Olivine (Mg2SiO4) N and Pyroxene (MgSiO3) N Compositions. *ACS Earth and Space Chemistry*, *3*(11), 2390-2403.

4. Morales-García, Á., Escatllar, A. M., Illas, F., & Bromley, S. T. (2019). Understanding the interplay between size, morphology and energy gap in photoactive TiO 2 nanoparticles. *Nanoscale*, *11*(18), 9032-9041.

5. Macià Escatllar, A., Morales-García, Á., Illas, F., & Bromley, S. T. (2019). Efficient preparation of TiO2 nanoparticle models using interatomic potentials. *The Journal of chemical physics*, *150*(21), 214305.

6. Cuko, A., Escatllar, A. M., Calatayud, M., & Bromley, S. T. (2018). Properties of hydrated TiO 2 and SiO 2 nanoclusters: dependence on size, temperature and water vapour pressure. *Nanoscale*, *10*(45), 21518-21532.

7. Macià Escatllar, A., Ugliengo, P., & Bromley, S. T. (2017). Computing Free Energies of Hydroxylated Silica Nanoclusters: Forcefield versus Density Functional Calculations. *Inorganics*, *5*(3), 41.

8. Cuko, A., Maciá, A., Calatayud, M., & Bromley, S. T. (2017). Global optimisation of hydroxylated silica clusters: A cascade Monte Carlo Basin Hopping approach. *Computational and Theoretical Chemistry*, *1102*, 38-43.